

[CC BY 4.0 DEED Attribution 4.0 International](#)

Access to this work was provided by the University of Maryland, Baltimore County (UMBC) ScholarWorks@UMBC digital repository on the Maryland Shared Open Access (MD-SOAR) platform.

Please provide feedback

Please support the ScholarWorks@UMBC repository by emailing scholarworks-group@umbc.edu and telling us what having access to this work means to you and why it's important to you. Thank you.



Apache Point Observatory (APO)/SMARTS Flare Star Campaign Observations. I. Blue Wing Asymmetries in Chromospheric Lines during Mid-M-Dwarf Flares from Simultaneous Spectroscopic and Photometric Observation Data

Yuta Notsu^{1,2} , Adam F. Kowalski^{1,2,3} , Hiroyuki Maehara⁴ , Kosuke Namekata⁵ , Kenji Hamaguchi^{6,7} , Teruaki Enoto^{8,9} , Isaiah I. Tristan^{1,2,3} , Suzanne L. Hawley¹⁰ , James R. A. Davenport¹⁰ , Satoshi Honda¹¹ , Kai Ikuta¹² , Shun Inoue⁸ , Keiichi Namizaki¹³ , Daisaku Nogami¹³ , and Kazunari Shibata^{14,15}

¹ Laboratory for Atmospheric and Space Physics, University of Colorado Boulder, 3665 Discovery Drive, Boulder, CO 80303, USA; Yuta.Notsu@colorado.edu

² National Solar Observatory, 3665 Discovery Drive, Boulder, CO 80303, USA

³ Department of Astrophysical and Planetary Sciences, University of Colorado Boulder, 2000 Colorado Avenue, Boulder, CO 80305, USA

⁴ Okayama Branch Office, Subaru Telescope, National Astronomical Observatory of Japan, NINS, Kamogata, Asakuchi, Okayama 719-0232, Japan

⁵ ALMA Project, National Astronomical Observatory of Japan, NINS, Mitaka, Tokyo, 181-8588, Japan

⁶ CRESST II and X-ray Astrophysics Laboratory, NASA/GSFC, Greenbelt, MD 20771, USA

⁷ Department of Physics, University of Maryland, Baltimore County, 1000 Hilltop Circle, Baltimore, MD 21250, USA

⁸ Department of Physics, Kyoto University, Sakyo, Kyoto 606-8502, Japan

⁹ RIKEN Cluster for Pioneering Research, 2-1 Hirosawa, Wako, Saitama 351-0198, Japan

¹⁰ Department of Astronomy, University of Washington, Seattle, WA 98195, USA

¹¹ Nishi-Harima Astronomical Observatory, Center for Astronomy, University of Hyogo, Sayo, Hyogo 679-5313, Japan

¹² Department of Multidisciplinary Sciences, The University of Tokyo, 3-8-1 Komaba, Meguro, Tokyo 153-8902, Japan

¹³ Department of Astronomy, Kyoto University, Sakyo, Kyoto 606-8502, Japan

¹⁴ Kwasan Observatory, Kyoto University, Yamashina, Kyoto 607-8471, Japan

¹⁵ School of Science and Engineering, Doshisha University, Kyotanabe, Kyoto 610-0321, Japan

Received 2023 January 18; revised 2023 September 23; accepted 2023 October 2; published 2024 January 25

Abstract

We conducted the time-resolved simultaneous optical spectroscopic and photometric observations of mid-M-dwarf flare stars YZ CMi, EV Lac, and AD Leo. Spectroscopic observations were obtained using Apache Point Observatory 3.5 m and Small and Moderate Aperture Research Telescope System 1.5 m telescopes during 31 nights. Among the 41 detected flares, seven flares showed clear blue wing asymmetries in the $H\alpha$ line, with various correspondences in flare properties. The duration of the blue wing asymmetries range from 20 minutes to 2.5 hr, including a flare showing the shift from blue to red wing asymmetry. Blue wing asymmetries can be observed during both white-light and candidate non-white-light flares. All of the seven flares showed blue wing asymmetries also in the $H\beta$ line, but there are large varieties on which other chromospheric lines showed blue wing asymmetries. One among the 7 flares was also observed with soft X-ray spectroscopy, which enabled us to estimate the flare magnetic field and length of the flare loop. The line-of-sight velocities of the blueshifted components range from -73 to -122 km s⁻¹. Assuming that the blueshifts were caused by prominence eruptions, the mass of upward-moving plasma was estimated to be 10^{15} – 10^{19} g, which are roughly on the relation between flare energy and erupting mass expected from solar coronal mass ejections (CMEs). Although further investigations are necessary for understanding the observed various properties, these possible prominence eruptions on M-dwarfs could evolve into CMEs, assuming the similar acceleration mechanism with solar eruptions.

Unified Astronomy Thesaurus concepts: [Stellar flares \(1603\)](#); [Stellar coronal mass ejections \(1881\)](#); [Optical flares \(1166\)](#); [Stellar x-ray flares \(1637\)](#); [M dwarf stars \(982\)](#); [Flare stars \(540\)](#); [Red dwarf flare stars \(1367\)](#); [Stellar chromospheres \(230\)](#)

1. Introduction

Solar flares are sudden brightness increases resulting from impulsive magnetic energy release through magnetic reconnection in the solar atmosphere (e.g., Shibata & Magara 2011 and references therein). They generate strong emissions at various wavelengths ranging from radio to high-energy X-rays and gamma rays. In the flaring solar atmosphere, part of the magnetic energy released by the magnetic reconnection in the corona is transported into the lower atmosphere (chromosphere and upper photosphere) through thermal conduction, radiative backwarming, and high-energy particles (e.g., high-energy

electrons). This process causes chromospheric evaporations and chromospheric condensations, producing bright coronal (e.g., X-ray), chromospheric (e.g., $H\alpha$), and photospheric radiation (e.g., Fisher et al. 1985; Allred et al. 2005).

It is also known that various types of stars produce flares (*stellar flares*). They are observed mainly as rapid increases and slow decays of the intensity in various wavelength bands (radio; optical; ultraviolet, hereafter UV; X-ray). In particular, young rapidly rotating stars, close binary stars, and magnetically active M-type main-sequence stars (dMe stars) show frequent and energetic flares (e.g., Lacy et al. 1976; Hawley & Pettersen 1991; Shibata & Yokoyama 2002; Gershberg 2005; Reid & Hawley 2005; Benz & Güdel 2010). Recent photometry from Kepler/the Transiting Exoplanet Survey Satellite (TESS) space telescopes (e.g., Maehara et al. 2012; Notsu et al. 2013b; Shibayama et al. 2013; Hawley et al. 2014; Davenport 2016; Notsu et al.



Original content from this work may be used under the terms of the [Creative Commons Attribution 4.0 licence](#). Any further distribution of this work must maintain attribution to the author(s) and the title of the work, journal citation and DOI.

2019; Paudel et al. 2019; Davenport et al. 2020; Feinstein et al. 2020; Medina et al. 2020; Maehara et al. 2021; Okamoto et al. 2021) and ground-based surveys (e.g., Howard et al. 2019; Jackman et al. 2021) have helped to refine statistical properties of stellar flares. Because of the similarities in observational properties between solar and stellar flares such as Neupert effect (Neupert 1968; Hawley et al. 1995; Güdel et al. 1996; Güdel et al. 2004; Mitra-Kraev et al. 2005; Tristan et al. 2023), they are considered to be caused by the same physical processes (i.e., plasma heating by accelerated particles and subsequent chromospheric evaporation, e.g., Hawley & Fisher 1992; Allred et al. 2006; Kowalski 2016; Namekata et al. 2020). Recently, stellar flares have been also getting more and more attention in terms of the effects on the exoplanet atmosphere and habitability (e.g., Lammer et al. 2007; Segura et al. 2010; Airapetian et al. 2016; Linsky 2019; Airapetian et al. 2020) and possible extreme events on our Sun (Aulanier et al. 2013; Shibata et al. 2013; Battersby 2019; Miyake et al. 2019; Notsu et al. 2019; Okamoto et al. 2021; Usoskin & Kovaltsov 2021; Buzulukova & Tsurutani 2022; Cliver et al. 2022).

Spectroscopic studies of solar and stellar flares have been carried out in order to understand the dynamics of plasma and the radiation mechanisms during flares. Past spectroscopic observations of solar flares have shown that chromospheric lines (e.g., $H\alpha$, $H\beta$, Ca II, Mg II) often exhibit asymmetric line profiles during flares. In particular, red wing asymmetries (enhancement of the red wing) have often been observed during solar flares (e.g., Švestka et al. 1962; Ichimoto & Kurokawa 1984; Canfield et al. 1990; Shoji & Kurokawa 1995; Berlicki 2007; Graham & Cauzzi 2015; Kuridze et al. 2015; Kowalski et al. 2017; Graham et al. 2020; Namekata et al. 2022a; Otsu et al. 2022). This is thought to be caused by the process known as the chromospheric condensation, which is the downward flow of cool plasma in the chromosphere, while Kuridze et al. (2015) also reported the enhancement of red side of the line profile around the line center (line center red asymmetry) caused by upflows. Blue wing asymmetries (enhancement of the blue wing) have also been observed mainly in the early phase of solar flares (e.g., Švestka et al. 1962; Canfield et al. 1990; Heinzel et al. 1994a; Kuridze et al. 2016; Panos et al. 2018; Tei et al. 2018; Huang et al. 2019; Li et al. 2019; Libbrecht et al. 2019). Švestka et al. (1962) found that, among the 92 studied solar flares, only 23% showed a blue asymmetry, while 80% exhibited a red asymmetry. Tang (1983) reported the similar result that an even lower fraction of 5% of flares have blue asymmetries. As one possibility, it is suggested that blue asymmetry is caused by an upward-moving cool plasma blob, which is lifted up by expanding hot plasma caused by the deep penetration of nonthermal electrons into the chromosphere during a flare (Tei et al. 2018; Huang et al. 2019; Zhu et al. 2019; Hong et al. 2020). However, the detailed origins and properties of these blue asymmetries are still controversial.

For example, these asymmetries could be also caused by either excess or lack of flux on one side of the line profile without upward-moving plasma.

Similar line asymmetries in chromospheric lines (especially $H\alpha$ line) have been observed during stellar flares on late-type stars (e.g., M-dwarf flare stars). For example, Houdebine et al. (1993), Crespo-Chacón et al. (2006), Wollmann et al. (2023), and Namizaki et al. (2023) reported red asymmetries in Balmer lines during flares on M-dwarf flare stars. Moreover, in the case

of M-dwarf flare stars, various blue asymmetries have been widely observed (e.g., Houdebine et al. 1990; Eason et al. 1992; Gunn et al. 1994; Crespo-Chacón et al. 2006; Hawley et al. 2007; Fuhrmeister et al. 2008 and Fuhrmeister et al. 2011; Vida et al. 2016; Honda et al. 2018; Vida et al. 2019; Muheki et al. 2020a; Muheki et al. 2020b; Johnson et al. 2021; Maehara et al. 2021). Not only on M-dwarfs, but blue asymmetries or blueshifted absorption during flares have been also observed during flares on the young active K dwarf LQ Hydrae (Flores Soriano & Strassmeier 2017) and young active G dwarf (solar-type star) EK Dra (Namekata et al. 2022c).

These previous studies have clarified large varieties of blue asymmetries. Fuhrmeister et al. (2008, 2011) investigated flares on M5.5 dwarfs Proxima Centauri and CN Leo, respectively, and they both reported blue asymmetry of $H\alpha$ line during flare onset and red asymmetry during decay, along with temporal evolution in the asymmetry pattern on the scale of minutes. Vida et al. (2016) reported several $H\alpha$ flares on the M4 dwarf V374 Peg showing blue wing asymmetries of $H\alpha$, $H\beta$, and $H\gamma$ lines with a maximum line-of-sight velocity of -675 km s^{-1} . Vida et al. (2016) also found that red-wing enhancements in the $H\alpha$ line were observed after blue wing asymmetries, which can suggest that some of the erupted cool plasma fell back on the stellar surface. Honda et al. (2018) reported a long-duration $H\alpha$ flare on the M4.5 dwarf EV Lac. During this flare, a blue wing asymmetry in the $H\alpha$ line with the velocity of $\sim -100 \text{ km s}^{-1}$ has been observed for $\gtrsim 2 \text{ hr}$ (almost from flare start to end). Maehara et al. (2021) reported a $H\alpha$ flare without clear brightening in continuum, which exhibited blue wing asymmetry lasting for $\sim 1 \text{ hr}$. The line-of-sight motions of cool plasma such as prominence eruptions can cause blue and/or red wing asymmetries of stellar spectral lines. Solar prominences and filaments are cool plasma blobs ($\sim 10,000 \text{ K}$) in the hot corona ($\gtrsim 10^6 \text{ K}$), and they are observed above the limb (prominences) and on the disk (filaments), respectively (Parenti 2014; Vial & Engvold 2015). In the case of the Sun, prominences are commonly observed in emission of Balmer lines (especially $H\alpha$ line), while filaments show absorption lines (Parenti 2014; Otsu et al. 2022). The eruptions of such solar prominences and filaments are often observed, and they are often associated with solar flares (e.g., Shibata & Magara 2011; Sinha et al. 2019). Such filament and/or prominence eruptions can evolve into coronal mass ejections (CMEs) if the erupted plasma is accelerated enough until the velocity exceeds the escape velocity (e.g., Gopalswamy et al. 2003; Seki et al. 2021). In analogy with solar prominence eruptions, if the cool stellar plasma is launched upward and seen above the limb,¹⁶ the emission can cause blueshifted or redshifted enhancements of the Balmer lines (e.g., Odert et al. 2020), and this can be eventually related with CMEs.

Several recent studies have discussed the blue wing asymmetries assuming they can be related with stellar mass ejections. Vida et al. (2019) reported a statistical study of 478 events with asymmetries in Balmer lines of M-dwarfs, which were found from more than 5500 spectra (similar events were also reported in Fuhrmeister et al. 2018). The velocity and mass of the possible ejected materials estimated from the blueshifted or redshifted excess in Balmer lines range from 100 to 300 km s^{-1}

¹⁶ Leitzinger et al. (2022) discussed that even filaments can cause enhancements in Balmer lines of M-dwarfs. It may be speculated that the plasma, which causes the enhancements, is not necessary to be seen above the limb, but is possible to be seen also on the disk.

Table 1
Target Star Basic Parameters

Star Name	Spectral Type ^a	U^a (mag)	g^a (mag)	V^a (mag)	d_{Gaia}^b (pc)	R_{star}^a (R_{\odot})	P_{rot}^c (days)	$v \sin i^d$ (km s^{-1})	i^d (deg)
YZ CMi (Gl 285)	dM4.5e	13.77	11.76	11.19	5.99	0.30	2.77	5.0	60
EV Lac (Gl 873)	dM3.5e	12.96	10.99	10.28	5.05	0.36	4.30	4.0	60
AD Leo (Gl 388)	dM3e	11.91	10.12	9.32	4.97	0.43	2.24	3.0	20

Notes.

^a The Spectral type, U - and V -band magnitudes, and stellar radius (R_{star}) values are from Table 1 of Kowalski et al. (2013). The g -band magnitudes are from Zacharias et al. (2013).

^b Stellar distance from Gaia DR2 catalog (Gaia Collaboration et al. 2018).

^c Rotation Period values (P_{rot}). The values of YZ CMi and EV Lac are those estimated from TESS data in Maehara et al. (2021), Muheki et al. (2020b), respectively. The P_{rot} value of AD Leo is from Morin et al. (2008).

^d Projected rotational velocities ($v \sin i$) and stellar inclination angle values (i), reported in Morin et al. (2008).

and 10^{15} – 10^{18} g, respectively. The correlations between the mass and kinetic energy of CMEs and the flare energy of associated flares on various types of stars have been discussed (e.g., Moschou et al. 2019; Maehara et al. 2021; Namekata et al. 2022c). They found that estimated stellar flare CME masses are consistent with the trends extrapolated from solar events, but kinetic energies are roughly 2 orders of magnitude smaller than expected. Maehara et al. (2021), Namekata et al. (2022c) suggested that this could be understood by the difference in the velocity between CMEs and prominence eruptions.

It is important to understand the properties of stellar CMEs in order to evaluate their effects not only on the mass and angular momentum loss of the star (e.g., Osten & Wolk 2015; Cranmer 2017; Odert et al. 2017; Wood et al. 2021) but also on the habitability of exoplanets (e.g., loss of atmosphere, atmospheric chemistry, radiation dose as described in Lammer et al. 2007; Segura et al. 2010; Airapetian et al. 2016; Scheucher et al. 2018; Tilley et al. 2019; Yamashiki et al. 2019; Airapetian et al. 2020; Chen et al. 2021). Attempts to detect stellar CMEs have not yet found the expected Type-II radio signatures (e.g., Crosley & Osten 2018; Villadsen & Hallinan 2019), but several candidates have been reported: line blue asymmetries (described above), post-flare UV and X-ray dimmings (Veronig et al. 2021; Loyd et al. 2022), and a possible Type-IV radio burst (Zic et al. 2020). However, our understanding of blue and red asymmetries in chromospheric lines and their connections with stellar flares and CMEs is still limited by the low number of samples observed in time-resolved spectroscopy simultaneously with high-precision photometry (see also Namekata et al. 2022b and Leitzinger & Odert 2022 for brief reviews of current stellar CME observations).

In order to investigate the connection between the blue and red asymmetries in Balmer lines and the properties of flares more in detail, we conducted the time-resolved simultaneous optical spectroscopic and photometric observations of mid-M-dwarf flare stars, during the 31 nights over 2 yr (2019 January–2021 February). Spectroscopic observations were conducted using the high-dispersion spectrographs of the Apache Point Observatory (APO) 3.5 m telescope and the Cerro Tololo Inter-American Observatory (CTIO) Small and Moderate Aperture Research Telescope System (SMARTS) 1.5 m telescope. Photometric observations were obtained from the 0.5 m telescope of APO (Astrophysical Research Consortium Small Aperture Telescope, hereafter ARCSAT) and 1 m and 0.4 m telescopes of the Las Cumbres Observatory Global Telescope (LCOGT) network, while 5 nights are also covered with the observation window of TESS. For the 3 nights among the total

31 nights, we also conducted the soft X-ray spectroscopic observations with Neutron Star Interior Composition Explorer (NICER). In Section 2, the details of our campaign monitoring observations and data analyses are described. In Section 3, we report the light curves and $H\alpha$ and $H\beta$ spectra of the flares detected in our campaign observations. We investigate whether the flares show blue wing asymmetries in $H\alpha$ and $H\beta$ lines. If the blue wing asymmetries are observed in $H\alpha$ and $H\beta$ lines, we also investigate whether other chromospheric lines (e.g., $H\gamma$, $H\delta$, Ca II K) also show blue wing asymmetries. In Section 4, we discuss the various properties of flares with blue wing asymmetries, and the implications from the observed blue wing asymmetries on the possible stellar mass ejections.

2. Data and Methods

2.1. Target Stars

During the 31 nights over 2 yr (2019 January–2021 February), we conducted time-resolved simultaneous optical spectroscopic and photometric observations of the three nearby mid-M-dwarf flare stars YZ CMi, EV Lac, and AD Leo. The basic parameters of these three target flare stars are listed in Table 1. The log of the observations is summarized in Table 2. These three stars have been known to flare frequently (e.g., Lacy et al. 1976; Hawley & Pettersen 1991; Kowalski et al. 2013; Muheki et al. 2020b; Namekata et al. 2020; Maehara et al. 2021; Paudel et al. 2021; Ikuta et al. 2023). Zeeman-broadening and Zeeman-Doppler Imaging observations of these stars have shown the existence of strong magnetic fields on the stellar surface (e.g., Saar & Linsky 1985; Johns-Krull & Valenti 2000; Reiners & Basri 2007; Morin et al. 2008; Kochukhov 2021).

2.2. Spectroscopic Data

Time-resolved spectroscopic observations were obtained at two facilities. For the 25 nights among the total 31 nights (Table 2), we conducted spectroscopic observations of the three target stars, using the ARC Echelle Spectrograph (ARCES; Wang et al. 2003) on the ARC 3.5 m telescope at Apache Point Observatory (APO). The wavelength resolution ($R = \lambda/\Delta\lambda$) is ~ 32000 , and the spectral coverage is 3800–10000 Å. This wavelength range includes $H\alpha$, $H\beta$, $H\delta$, $H\gamma$, $H\epsilon$, Ca II H&K, Ca II 8542 Å, He I D3 5876, and Na I D1 and D2 lines. The exposure times are listed in Table 2, which were determined to achieve signal-to-noise ratio (S/N) values ~ 40 – 50 at the continuum level around the $H\alpha$ 6563 Å line. We note that the APO/ARCES spectroscopic data have a relatively long

Table 2
Observation Log

Telescope/Instrument (Data Type)	UT Date (MJD)	Time ^a (hr)	Exp. Time (s)
YZ CMi			
ARC 3.5 m/ARCES (3800–10000 Å; $\lambda/\Delta\lambda \sim 32000$)	2019 Jan 26 (58509)	7.2	600, 900
	2019 Jan 27 (58510)	7.5	300
	2019 Jan 28 (58511)	7.2	300, 600
	2019 Dec 2 (58819)	1.8	300
	2019 Dec 8 (58825)	2.4	300
	2019 Dec 12 (58829)	5.8	300
	2019 Dec 15 (58832)	1.9	300
	2020 Jan 14 (58862)	3.9	300
	2020 Jan 18 (58866)	4.9	300, 600
	2020 Jan 20 (58868)	4.9	300, 450, 600
	2020 Dec 3 (59186)	4.1	300, 600
	2020 Dec 6 (59189)	5.3	300, 450
	2020 Dec 7 (59190)	5.7	300, 360
	2021 Jan 31 (59245)	9.9	450, 600, 900
	2021 Feb 4 (59249)	1.8	900
SMARTS 1.5 m/CHIRON (4500–8900 Å; $\lambda/\Delta\lambda \sim 25000$)	2020 Jan 16 (58864)	5.2	600
	2020 Jan 17 (58865)	4.2	600
	2020 Jan 18 (58866)	6.0	600
	2020 Jan 19 (58867)	5.0	600
	2020 Jan 20 (58868)	6.0	600
	2020 Jan 21 (58869)	6.0	600
	2020 Jan 22 (58870)	6.0	600
	2020 Jan 23 (58871)	6.0	600
ARCSAT 0.5 m/flarecam (<i>u</i> -, <i>g</i> -band photometry) ^b	2019 Jan 26 (58509)	1.0 (<i>u</i>), 7.0 (<i>g</i>)	30 (<i>u</i>), 4, 15, 30 (<i>g</i>)
	2019 Jan 27 (58510)	7.3 (<i>u</i>), 7.3 (<i>g</i>)	30 (<i>u</i>), 4 (<i>g</i>)
	2019 Jan 28 (58511)	7.0 (<i>u</i>), 7.3 (<i>g</i>)	30 (<i>u</i>), 4, 6, 12, 20 (<i>g</i>)
	2019 Dec 2 (58819)	1.2 (<i>u</i>), 1.2 (<i>g</i>)	30 (<i>u</i>), 6 (<i>g</i>)
	2019 Dec 12 (58829)	7.2 (<i>u</i>), 7.2 (<i>g</i>)	30 (<i>u</i>), 6 (<i>g</i>)
	2019 Dec 15 (58829)	2.6 (<i>u</i>), 2.6 (<i>g</i>)	30 (<i>u</i>), 6 (<i>g</i>)
	2020 Jan 14 (58862)	5.6 (<i>u</i>), 5.6 (<i>g</i>)	30 (<i>u</i>), 6 (<i>g</i>)
	2020 Jan 18 (58866)	6.2 (<i>u</i>), 6.2 (<i>g</i>)	30 (<i>u</i>), 6 (<i>g</i>)
	2020 Jan 19 (58867)	7.5 (<i>u</i>), 7.5 (<i>g</i>)	30 (<i>u</i>), 6 (<i>g</i>)
	2020 Jan 20 (58868)	7.4 (<i>u</i>), 7.4 (<i>g</i>)	30 (<i>u</i>), 6 (<i>g</i>)
	2020 Dec 3 (59186)	4.1 (<i>g</i>)	6 (<i>g</i>)
	2020 Dec 6 (59189)	6.4 (<i>u</i>), 6.4 (<i>g</i>)	30 (<i>u</i>), 6 (<i>g</i>)
	2020 Dec 7 (59190)	6.1 (<i>u</i>), 6.1 (<i>g</i>)	30 (<i>u</i>), 6 (<i>g</i>)
	2021 Jan 31 (59245)	7.4 (<i>u</i>), 7.4 (<i>g</i>)	30 (<i>u</i>), 6 (<i>g</i>)
	2021 Feb 4 (59249)	0.6 (<i>u</i>), 0.6 (<i>g</i>)	30 (<i>u</i>), 6 (<i>g</i>)
LCO 1 m/Sinistro (<i>U</i> -band photometry) ^b	2020 Jan 16 (58864)	5.1	25
	2020 Jan 17 (58865)	0.8	25
	2020 Jan 18 (58866)	8.1	10, 25
	2020 Jan 19 (58867)	4.2	10
	2020 Jan 20 (58868)	4.5	10
	2020 Jan 21 (58869)	4.1	10
	2020 Jan 22 (58870)	4.0	10
	2020 Jan 23 (58871)	6.2	10
	2020 Jan 24 (58872)	3.2	10
	2020 Jan 25 (58873)	5.3	10
	2020 Jan 26 (58874)	5.4	10
	2020 Jan 27 (58875)	0.9	10
LCO 0.4 m/SBIG (<i>V</i> -band photometry) ^b	2020 Jan 16 (58864)	5.4	6
	2020 Jan 17 (58865)	2.3	6
	2020 Jan 18 (58866)	9.6	6
	2020 Jan 19 (58867)	4.9	6
	2020 Jan 20 (58868)	10.1	6
	2020 Jan 21 (58869)	6.7	6
	2020 Jan 22 (58870)	5.7	6
	2020 Jan 23 (58871)	5.9	6
	2020 Jan 24 (58872)	3.3	6

Table 2
(Continued)

Telescope/Instrument (Data Type)	UT Date (MJD)	Time ^a (hr)	Exp. Time (s)
TESS (TESS-band photometry) ^b	Covering our observations on 2019 Jan 26–28 and 2021 Jan 31–Feb 4		120
NICER (0.2–12 keV X-ray)	2019 Jan 26 (58509)	$\sim 0.5 \times 3$...
	2019 Jan 27 (58510)	$\sim 0.5 \times 4$...
	2019 Jan 28 (58511)	$\sim 0.5 \times 3$...
EV Lac			
ARC 3.5 m/ARCES (3800–10000 Å; $\lambda/\Delta\lambda \sim 32000$)	2019 Dec 15 (58832)	5.1	240, 250, 300
	2020 Aug 26 (59087)	4.4	240, 300, 340, 360, 400
	2020 Aug 27 (59088)	4.2	300
	2020 Aug 29 (59090)	4.3	300, 360, 600
	2020 Aug 30 (59091)	0.7	300, 600
	2020 Sep 1 (59093)	3.0	300
	2020 Sep 2 (59094)	4.4	300
ARCSAT 0.5 m/flarecam (<i>u</i> -, <i>g</i> -band photometry) ^b	2019 Dec 15 (58832)	2.8 (<i>u</i>), 2.9 (<i>g</i>)	20 (<i>u</i>), 3 (<i>g</i>)
	2020 Aug 26 (59087)	8.0 (<i>u</i>), 8.0(<i>g</i>)	20 (<i>u</i>), 3 (<i>g</i>)
	2020 Aug 27 (59088)	7.9 (<i>u</i>), 7.9 (<i>g</i>)	20 (<i>u</i>), 3 (<i>g</i>)
	2020 Aug 29 (59090)	4.2 (<i>u</i>), 4.2 (<i>g</i>)	20 (<i>u</i>), 3 (<i>g</i>)
	2020 Aug 30 (59091)	0.5 (<i>u</i>), 0.5 (<i>g</i>)	20 (<i>u</i>), 3 (<i>g</i>)
	2020 Sep 1 (59093)	2.1 (<i>u</i>), 2.1 (<i>g</i>)	20 (<i>u</i>), 3 (<i>g</i>)
	2020 Sep 2 (59094)	8.5 (<i>u</i>), 8.5 (<i>g</i>)	20 (<i>u</i>), 3 (<i>g</i>)
AD Leo			
ARC 3.5 m/ARCES (3800–10000 Å; $\lambda/\Delta\lambda \sim 32000$)	2019 May 17 (58620)	3.6	180, 200, 300
	2019 May 18 (58621)	3.6	200, 240, 300
	2019 May 19 (58622)	3.6	200, 240, 300
ARCSAT 0.5 m/flarecam (<i>u</i> -, <i>g</i> -band photometry) ^b	2019 May 17 (58620)	2.8 (<i>u</i>), 2.8 (<i>g</i>)	20 (<i>u</i>), 1 (<i>g</i>)
	2019 May 18 (58621)	2.8 (<i>u</i>), 3.0 (<i>g</i>)	20 (<i>u</i>), 1 (<i>g</i>)
	2019 May 19 (58622)	2.9 (<i>u</i>), 2.9 (<i>g</i>)	20 (<i>u</i>), 1 (<i>g</i>)

Notes.^a Time is the total monitoring time for the night.^b Filter profiles of these bands are shown in Figure 1.

overhead and read-out time: ~ 180 s in total. The data reduction methods of APO 3.5 m/ARCES spectroscopic data are the same as in Notsu et al. (2019). We conducted standard image reduction procedures such as bias subtraction, flat-fielding, and scattered light subtraction, using the ECHELLE package in IRAF¹⁷ and PyRAF¹⁸ software. We used a Th/Ar lamp for wavelength calibration. We also applied the heliocentric radial velocity correction using the ECHELLE package.

For the 8 nights among the total 31 nights (Table 2), we conducted spectroscopic observations of one of the target stars YZ CMi, using the cross-dispersed, fiber-fed echelle CTIO High ResolutiON (CHIRON) spectrograph (Tokovinin et al. 2013) attached to the SMARTS 1.5 m telescope at CTIO. For the 2 among these 8 nights (Table 2), we also observed YZ CMi, using APO 3.5 m/ARCES. The wavelength range and wavelength resolution of our CHIRON data are 4500–8900 Å and

$R \sim 25,000$, respectively. This wavelength range includes H α , H β , Ca II 8542 Å, He I D3 5876, and Na I D1 and D2 lines. The exposure time was 600 s (Table 2), which was determined to achieve S/N values ~ 40 at the continuum level around the H α 6563 Å line. The spectra were reduced using the CHIRON pipeline described in Tokovinin et al. (2013).

2.3. Photometric Data

Time-resolved photometric observations were done by using two ground-based facilities (ARCSAT and LCOGT) and TESS satellite. We conducted ground-based photometric observations using 0.5 m ARCSAT for the 24 nights (Table 2), simultaneously with the spectroscopic observations using APO 3.5 m/ARCES. We note that, among the 25 nights when we conducted APO 3.5 m/ARCES spectroscopic observations, we have no ARCSAT 0.5 m photometric data on 2019 December 8 because of the bad weather condition. We carried out *u* and *g*-band photometric observations using the Flarecam instrument of ARCSAT 0.5 m (Hilton 2011; Kowalski et al. 2013), which has enhanced UV sensitivity and rapid filter wheel rotation. The exposure times are listed in Table 2. Considering the filter wheel rotation time, the typical time cadence for each band is

¹⁷ IRAF is distributed by the National Optical Astronomy Observatories, which are operated by the Association of Universities for Research in Astronomy, Inc., under cooperative agreement with the National Science Foundation.

¹⁸ PyRAF is part of the stscipython package of astronomical data analysis tools and is a product of the Science Software Branch at the Space Telescope Science Institute.

Table 3
Quiescent Luminosities of Continuum Bands and Quiescent Flux Densities Around Lines

Star Name	$\log L_{U,q}^a$	$\log L_{u,q}^a$	$\log L_{g,q}^a$	$\log L_{V,q}^a$	$\log L_{TESS,q}^a$	$F_{H\alpha,q}^{cont\ b}$	$F_{H\beta,q}^{cont\ b}$
YZ CMi	28.6	28.5	29.57	29.65	30.99	25.2	8.3
EV Lac	28.8	28.7	29.80	29.87	31.11	57.0	20.3
AD Leo	29.2	29.1	30.17	30.23	31.37	128.5	48.1

Notes.

^a The quiescent luminosity values in U , u , g , V , and TESS bands (see Figure 1). Units are ergs per second.

^b Quiescent flux densities at the continuum levels around the lines ($H\alpha$, $H\beta$ lines). Units are 10^{-14} erg s $^{-1}$ cm $^{-2}$ Å $^{-1}$. The continuum regions are determined by using the definitions in Table 3 of Kowalski et al. (2013).

50–60 s. Dark subtraction and flat-fielding were performed using PyRAF software in the standard manner before the photometry. Aperture photometry was performed using AstroimageJ (Collins et al. 2017). We used nearby stars as the magnitude references.

We also conducted ground-based photometric observations of one of the target stars YZ CMi, using the LCOGT network (Brown et al. 2013). These Las Cumbres Observatory (LCO) observations were conducted for 12 nights (Table 2) to support SMARTS 1.5 m/CHIRON spectroscopic observations. Using LCO 1 m telescopes with the Sinistro cameras, we carried out U -band photometric observations with exposure times of 10 and 25 s (Table 2). V -band photometric observations were conducted using LCO 0.4 m telescopes with the SBIG STL6303 cameras, and the exposure times are 6 s (Table 2). The data were reduced with the LCOGT automatic pipeline BANZAI,¹⁹ which masks bad-pixels, applies an astrometric solution, and performs bias and dark subtraction. Aperture photometry was performed using AstroimageJ (Collins et al. 2017), and we used nearby stars as the magnitude references.

Among the 31 nights that we conducted the above ground-based spectroscopic and photometric observations, the two terms observing one of the target star YZ CMi (2019 January 26–28 and 2021 January 31–February 4) were also covered with the observation window of TESS (Ricker et al. 2015; Table 2). We used the 120 s time cadence TESS Sectors 7 and 34 Pre-search Data Conditioned Simple Aperture Photometry (PDC-SAP) light-curve data (Vanderspek et al. 2018) of YZ CMi, retrieved from the Multimission Archive at the Space Telescope (MAST) Portal site,²⁰ as we have done in Maehara et al. (2021). The data release (DR) numbers of Sectors 7 and 34 data that we used are DR9 (Fausnaugh et al. 2019) and DR50 (Fausnaugh et al. 2021), respectively.

2.4. X-Ray Data

The X-ray instrument NICER (Gendreau et al. 2016) on board the International Space Station (ISS) conducted monitoring observations of YZ CMi on 2021 January 26, 27, and 28 (Observation ID: 1200510101–1200510103). This was scheduled for simultaneously observations with the ARC 3.5 m/ARCES spectroscopy, ARCSAT 0.5 m photometry, and TESS photometry of YZ CMi (Table 2). NICER observed YZ CMi for about ~ 2 ks for each ISS orbit (about 90 minutes) and 3–4 times every day (Table 2).

NICER X-ray Timing Instrument (XTI) is an array of aligned 56 X-ray modules, each of which consists of a set of an X-ray concentrator (XRC; Okajima et al. 2016) and a silicon drift

detector (SDD; Prigozhin et al. 2016). Each XRC concentrates X-rays within a $\sim 3'$ radius field of view to the paired SDD, which detects each photon at accuracy at ~ 84 ns. The XTI as a whole has one of the largest collecting areas among X-ray instruments between 0.2 and 12 keV (~ 1900 cm $^{-2}$ at 1.5 keV). We use 50 XTI modules as the remaining six (ID: 11, 14, 20, 22, 34, 60) are inactive or noisy.

As also done in Hamaguchi et al. (2023), we reprocess the data sets with the NIC calibration ver. CALDB XTI(20210707) using `nicerl2` in HEASoft ver. 6.29c and NICERDAS ver. V008c. Since NICER is not an imaging instrument, we evaluate particle background level using `nibackgen3C50` ver. v7b with the parameters `dtmin` = 10.0, `dtmax` = 60.0, `hbcut` = 0.1, `s0cut` = 30.0 (Remillard et al. 2022).

2.5. Flare Luminosities and Energies

In the following sections, the flare luminosities and energies are calculated for continuum bands and the chromospheric emission lines. In this process, the distance of the target stars (Table 1), the quiescent luminosities of photometric bands ($L_{band,q}$), and the quiescent flux densities at the continuum levels around the lines ($F_{line,q}^{cont}$) are used.

Quiescent luminosities of photometric bands ($L_{U,q}$, $L_{u,q}$, $L_{g,q}$, $L_{V,q}$, $L_{TESS,q}$) are estimated as in the following and are listed in Table 3. The U -band quiescent luminosities $L_{U,q}$ are taken from Table 1 of Kowalski et al. (2013). The u -band quiescent luminosities $L_{u,q}$ are converted from $L_{U,q}$, using the flux-calibrated quiescent spectroscopic data of the three target stars reported in Kowalski et al. (2013)²¹ and the bandpass data of *sdss* u band (used in ARCSAT) and LCO U band.²² As an example, the quiescent spectrum of YZ CMi taken from Kowalski et al. (2013) is shown with the u - and U -bands filter data in Figure 1(a). The g - and V -bands quiescent luminosities $L_{g,q}$ and $L_{V,q}$ are calculated from the same flux-calibrated quiescent spectroscopic data (Kowalski et al. 2013), the bandpass data of *sdss* g band (used in ARCSAT) and LCO V band, and the stellar distance d_{Gaia} (Table 1). In Figure 1(b), the g - and V -bands filter data are shown with the quiescent spectrum of YZ CMi as an example. The TESS-band quiescent luminosities $L_{TESS,q}$ are also calculated by using the flux-calibrated quiescent spectra, the filter data, and the stellar distance d_{Gaia} . In the case of YZ CMi, as shown in Figure 1(c), the filter curve is convolved with an M4 near-UV (NUV) to near-IR (NIR) spectral template from Davenport et al. (2012),

²¹ The spectroscopic data are available at <https://doi.org/10.26093/cds/vizier.22070015>.

²² The bandpass data (LCO U , *sdss* u , *sdss* g , LCO V , and TESS) used in this study, which are also shown in Figure 1, are taken from the SVO Filter Profile Service <http://svo2.cab.inta-csic.es/theory/fps/> (Rodrigo et al. 2012; Rodrigo & Solano 2020).

¹⁹ <https://github.com/LCOGT/banzai>

²⁰ <https://mast.stsci.edu/portal/Mashup/Clients/Mast/Portal.html>

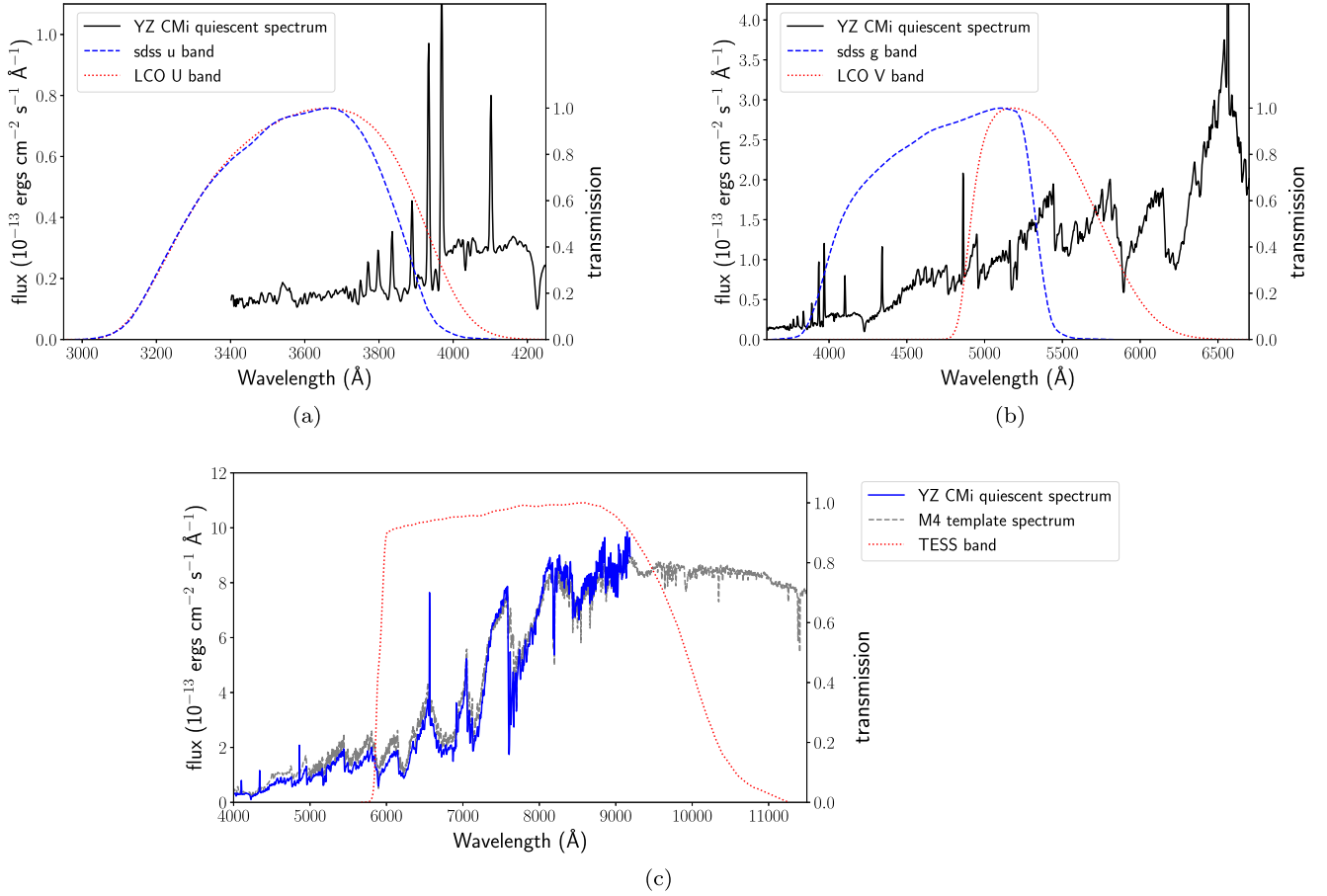


Figure 1. (a) Flux-calibrated quiescent spectrum for YZ CMi (black filled line) from Kowalski et al. (2013), with the photon transmission bandpass data of sdss *u* band and LCO *U* band. (b) The same as (a), but with the bandpass data of sdss *g* band and LCO *V* band. (c) Flux-calibrated quiescent spectrum for YZ CMi (blue filled line) from Kowalski et al. (2013), with the scaled NUV–NIR M4 template (thin gray dashed line) from Davenport et al. (2012), which is used to calculate the quiescent luminosity for YZ CMi in the TESS bandpass (red dotted line). The scaling normalization of the template spectrum is done by using the wavelength regions of 7000–7500 and 8000–9000 Å.

which is normalized to the above flux-calibrated spectrum of YZ CMi from Kowalski et al. (2013). The normalization is done by using the wavelength regions of 7000–7500 and 8000–9000 Å.

It is noted that, when calculating $L_{\text{TESS},q}$, the actual data are used for calculation at the wavelength where the data exist (<9168 Å), while the templates are only used in the remaining redder part (>9168 Å).

This method is basically the same as that done for an M4-dwarf flare star GJ1243 in Davenport et al. (2020). As for the other target stars EV Lac and AD Leo, we estimated $L_{\text{TESS},q}$ values with the basically same method using the flux-calibrated quiescent spectra, the filter data, and the stellar distances. The data of flux-calibrated spectra of EV Lac and AD Leo were taken from Kowalski et al. (2013). The M3 spectral template from Davenport et al. (2012) is used for AD Leo instead of the M4 template for YZ CMi and EV Lac.

The flare luminosities in the photometric bands ($L_{\text{band,flare}}(t)$) are calculated from the quiescent luminosities $L_{\text{band},q}$ (Table 3) and the relative fluxes during the flares ($\Delta f_{\text{band,flare}}(t)$):

$$L_{\text{band,flare}}(t) = L_{\text{band},q} \times \Delta f_{\text{band,flare}}(t). \quad (1)$$

The relative flux (see Figures 2–7 in Section 3.1) is here defined as $\Delta f(t) = (f(t) - f_{\text{ave}})/f_{\text{ave}}$, where $f(t)$ is flux, and f_{ave} is average flux of the nonflare phase. The flare energies in the

photometric bands ($E_{\text{band,flare}}$) are calculated by integrating $L_{\text{band,flare}}$ over the flare duration:

$$E_{\text{band,flare}} = \int L_{\text{band,flare}}(t) dt \quad (2)$$

$$= L_{\text{band},q} \times \int \Delta f_{\text{band,flare}}(t) dt \quad (3)$$

$$\equiv L_{\text{band},q} \times \text{ED}_{\text{band,flare}}, \quad (4)$$

where ED_{band} are equivalent durations (see Hunt-Walker et al. 2012).

In this study, we identified flares in the photometric bands when the relative flux $\Delta f_{\text{band,flare}}(t)$ is larger than $3 \times \sigma_{\text{band}}$ at around the flare peak for multiple data points, and the light-curve shape looks consistent with stellar optical flares (i.e., rapid increase and gradual decay as in Davenport et al. 2014; Okamoto et al. 2021). σ_{band} is the standard deviation of the relative flux in each band on each night for the phases without flares.

If no clear flares are identified in the photometric bands during the flares in $\text{H}\alpha$ and $\text{H}\beta$ lines, the upper limit of flare peak luminosity (L_{band} in Table 4) is estimated by applying this detection threshold $\Delta f_{\text{band,flare}} < 3 \times \sigma_{\text{band}}$ to Equation (1). The upper limit of flare energy (E_{band} in Table 4) is calculated by assuming the light curve shows the linear decay with the peak amplitude $3 \times \sigma_{\text{band}}$ and the decay time comparable to

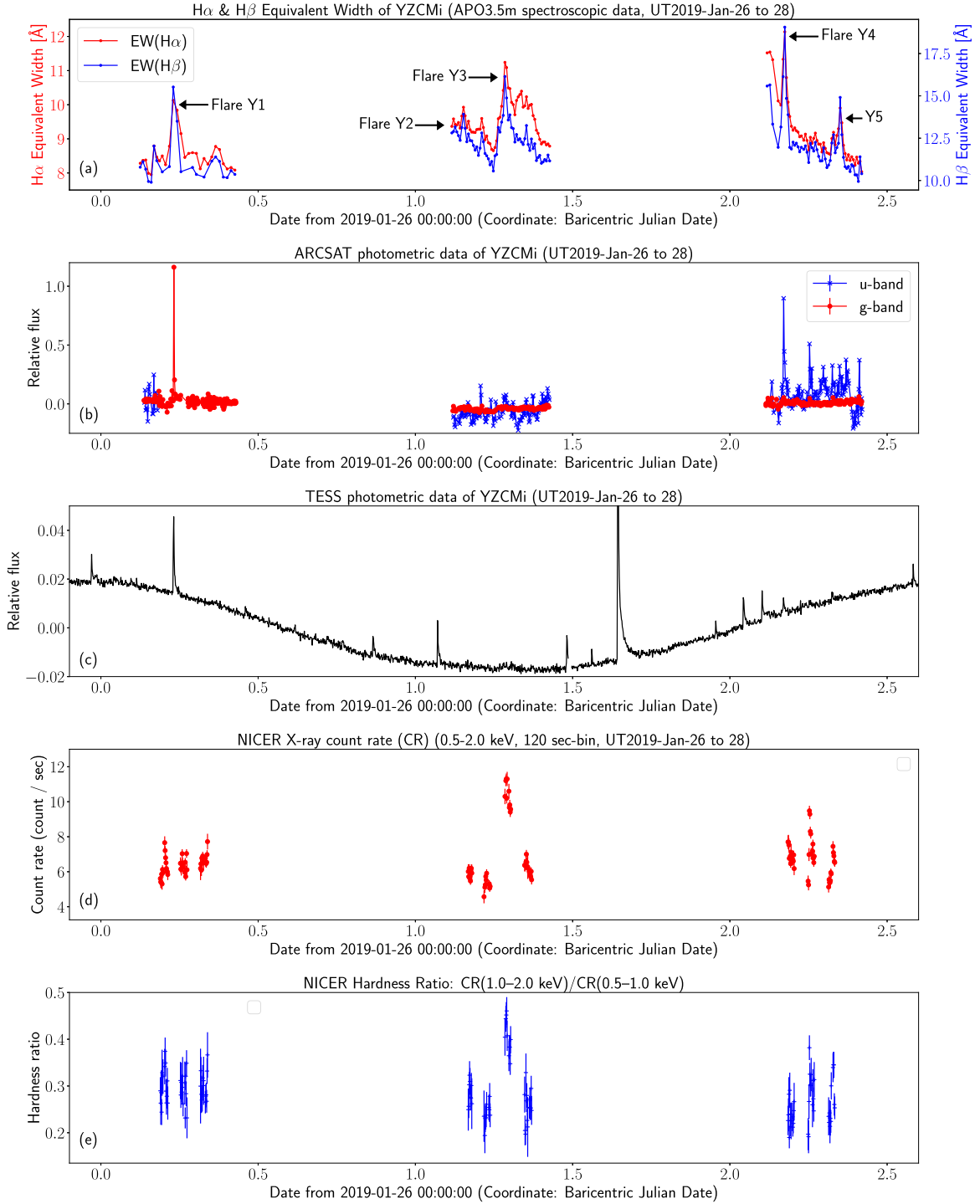


Figure 2. Summary light curves of YZ CMi during the campaign season [i] 2019 January 26–28. The horizontal axes represent the observation time in Barycentric Julian Date (BJD). The data points correspond to the middle time of each exposure, and this is the same for all the figures of the light curves in the following of this paper. (a) H α and H β equivalent width values from APO 3.5 m spectroscopic data. Red and blue symbols correspond to H α and H β EWs, respectively. Black arrows indicate flares. (b) u- and g-band relative flux light curves from ARCSAT photometric data. Blue asterisks and red circles correspond to u- and g-band data, respectively. Relative flux is here defined as $(f - f_{\text{ave}})/f_{\text{ave}}$, where f is flux, and f_{ave} is average flux of the nonflare phase. This definition is the same for the following figures of this paper. (c) TESS-band relative flux light curve from TESS photometric data. (d) Background-subtracted X-ray count rates [count per second] from NICER data in 0.5–2.0 keV. (e) X-ray hardness ratio (count rate (1.0–2.0 keV)/count rate (0.5–1.0 keV)) from NICER data.

the H α flare duration ($\Delta t_{\text{H}\alpha}^{\text{flare}}$ in Table 4). Then, we apply $\text{ED}_{\text{band, flare}} = 0.5 \times (3 \times \sigma_{\text{band}}) \times \Delta t_{\text{H}\alpha}^{\text{flare}}$ in Equation (4) for estimating the upper limit of flare energy.

The quiescent flux densities at the continuum levels around the H α and H β lines ($F_{\text{H}\alpha, \text{q}}^{\text{cont}}$ and $F_{\text{H}\beta, \text{q}}^{\text{cont}}$) are calculated based on the flux-calibrated quiescent spectra of the target stars from Kowalski

et al. (2013; see Figure 1), and the values are listed in Table 3. In this process, the continuum regions are determined by using the definitions in Table 3 of Kowalski et al. (2013). Flare luminosities in H α and H β lines ($L_{\text{line, flare}}(t)$) can be calculated from the quiescent fluxes ($F_{\text{line, q}}^{\text{cont}}$ in Table 3, and $F_{\text{line}}^{\text{cont}}(t)$ is the flux at the continuum level), relative fluxes at the continuum level around

Table 4
List of All Flares Detected in H α /H β Lines

ID ^a	WLF ^b Assym. ^c	UT Date	$t_{\text{start}}^{\text{flare d}}$ (JD/BJD)	Peak Luminosity ^{e,f} (10^{27} erg s ⁻¹)						Energy ^{g,h} (10^{31} erg)						$\Delta t_{\text{H}\alpha}^{\text{flare d,h}}$ (hr)
				L_U	L_u	L_g	L_{TESS}^i L_V^i	$L_{\text{H}\alpha}$	$L_{\text{H}\beta}$	E_U	E_u	E_g	E_{TESS}^i E_V^i	$E_{\text{H}\alpha}$	$E_{\text{H}\beta}$	
Y1	WL	2019 Jan 26	2458509.706	419	320	2.4–2.8	2.0–2.3	11	15	0.73–0.84	0.37–0.42	1.5
Y2	NEP	2019 Jan 27	before obs.	...	<8	<16	<33	1.3	1.0	...	<4.1	<8.9	<19	>0.74	>0.49	>3.2
Y3	NWL, (B)	2019 Jan 27	2458510.748	...	<8	<16	<33	2.8	1.8	...	<5.6	<12	<26	1.7	0.76	4.3
Y4	WL, (R)	2019 Jan 28	2458511.654	...	22	16	73	4.2–4.3	3.0–3.1	...	0.8	0.7	6.0	0.92–0.93	0.51–0.52	1.1
Y5	NWL	2019 Jan 28	2458511.819	...	<5	<9	<29	1.7–1.8	1.5–1.6	...	<1.0	<1.9	<6.5	0.38–0.40	0.26–0.27	1.3
Y6	NWL, (B)(R)	2019 Dec 12	2458829.841	...	<8	<1.8	...	3.6–3.8	1.8–1.9	...	<7.2	<16	...	>3.9	>1.8	>4.9
Y7	WL, (B?)	2020 Jan 14	2458862.830	...	15	19	...	1.8–2.1	1.4–1.6	...	4.9	3.9	...	1.1–1.2	0.76–0.82	2.9
Y8	WL	2020 Jan 14	2458862.951	...	1249	1492	...	10	9.6	...	12	13	...	>0.88	>0.71	>0.4
Y9	WL	2020 Jan 16	before obs.	103	202	3.4	3.3	3.7	6.0	>0.72	>0.66	>1.7
Y10	WL, (R)	2020 Jan 16	2458864.670	44	2.8	3.0	1.8	0.84	0.89	1.2
Y11	WL, (R)	2020 Jan 16	2458864.719	97	144	3.5–3.9	3.1–3.3	1.8	3.2	1.2–1.4	0.89–0.97	2.0
Y12	WL, (R)	2020 Jan 18	2458866.677	84	71	63	47	3.9–4.5	3.4–3.6	5.6	11	16	4.2	4.2–4.8	3.0–3.2	5.7
Y13	WL	2020 Jan 18	2458866.914	...	38	63	32	2.0	1.7	...	1.5	1.9	0.8	0.97	0.60	2.3
Y14	WL	2020 Jan 19	2458867.788	21	14	21	22	2.3–2.7	1.9–2.1	2.1	1.9	4.2	3.3	0.54–0.67	0.40–0.47	1.2
Y15	WL	2020 Jan 19	2458867.844	...	292	547	...	2.4–3.7	2.7–3.5	...	8.0	13	...	>0.24	>0.07	>0.3
Y16	WL, (R)	2020 Jan 20	before obs.	...	24	21	30	4.0	4.3	...	2.4	1.7	0.7	>2.4	>2.4	>2.5
Y17	WL, (R)	2020 Jan 20	2458868.707	...	29	25	34	4.2–5.0	5.2–5.7	...	15	6.3	9.8	3.4–3.7	4.2–4.3	6.0
Y18	WL, (B)	2020 Jan 21	2458869.591	41	41	2.6–2.8	1.9	4.6	2.4	1.5–1.6	1.3	3.4
Y19	WL, (R)	2020 Jan 21	2458869.738	59	41	4.8–5.1	4.5–4.9	11	4.4	>3.3	>2.5	>2.5
Y20	WL	2020 Jan 22	2458870.669	87	46	1.5–1.9	1.3–1.7	5.8	2.2	0.52–0.56	0.26–0.28	2.0
Y21	WL	2020 Jan 23	2458871.586	21	<17	1.6	1.6	3.8	<5.0	0.44	0.40	1.7
Y22	NEP	2020 Jan 23	2458871.656	1.9	1.9	0.74	0.59	3.2
Y23	WL, (B)	2020 Dec 6	before obs.	...	397	461	...	4.1–4.5	3.0–3.2	...	16	22	...	>1.1	>0.59	>1.3
Y24	WL	2020 Dec 6	2459189.892	...	23	16	...	1.7–1.8	1.4–1.5	...	0.5	0.6	...	0.25–0.26	0.17–0.18	0.7
Y25	WL	2020 Dec 7	before obs.	...	27	20	...	1.9–2.0	2.4–2.5	...	0.8	0.5	...	>0.43	>0.39	>0.8
Y26	NWL	2020 Dec 7	2459190.839	...	<8	<18	...	1.8	1.5	...	<7.2	<16	...	0.82–0.86	0.59–0.62	1.9
Y27	WL	2020 Dec 7	2459190.916	...	32	28	...	1.7	1.1	...	1.2	0.4	...	0.41–0.42	0.29–0.30	0.8
Y28	WL, (R)	2020 Dec 7	2459190.952	...	30	28	...	2.9–3.3	3.0–3.3	...	1.7	1.0	...	0.71	0.52	1.7
Y29	WL	2021 Jan 31	2459245.674	...	43	63	57	1.3–1.4	0.94–0.95	...	3.3	1.8	2.5	1.7	0.95	5.3
E1	NEP, (B)	2019 Dec 15	2458832.556	4.3	2.2	2.9	1.4	3.6
E2	WL, (B)	2019 Dec 15	2458832.705	...	23	37	...	2.8–2.9	1.3–1.4	...	1.1	0.7	...	0.58	0.16–0.17	0.9
E3	WL	2020 Aug 26	before obs.	...	13	<8	...	2.0–2.2	1.9–2.1	...	1.0	<3.3	...	>0.74	>0.55	>2.3
E4	WL	2020 Aug 26	2459087.906	...	16	29	...	1.5–1.9	2.2–2.5	...	1.4	2.0	...	>0.47	>0.47	>2.1
E5	WL, (R)	2020 Aug 27	2459088.846	...	1618	2708	...	22–47	21–35	...	84	106	...	7.3–10.4	6.7–9.1	3.5
E6	WL	2020 Aug 29	before obs.	...	10	14	...	1.3–1.9	0.70–0.74	...	0.3	0.7	...	>0.53	>0.35	>2.7
E7	NEP	2020 Sep 1	before obs.	3.0–3.2	2.3–2.4	>1.2	>0.88	>2.1
E8	WL	2020 Sep 2	2459094.811	...	24	<9	...	0.78–0.81	0.68–0.70	...	0.1	<2.4	...	0.17–0.19	0.12–0.13	1.4
E9	WL	2020 Sep 2	2459094.884	...	14	<9	...	1.2–1.3	1.4	...	0.9	<4.5	...	0.55–0.61	0.55–0.58	2.7
A1	NEP	2019 May 17	before obs.	3.7	1.9	>0.85	>0.35	>1.1

Table 4
(Continued)

ID ^a	WLF ^b Assym. ^c	UT Date	$t_{\text{start}}^{\text{flare d}}$ (JD/BJD)	Peak Luminosity ^{e,f}						Energy ^{g,h}						$\Delta t_{\text{H}\alpha}^{\text{flare d,h}}$ (hr)
				(10 ²⁷ erg s ^{−1})						(10 ³¹ erg)						
				L_U	L_u	L_g	L_{TESS}^i L_V^i	$L_{\text{H}\alpha}$	$L_{\text{H}\beta}$	E_U	E_u	E_g	E_{TESS}^i E_V^i	$E_{\text{H}\alpha}$	$E_{\text{H}\beta}$	
A2	WL, (R)	2019 May 18	2458621.676	...	61	72	...	4.5–4.9	4.8–5.0	...	3.0	1.6	...	0.52–0.58	0.55–0.57	1.0
A3	NEP, (B)	2019 May 19	before obs.	7.4	3.7	...	>2.7	>1.4	...	>5.3	>2.5	>3.1

Notes.

^a Flare ID. Flares Y1–Y29 are on YZ CMi, Flares E1–E9 are on EV Lac, and Flares A1–A3 are on AD Leo.

^b The 6 flares with the mark for not enough photometric data (“NEP”) do not have enough photometric data to judge whether the flares are white-light (WL) or non-white-light (NWL) flares. The 31 flares with the mark “WL” are identified as WL flares. The 4 flares with the mark “NWL” are identified as *candidate* NWL flares. See Section 4.1 for the classification criteria.

^c Flares with “(B)” showed clear blue wing asymmetries in H α line, while those with “(B?)” showed possible blue wing asymmetries but not so clear. Flares with “(R)” showed clear red wing asymmetries in H α line.

^d The flare start time ($t_{\text{start}}^{\text{flare}}$) and flare duration ($\Delta t_{\text{H}\alpha}^{\text{flare}}$) are measured from the H α light curve. Flares Y1–Y5 and Y29 are shown with BJD. Other flares are shown with JD.

^e As for the peak luminosities in photometric bands (L_U , L_u , L_g , L_V , and L_{TESS}), we selected the peaks that are considered to be most physically associated with the flare peaks in the H α and H β lines. This means that the largest flare peaks in photometric bands are not necessarily selected, but those most closest in time with the flare peaks in the H α and H β lines are basically selected.

^f The upper limit marks “<” for the peak luminosities in photometric bands (L_U , L_u , L_g , L_V , and L_{TESS}) show that the clear flare emission is not identified in this band, and the detection threshold value “ $\Delta f_{\text{band,flare}} < 3 \times \sigma_{\text{band}}$ ” is shown (see Section 2.5 for the details).

^g The upper limit marks “<” for the flare energies in photometric bands (E_U , E_u , E_g , E_V , and E_{TESS}) show that the clear flare emission is not identified in this band, and the upper limit flare energies are shown (see Section 2.5 for the estimation method). As for Flare A3, the lower limit of flare energies are listed with the marks “>” to show the energy values from the available data, since only the late phase of this Flare A3 was observed in photometric bands, and it is highly possible that there are additional white-light emission (see also Section 3.7). Most of the LCO U - and V -band photometric data (except for Flare Y14) have some data gaps. Because of this, E_U and E_V values can be lower limit values except for Flare Y14.

^h The lower limit marks (“>”) for the $E_{\text{H}\alpha}$, $E_{\text{H}\beta}$, and $\Delta t_{\text{H}\alpha}^{\text{flare}}$ show that the total flare phases were not observed in the Balmer lines, and only lower limit of these values are measured. In these cases, the flare energy values in photometric bands (E_U , E_u , E_g , E_V , E_{TESS}) can be larger than the listed values, but the lower limit marks (“>”) are not added for these photometric flare energy values, since it is not necessarily obvious whether there are additional (unobserved) white-light emissions even if the total flare phases were not observed in the Balmer lines (except for Flare A3 described in the footnote (g)). As for Flares Y2, Y6, and E3, the upper limit values of photometric flare energies (E_u , E_g , and E_{TESS}) with the marks “<” are shown (see footnote (g)), but the real upper limit values of E_u , E_g , and E_{TESS} could be larger than the listed values, as the total flare phases of these flares were not observed in the Balmer lines (see the lower limit marks are shown for the $E_{\text{H}\alpha}$, $E_{\text{H}\beta}$, and $\Delta t_{\text{H}\alpha}^{\text{flare}}$ values of these flares).

ⁱ As for Flares Y1–Y5 and Y29, TESS-band data are listed. As for Flares Y9–Y22, V -band data are listed.

the lines $\Delta f_{\text{line}}^{\text{cont}}(t) = (f_{\text{line}}^{\text{cont}}(t) - f_{\text{ave, line}}^{\text{cont}})/f_{\text{ave, line}}^{\text{cont}}$, the stellar distance d_{Gaia} (Table 1), and the equivalent width (EW) of the flare component $\text{EW}_{\text{line, flare}}(t) = \text{EW}_{\text{line}}(t) - \text{EW}_{\text{line, q}}$ where $\text{EW}_{\text{line, flare}}(t)$ is the EW of the flare component, $\text{EW}_{\text{line}}(t)$ is the total EW, and $\text{EW}_{\text{line, q}}$ is the EW at the quiescent level; see also Figures 2–7 in Section 3.1)²³:

$$L_{\text{line, flare}}(t) = 4\pi d_{\text{Gaia}}^2 \times (F_{\text{line}}^{\text{cont}}(t) \times \text{EW}_{\text{line}}(t) - F_{\text{line, q}}^{\text{cont}} \times \text{EW}_{\text{line, q}}) \quad (5)$$

$$= 4\pi d_{\text{Gaia}}^2 \times F_{\text{line, q}}^{\text{cont}} \times \left[(1.0 + \Delta f_{\text{line}}^{\text{cont}}(t)) \times (\text{EW}_{\text{line, flare}}(t) + \text{EW}_{\text{line, q}}) - \text{EW}_{\text{line, q}} \right] \quad (6)$$

$$= 4\pi d_{\text{Gaia}}^2 \times F_{\text{line, q}}^{\text{cont}} \times \left[(1.0 + \Delta f_{\text{line}}^{\text{cont}}(t)) \times \text{EW}_{\text{line, flare}}(t) + \Delta f_{\text{line}}^{\text{cont}}(t) \times \text{EW}_{\text{line, q}} \right]. \quad (7)$$

Flare energies in H α and H β lines ($E_{\text{line, flare}}$) can be calculated by integrating $L_{\text{line, flare}}$ over the flare duration:

$$E_{\text{line, flare}} = \int L_{\text{line, flare}}(t) dt \quad (8)$$

$$= 4\pi d_{\text{Gaia}}^2 \times F_{\text{line, q}}^{\text{cont}} \times \int \left[(1.0 + \Delta f_{\text{line}}^{\text{cont}}(t)) \times \text{EW}_{\text{line, flare}}(t) + \Delta f_{\text{line}}^{\text{cont}}(t) \times \text{EW}_{\text{line, q}} \right] dt. \quad (9)$$

In this study, g -band flux observations are mainly used for estimating $\Delta f_{\text{line}}^{\text{cont}}(t)$ at the continuum level around the H α and H β lines. Since the g -band flux changes can be larger than the changes of the real local continuum levels around H α and H β lines considering the typical M-dwarf flare spectra (see Kowalski et al. 2013), the resultant values are shown with the ranges (e.g., $L_{\text{H}\beta} = 2.0\text{--}2.3 \times 10^{27} \text{ erg s}^{-1}$ for Flare Y1); the lower values do not take into account any continuum flux changes ($\Delta f_{\text{line}}^{\text{cont}}(t) = 0$ in Equations (7) and (9)), and the upper values correspond to the values incorporating g -band flux changes ($\Delta f_{\text{line}}^{\text{cont}}(t)$ taken from g -band light curves). We use the same method when we estimate the flare peak luminosities (L) and flare energies (E) in the H α and H β lines of all the other flares listed in Table 4. The TESS-band continuum fluxes are not used in this process even for flares with TESS data (e.g., Flare Y1), since most of the flares in this study have no TESS data (Table 4).

In addition, as for the peak luminosities in photometric bands (U , u , g , V , and TESS bands) in Table 4, we selected the peaks that are considered to be most physically associated with the flare peaks in the H α and H β lines. This means that the largest flare peaks in photometric bands are not necessarily selected, but those closest in time with the flare main peaks in the H α and H β lines are basically selected. The detailed descriptions for the individual flares are in Sections 3.2–3.7 and Appendices A.1–A.18. In contrast, all changes (peaks) of the photometric-band luminosity (not only the highest peaks) during the whole flare duration in H α line ($\Delta f_{\text{H}\alpha}^{\text{flare}}$) are taken into account for calculating the flare energies following Equation (9).

²³ We note that equivalent width of a spectral line is defined as an area of the line on a plot of the continuum-normalized intensity as a function of wavelength, and in this study, we define that the positive value of the EW indicates line emission so that an increase (positive change) of equivalent width indicates an increase of emission line flux. This positive EW definition is the same as one of our previous papers Honda et al. (2018) but is opposite to our other previous papers Namekata et al. (2020), Maehara et al. (2021).

It is noted that some flares reported in this study seem to be superimposed on potential decay tails of previous flares, and this could affect the values of flare luminosities and energies. However, we do not correct for this issue, since it is difficult to correctly subtract the component of previous flares. The potential errors caused from this point should be kept in mind when discussing flare luminosities (see also descriptions for each flare in the following sections of this paper). Moreover, some flares show an extra blueshifted and/or redshifted component (see the discussions in the following sections), but the flare luminosity and energy values were not corrected for this. The emission contributions from the blueshifted and/or redshifted extra components are included in the resultant flare luminosity and energy values. The reason is that main discussions are not affected without any correction since the purpose of this paper is not discussing the detailed energy partition of flares, and the order-of-magnitude estimates of flare energies are sufficient for the purposes of this paper.

3. Flare Light Curves and Spectra

3.1. Observational Summary

As described in Section 2, we conducted the time-resolved simultaneous optical spectroscopic and photometric observations of the three target stars YZ CMi, EV Lac, and AD Leo during the 31 nights in total (Table 2). YZ CMi was observed during the five campaign seasons: [i] 2019 January (3 nights), [ii] 2019 December (4 nights), [iii] 2020 January (9 nights), [iv] 2020 December (3 nights), and [v] 2021 January–February (2 nights). EV Lac was observed during the two campaign seasons: [vi] 2019 December (1 night) and [vii] 2020 August–September (6 nights). AD Leo was observed during the one campaign season [viii] 2019 May (3 nights). Figures 2–7 show the all light curves from the campaigns.

We note that flares are defined from the H α and H β data since the main purpose of this paper is to investigate the blue and red asymmetries of Balmer lines during flares, as described in the Introduction section. It could be possible by definition that blue and red asymmetries occur with (i) flare emissions of Balmer lines below the detectable level, or (ii) in absence of flare-enhanced Balmer emission. For example, if the prominence eruption causes the line asymmetries (see the references in the Introduction section), the detectability of prominence eruption could be unrelated with that of the flare emission itself in Balmer lines. However, distinguishing among these alternative scenarios is beyond the scope of the current paper, since the main purpose of this paper is to report blue asymmetries of Balmer lines associated with clear flares, and to discuss the properties of blue asymmetries with flare properties. We note that there are no clear blue and/or red line asymmetries without clear flares in Balmer lines (see figures in the following part of this paper), and all line asymmetries in our observations are associated with flares in Balmer lines. Therefore, our approach does not ultimately cause any major ambiguities.

In total, 41 flares are detected as shown in Figures 2–7 and listed in Table 4. We label the 41 flares by the first character of each the target star: Flares Y1–Y29 on YZ CMi, Flares E1–E9 on EV Lac, and Flares A1–A3 on AD Leo. As can be seen in Figures 2–7, the H α and H β light curves are almost always variable (e.g., Figure 3(c)) compared with the photometric data, and this makes it difficult to define *nonflare* or *quiescent* phases for many nights. Since the duration of flares in Balmer

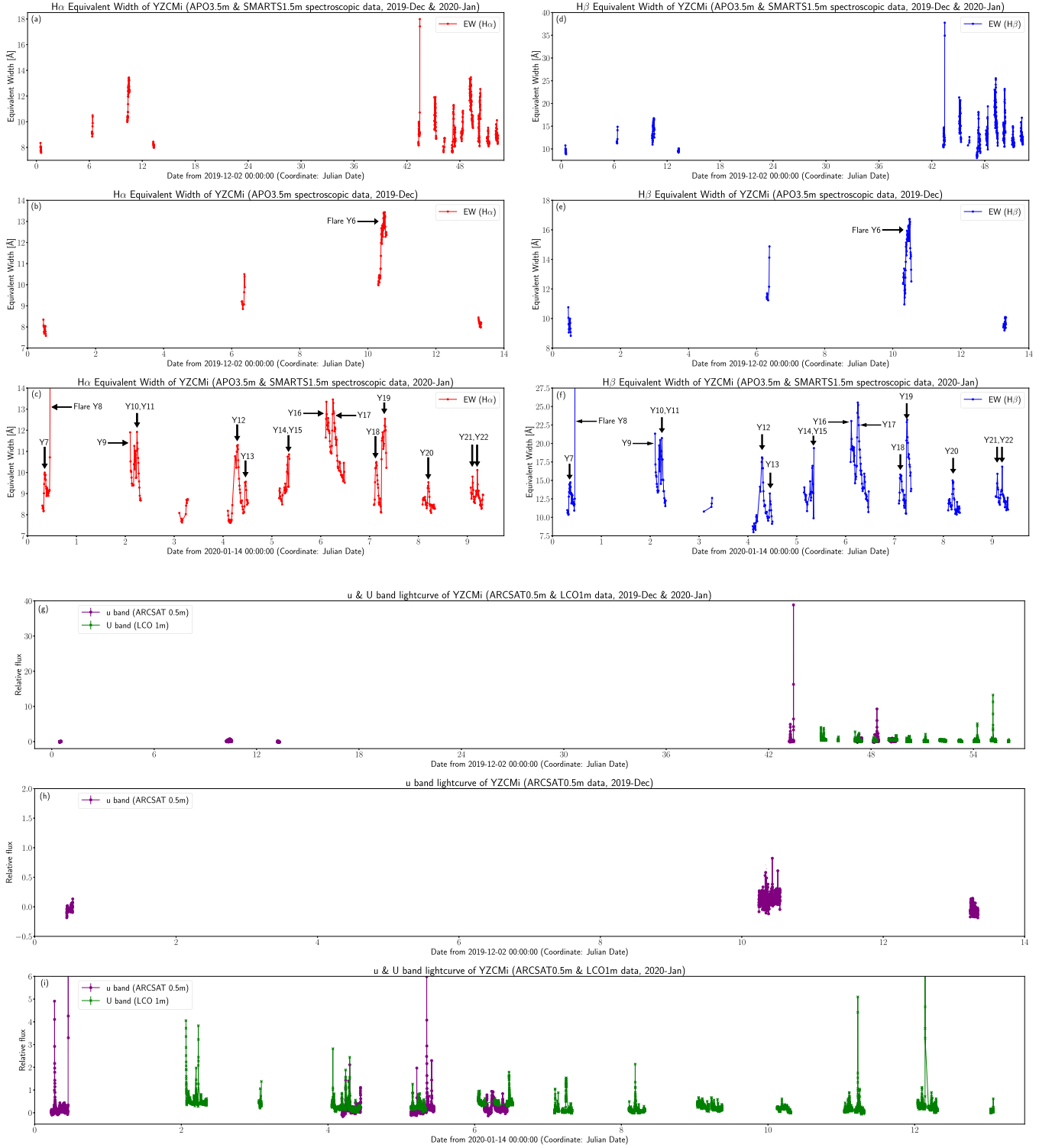


Figure 3. Summary light curves of YZ CMi during the campaign seasons [ii] 2019 December and [iii] 2020 January. The horizontal axes represent the observation time in Julian Date (JD). (a) and (d) $H\alpha$ and $H\beta$ equivalent width values from APO 3.5 m and SMARTS 1.5 m spectroscopic data for both campaign seasons [ii] and [iii]. (b) and (e) The same as (a) and (d), but only for the campaign season [ii]. (c) and (f) The same as (a) and (d), but only for the campaign season [iii]. Black arrows in (b) and (c) indicate flares. (g) u -band and U -band relative light curves from ARCSAT 0.5 m and LCO 1 m photometric data (purple and green symbols, respectively) for both campaign seasons [ii] and [iii]. (h) The same as (g) but only for the campaign season [ii]. (i) The same as (h) but only for the campaign season [iii].

lines can be relatively long (e.g., up to a few hours) in many cases, there can be a lot of flares overlapping with other flares, or in other words, the other flare starts before the preceding flare emission completely decays (e.g., Flares Y16 and Y17 in

Figure 3(c)). Moreover, there are also many *partial* flares (e.g., Flare A3 in Figure 7(a)), and their observed flare properties (e.g., flare energies) could include various uncertainties since only the portions of flare phases were observed.

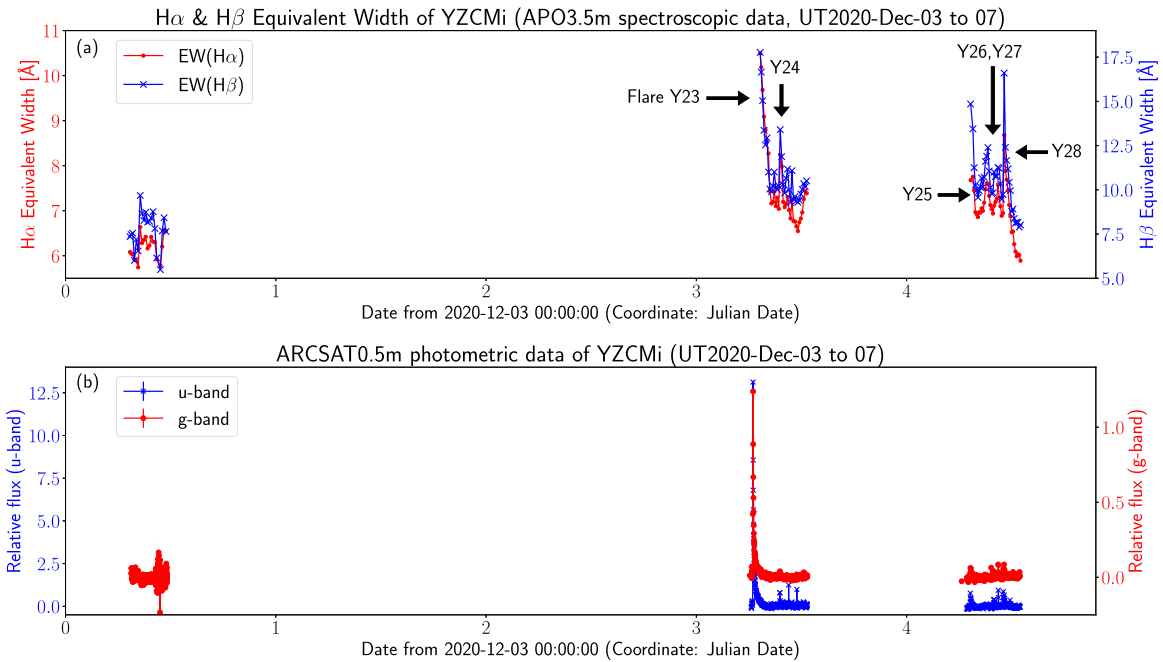


Figure 4. Summary light curves of YZ CMi during the campaign season [iv] 2020 December 3–7. The horizontal axes represent the observation time in the time coordinate of Julian Date (JD). (a) $H\alpha$ and $H\beta$ equivalent width values from APO 3.5 m spectroscopic data. Red and blue symbols correspond to $H\alpha$ and $H\beta$ EWs, respectively. Black arrows indicate flares. (b) u - and g -band relative flux light curves from ARCSAT 0.5m photometric data. Blue asterisks and red circles correspond to u - and g -band data, respectively.

The main purpose of this paper is to understand the existence of various blue asymmetry events among various Balmer line flares, and some uncertainty of definitions of each flare could be left, as long as they are not expected to cause a serious problem for the main conclusion of this paper. Then, we defined flares with rough definition as a phase having clear emission *increase*: the EW amplitude of $H\alpha \gtrsim +(0.5-1) \text{ \AA}$, compared with nearby *quiescent* phase (or the phase having locally smaller emission compared with nearby data points). The threshold values are roughly determined for each observation period, considering the data S/N and quiescent level modulations ($\gtrsim +(0.5-1) \text{ \AA}$ for YZ CMi; $\gtrsim +0.5 \text{ \AA}$ for EV Lac and AD Leo), and the values are also described in the following paragraphs of this subsection. There are flares with multiple peaks (e.g., Flare Y3 in Figure 2(a)), but they are basically broadly classified into one long-timescale flare if the $H\alpha$ EW amplitude of these multiple peaks are smaller than the threshold $\lesssim +(0.5-1) \text{ \AA}$ (e.g., Flare Y6). We briefly describe how each flare is defined in the following paragraphs of this section. All of the uncertainties of the flare definition described in this subsection should be kept in mind for the remainder of the analyses and discussions in this paper.

Figure 2 shows the light curves of YZ CMi during the campaign season [i] 2019 January 26–28. During this campaign season [i], YZ CMi was observed with APO 3.5 m optical high-dispersion spectroscopy, ARCSAT ground-based photometry (u and g bands), TESS space photometry Sector 7, and NICER X-ray spectroscopy. Five flares (Y1–Y5) were detected in the $H\alpha$ and $H\beta$ EW data in Figure 2(a). These five flares were defined as phases showing the $H\alpha$ EW increase of $\gtrsim 1 \text{ \AA}$ compared with nearby local *quiescent* phase on each night (EW of $H\alpha \sim 8.0-8.6 \text{ \AA}$ in the period of 2019 January 26–28). With this definition, a small amplitude increase after Flare Y1 at ~ 0.4 day in Figure 2(a) was not counted as a flare. Flares Y2 and Y3 consist of multiple peaks, but we only

broadly classified into two flares since the peaks during Flare Y2 and Y3 have $H\alpha$ EW amplitudes smaller than $\sim 1 \text{ \AA}$, and the light curve returned below the threshold only once at ~ 1.25 days in Figure 2(a) during the observation on 2019 January 27th (see also Section 3.2). Flares Y4 and Y5 could be classified into one flare since there is a continuous decreasing trend over the observation period of this night (2019 January 28th), but we classified them into two flares since both peaks have amplitudes larger than $\sim 1 \text{ \AA}$. It is then probable that independent flares can cause the time evolution of the EWs, and there can be some meanings to separately classify them (as Flares Y4 and Y5) and investigate whether each peak has line asymmetries, considering the main purpose of this paper. There is also a $H\alpha$ emission increase at around the beginning of the observation data on 2019 January 28 before Flare Y4 (at ~ 2.13 days in Figure 2(a)), but we do not define this as a flare since only three data points with relatively low S/N exist, and it is difficult to judge whether it showed line asymmetries for these data points (see also figures in Appendix A.2). In other words, this event cannot contribute to the main purpose of this paper even if it is counted as a flare, since it cannot be used for the line asymmetry classification.

Among these five flares, only Flare Y3 was observed with NICER X-ray data (Figures 2(d) and (e)). The parameters of these five flares are listed in Table 4, and these flares are described in detail in Section 3.2 and Appendices A.1–A.2.

Figure 3 shows the light curves of YZ CMi during the two campaign seasons [ii] 2019 December and [iii] 2020 January. During the campaign season [ii], YZ CMi was observed with APO 3.5 m optical high-dispersion spectroscopy and ARCSAT ground-based photometry (u and g bands; Table 2). During the latter season [iii], YZ CMi was observed with APO 3.5 m spectroscopy on 2020 January 14, 18, and 20, and with SMARTS 1.5 m spectroscopy on every night from 2020 January 16 to January 23 (Table 2). ARCSAT photometry

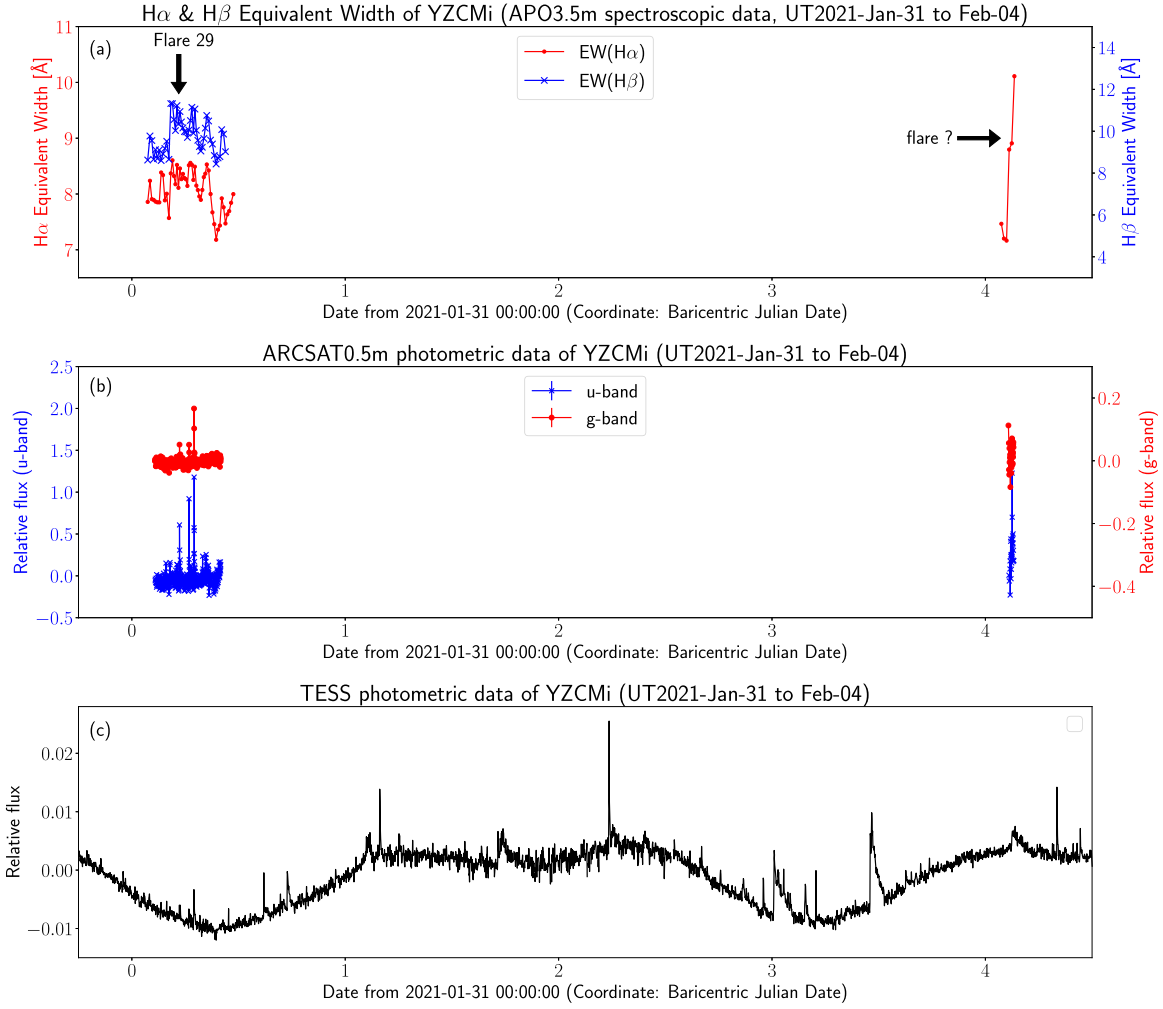


Figure 5. Summary light curves of YZ CMi during the campaign season [v] 2021 January 31–February 4. The horizontal axes represent the observation time in Barycentric Julian Date (BJD). (a) and (b) H α and H β equivalent width and u - and g -band relative flux light curves are plotted with the same symbols as Figure 4. (c) TESS-band relative flux light curve from TESS photometric data.

(u and g bands) and LCO photometry (U and V bands) were conducted during the nights with APO 3.5 m spectroscopy and SMARTS 1.5 m spectroscopy, respectively. We note that LCO observations continued until January 27 after the SMARTS 1.5 m spectroscopic observations finished on 2020 January 27 (Table 2 and Figure 3(c)).

As a result, 17 flares (Flares Y6–Y22) were detected in H α and H β data during these extensive campaign seasons (Figures 3(a) and (b)). These 17 flares were defined as phases showing the H α EW increase of $\gtrsim 1$ Å compared with the nearby local *quiescent* phase on each night. During the campaign seasons [ii] and [iii], there are flare-like increases at ~ 6.2 – 6.3 days in Figure 3(b) (2019 December 8) and at ~ 3.2 – 3.3 days in Figure 3(c) (2020 January 17), but we did not classify them into flares since a few data points with low S/N only exist and it is not possible to discuss whether they showed line asymmetries. In other words, these events cannot contribute to the main purpose of this paper even if they are counted as flares. Flare Y6 has multiple peaks, but these peaks are not separated into multiple independent flares, since the amplitude of each peak is only $\lesssim 1$ Å, and the H α EW value was continuously much larger (> 2.5 – 3.0 Å) than the local *quiescent* level (~ 10.0 – 10.2 Å) (see also Section 3.3). Although Flare Y8 has only three data points after the flare

start, this is counted as a flare since this has a very larger amplitude (~ 9 Å) compared with other flares, and it is possible to discuss the line profiles (see also Appendix A.3). As for Flares Y10 and Y11, the H α EW did not come back to the quiescent level between these two flares, and it was still at ~ 9.7 – 9.8 Å, but we classified these two events into two flares (Y10 and Y11), since both of the two have duration of $\gtrsim 1$ hr, and the emission has a clear local minimum between the two whose amplitude is $\gtrsim 1$ Å (see also Appendix A.4). It is then probable that independent flares can cause these time evolution of the EWs, and there can be some meanings to separately classify them (as Flares Y10 and Y11) and investigate whether each peak has line asymmetries, considering the main purpose of this paper. Moreover, Flares Y14 and Y15, and Y16 and Y17 are classified into separated two flares, respectively, because of the same reason with the above Flares Y10 and Y11 (see also Appendices A.6 and A.7). In addition, Flares Y16 and Y17 are similar to Flares Y4 and Y5 mentioned above for the point that they showed a continuous decreasing trend over the whole observation period of this night (2019 January 20), but they are treated as two flares because of the same reason with Flares Y4 and Y5 in the above.

These 17 flares (Flares Y6–Y22) are listed in Table 4 and are described with more detailed figures in Sections 3.3–3.4 and

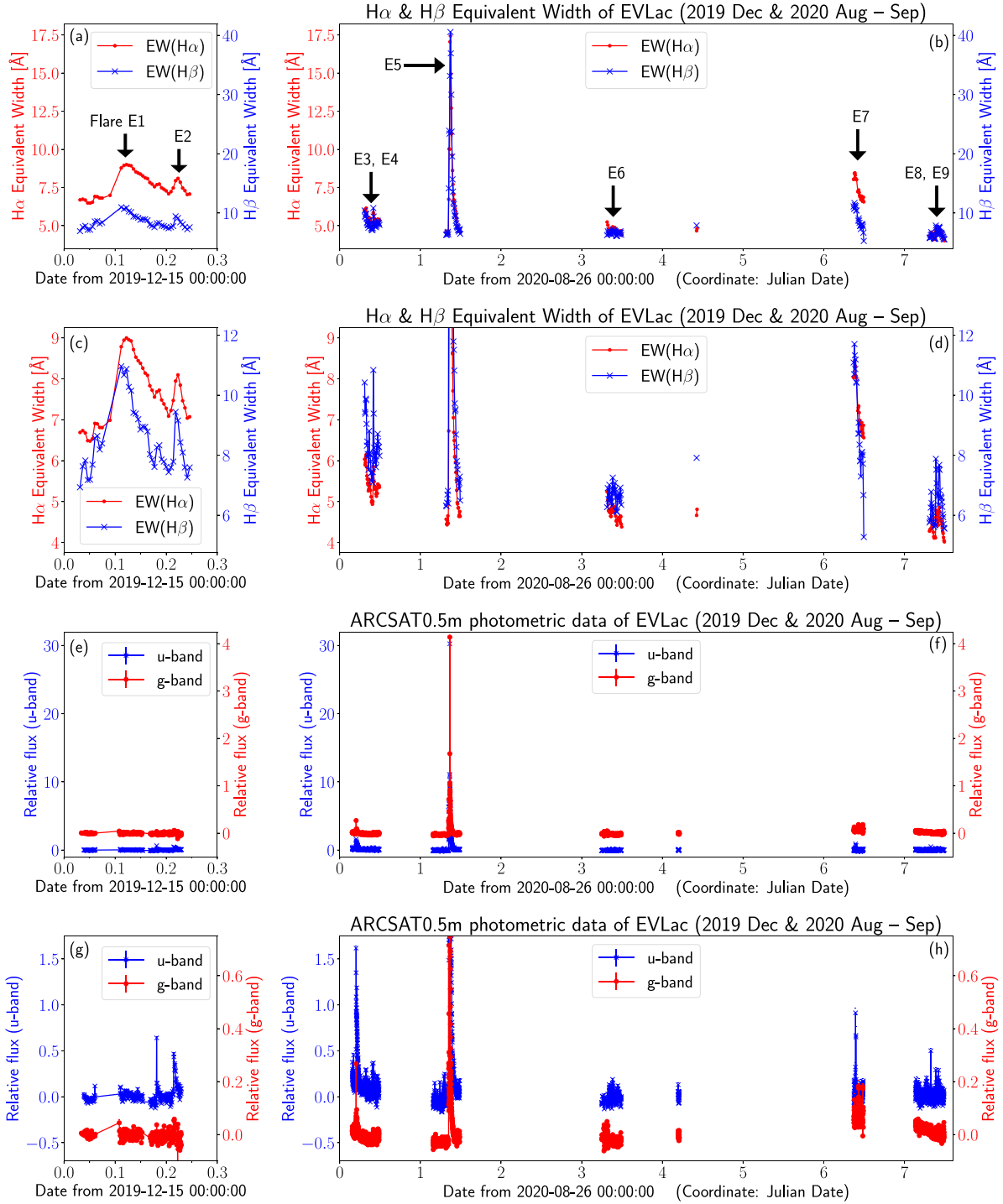


Figure 6. Summary light curves of EV Lac during the two campaign seasons [vi] 2019 December 15 and [vii] 2020 August 26–September 2. The horizontal axes represent the observation time in Julian Date (JD). $H\alpha$ and $H\beta$ equivalent width and u - and g -band relative flux light curves are plotted with the same symbols as Figure 4. Panels (a), (c), (e), and (g) are the data from the campaign season [vi], while panels (b), (d), (f), and (h) are from the campaign season [vii]. Panels (c), (d), (g), and (h) are vertical axis enlarged figures of (a), (b), (e), and (f), respectively.

Appendices A.3–A.9. Figures 3(a) and (b) also show that the $H\alpha$ and $H\beta$ EW values of the quiescent phase (nonflare phase) exhibit variability among the observation dates; this could be related with the rotational modulations, considering the rotation period of 2.77 days (Table 1).

Figure 4 shows the light curves of YZ CMi during the campaign season [iv] 2020 December 3–7. During this campaign season [iv], YZ CMi was observed with APO 3.5 m optical high-dispersion spectroscopy and ARCSAT ground-

based photometry (u and g bands). Six flares (Y23–Y28) were detected in the $H\alpha$ and $H\beta$ EW data in Figure 4(a).

These six flares were defined as phases showing the $H\alpha$ EW increase of $\gtrsim 1$ Å compared with nearby local *quiescent* phase on each night ($H\alpha$ EW ~ 6 – 7 Å). As for the data of 2020 December 7, three $H\alpha$ emission increase peaks with smaller amplitude (EW amplitude of $H\alpha \gtrsim 0.5$ Å) were classified into separated flares (Flares Y25, Y26, and Y27). This is because there are peaks whose duration is $\gtrsim 1$ hr, and the emission of

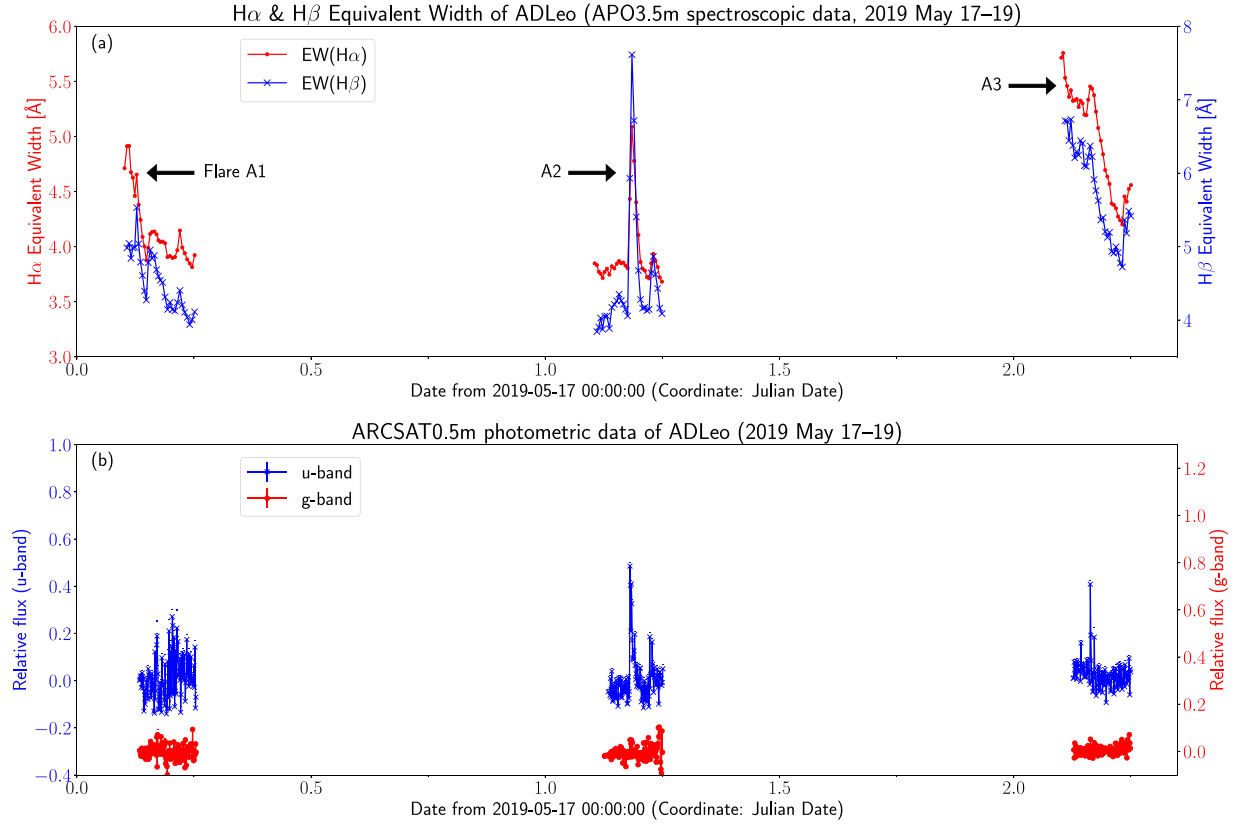


Figure 7. Summary light curves of AD Leo during the campaign season [viii] 2019 May 17–19. The horizontal axes represent the observation date in the time coordinate of Julian Date (JD). $H\alpha$ and $H\beta$ equivalent width and u - and g -band relative flux light curves are plotted with the same symbols as Figure 4.

each peak clearly come back to local *quiescent* phase (see also figures in Appendix A.10). It is then probable that independent flares can cause the time evolution of the EWs, and there can be some meanings to separately classify them (as Flares Y25, Y26, and Y27) and investigate whether each peak has line asymmetries, for the main purpose of this paper. These flares are listed in Table 4 and are described with more detailed figures in Section 3.5 and Appendix A.10.

Figure 5 shows the light curves of YZ CMi during the campaign season [v] 2021 January 31–February 4. During this campaign season [v], YZ CMi was observed with APO 3.5 m optical high-dispersion spectroscopy, ARCSAT ground-based photometry (u and g bands), and TESS space photometry Sector 34. One flare (Y29) was detected in the $H\alpha$ and $H\beta$ equivalent width data in Figure 5(a). There could be a flare on February 4 as shown with the description “flare ?” in Figure 5(a), but the S/N was low due to bad weather. These flares are listed in Table 4 and are described with more detailed figures in Appendix A.11.

Figure 6 shows the light curves of EV Lac during the two campaign seasons [vi] 2019 December 15 and [vii] 2020 August 26–September 2. During these two campaign seasons [vi] and [vii], EV Lac was observed with APO 3.5 m optical high-dispersion spectroscopy and ARCSAT ground-based photometry (u and g bands). Nine flares (E1–E9) were detected in the $H\alpha$ and $H\beta$ EW data in Figures 6(a) and (b). These nine flares were defined as phases showing the $H\alpha$ EW increase of $\gtrsim 0.5$ Å compared with nearby local *quiescent* phase on each night ($H\alpha$ EW ~ 5 – 7 Å). These flares are listed in Table 4 and are described with more detailed figures in Section 3.6 and Appendices A.12–A.16.

Figure 7 shows the light curves of AD Leo during the campaign season [viii] 2019 May 17–19. During this campaign season [viii], AD Leo was observed with APO 3.5 m optical high-dispersion spectroscopy and ARCSAT ground-based photometry (u and g bands). Three flares (A1–A3) were detected in the $H\alpha$ and $H\beta$ EW data in Figure 7(a). These three flares were defined as phases showing the $H\alpha$ EW increase of $\gtrsim 0.5$ Å compared with nearby local *quiescent* phase on each night ($H\alpha$ EW ~ 5 – 7 Å). These flares are listed in Table 4 and are described with more detailed figures in Section 3.7 and Appendices A.17–A.18.

Next, we investigate whether blue wing asymmetries (enhancements of blue wings) are seen in the hydrogen Balmer $H\alpha$ and $H\beta$ lines. If the blue wing asymmetries are observed during a flare in $H\alpha$ and $H\beta$ lines, we also investigate whether other major chromospheric lines ($H\gamma$, $H\delta$, Ca II K, Ca II 8542, He I D3, Na I D1 and D2, $H\epsilon$ + Ca II H) also show blue wing asymmetries. As reported in the following subsections and listed in Tables 4 and 5, seven flares (Flares Y3, Y6, Y18, Y23, E1, E2, and A3) among all the 41 flares showed clear blue wing asymmetries in $H\alpha$ and $H\beta$ lines. These seven flares are also marked as “(B)” in Table 4. In Sections 3.2–3.7, we discuss the detailed flare light curves and flare chromospheric line spectra from the observation dates when blue wing asymmetries in $H\alpha$ and $H\beta$ lines were detected (YZCMi, 2019 January 27, 2019 December 12, 2020 January 18, and 2020 December 6; EV Lac, 2019 December 15; AD Leo, 2019 May 19). The data of the observation dates when blue wing asymmetries were not detected are shown in Appendix. In this paper, we focus our analysis on the flares with blue wing asymmetries; the flares without blue asymmetries (e.g., flares only with red

Table 5
Flares Showing Blue Wing Asymmetries

Flare	Star Name	UT Date	WLF	$E_{H\alpha}$ (10^{31} erg)	$\Delta t_{H\alpha}^{\text{flare}}$ (hr)	$\Delta t_{H\alpha}^{\text{blueasym}}$ (minutes)	$v_{\text{blue,max}}^{H\alpha}$ (km s^{-1})	Other Lines ^a
Y3	YZ CMi	2019 Jan 27	NWL	1.7	4.3	$\sim 20 \times 2$	-200	[B] H β , H γ , H δ , H ϵ , Ca II H&K [NB] Ca II 8542, Na D1 and D2, He D3
<p>(1) The clear short-lived Hα blue wing asymmetries up to $\sim -200 \text{ km s}^{-1}$ were seen twice (20 minutes \times 2) during the Hα flare over 4 hr.</p> <p>(2) As for Hβ, Hγ, Hδ, Hϵ, and Ca II H&K lines, blue wing asymmetries are not so clear at around the time of the first Hα blue asymmetry (time [3] in Figures 8–11), while they are clearly seen at around the second one (time [5] in Figures 8–11).</p> <p>(3) Some red-wing enhancements (or almost symmetric broadened wing components) were also seen for Hα, Hβ, Hγ, Hδ, Hϵ, and Ca II H&K lines (e.g., $\pm 150 \text{ km s}^{-1}$ for Hα line).</p> <p>(4) Equivalent width light curves (Figure 8): Hα and Ca II K evolve similarly while other Balmer lines, Ca II 8542, Na I D1 and D2, and He I D3 lines decrease faster.</p> <p>(5) No clear white-light flux enhancements during the flare even in TESS high-precision photometric data, while there are very small <i>suggestive</i> increases ($E_{\text{TESS}} < 2.6 \times 10^{32} \text{ erg}$).</p> <p>(6) Flare emission was observed also in NICER soft X-ray data ($E_X(0.5\text{--}2.0 \text{ keV}) = 2.6 \times 10^{32} \text{ erg}$, and $E_{\text{Xray,flare}}(\text{GOES band}) = 4.7 \times 10^{31} \text{ erg}$).</p>								
Y6	YZ CMi	2019 Dec 12	NWL	> 4.1	> 4.9	90–120	-200	[B] H β [NB] H γ , H δ , H ϵ , Ca II H&K, Ca II 8542, Na D1 and D2, He D3
<p>(1) The clear Hα blue wing enhancement up to $\sim -200 \text{ km s}^{-1}$ was seen in early phase of the flare, while the line profile gradually shifted to the red-wing enhancement up to $\sim +200 \text{ km s}^{-1}$, during the H$\alpha$ flare over 4.9 hr.</p> <p>(2) Similar shift from blue to red wing asymmetry was also seen in Hβ line (from ~ -150 to $\sim +150 \text{ km s}^{-1}$).</p> <p>(3) Late-phase red wing asymmetries were also seen clearly in Hγ and Hδ lines, and possibly in He I D3 5876 line.</p> <p>(4) There are at least two short white-light continuum enhancements ($\lesssim 10$ minutes each) in the middle/late phase of the flare, but there are no other clear white-light enhancements that are considered to be physically associated with the early main increasing phase of the whole Hα flare.</p>								
Y18	YZ CMi	2020 Jan 21	WL	1.5–1.6	3.4	60	-200	[B] H β [NB] Ca II 8542, Na D1 and D2, He D3
<p>(1) The blue wing enhancements up to ~ -200 and $\sim -150 \text{ km s}^{-1}$ were seen in Hα and Hβ lines, respectively, during the decay phase of the flare.</p> <p>(2) The multiple white-light continuum flux enhancements during the Hα flare.</p>								
Y23	YZ CMi	2020 Dec 6	WL	colored > 1.1	> 1.3	> 45	-250	[B] H β , H γ , H δ , H ϵ , Ca II H&K, Na D1 and D2, He D3 [NB] Ca II 8542
<p>(1) The clear white-light continuum flux enhancements ($\sim 1260\%$ and $\sim 125\%$ in u and g bands, respectively) observed before the start of the spectroscopic observation.</p> <p>(2) The Hα and Hβ blue wing enhancements up to ~ -250 and $\sim -200 \text{ km s}^{-1}$, respectively, were seen almost over the whole observed phase of the flare, while the velocities of blue wing enhancements decayed gradually.</p> <p>(3) Blue wing enhancements were seen in all the lines except for Ca II 8542, while the velocities of blue wing enhancements are different among the lines.</p>								
E1	EV Lac	2019 Dec 15	NEP	2.9	3.6	$\gtrsim 60$	-200	[B] H β , H γ , H δ , Ca II H&K [NB] H ϵ , Ca II 8542, Na D1 and D2, He D3
<p>(1) Only the late-phase of the flare was observed with ARCSAT photometry, so it is possible there were increases of the continuum white-light flux in the early phase of the flare.</p> <p>(2) The Hα and Hβ blue wing enhancements up to ~ -200 and $\sim -150 \text{ km s}^{-1}$, respectively, were seen, but the duration of the blue wing enhancement in Hβ line (~ 0.5 hr) is shorter than that of Hα line ($\gtrsim 1$ hr).</p> <p>(3) The blue wing enhancements were also seen for Hγ, Hδ, and Ca II H&K lines, while possible slight blueshifts of the line peak were also seen in Ca II 8542 and He I D3 lines.</p>								
E2	EV Lac	2019 Dec 15	WL	0.58	0.9	20	-150	[B] H β , H γ [NB] H δ , H ϵ , Ca II H&K, Ca II 8542, Na D1 and D2, He D3
<p>(1) The Hα and Hβ blue wing enhancements up to $\sim -150 \text{ km s}^{-1}$ were seen for the durations 20 and 10 minutes, respectively.</p> <p>(2) The clear white-light continuum flux increase was observed almost simultaneously with the Hα and Hβ blue wing enhancements.</p> <p>(3) The blue wing enhancements were also seen for Hγ lines, while possible slight line peak blueshifts were also seen in Ca II H&K lines.</p>								
A3	AD Leo	2019 May 19	NEP	> 5.3	> 3.1	120–150		[B] H β , H γ , H δ , H ϵ , Ca II K, Ca II 8542, He D3 [NB] Na D1 and D2
<p>(1) Flare already started when the observation started, so it is possible there were increases of the continuum white-light flux before the observation started.</p> <p>(2) The Hα and Hβ blue wing enhancements up to -150 to -200 km s^{-1} were seen, which continued for more than 2 hr until the flare decayed.</p> <p>(3) Blue wing enhancements were seen in all the lines except for Na I D1 and D2, while the velocities of blue wing enhancements are different among the lines.</p>								

Table 5
(Continued)

Flare	Star Name	UT Date	WLF	$E_{H\alpha}$ (10^{31} erg)	$\Delta t_{H\alpha}^{\text{flare}}$ (hr)	$\Delta t_{H\alpha}^{\text{blueasym}}$ (minutes)	$v_{H\alpha, \text{blue, max}}^{\text{H}\alpha}$ (km s^{-1})	Other Lines ^a
V2016 ^b	V374 Peg	2005 Aug 20	...	$\sim 10^2$	~ 3	15–40 minutes \times 3	–675	[B] H α , H β , H γ [NB] He D3 (not clearly mentioned in Vida et al. 2016)
<p>(1) Three consecutive blue-wing enhancements in Balmer lines. All three blue-wing asymmetries occurred during a single flare with flaring energy $\sim 10^{33}$ erg (see Moschou et al. 2019), with the third event being the strongest, corresponding to projected velocity of -675 km s^{-1}. This event showed not only blue wing asymmetries but also clearly separated additional emission components (see Figure 2 of Leitzinger et al. 2022).</p>								
H2018 ^b	EV Lac	2015 Aug 15	...	2.0	2.6	120	–200	...
<p>(1) A blue wing asymmetry in the Hα line has been observed for $\gtrsim 2$ hr (almost from flare start to end). (2) The possible existence of absorption components in the red wing of the Hα line was reported when the Hα line showed blue wing asymmetry.</p>								
M2021 ^b	YZ CMi	2019 Jan 18	no	0.47	1.2	80	–150	--
<p>(1) A Hα flare without clear brightening in continuum, which exhibited blue wing asymmetry lasting for ~ 1 hr.</p>								

Notes. WLF: this column describes whether the flare is identified as white-light flare (WL) or non-white-light flare (NWL), while stars with “NEP” do not have enough photometric data for the WL or NWL identification (from Table 4). $\Delta t_{H\alpha}^{\text{flare}}$: flare duration in H α line (from Table 4). $E_{H\alpha}$: flare energy in H α line (from Table 4). $\Delta t_{H\alpha}^{\text{blueasym}}$: duration of H α blue wing asymmetry (e.g., the double-headed arrow in Figure 10(a)). $v_{H\alpha, \text{blue, max}}^{\text{H}\alpha}$: the maximum velocity of blue wing enhancements estimated by eye. Other lines: [B] and [NB] show the lines with and without blue wing asymmetries, respectively.

^a There are no observation data of H γ , H δ , H ϵ , Ca II H&K lines for Flare Y18, since these lines are not included in the wavelength range of SMARTS 1.5 m/CHIRON.

^b V2016, H2018, and M2021 are flares with clear blue wing asymmetries reported in Vida et al. (2016), Honda et al. (2018), and Maehara et al. (2021), respectively. They are listed here just for comparison. As for chromospheric lines, H α line is only observed in Honda et al. (2018), Maehara et al. (2021). There were no white-light observation data in Vida et al. (2016), Honda et al. (2018). The flare energy value of V2016 is from Moschou et al. (2019).

asymmetries and symmetric broadening) are briefly summarized in Section 4.5 and will be discussed in detail in our future papers.

3.2. Flares Y2 and Y3 (Blue Wing Asymmetry) Observed on 2019 January 27

On 2019 January 27, two flares (Flares Y2 and Y3) were detected in H α and H β lines as shown in Figure 8(a). During Flare Y2, the H α and H β EWs increased to 9.9 Å and 13.9 Å, respectively, and the flare duration in H α ($\Delta t_{H\alpha}^{\text{flare}}$) is > 3.2 hr (Table 4). We note that Flare Y2 was in progress when the observation was started. Flare Y3 has the larger amplitude than Flare Y2. During Flare Y3, the H α and H β EWs increased to 11.2 Å and 16.1 Å, respectively, and the flare duration $\Delta t_{H\alpha}^{\text{flare}}$ is 4.3 hr (Table 4). In addition to chromospheric lines, Flare Y3 is detected also in NICER X-ray data (Figure 8(d)). The white-light (WL) flux observed by ARCSAT u and g bands and TESS did not show clear enhancements above the photometric errors of the data ($3\sigma_u = 22.9\%$, $3\sigma_g = 4.2\%$, and $3\sigma_{\text{TESS}} = 0.34\%$) during these two flares (Figures 8(b) and (c)). As described in Section 2.5, $3 \times$ the standard deviation ($3\sigma_u$, $3\sigma_g$, and $3\sigma_{\text{TESS}}$) of the relative flux in the quiescent phase for each night is used for the detection threshold of the WL flare emission. There are very small *suggestive* increases in u and g bands and TESS data around time 6–8 hr in Figures 8(b) and (c), although this is still smaller than the threshold ($3\sigma_{\text{TESS}} = 0.34\%$). We also note that these small increases could be caused by the emission lines (e.g., Balmer lines) included in u , g , and TESS bands.

We estimated the upper limits to the flare component peak luminosities and flare energies in u , g , and TESS bands, following the method described in Section 2.5, and the resultant values (L_u , L_g , L_{TESS} , E_u , E_g , and E_{TESS}) are in Table 4. The flare component peak luminosities and flare

energies of H α and H β lines ($L_{H\alpha}$, $L_{H\beta}$, $E_{H\alpha}$, and $E_{H\beta}$) are also estimated and listed in Table 4, following the method described in Section 2.5. Since Flare Y2 already started when the observation was started, the real flare energy values could be larger than the values listed here.

The H α and H β line profiles during Flares Y2 and Y3 are shown in Figures 9 and 10. The clear H α blue wing asymmetries with blue wing enhancements up to $\sim -200 \text{ km s}^{-1}$ were seen twice at around the time [3] and [5] during Flare Y3 (Figures 8–10). The durations of these two blue wing asymmetries were both only ~ 20 minutes. As for H β line, the blue wing asymmetry was not so clear at around the time [3], while the blue wing asymmetry with wing enhancements up to $\sim -150 \text{ km s}^{-1}$ was clearly seen at around the time [5]. In addition to blue wing asymmetries, we note that red wing components of H α and H β lines show some enhancements up to $\sim +150 \text{ km s}^{-1}$ (e.g., see the time [3], [4], and [6] in Figures 9 and 10), and it can be interpreted that almost symmetric broadened wing components are seen at around these times.

The EW light curves of H γ , H δ , Ca II K, Ca II 8542, Na I D1 and D2, and He I D3 5876 lines are also shown in Figures 8(e), (f), and (g).²⁴ The profiles of these lines and H ϵ + Ca II H lines during Flare Y3 are shown in Figure 11. Since S/N of the spectroscopic data around these lines are smaller than those of H α and H β lines, we integrate two or three temporally adjacent spectra into one spectra (see time resolution of the H γ , H δ , Ca II K, Na I D1 and D2, and He I D3 5876 lightcurve data in Figure 8). In Figure 11, such time-integrated data are shown with the prime mark, and for example, the time [3'] in

²⁴ In this paper, the EW light curve of H ϵ + Ca II H lines are not plotted, and only snapshot spectra of H ϵ + Ca II H lines are shown as in Figures 11(k) and (l), since these two lines can overlap with each other.

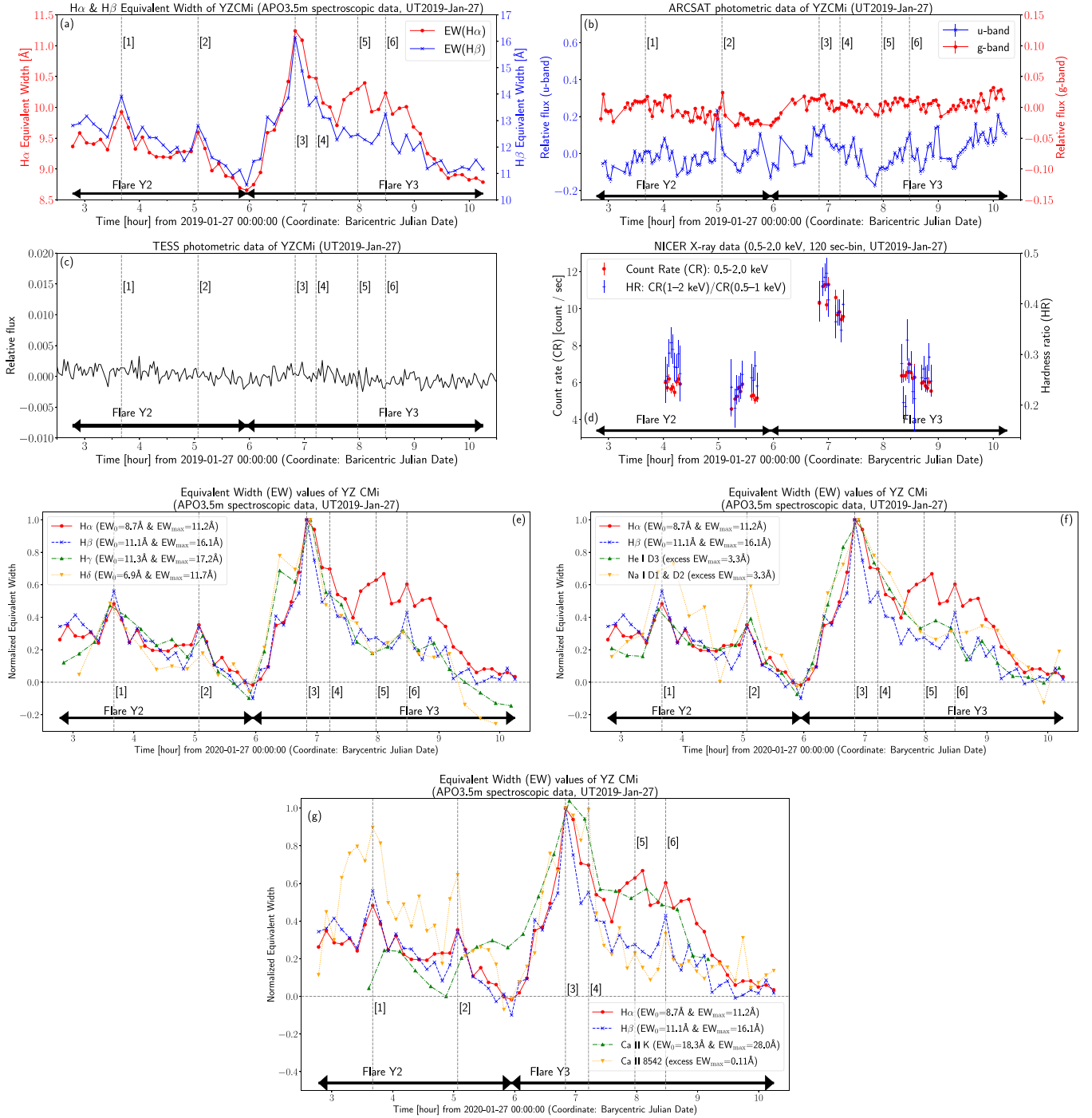


Figure 8. Light curves of YZ CMi on 2019 January 27 showing Flares Y2 and Y3. The horizontal axes represent the observation time in the time coordinate of Barycentric Julian Date (BJD). The gray dashed lines with numbers ([1]–[6]) correspond to the time shown with the same numbers in Figures 9–11. (a) $H\alpha$ and $H\beta$ equivalent width light curves from APO 3.5 m spectroscopic data. Red and blue symbols correspond to $H\alpha$ and $H\beta$ EWs, respectively. The black double-headed arrows indicate the start and end time of Flares Y2 and Y3 (see $\Delta t_{H\alpha}^{\text{flare}}$ in Table 4). (b) u - and g -band relative flux light curves from ARCSAT0.5m photometric data. Blue asterisks and red circles correspond to u - and g -band data, respectively. (c) TESS-band relative flux light curve from TESS photometric data. (d) Red circles are background-subtracted X-ray count rates [count per second] from NICER data in 0.5–2.0 keV. Blue plus marks are X-ray hardness ratio (count rate (1.0–2.0 keV)/count rate (0.5–1.0 keV)) from NICER data. (e) EW light curves of $H\alpha$ (red symbols), $H\beta$ (blue), $H\gamma$ (green), and $H\delta$ (orange) from APO 3.5 m spectroscopic data. The EW values are normalized with their peak and quiescent values (EW_{max} and EW_0). (f) Same as (e), but for $H\alpha$ (red symbols), $H\beta$ (blue), He I D3 (green), and Na I D1 and D2 (orange). As for He I D3 and Na I D1 and D2 lines, excess EWs (differences from the quiescent components) are plotted. (g) Same as (e), but for $H\alpha$ (red symbols), $H\beta$ (blue), Ca II K (green), and Ca II 8542 (orange). As for Ca II 8542 line, excess EWs (differences from the quiescent components) are plotted.

Figure 11 shows the time 6.79–7.00 hr, which include time [3] (Figures 8 and 9). The same way of using the prime mark is applied to all figures in the following of this paper.

As for $H\gamma$, $H\delta$, He, and Ca II H&K lines, the blue wing asymmetries were not so clear at around the time [3'], while the

blue asymmetries with wing enhancements of up to -50 to -100 km s^{-1} were seen at around the time [5']. At around the time [3'], blue wing asymmetries are not clearly seen for these lines, but almost symmetric broadened wing components ($\pm 150 \text{ km s}^{-1}$) can be seen, and these symmetric wing

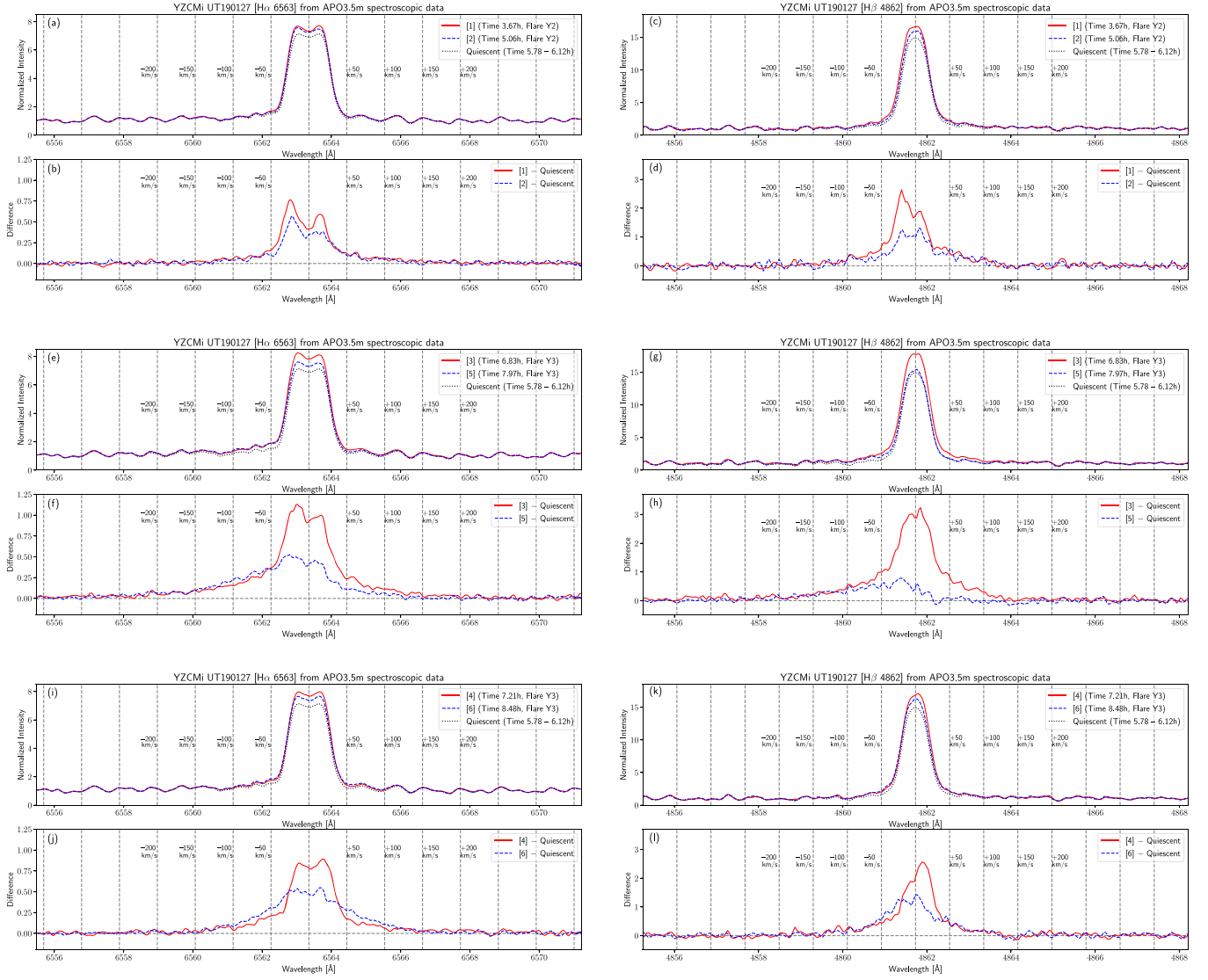


Figure 9. (a) Line profiles of the $H\alpha$ emission line during Flare Y2 on 2019 January 27 from APO 3.5 m spectroscopic data. The horizontal and vertical axes represent the wavelength and flux normalized by the continuum. The gray vertical dashed lines with velocity values represent the Doppler velocities from the $H\alpha$ line center. The red solid and blue dashed lines indicate the line profiles at the time [1] and [2], respectively, which are indicated in Figure 8 (light curves) and are during Flare Y2. The black dotted line indicates the line profiles in quiescent phase, which are the average profile during 5.78–6.12 hr on this date (see Figure 8(a)). (e) Same as panel (a), but the line profiles at the time [3] and [5] during Flare Y3. (i) Same as panel (a), but the line profiles at the time [4] and [6] during Flare Y3. It is noted that the profiles at time [3]–[6] are not plotted in order (those at [3] and [5] are in (e)–(h), while those at [4] and [6] are in (i)–(l)), so that the blue asymmetries at time [3] and [5] are plotted in the same panels. (c), (g), and (k) Same as panels (a), (e), and (i), respectively, but the line profiles for the $H\beta$ emission line. (b), (d), (f), (h), (j), and (l) Same as panels (a), (c), (e), (g), (i), and (k), respectively, but the line profile differences from the quiescent phase.

components can be similar to those seen in $H\alpha$. In addition, the redshifted absorption components were seen especially in Ca II H&K lines together with blue wing asymmetries at around the time [5'], and this component looks larger than the noise level. Similar redshifted components have been observed in the previous observation of $H\alpha$ blue wing asymmetry (Honda et al. 2018), but currently, the physical origin of them is still unclear. It is also important to discuss the origin of the redshifted absorption in the future studies (see also Section 4.5 for future prospects of redshifts of lines).

The clear blue wing asymmetries were not seen in Ca II 8542, Na I D1 and D2, and He I D3 5876 lines, while Na I D1 and D2, and He I D3 5876 lines show slight (-10 to -20 km s^{-1}) blueshifts at around the time [5'] (Figure 11(j)). The EW light curves in Figures 8(e), (f), and (g) show that $H\alpha$ and Ca II K evolve similarly while other Balmer lines decrease

faster during Flare Y3. We also note that Ca II 8542 and Na D lines show relatively large responses in Flare Y2, while other lines show smaller responses compared to Flare Y3.

We generate a background-subtracted X-ray light curve between 0.5 and 2 keV for the NICER X-ray data. The light curve shows a count rate increase by a factor of 2 on the second day, which coincides with Flare Y3 in the $H\alpha$ band (Figure 8). The photon count in the other intervals hovers around 6–7 cts s^{-1} with a few small flare-like variations.

We applied an adaptive binning to the light curve with a Bayesian block algorithm (Scargle et al. 2013; see Figures 12(a) and (b)) and used those blocks for a spectral analysis of Flare Y3. We assume Block 5 just before the flare onset to represent the flare's nonflaring (quiescent) emission. The spectrum shows a hump between 0.5 and 1 keV, which originates from the Fe L and O K lines and the weak Mg and Si

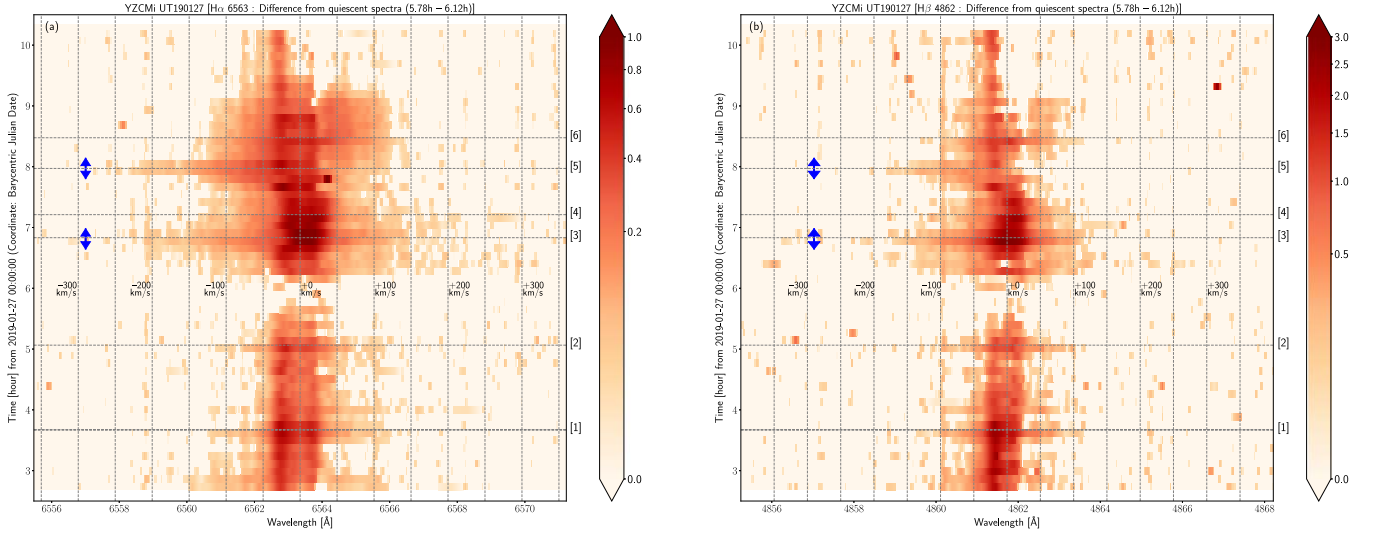


Figure 10. (a) Time evolution of the $H\alpha$ line profile covering Flares Y2 and Y3 on 2019 January 27. The horizontal and vertical axes represent the wavelength and the observation time in the time coordinate of Barycentric Julian Date (BJD). The gray vertical dashed lines with velocity values represent the Doppler velocities from the $H\alpha$ line center. The gray horizontal dashed lines indicate the time [1]–[6], which are shown in Figures 8 (light curves) and 9 (line profiles). The color map represents the line profile changes from the quiescent profile (see Figures 9(b), (f), and (j)). The blue double-headed arrows roughly represent the times when blue wing asymmetries were clearly seen and used for estimating the duration of blue wing asymmetries (see $\Delta t_{H\alpha}^{\text{blueasym}}$ in Table 5). (b) Same as panel (a), but for the $H\beta$ line profile.

K lines. We reproduce the spectral shape by an optically thin thermal plasma emission (apec Smith et al. 2001) model with two temperature components at 0.26 and 0.97 keV (3.1×10^6 and 1.1×10^7 K) and an elemental abundance at 0.52 solar (see also temperature and emission measure, hereafter EM, values of the quiescent component shown in Figure 12(e)). However, the fit is not statistically acceptable at above 3σ due to the line-like excesses at 0.51 and 1.22 keV.

Figure 13 shows time-resolved X-ray spectra during Flare Y3. The flare spectrum near the peak is significantly harder than the quiescent spectrum, with a strong oxygen K line at 0.64 keV. Since we measure the X-ray flux variation during the flare in this study, we fit each spectrum by a one-temperature apec model with independent oxygen and iron elemental abundances on top of the best-fit quiescent spectrum model.

The resultant values of the temperatures (T) and EMs ($EM = n^2 V$) are shown in Figure 12(e). Here, n is the electron density, and V is the volume. Using the modeling results, the X-ray luminosities in the 0.5–2.0 keV band ($L_{X\text{ray,flare}}(0.5\text{--}2.0\text{ keV})$) and the GOES band ($1.5\text{--}12.4\text{ keV} = 1\text{--}8\text{ \AA}$, $L_{X\text{ray,flare}}(\text{GOES band})$)²⁵ were calculated and shown in Figures 12(c) and (d) with $H\alpha$ light curve. From this figure, we can see that $H\alpha$ flare duration is longer than that of soft X-ray. The X-ray energy of Flare Y3 in the 0.5–2.0 keV band ($E_{X\text{ray,flare}}(0.5\text{--}2.0\text{ keV})$) and the GOES band ($E_{X\text{ray,flare}}(\text{GOES band})$) are also calculated to be 2.6×10^{32} and 4.7×10^{31} erg. $E_{X\text{ray,flare}}(0.5\text{--}2.0\text{ keV})$ is ~ 15 times larger than the $H\alpha$ flare energy ($E_{H\alpha} = 1.7 \times 10^{31}$ erg) and at least slightly larger than the upper-limit of TESS WL flare energy ($E_{\text{TESS}} < 2.6 \times 10^{32}$ erg).

3.3. Flare Y6 (Blue Wing Asymmetry) Observed on 2019 December 12

On 2019 December 12, a flare (Flare Y6) was detected in $H\alpha$ and $H\beta$ lines as shown in Figure 14(a). During Flare Y6, the

$H\alpha$ and $H\beta$ EWs increased to 13.5 \AA and 16.8 \AA , respectively, and $\Delta t_{H\alpha}^{\text{flare}}$ is > 4.9 hr (Table 4). The observation ended in the decay of Flare Y6. The continuum flux observed by ARCSAT u and g bands shows (at least two) short ($\lesssim 10$ minutes each) enhancements during Flare Y6 (Figures 14(b) and (c)). The amplitudes of these short continuum enhancements in u band are $\sim 60\%$ (around the time 10.3–10.4 hr) and $\sim 40\%$ (around the time 12.2–12.3 hr), and those in g band are $\sim 4\%$ – 5% (around the time 10.3–10.4 hr) and $\sim 5\%$ – 6% (around the time 12.2–12.3 hr).

Although there are continuum enhancements around the times 10.3–10.4 and 12.2–12.3 hr, there are no clear WL emissions that are considered to be physically associated with the early increasing phase of the $H\alpha$ and $H\beta$ flare emission (time before ~ 10 hr). Considering this, the flare peak luminosities of Flare Y6 listed in Table 4 are upper limit values considering the photometric error values ($3\sigma_u = 26\%$, and $3\sigma_g = 4.9\%$): $L_u < 8 \times 10^{27} \text{ erg s}^{-1}$ and $L_g < 1.8 \times 10^{28} \text{ erg s}^{-1}$ (see Section 2.5). As for flare energies, only the upper limit values are calculated from these upper limit peak luminosities following the method in Section 2.5: $E_u < 7.2 \times 10^{31} \text{ erg}$ and $E_g < 1.6 \times 10^{32} \text{ erg}$. These upper limit values are larger than the values that can be estimated by only integrating the clear peaks around the times 10.3–10.4 and 12.2–12.3 hr ($E_u = 6 \times 10^{30} \text{ erg}$, and $E_g = 3 \times 10^{30} \text{ erg}$). We also estimated $L_{H\alpha}$, $L_{H\beta}$, $E_{H\alpha}$, and $E_{H\beta}$ values, which are listed in Table 4. Since the observation ended before Flare Y6 ended, the real flare energy values can be larger than the values listed here.

The $H\alpha$ and $H\beta$ line profiles during Flare Y6 are shown in Figures 15 and 16. The clear $H\alpha$ blue wing enhancement (blue wing asymmetry) up to $\sim -200 \text{ km s}^{-1}$ was seen in early phase of the flare (e.g., time [1]), while the line profile gradually shifted to the red-wing enhancement (red wing asymmetry) up to $\sim +200 \text{ km s}^{-1}$ (e.g., time [4]; Figures 14–16). The evolution of the $H\alpha$ line from blueshifted to redshifted line wing asymmetry is particularly evident. $H\beta$ line also shows the time evolution from the blue wing

²⁵ GOES band is the soft X-ray band used for the solar soft X-ray flux observation with the Geostationary Operational Environmental Satellite.

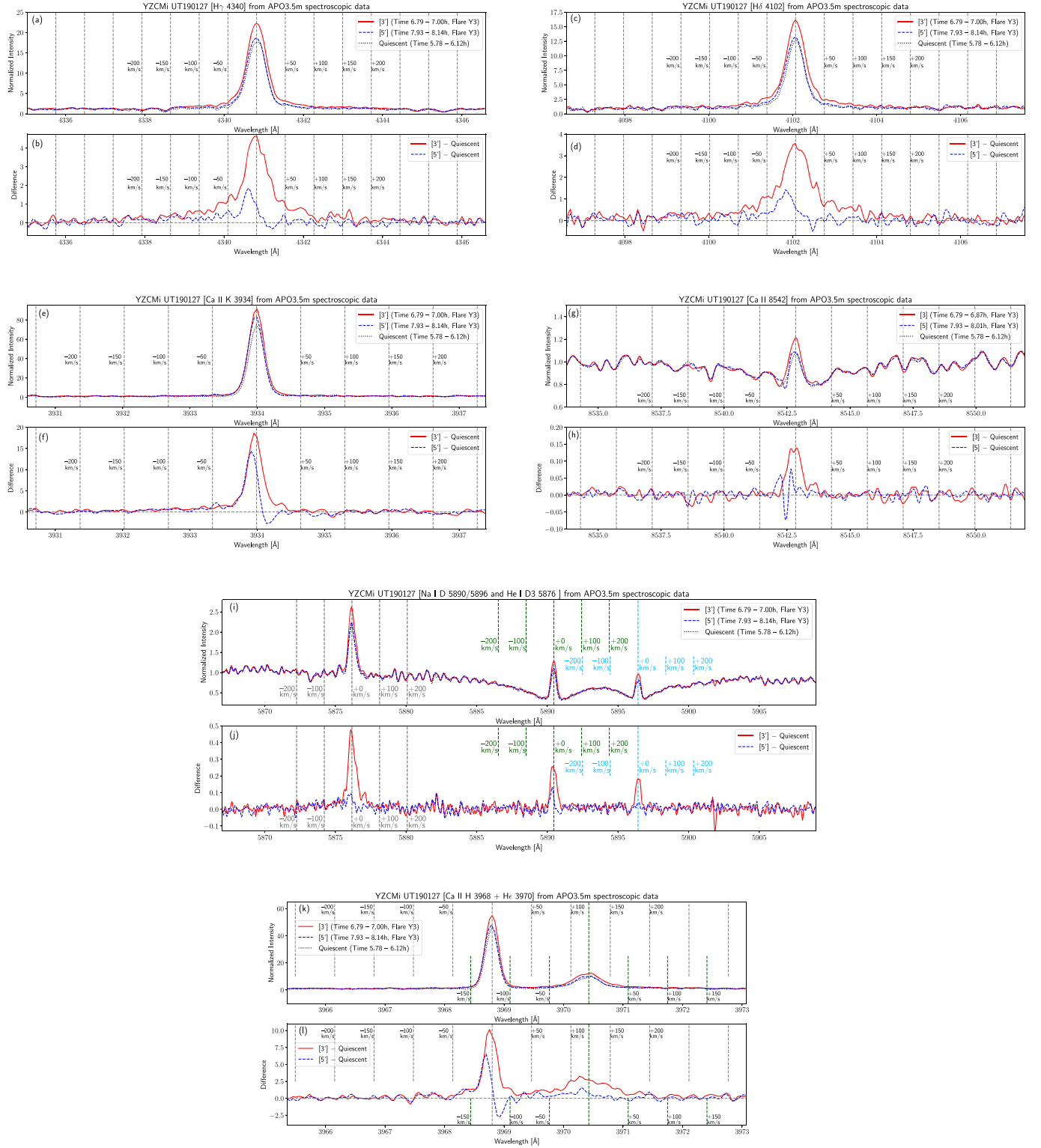


Figure 11. (a) Line profiles of the $H\gamma$ line when the $H\alpha$ line shows blue wing asymmetries (see Figures 9(e) and (f)) during Flare Y3 on 2019 January 27 from APO 3.5 m spectroscopic data. The horizontal and vertical axes represent the wavelength and flux normalized by the continuum. The gray vertical dashed lines with velocity values represent the Doppler velocities from the $H\gamma$ line center. The red solid and blue dashed lines indicate the integrated line profiles over the time [3'] (time 6.79–7.00 hr) and [5'] (time 7.93–8.14 hr) on this date, which include the time [3] and [5] in Figure 8 (light curves), respectively. (c), (e), (g), (i), and (k) Same as panel (a), but for $H\delta$, Ca II K, Ca II 8542, Na I D1 and D2 (5890 and 5896) and He I D3 5876, and H ϵ + Ca II H lines, respectively. As for the Ca II 8542 line, the data at the time [3] and [5] are plotted (not [3'] and [5']). (b), (d), (f), (h), (j), and (l) Same as panels (a), (c), (e), (g), (i), and (k), respectively, but the line profile changes from the quiescent phase.

asymmetry to the red wing asymmetry (Figures 15 and 16), which is very similar to that of $H\alpha$ line. The wing enhancements of these blue and red wing asymmetries in

$H\beta$ line are slightly smaller than those in $H\alpha$ line: from ~ -200 to $\sim +200$ km s^{-1} in $H\alpha$ line, and from ~ -150 to $\sim +150$ km s^{-1} in $H\beta$ line.

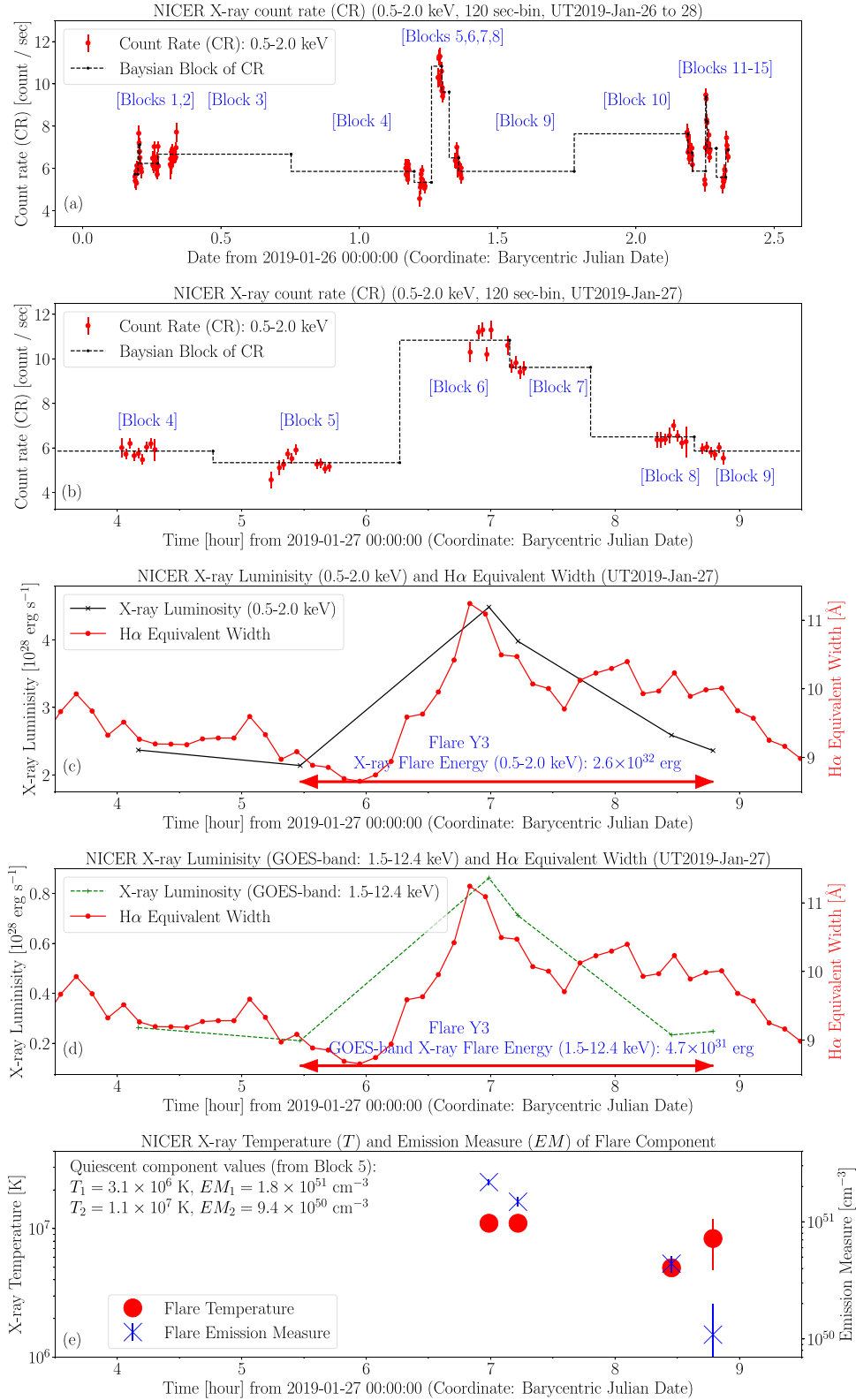


Figure 12. (a) NICER X-ray light curve of YZ CMi over the whole 3 days NICER observation period from UT 2019 January 26 to 28. The red circles are NICER X-ray count rates [count per second] in 0.5–2.0 keV. The black dotted line shows Bayesian block light curve (see Scargle et al. 2013) of the count rates, and each block is shown with the number. (b) NICER X-ray light curve of YZ CMi on 2019 January 27 showing Flare Y3. The symbols are plotted in the same way as (a). (c) Light curves of NICER X-ray luminosity (0.5–2.0 keV, black x-marks) and H α equivalent width (red circles) on UT 2019 January 27, showing Flare Y3. (d) Light curves of NICER X-ray luminosity in GOES band (1.5–12.4 keV, green plus marks) and H α equivalent width (red circles) on UT 2019 January 27, showing Flare Y3. (e) Light curves of NICER X-ray temperature (red circles) and emission measure (blue asterisks) of the flare component during Flare Y3 on UT 2019 January 27. The values are derived from the X-ray spectral fitting shown in Figure 13.

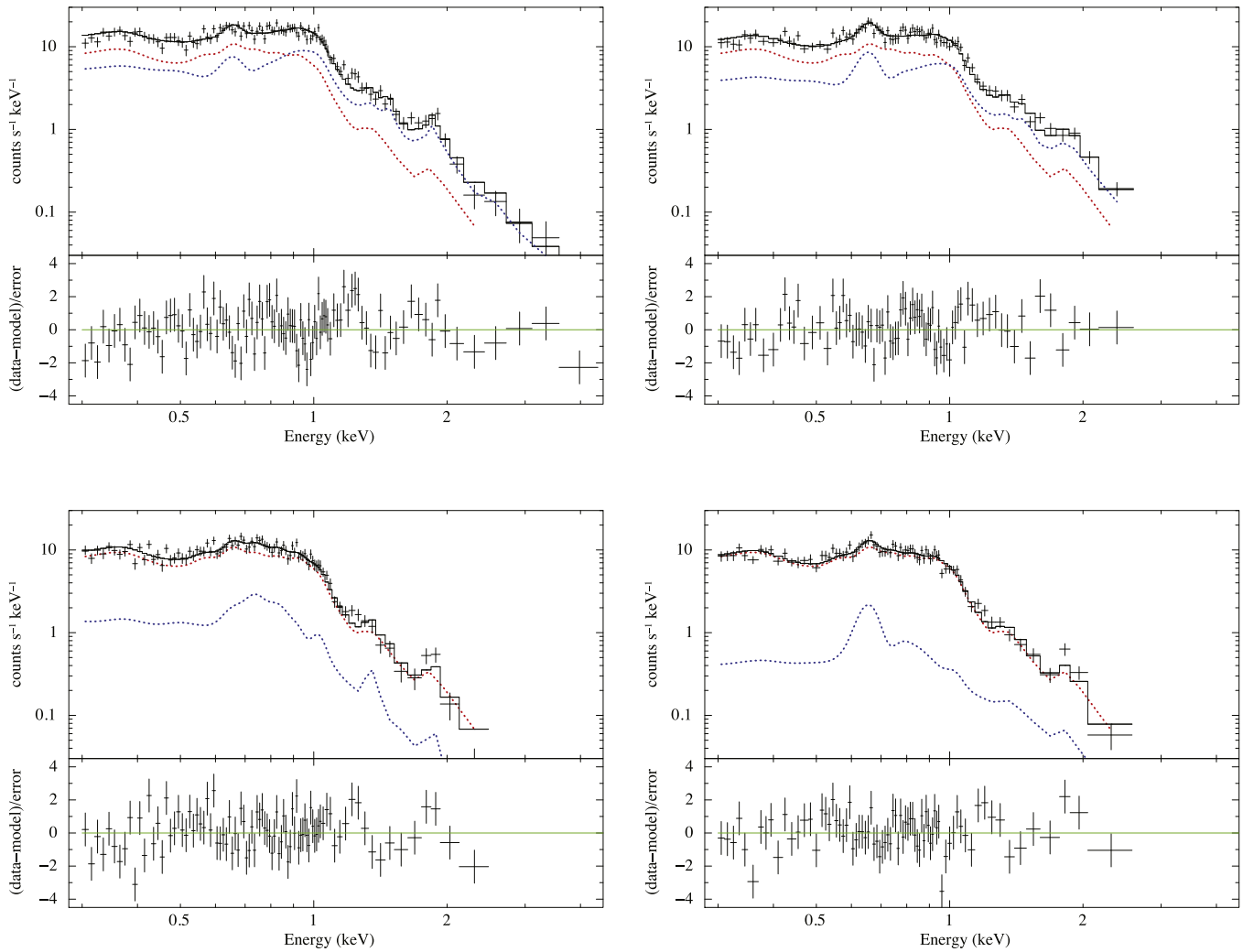


Figure 13. NICER X-ray spectra of Flare Y3: observation + model (Block 6, top left; Block 7, top right; Block 8, bottom left; Block 9, bottom right). The red and blue dotted lines show the preflare and flare components in the model. The black solid line shows the sum of these components.

The EW light curves of $H\gamma$, $H\delta$, Ca II K , Ca II 8542 , Na I D1 and D2 , and He I D3 5876 lines are also shown in Figures 14(c), (d), and (e). The profiles of these lines and $\text{H}\epsilon + \text{Ca II H}$ lines during Flare Y6 are shown in Figures 17 and 18. As for $H\gamma$ and $H\delta$ lines, the blue wing asymmetries in the early phase of the flare are not so evident (time [1'], [2'], and [3'] in Figure 17) while the red wing asymmetries in the later phase are seen (time [4'] in Figure 17). Similar time evolution of red wing asymmetry was seen also in He I D3 5876 line, but the possible red wing asymmetry component at time [4'] was very small ($\lesssim 50 \text{ km s}^{-1}$) (Figure 18(j)). As for Ca II H\&K , Ca II 8542 , Na I D1 and D2 , and $\text{H}\epsilon$ lines, the line asymmetries are not readily detected (Figure 18).

3.4. Flares Y18 (Blue Wing Asymmetry) and Y19 Observed on 2020 January 21

On 2020 January 21, two flares (Flares Y18 and Y19) were detected in $H\alpha$ and $H\beta$ lines as shown in Figure 19(a). As for Flare Y18, the $H\alpha$ and $H\beta$ EWs increased up to 10.5 \AA and 15.8 \AA , respectively, and $\Delta t_{H\alpha}^{\text{flare}}$ is 3.4 hr (Table 4). In addition to these enhancements in Balmer emission lines, the continuum flux from the LCO U - and V -band increase is at least $\sim 90\%$, and $\sim 5\%$, respectively, during Flare Y18 (Figure 19(b)). We note

that the LCO photometric observation has gaps in the later phase of Flare Y18, and it could be possible that we missed the continuum flux increase during this time. As for Flare Y19, the $H\alpha$ and $H\beta$ EWs increased to 12.5 \AA and 23.2 \AA , respectively, and $\Delta t_{H\alpha}^{\text{flare}}$ is $> 2.5 \text{ hr}$ (Table 4). We note that the observation finished before Flare Y19 ended. In addition to these enhancements in Balmer emission lines, the continuum flux observed with LCO U and V band increased at least by $\sim 130\%$ – 140% , and $\sim 5\%$ – 10% , respectively, during Flare Y19 (Figure 19(b)). The LCO photometric observation has gaps during Flare Y19, and it is possible that we missed the continuum brightness increase components during the gap time.

We estimated the flare component peak luminosities and flare energies in U and V bands, and the resultant values (L_U , L_V , E_U , and E_V) are in Table 4. The values listed here could be only the lower limit values, since the LCO observation has gaps during both Flares Y18 and Y19, (Figure 19(b)), and in the case of Flare Y19, the observation also finished before the flare ended. The $L_{H\alpha}$, $L_{H\beta}$, $E_{H\alpha}$, and $E_{H\beta}$ values are also estimated and listed in Table 4. The $H\alpha$ and $H\beta$ energy values of Flare Y19 listed here are only the lower limit values, since the observation finished before Flare Y19 ended.

The $H\alpha$ and $H\beta$ line profiles during Flares Y18 and Y19 are shown in Figures 20–22. During Flare Y18, the blue wing

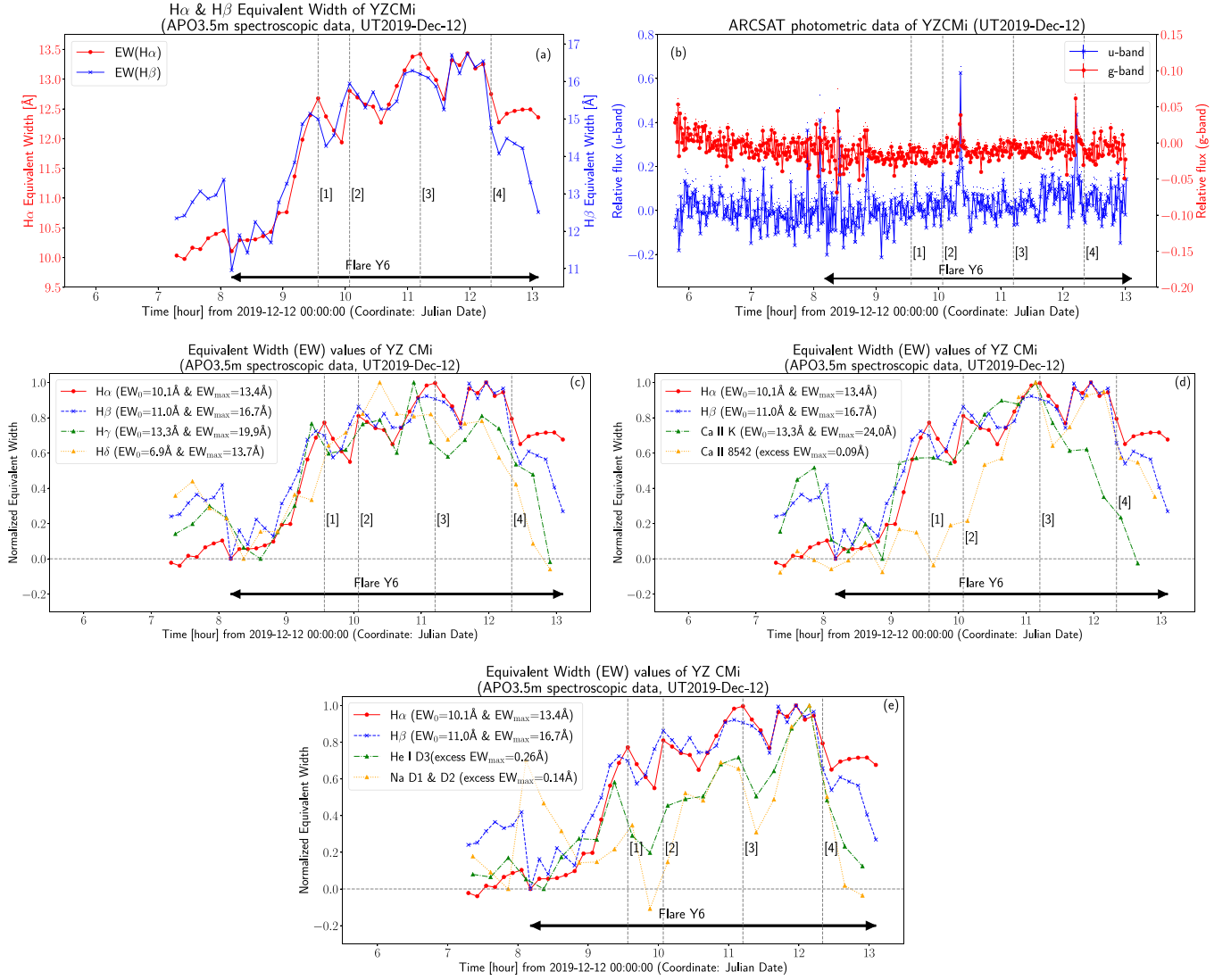


Figure 14. Light curves of YZ CMi on 2019 December 12 summarizing the multiline behavior of Flare Y6. The data are plotted in (a), (b), (c), (d), and (e) similarly with Figures 8(a), (b), (e), (g), and (f), respectively, but the horizontal axes are in the time coordinate of Julian Date (JD). The gray dashed lines with numbers ([1]–[4]) correspond to the time shown with the same numbers in Figures 15 and 16.

asymmetry of $H\alpha$ line was detected over about 1 hr around the flare peak (Figure 22). The enhancements of the blue wing of $H\alpha$ line were the largest at around the beginning of the decay phase (time [3] and [4] in Figures 19(a), 20, and 22), and we can see the enhancements up to $\sim 200 \text{ km s}^{-1}$ then. These blue wing enhancements up to $\sim 150 \text{ km s}^{-1}$ were also possibly seen in $H\beta$ line (time [3] and [4] in Figure 20(h)); though, the S/N of the data is relatively low. During Flare Y19, the $H\alpha$ line showed the line wing broadenings ($\sim \pm 150$ – 200 km s^{-1}) twice during flares: one at around the time [5]–[7], and the other at around the time [8]–[10] (Figures 21 and 22). During these broadenings, the red wing of the $H\alpha$ line was slightly enhanced. The $H\beta$ line showed the similar line wing broadening ($\sim \pm 150$ – 200 km s^{-1}) at around the time [5]–[7], but the wing broadening in $H\beta$ line was not seen in the later phase at around the time [8]–[10] (Figures 21 and 22).

The EW light curves of Ca II 8542, Na I D1 and D2, and He I D3 5876 lines are also shown in Figure 19(c). The profiles of these lines during Flare Y19 are shown in Figure 23. Line asymmetries were not clearly seen in these lines.

3.5. Flares Y23 (Blue Wing Asymmetry) and Y24 Observed on 2020 December 6

On 2020 December 6, two flares (Flares Y23 and Y24) were detected in $H\alpha$ and $H\beta$ lines as shown in Figure 24(a). Flare Y23 already started when the spectroscopic observation started. The $H\alpha$ and $H\beta$ EWs decreased from 10.5 \AA and 17.8 \AA , respectively, and $\Delta t_{H\alpha}^{\text{flare}}$ is $> 1.3 \text{ hr}$ (Table 4). The photometric observation captured early phase of the flare since it started $\sim 1 \text{ hr}$ before the spectroscopic observation started. During Flare Y23, the continuum brightness observed with ARCSAT u and g bands increased by $\sim 1260\%$ and $\sim 125\%$, respectively (Figure 24(b)). As for Flare Y24, the $H\alpha$ and $H\beta$ EWs increased to 8.2 \AA and 13.4 \AA , respectively, and $\Delta t_{H\alpha}^{\text{flare}}$ is 0.7 hr (Table 4). In addition to these enhancements in Balmer emission lines, the continuum brightness observed with ARCSAT u and g bands increased by $\sim 70\%$ – 75% and $\sim 4\%$, respectively, during Flare Y24 (Figure 24(b)).

We estimated L_u , L_g , E_u , E_g , $L_{H\alpha}$, $L_{H\beta}$, $E_{H\alpha}$, and $E_{H\beta}$ values, and they are listed in Table 4. Since the initial phase of Flare Y23 was not observed in the spectroscopic observation, the $H\alpha$

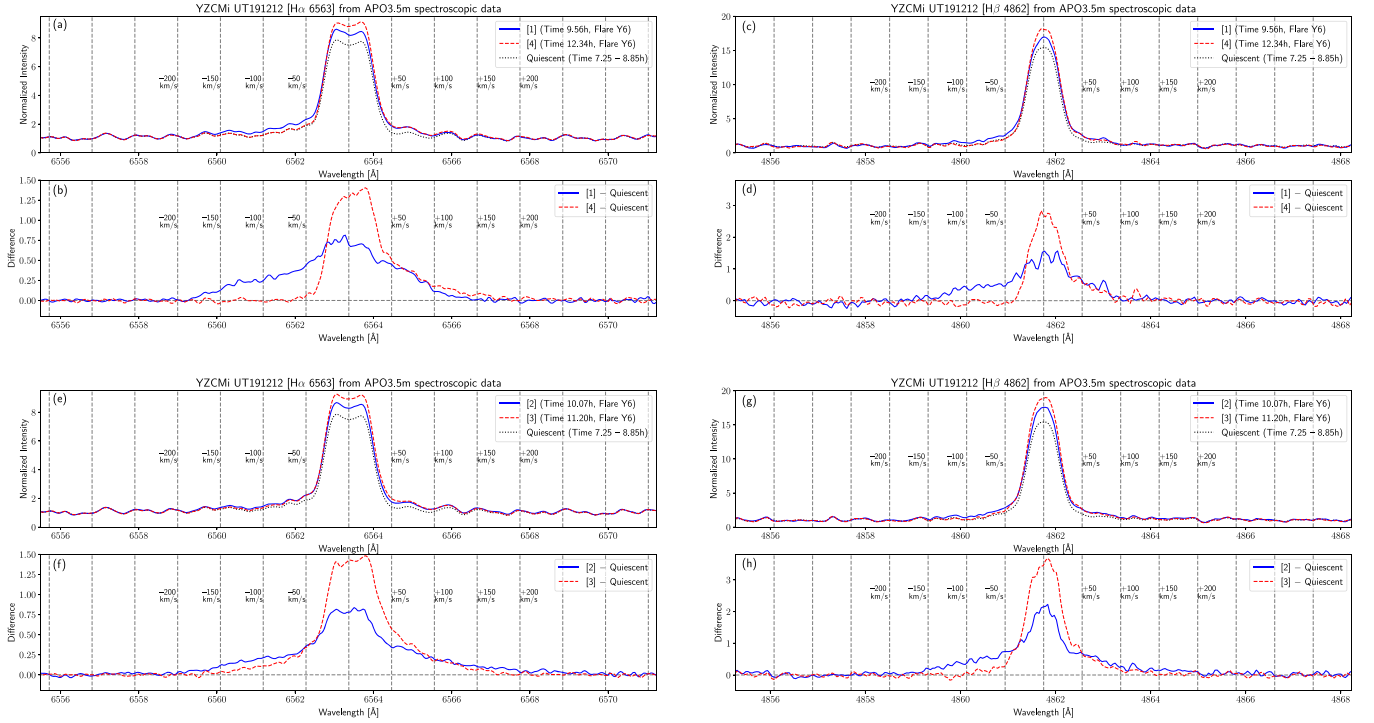


Figure 15. Line profiles of the $H\alpha$ and $H\beta$ emission lines during Flare Y6 on 2019 December 12 from APO 3.5 m spectroscopic data, which are plotted similarly with Figure 9. It is noted that the line profiles at the time [1] and [4] are in panels (a)–(d), while those at the time [2] and [3] are in (e)–(h).

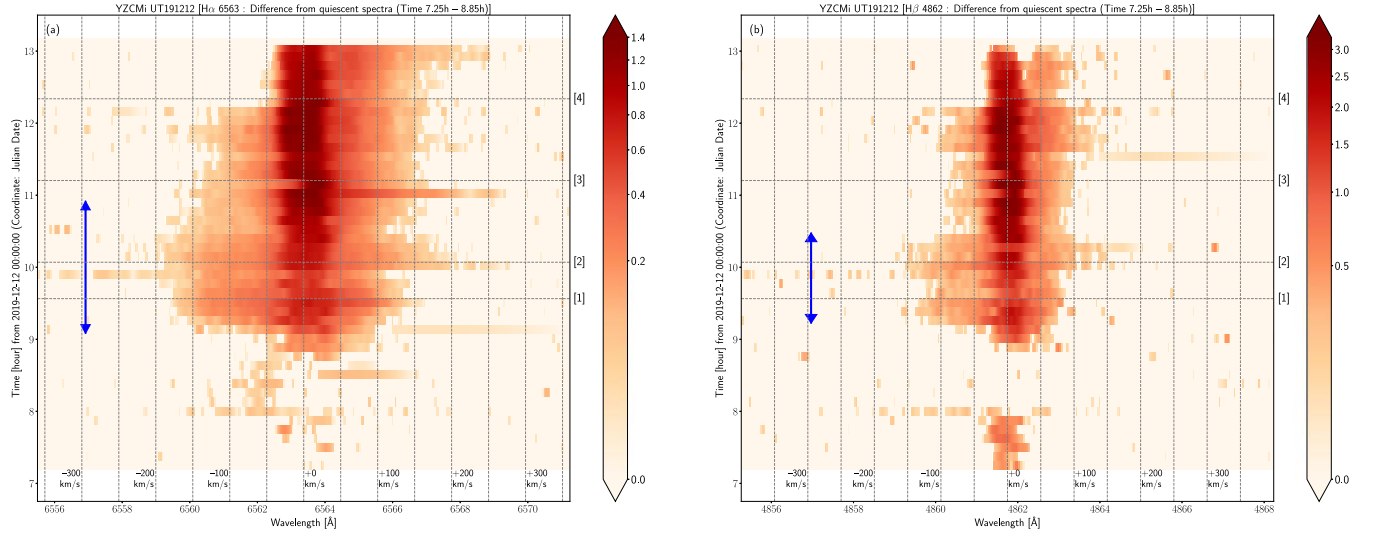


Figure 16. Time evolution of the $H\alpha$ and $H\beta$ line profiles covering Flare Y6 on 2019 December 12, which are plotted similarly with Figure 10, but the vertical axes are in the time coordinate of Julian Date (JD). The gray horizontal dashed lines indicate the time [1]–[4], which are shown in Figures 14 (light curves) and 15 (line profiles).

and $H\beta$ luminosities and flare energies of Flare Y23 estimated here are only lower limit values.

The $H\alpha$ and $H\beta$ line profiles during Flares Y23 and Y24 are shown in Figures 25 and 26. The blue wing of $H\alpha$ line was enhanced during Flare Y23 (time [1]–[4] in Figures 25(b), (f), and 26(a)). This blue wing asymmetry was the largest at time [1] (up to $\sim -250 \text{ km s}^{-1}$) and continued until around the end of the flare (time [4]), while the velocity of blue wing enhancement decayed gradually. The similar time evolution with the blue wing asymmetry (up to $\sim -200 \text{ km s}^{-1}$) was seen also in the $H\beta$ line (time [1]–[4] in Figures 25(d), (h), and 26(b)), but the line wing asymmetries at around the time [1]

and [2] were not as clear compared to those of $H\alpha$ line (Figures 25(b), and 26(b)). During Flare Y24, there were no clear blue or red wing asymmetries in $H\alpha$ and $H\beta$ lines (time [5] and [6] in Figures 25 and 26), and the line profiles showed roughly symmetrical broadenings with $\sim \pm 100\text{--}200 \text{ km s}^{-1}$ at around the peak time of the flares.

The EW light curves of $H\gamma$, $H\delta$, Ca II K , Ca II 8542 , Na I D1 and D2 , and He I D3 5876 lines are also shown in Figures 24(c), (d), and (e). The profiles of these lines and $\text{H}\epsilon + \text{Ca II H}$ lines during Flare Y23 are shown in Figure 27. At around time [1] or [1'] (Figure 27), slight blue asymmetries (slight blue wing enhancements) were seen in all the lines

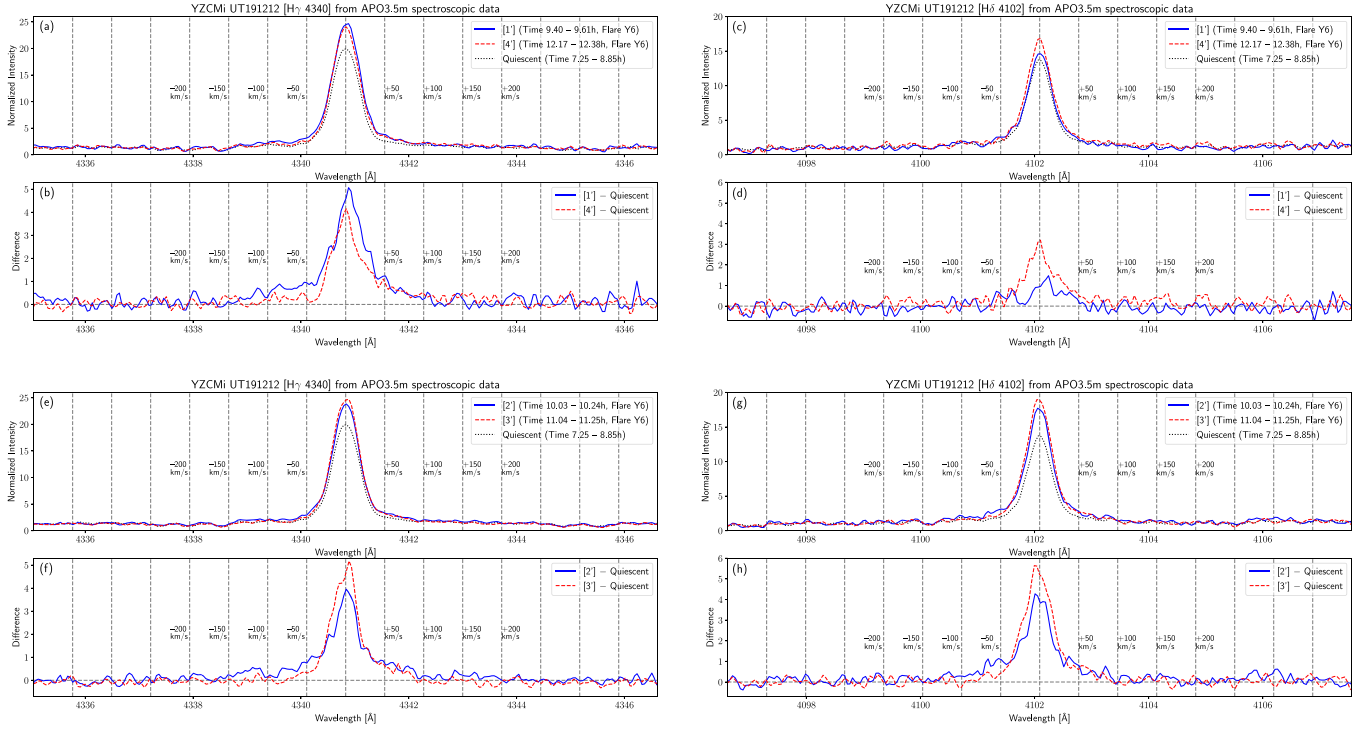


Figure 17. (a)–(d) Line profiles of the $H\gamma$ and $H\delta$ emission lines during Flare Y6 on 2019 December 12 from APO 3.5 m spectroscopic data, which are similarly plotted with Figure 15. The blue solid and red dashed lines indicate the integrated line profiles over the time [1'] (time 9.40–9.61 hr) and [4'] (time 12.17–12.38 hr) on this date, which include the time [1] and [4] in Figure 14 (light curves), respectively. (e)–(h) Same as (a)–(d), but the line profiles integrated over the time [2'] (time 10.03–10.24 hr) and [3'] (time 11.04–11.25 hr), which include the time [2] and [3] in Figure 14 (light curves), respectively.

except for $\text{Ca II } 8542$, while the blue wing asymmetry velocities are different among the lines. For example, Ca II K line shows blue asymmetry up to -100 to -50 km s^{-1} while $H\gamma$ line shows up to -150 to -100 km s^{-1} .

3.6. Flares E1 (Blue Wing Asymmetry) and E2 (Blue Wing Asymmetry) Observed on 2019 December 15

On 2019 December 15, two flares (Flares E1 and E2) were detected on EV Lac in $H\alpha$ and $H\beta$ lines as shown in Figure 28(a). As for Flare E1, the $H\alpha$ and $H\beta$ EWs increased to 9.0 \AA and 11.0 \AA , respectively, and $\Delta t_{H\alpha}^{\text{flare}}$ is 3.6 hr (Table 4). Only the late phase of Flare E1 was observed with ARCSAT u and g bands, and an increase of the continuum flux was observed in late phase at ~ 4.3 – 4.4 hr (Figure 28(b)). It is possible there were increases of the continuum flux in the early phase of Flare E1. As for Flare E2, the $H\alpha$ and $H\beta$ EWs increased to 8.1 \AA and 9.4 \AA , respectively, and $\Delta t_{H\alpha}^{\text{flare}}$ is 0.9 hr (Table 4). In addition to these enhancements in Balmer emission lines, the continuum brightness observed with ARCSAT u and g bands increased by $\sim 60\%$ – 65% and $\sim 5\%$, respectively, during Flare E2 (Figure 28(b)).

The L_u , L_g , E_u , E_g , $L_{H\alpha}$, $L_{H\beta}$, $E_{H\alpha}$, and $E_{H\beta}$ values are listed in Table 4. As for Flare E1, we did not estimate L_u , L_g , E_u , and E_g values, since only the late phase of Flare E1 was observed with ARCSAT u and g bands, and no clear increases of the continuum brightness were observed in the late phase (Figure 28(b)).

The $H\alpha$ and $H\beta$ line profiles during Flares E1 and E2 are shown in Figures 29 and 30. The blue wing of $H\alpha$ line was enhanced (up to -150 – 200 km s^{-1}) during the early phase of Flare E1 (time [1] in Figures 29(b) and 30(a)). The similar blue wing asymmetry (up to -150 km s^{-1}) was seen also in the $H\beta$

line (time [1] in Figures 29(d) and 30(b)), but the duration of the blue wing asymmetry in $H\beta$ line (~ 0.5 hr) is shorter than that of $H\alpha$ line ($\gtrsim 1$ hr) (Figure 30). The blue wing asymmetry in $H\alpha$ and $H\beta$ lines (up to -150 km s^{-1}) were also seen at around the peak time of Flare E2 (time [1] in Figures 29(b) and 30(a)). The duration of the blue wing asymmetry in $H\alpha$ and $H\beta$ lines during Flare E2 were ~ 20 and ~ 10 minutes, respectively.

The EW light curves of $H\gamma$, $H\delta$, Ca II K , $\text{Ca II } 8542$, Na I D1 and D2 , and $\text{He I D3 } 5876$ lines are also shown in Figures 28(c), (d), and (e). The profiles of these lines and $\text{H}\epsilon + \text{Ca II H}$ lines during Flares E1 and E2 are shown in Figure 31. As for $H\gamma$ line, the blue wing asymmetries up to $\sim -100 \text{ km s}^{-1}$ are seen during both Flares E1 and E2. As for $H\delta$ and Ca II H\&K lines, possible blue wing enhancements (up to $\sim -50 \text{ km s}^{-1}$) are seen during Flare E1, while line wing asymmetries of these lines are not clearly seen during Flare E2. The line asymmetries of $\text{H}\epsilon$, $\text{Ca II } 8542$, Na I D1 and D2 , and He I D3 lines are not so clear during both E1 and E2. However, we also note that there could be some slight peak blueshifts in the lines, for which we do not see clear line wing enhancements (e.g., Ca H\&K lines during Flare E2, He I D3 and $\text{Ca II } 8542$ lines during Flare E1).

3.7. Flare A3 (Blue Wing Asymmetry) Observed on 2019 May 19

On 2019 May 19, one flare (Flare A3) was detected on AD Leo in $H\alpha$ and $H\beta$ lines as shown in Figure 32(a). Flare A3 already started when the observation started. The $H\alpha$ and $H\beta$ EWs increased to 5.8 \AA and 6.7 \AA , respectively, and the $\Delta t_{H\alpha}^{\text{flare}}$ is > 3.1 hr (Table 4). In addition to these enhancements in Balmer emission lines, the continuum flux observed with

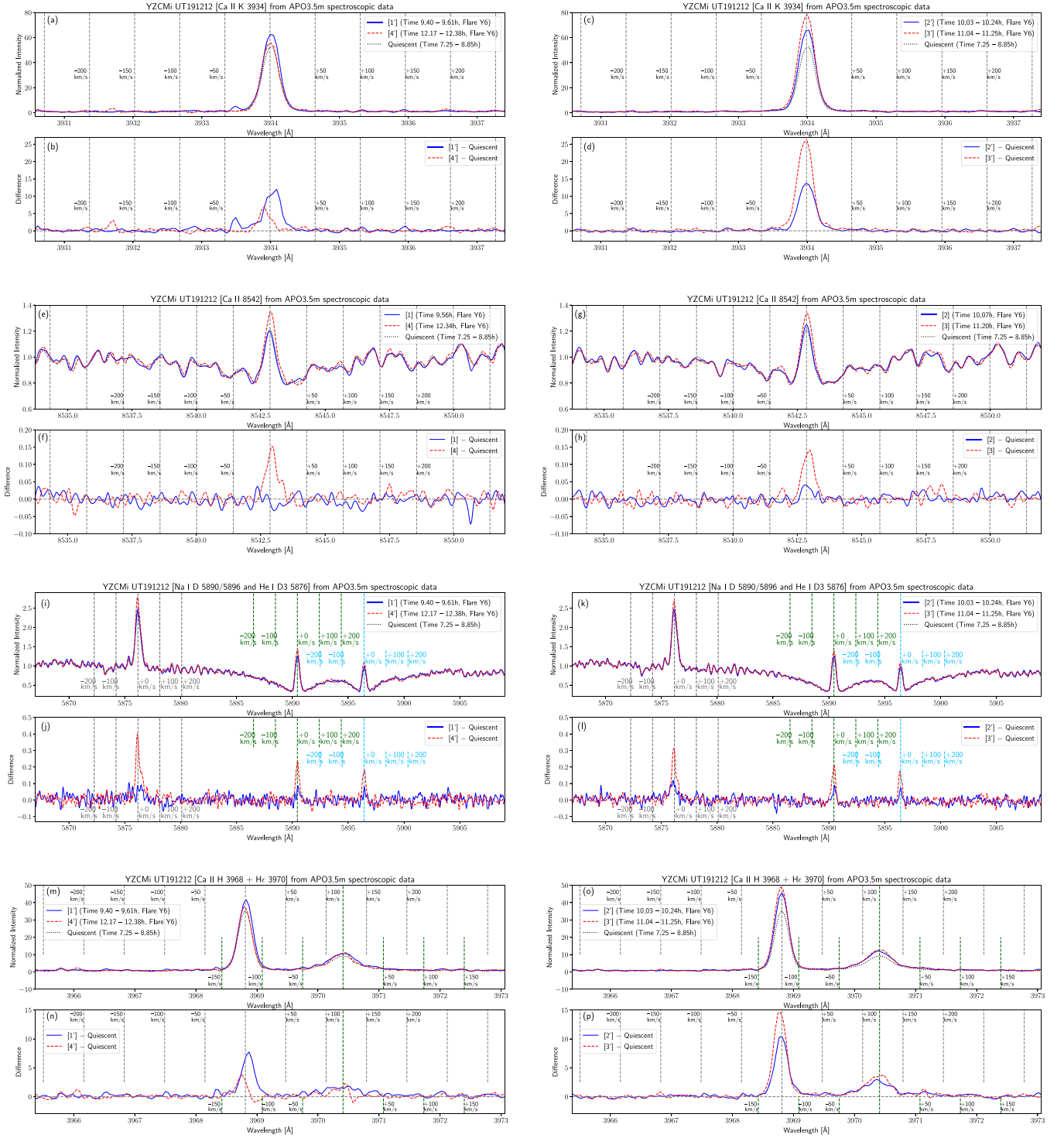


Figure 18. Same as Figure 17 but for Ca II K, Ca II 8542, Na I D1 and D2 (5890 and 5896)+He I D3 5876, and He + Ca II H lines, respectively. As for the Ca II 8542 line, the data at the time [1]–[4] are plotted (not [1']–[4']).

ARCSAT u and g bands increased by $\sim 40\%$ and $\sim 3\%$ – 4% , respectively,

at around time ~ 3.9 – 4 hr during Flare A3 (Figure 32(b)). However, the photometric observation covered only the latter portion of the flare, and the flare already had started when the observation started. Because of these, we cannot judge whether the main H α and H β flare emission components are associated with WL flares or not. In these cases, we also do not list the flare peak luminosities in the continuum bands (u and g bands)

in Table 4. The lower limits of flare energies in the continuum bands (u and g bands) are estimated to be $E_u > 2.7 \times 10^{31}$ erg, and $E_g > 1.4 \times 10^{31}$ erg from the existing data period. Since Flare A3 already started when the observation started, the $L_{H\alpha}$, $L_{H\beta}$, $E_{H\alpha}$, and $E_{H\beta}$, which are also listed in Table 4, are only lower limit values.

The H α and H β line profiles during Flare A3 are shown in Figures 33 and 34. It is noted that the data on 2019 May 18 (see Figures 100(a)) are used for quiescent profiles in these figure,

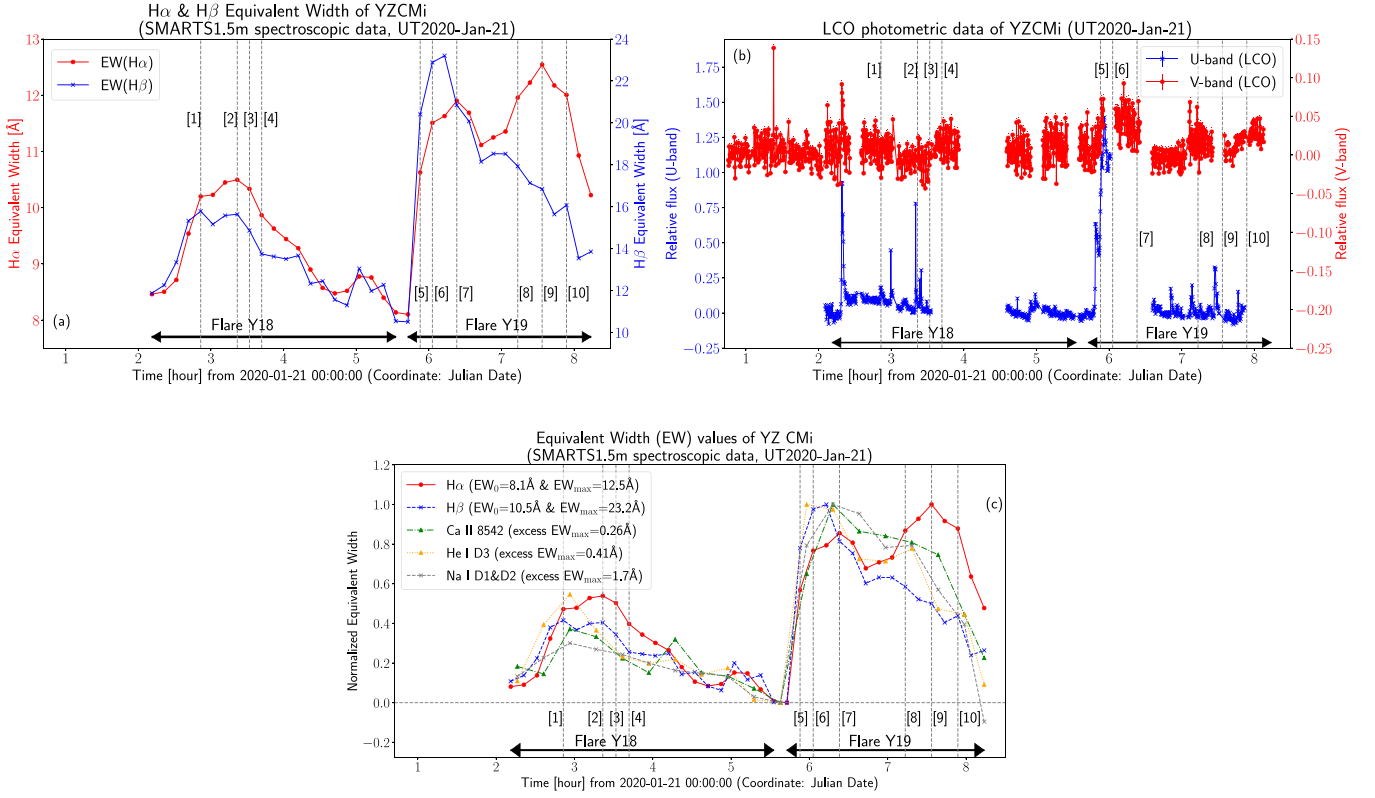


Figure 19. Light curves of YZ CMi on 2020 January 21 showing Flares Y18 and Y19. The data are plotted similarly with Figure 14, but the the chromospheric line emission data are from the SMARTS 1.5 m spectroscopic data, which include only H α , H β , Ca II 8542, He I D3, and Na I D1 and D2 lines. Different from Figure 14(b), the LCO U- and V-band photometric data are plotted in (b). The gray dashed lines with numbers [1]–[10] correspond to the time shown with the same numbers in Figures 20–22.

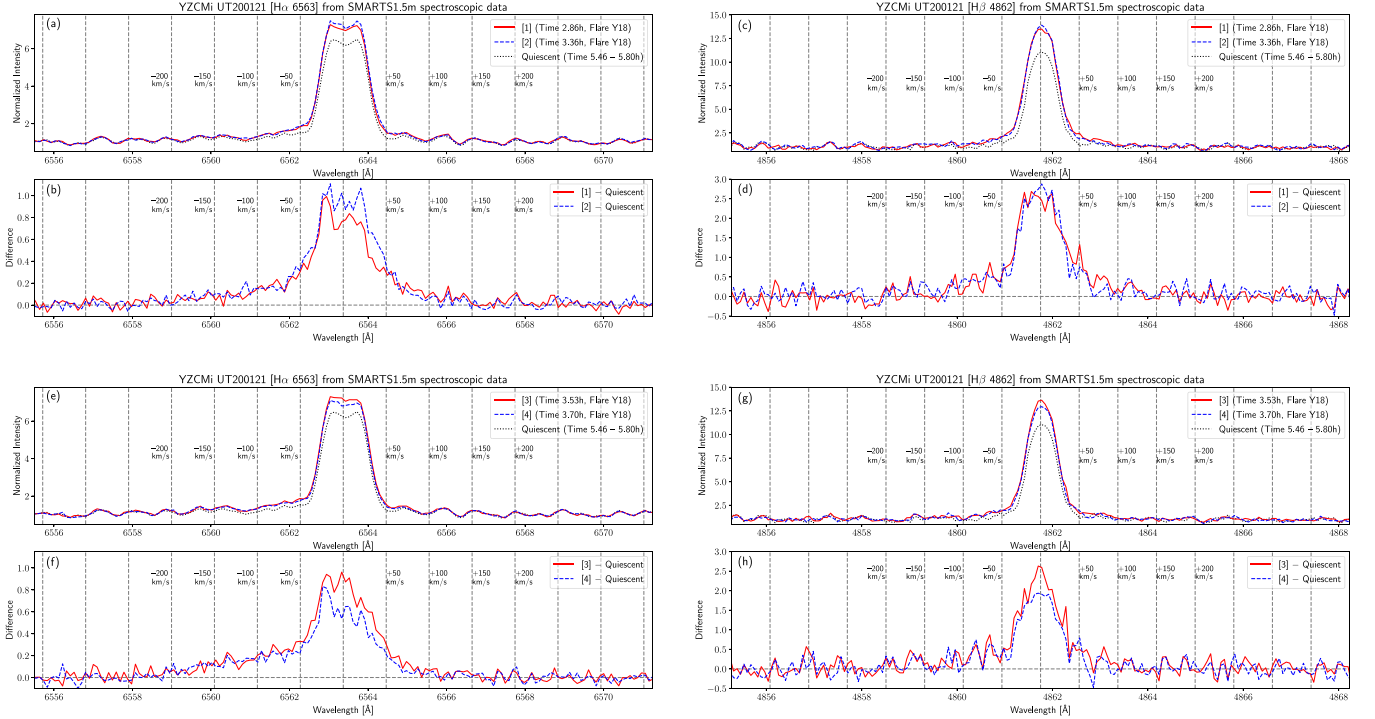


Figure 20. Line profiles of the H α and H β emission lines during Flare Y18 (at the time [1]–[4]) on 2020 January 21 from SMARTS 1.5 m spectroscopic data, which are plotted similarly with Figure 9.

since the quiescent phase data are limited (or there could be no quiescent phase) on 2019 May 19 as seen in Figure 32. During Flare A3, the blue wings of H α and H β lines were enhanced up

to -150 to -200 km s $^{-1}$ (time [1]–[3] in Figures 33(b) and (d)). These blue wing asymmetries continued for more than 2 hr until the flare decayed (Figure 34).

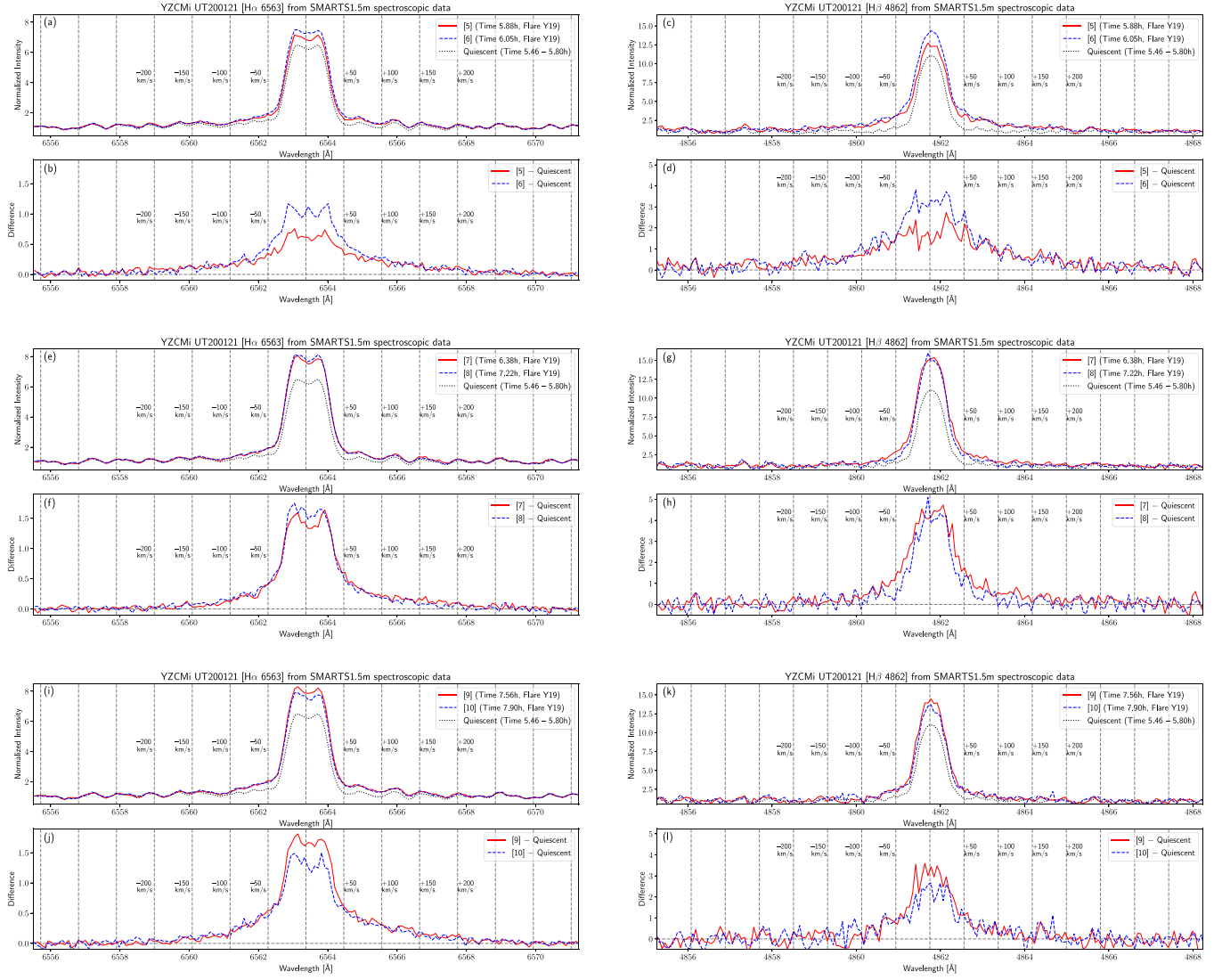


Figure 21. Line profiles of the $H\alpha$ and $H\beta$ emission lines during Flare Y19 (at the time [5]–[10]) on 2020 January 21 from SMARTS 1.5 m spectroscopic data, which are plotted similarly with Figure 9.

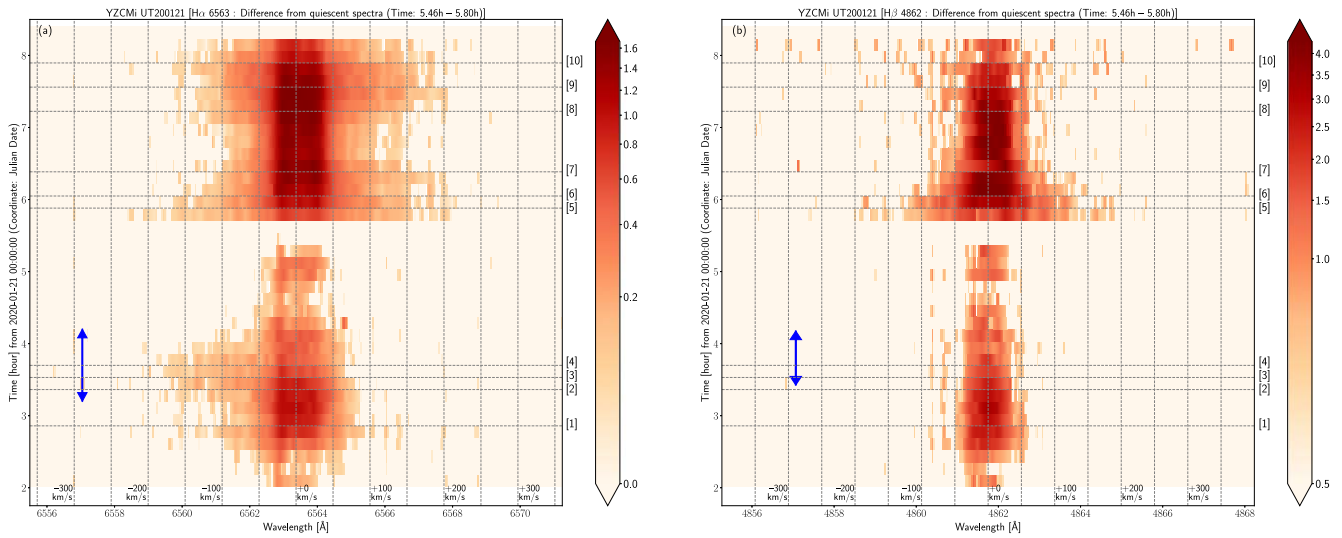


Figure 22. Time evolution of the $H\alpha$ and $H\beta$ line profiles covering Flares Y18 and Y19 on 2020 January 21, which are similarly plotted with Figure 16 (from the SMARTS 1.5 m spectroscopic data). The gray horizontal dashed lines indicate the time [1]–[10], which are shown in Figure 19 (light curves) and Figures 20 and 21 (line profiles).

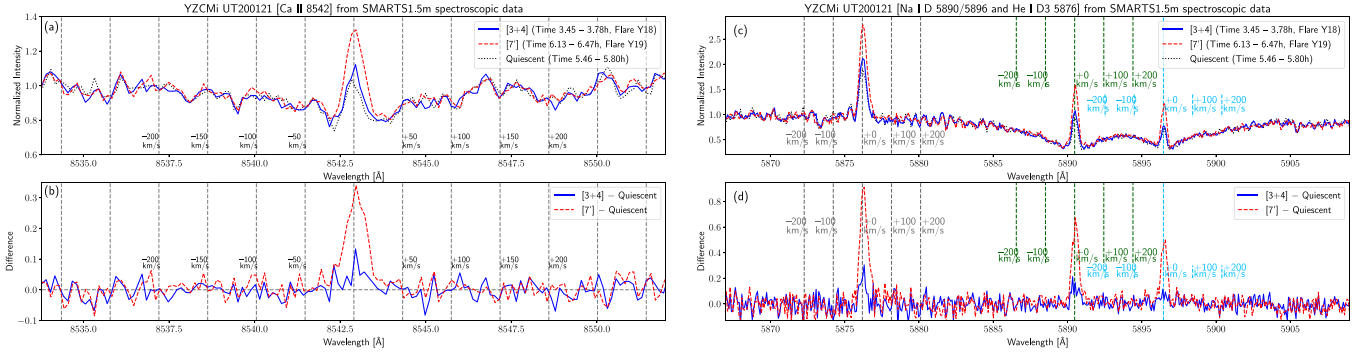


Figure 23. (a) and (b) Line profiles of the Ca II 8542 line during Flares Y18 and Y19 on 2020 January 21 from SMARTS 1.5 m spectroscopic data, similarly plotted with Figures 21 and 21. The blue solid and red dashed lines indicate the integrated line profiles over the time [3+4] (time 3.45–3.78 hr) and [7] (time 6.13–6.47 hr) on this date, which include the time [3] and [4] and [7] in Figure 19 (light curves), respectively. (c) and (d) Same as (a) and (b), but the line profiles for the Na I D1 and D2 (5890 and 5896) and He I D3 5876 line.

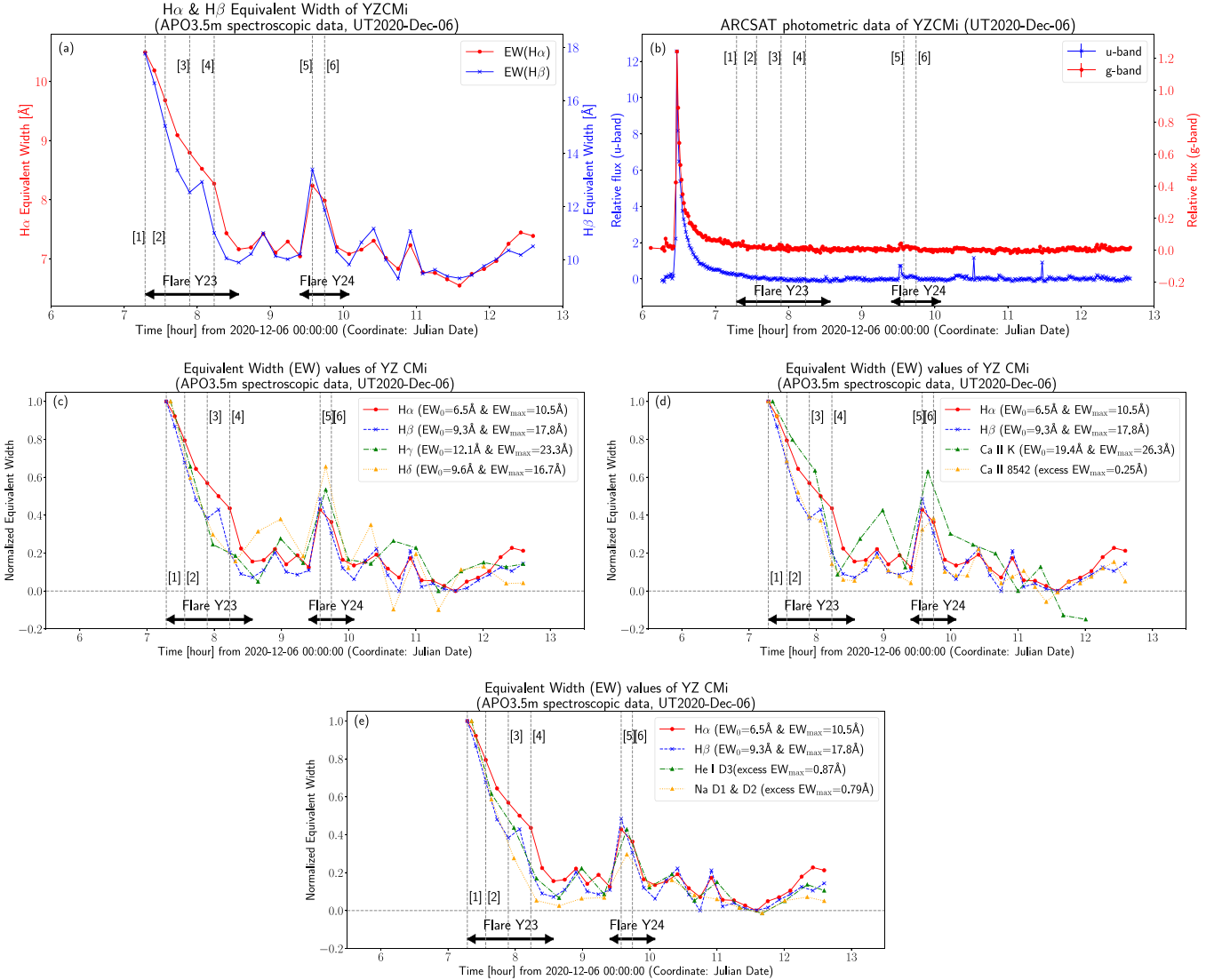


Figure 24. Light curves of YZ CMi on 2020 December 6 showing Flares Y23 and Y24, which are plotted similarly with Figure 14. The gray dashed lines with numbers ([1]–[6]) correspond to the time shown with the same numbers in Figures 25 and 26.

The EW light curves of $H\gamma$, $H\delta$, Ca II K, Ca II 8542, Na I D1 and D2, and He I D3 5876 lines are also shown in Figures 32(c), (d), and (e). The profiles of these lines and Ca II H and H ϵ lines during Flare A3 are shown in Figure 35.

As for $H\gamma$, $H\delta$, H ϵ , Ca II H&K, Ca II 8542, and He I D3 lines, the blue wing asymmetries similar to $H\alpha$ and $H\beta$ lines are seen during Flare A3; though, the velocities of peak wing enhancements are different.

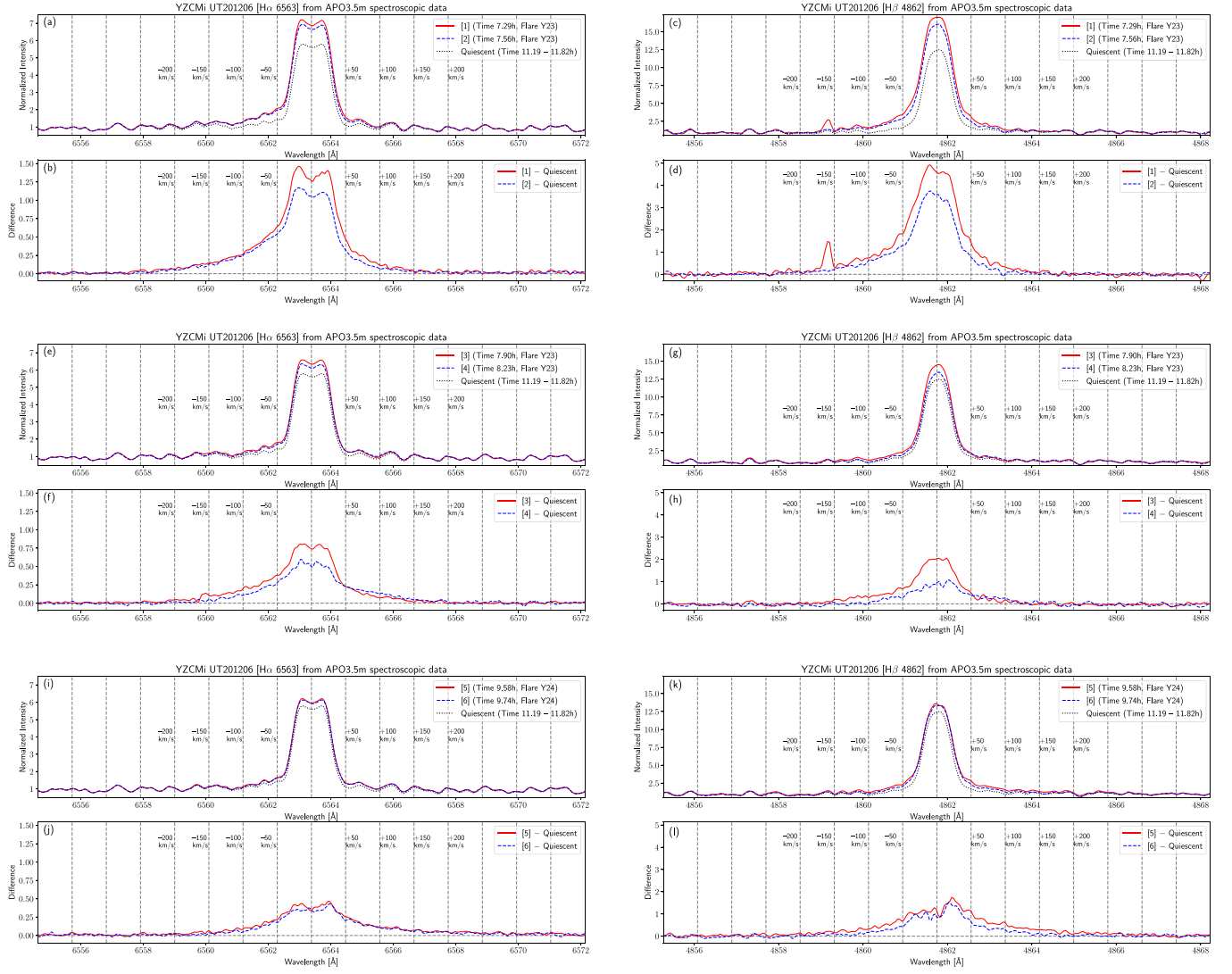


Figure 25. Line profiles of the $H\alpha$ and $H\beta$ emission lines during Flares Y23 and Y24 (at the time [1]–[6]) on 2020 December 6 from APO 3.5 m spectroscopic data, which are plotted similarly with Figure 9.

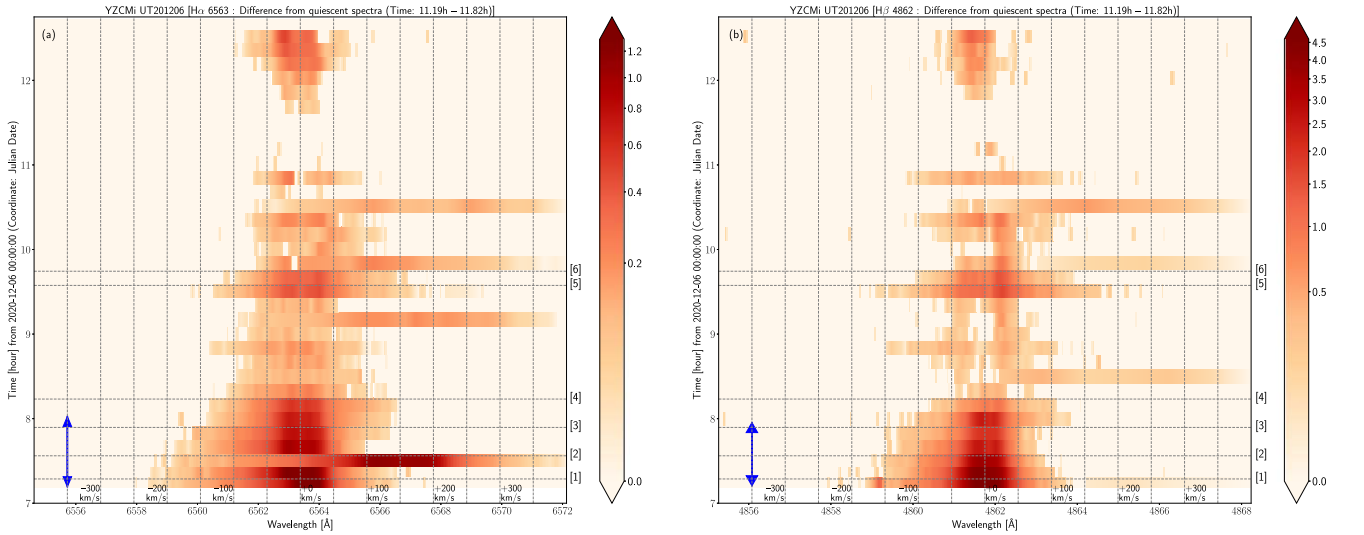


Figure 26. Time evolution of the $H\alpha$ and $H\beta$ line profiles covering Flares Y23 and Y24 on 2020 December 6, which are shown similarly with Figure 16. The gray horizontal dashed lines indicate the time [1]–[6], which are shown in Figures 24 (light curves) and 25 (line profiles).

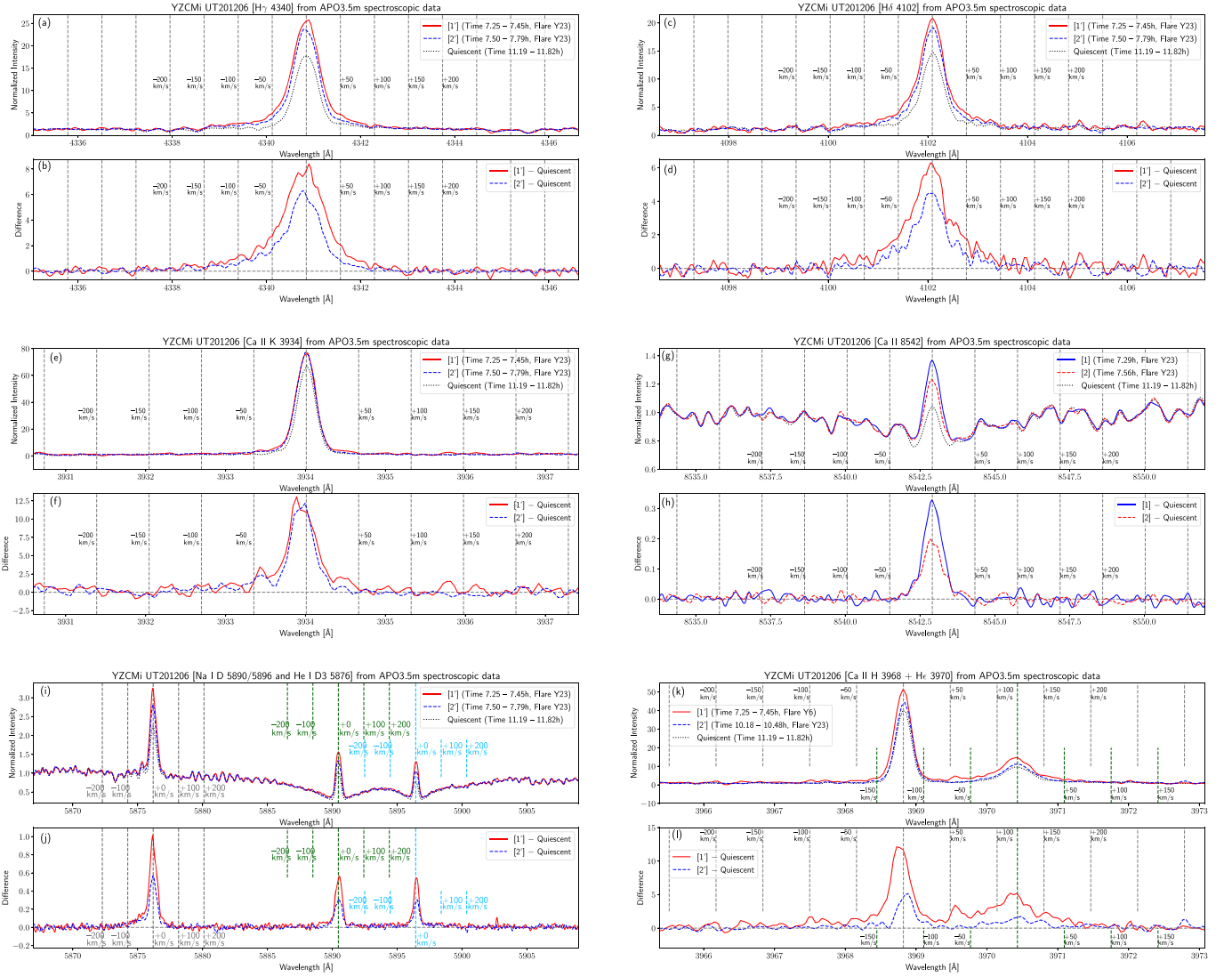


Figure 27. (a) and (b) Line profiles of the $H\gamma$ emission line during Flare Y23 on 2020 December 6 from APO 3.5 m spectroscopic data, which are similarly plotted with Figure 25. The blue solid and red dashed lines indicate the integrated line profiles over the time [1] (time 7.25–7.45 hr) and [2] (time 7.50–7.79 hr) on this date, which include the time [1] and [2] in Figure 24 (light curves), respectively. (c) and (d), (e) and (f), (g) and (h), (i) and (j), and (k) and (l) Same as panels (a) and (b), but for $H\delta$, Ca II K, Ca II H 8542, Na I D1 and D2 (5890 and 5896)+He I D3 5876, and H ϵ + Ca II H lines, respectively. As for the Ca II 8542 line, the data at the time [1] and [2] are plotted (not [1] and [2]).

4. Discussions

4.1. Luminosities and Energies of Flares in Photometric Bands and $H\alpha$ Line

In this study, we observed flares in chromospheric lines (e.g., $H\alpha$ line) and WL continuum emission bands (e.g., u and g bands), as summarized in Section 3.1 and Table 4.

Among the total 41 flares observed in this paper, 6 flares (Flares Y2, Y22, E1, E7, A1, and A3 marked with “NEP” in Table 4) do not have appropriate data sets for judging whether the flares showed corresponding WL continuum flux enhancements. As for the four (Flares Y2, E7, A1, and A3) among these six flares, the initial part of the flare time evolution was not observed both in the spectroscopic and photometric data, while the other two flares (Flares Y22 and E1) have large data gaps in the photometric data. We classified the remaining 35 flares into WL flares and non-white-light (NWL) flares. The procedure is summarized as follows:

- (i) As also described in Section 2.5, if the relative flux ($\Delta f_{\text{band, flare}}(t)$) shows the increase whose peak amplitude is larger than the photometric error ($3\sigma_{\text{band}}$) and the associated flare decays over multiple data points, we judge that flare emission is identified in the photometric band.
- (ii) The M-dwarf flare amplitudes are generally larger in blue bands as seen for Flare Y4 in Figure 52 as well as in previous studies (e.g., Hawley & Pettersen 1991; Namekata et al. 2020) since flare optical continuum spectra have much higher temperature than those in the quiescent phase (Kowalski et al. 2010; Kowalski et al. 2019; Howard et al. 2020). Considering this point, flares are classified as WL flares in this paper if the flare emissions in U or u bands are identified. One exception is Flare Y1, which showed clear WL emissions in g and TESS bands while there are no available u -band observation data (Figure 49). If there are no flare emissions identified in

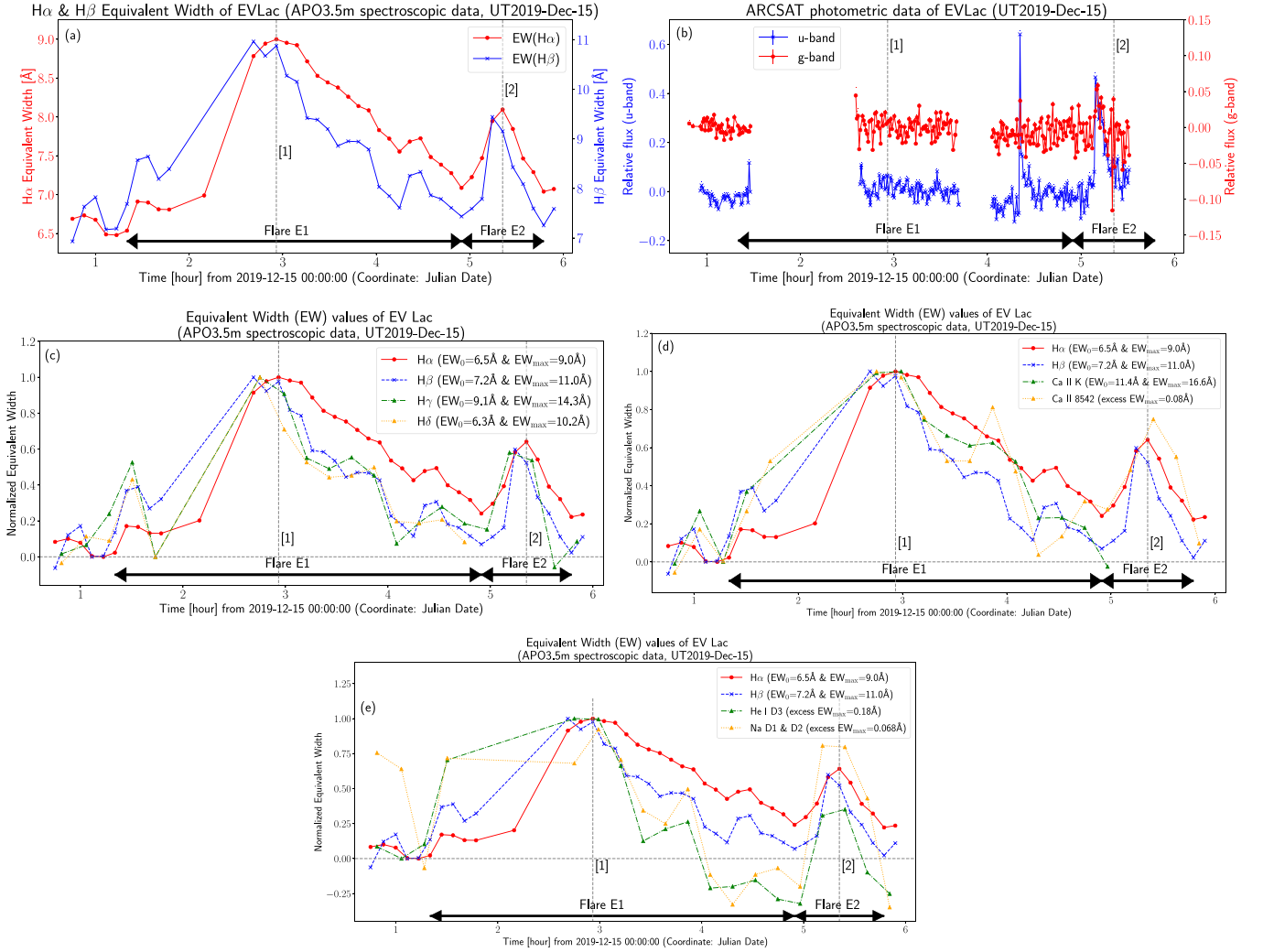


Figure 28. Light curves of EV Lac on 2019 December 15 showing Flares E1 and E2, which are plotted similarly with Figure 14. The gray dashed lines with numbers ([1] and [2]) correspond to the time shown with the same numbers in Figures 29 and 30.

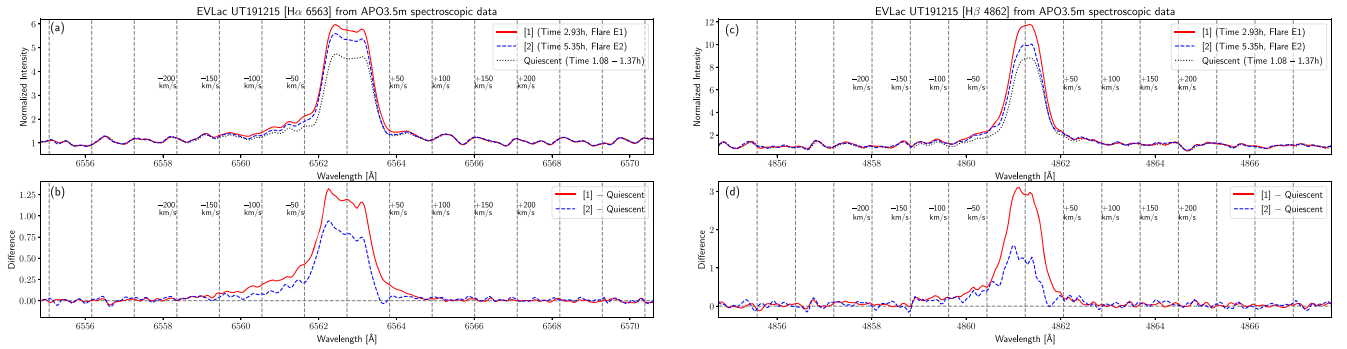


Figure 29. Line profiles of the $H\alpha$ and $H\beta$ emission lines during Flares E1 and E2 (at the time [1] and [2]) on 2020 December 6 from APO 3.5 m spectroscopic data, which are plotted similarly with Figure 9.

any photometric bands with the above threshold, the flare is identified as NWL flares.

- (iii) It is noted that the threshold $3\sigma_{\text{band}}$ may depend on the data quality (S/N) of each night. The classification of WL flares and NWL flares could be somewhat affected from this point. Moreover, the flare colors in the optical band can include some variety among events (see Kowalski et al. 2019), and the WL or NWL classification based on one band (U or u band in this study) could leave us some

bias. However, the purpose of the WL or NWL classification in this study is only to show that the blue wing asymmetries can exist both in clear WL flares and candidate NWL flares (see Section 4.2). In other words, it is sufficient to investigate whether each flare shows WL emissions within the available data set for each flare (whose data quality has some variety among each event). From this point of view, a detailed statistical classification of WL or NWL flares is beyond the scope of this paper,

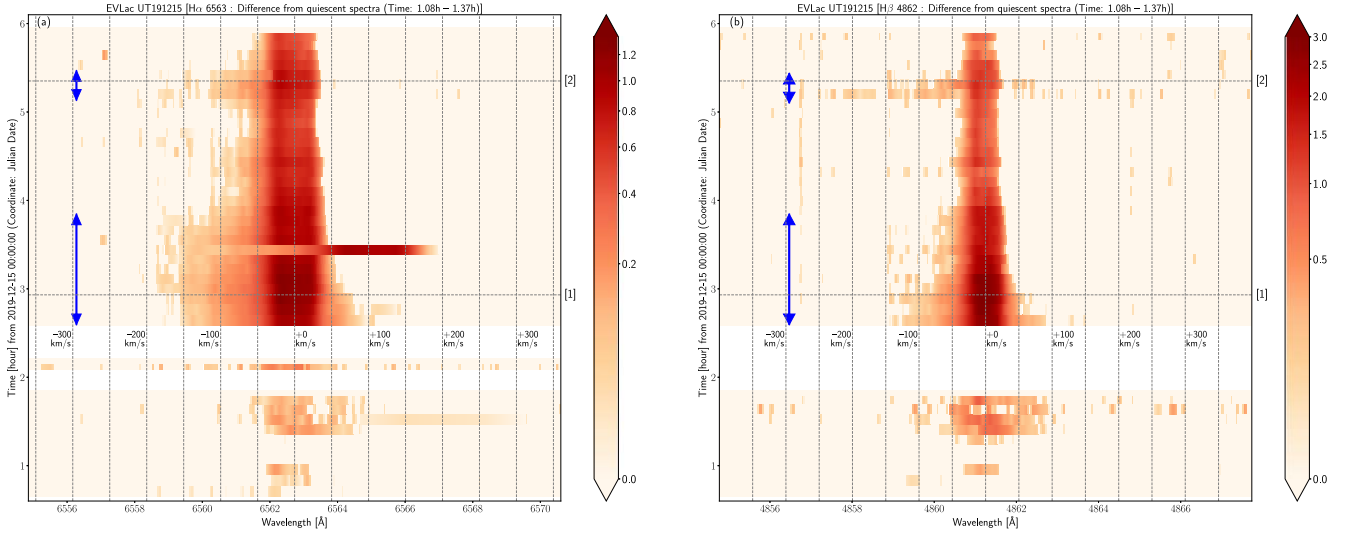


Figure 30. Time evolution of the $H\alpha$ and $H\beta$ line profiles covering Flares E1 and E2 on 2019 December 15, which are shown similarly with Figure 16. The gray horizontal dashed lines indicate the time [1] and [2], which are shown in Figures 28 (light curves) and 29 (line profiles).

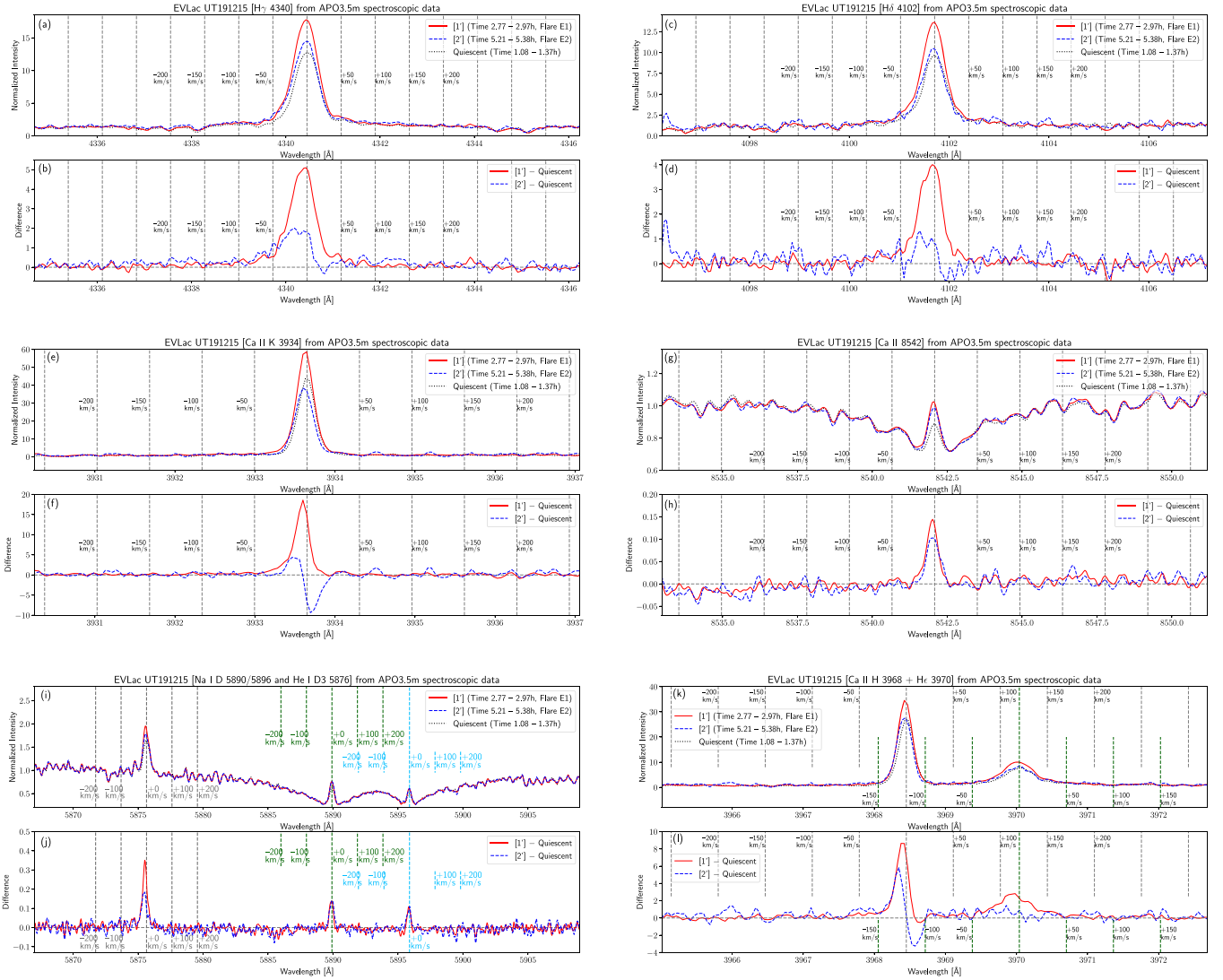


Figure 31. (a) and (b) Line profiles of the $H\gamma$ emission line during Flares E1 and E2 on 2019 December 15 from APO 3.5 m spectroscopic data, which are similarly plotted with Figure 29. The blue solid and red dashed lines indicate the integrated line profiles over the time [1] (time 2.77–2.97 hr) and [2] (time 5.21–5.38 hr) on this date, which include the time [1] and [2] in Figure 28 (light curves), respectively. (c) and (d), (e) and (f), (g) and (h), (i) and (j), and (k) and (l) Same as panels (a) and (b), but for $H\delta$, Ca II K, Ca II 8542, Na I D1 and D2 (5890 and 5896)+He I D3 5876, and $H\epsilon$ + Ca II H lines, respectively.

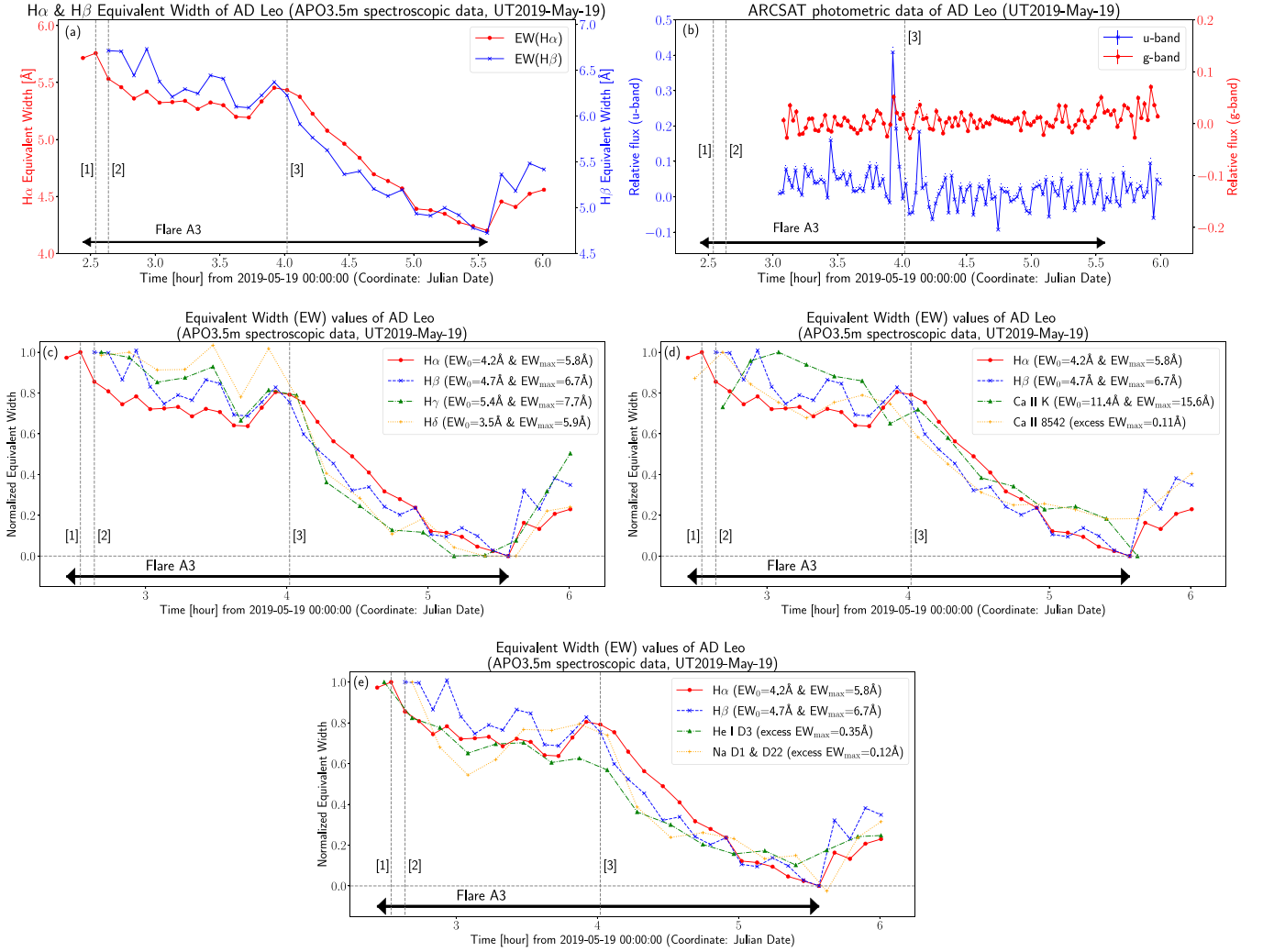


Figure 32. Light curves of AD Leo on 2019 May 19 showing Flare A3, which are plotted similarly with Figure 14. The gray dashed lines with numbers ([1]–[3]) correspond to the time shown with the same numbers in Figures 33 and 34.

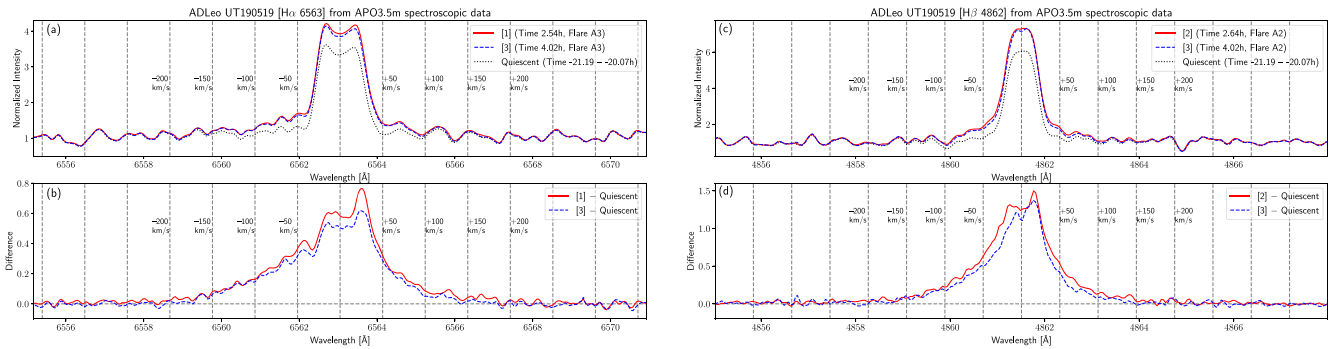


Figure 33. Line profiles of the $H\alpha$ and $H\beta$ emission lines during Flare A3 (at the time [1] or [2], and [3]) on 2019 May 19 from APO 3.5 m spectroscopic data, which are plotted similarly with Figure 9. The black dotted lines indicate the line profiles in quiescent phase, which are the average profile during -21.19 to -20.07 hr from the data on 2019 May 18 (2.81–3.93 hr in Figure 100(a)).

considering that most of the photometric data are from the ground-based observations with small ARCSAT and LCO telescopes including some data gaps. We note here that the future studies on the WL or NWL associations during $H\alpha$ and $H\beta$ flares are necessary with a more comprehensive and more well-observed data set (e.g., TESS-like high-precision space photometry, in blue optical wavelength band).

As a result, 31 flares showed corresponding WL continuum flux enhancements, and are classified here as WL flares (marked with “WL” in Table 4). The remaining 4 flares (Flares Y3, Y5, Y6, and Y26 marked with “NWL” in Table 4) are classified as *candidate* NWL flares in this study. It is noted three (Flares Y3, Y5, and Y26) among these 4 flares showed marginal WL increases comparable to photometric errors (see Figures 8, 52, and 76), while the other one Flare Y6 showed

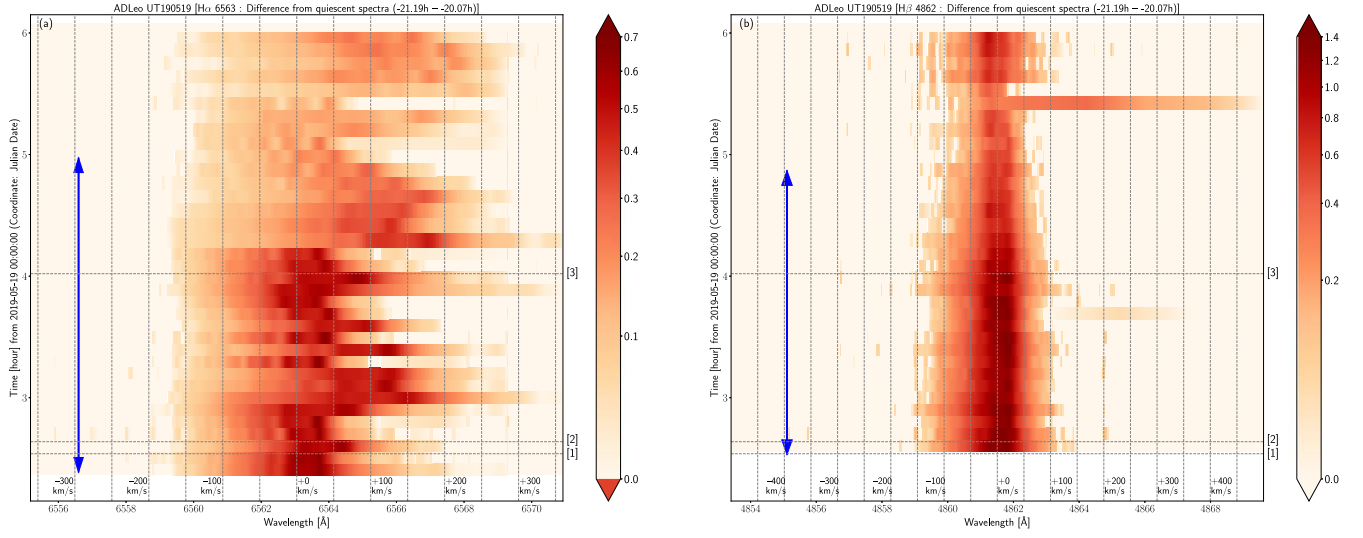


Figure 34. Time evolution of the H α and H β line profiles covering Flare A3 on 2019 May 19, which are shown similarly with Figure 16. The gray horizontal dashed lines indicate the time [1]–[3], which are shown in Figures 32 (light curves) and 33 (line profiles).

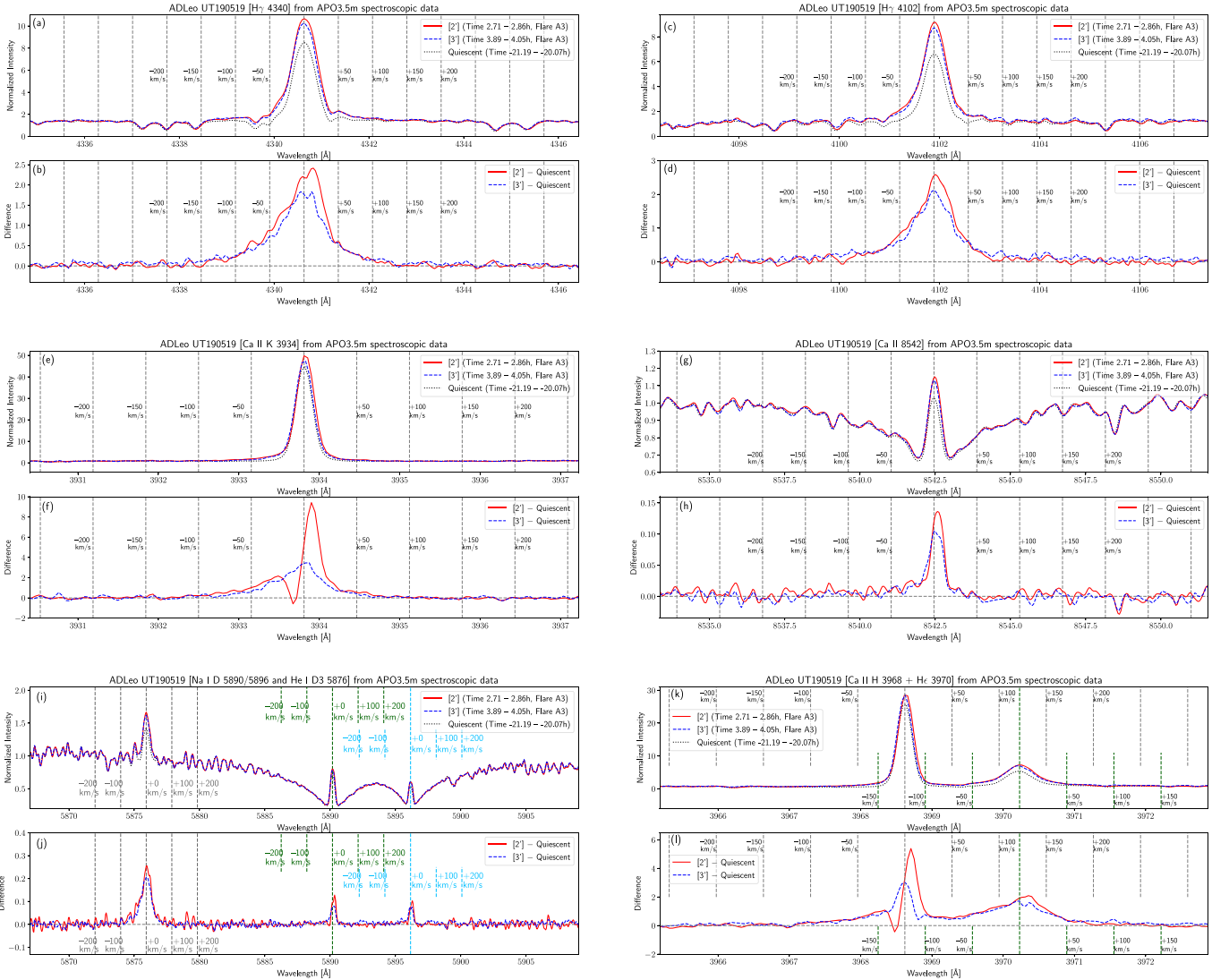


Figure 35. (a) and (b) Line profiles of the H γ emission line during Flare A3 on 2019 May 19 from APO 3.5 m spectroscopic data, which are similarly plotted with Figure 33. The blue solid and red dashed lines indicate the integrated line profiles over the time [2] (time 2.71–2.86 hr) and [3] (time 3.89–4.05 hr) on this date, which include the time [2] and [3] in Figure 32 (light curve), respectively. (c) and (d), (e) and (f), (g) and (h), (i) and (j), and (k) and (l) Same as panels (a) and (b), but for H δ , Ca II K, Ca II H 8542, Na I D1 and D2 (5890 and 5896)+He I D3 5876, and H ϵ + Ca II H lines, respectively.

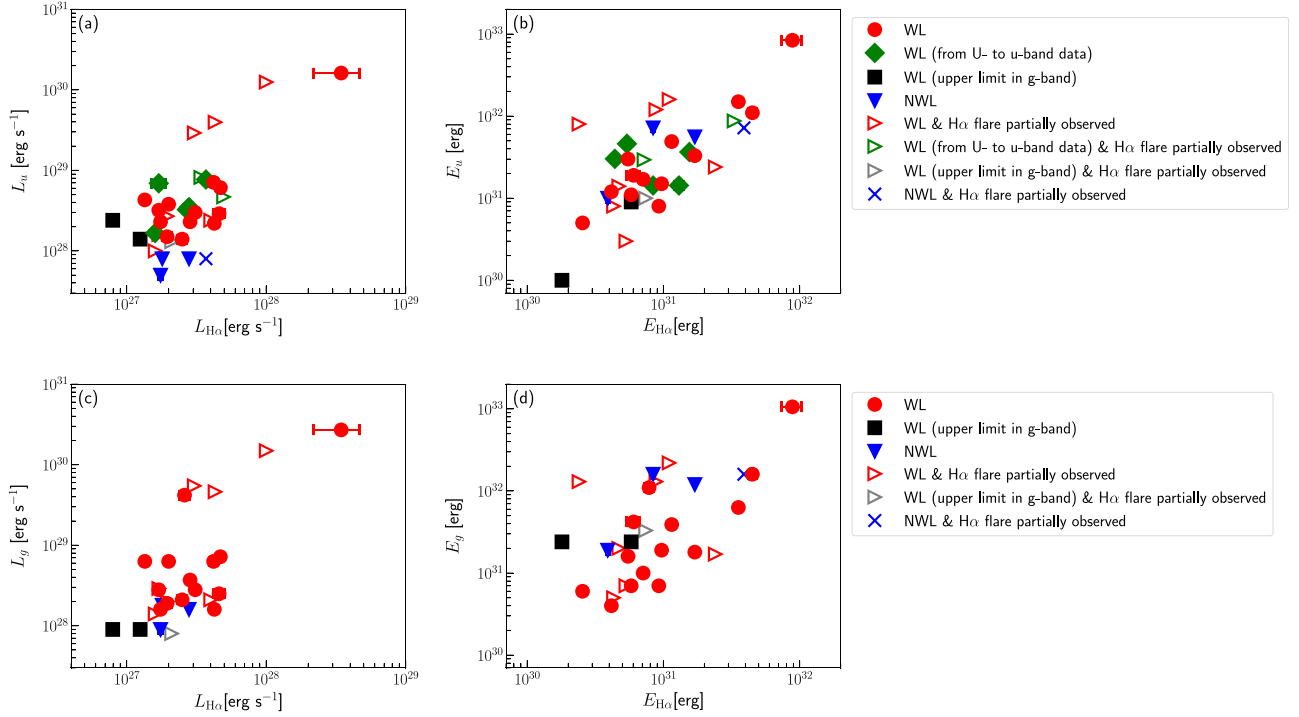


Figure 36. Scatter plot of flare peak luminosities and energies in u and g bands (L_u , E_u , L_g , and E_g) and $H\alpha$ line ($L_{H\alpha}$ and $E_{H\alpha}$). Red filled circles represent the flares identified as white-light flares (“WL” in Table 4) and whose $H\alpha$ flare emission was observed from the flare start to end. Green filled diamonds represent the flares with the same properties as those marked with red filled circles, but their L_u and E_u values are converted from their LCO U -band values assuming the luminosity ratio between these two bands (see Table 3), since these stars were observed not in the ARCSAT u - and g -bands data but in the LCO U band (the L_g and E_g values of these stars are not available, so these stars are not in (c) and (d)). It is noted that, because of some data gaps of the LCO U -band photometric observations, the plotted E_u values can be lower limit values, although the L_u values are less likely lower limit values since the peaks corresponding to the $H\alpha$ flare peaks are already selected (see also footnotes of Table 4). Black filled squares are flares with the same properties as those marked with red filled circles, but the upper limit values are estimated for L_g , and E_g values, while the exact L_u , and E_u values of these flares are measured. Blue downward triangles are the flares identified as *candidate* non-white-light flares (“NWL” in Table 4). As for these stars, the plotted L_u values show the upper limit values from Table 4. Red open rightward triangles represent the flares identified as white-light flares but whose $H\alpha$ flare phase was only partially observed (only the lower limit values for $\Delta t_{H\alpha}^{\text{flare}}$ are listed in Table 4). As for these stars, the plotted $L_{H\alpha}$ values can be the lower limit values. Green open rightward triangles are the flares with the same properties as those marked with red open rightward triangles, but their u -band values are converted from their LCO U -band values as the green filled diamonds. Gray open rightward triangles are the flares with the same properties as those marked with red open rightward triangles, but the upper limit values are estimated for L_g , and E_g values, while the exact L_u , and E_u values of these flares are measured. Blue cross marks are the flares identified as *candidate* non-white-light flares (“NWL” in Table 4) and whose $H\alpha$ flare emission was only partially observed. The six flares (“NEP” in Table 4) without enough data for judging whether the flares are WL or NWL flares are not included in this figure.

WL emission peaks in late phase of the $H\alpha$ and $H\beta$ flare; though, we judged that there are no clear WL emissions that are considered to be physically associated with the early main increasing phase of the the $H\alpha$ and $H\beta$ flare (see Figure 14).

The flare energy partition among different wavelengths is an important topic of stellar flares since this can have constraints on how flare energy release occur in the different layers of flaring atmosphere from photosphere to corona (e.g., Osten & Wolk 2015; Guarcello et al. 2019; Stelzer et al. 2022). We, here, briefly mention this topic on the basis of our observation data; though, the main topic of this paper is blue wing asymmetries of chromospheric lines, and detailed discussions on the flare energy partition are beyond the scope of this paper.

In Figure 36, we compare flare peak luminosities and energies in photometric bands (u and g bands) and $H\alpha$ line.

Figure 36(b) suggests a rough correlation between the flare energies especially between u band and $H\alpha$ line, but detailed quantitative conclusions are beyond the scope of this paper considering some uncertainties of the observation data available in this study (e.g., there are some gaps in the photometric data and many flares only partially observed as shown with various symbols in this figure). We will come back to this point in our future paper, discussing in detail the differences of time evolution of various chromospheric lines during stellar flares

(e.g., Kowalski et al. 2013). In addition, related with this topic, soft X-ray energy of Flare Y3 is mentioned in Section 4.4.

4.2. Flares Showing Blue Wing Asymmetries

In this study, 41 flares were detected from the total 31 night observations, as summarized in Section 3.1 and Table 4. Among these, 7 flares (Flares Y3, Y6, Y18, Y23, E1, E2, and A3 in Sections 3.2–3.7) showed clear blue wing asymmetries in $H\alpha$ line. Various notable properties, which are described in Sections 3.2–3.7, are summarized in Table 5. For reference, three flares with $H\alpha$ blue wing asymmetries in Vida et al. (2016), Honda et al. (2018), and Maehara et al. (2021) are also listed in this Table 5 (“V2016,” “H2018,” and “M2021,” respectively). In Table 5, we list $v_{\text{blue,max}}^{H\alpha}$ values, which are the maximum velocities of blue wing enhancements of $H\alpha$ line measured by eye. The same velocity values for other lines showing blue asymmetries (e.g., $v_{\text{blue,max}}^{H\beta}$) are also listed in Table 6. We discuss blue wing asymmetry velocities more in detail by the line fitting method in Section 4.3. As summarized in Table 5 and described in the following, there are various correspondences in flare properties (e.g., durations of blue wing asymmetries, intensities of WL emissions, blue wing asymmetries in various chromospheric lines).

Table 6
Velocities and Masses of Blue Wing Asymmetry Flares

	Y3		Y6	Y18	Y23	E1	E2	A3
	[3] ^a	[5] ^a						
$v_{\text{blue,max}}^{\text{H}\alpha}$ [km s ⁻¹] ^b	-250	-250	-200	-200	-250	-200	-150	-200
$v_{\text{blue,max}}^{\text{H}\beta}$ [km s ⁻¹] ^b	-200	-200	-150	-150	-200	-150	-150	-150
$v_{\text{blue,max}}^{\text{H}\gamma}$ [km s ⁻¹] ^b	-100	-100	[NB]	...	-150	-100	-100	-150
$v_{\text{blue,max}}^{\text{H}\delta}$ [km s ⁻¹] ^b	-100	-75	[NB]	...	-100	-50	[NB]	-150
$v_{\text{blue,max}}^{\text{H}\epsilon}$ [km s ⁻¹] ^b	-50	-50	[NB]	...	-75	[NB]	[NB]	-100
$v_{\text{blue,max}}^{\text{CaK}}$ [km s ⁻¹] ^b	-50	-50	[NB]	...	-100	-50	[NB]	-100
$v_{\text{blue,max}}^{\text{CaH}}$ [km s ⁻¹] ^b	-50	-50	[NB]	...	-75	-50	[NB]	-100
$v_{\text{blue,max}}^{\text{Ca8542}}$ [km s ⁻¹] ^b	[NB]	[NB]	[NB]	[NB]	[NB]	[NB]	[NB]	-50
$v_{\text{blue,max}}^{\text{NaD1\&D2}}$ [km s ⁻¹] ^b	[NB]	[NB]	[NB]	[NB]	-100	[NB]	[NB]	[NB]
$v_{\text{blue,max}}^{\text{He D3}}$ [km s ⁻¹] ^b	[NB]	[NB]	[NB]	[NB]	-100	[NB]	[NB]	-50
$v_{\text{blue,fit}}^{\text{H}\alpha}$ [km s ⁻¹]	-105 ⁺¹¹ ₋₈	-88 ⁺⁸ ₋₉	-122 ⁺¹ ₋₁	-115 ⁺² ₋₅	-106 ⁺¹ ₋₃	-87 ⁺⁷ ₋₉	-73 ⁺¹¹ ₋₁₈	-106 ⁺⁰ ₋₃
$\text{EW}_{\text{blue,fit}}^{\text{H}\alpha}$ [Å]	0.23 ^{+0.04} _{-0.03}	0.45 ^{+0.08} _{-0.08}	0.32 ^{+0.01} _{-0.01}	0.27 ^{+0.01} _{-0.02}	0.45 ^{+0.02} _{-0.03}	0.39 ^{+0.07} _{-0.08}	0.19 ^{+0.07} _{-0.04}	0.16 ^{+0.00} _{-0.01}
$v_{\text{blue,fit}}^{\text{H}\beta}$ [km s ⁻¹]	-97 ⁺¹ ₋₆	-90 ⁺¹⁰ ₋₁₂	-107 ⁺¹ ₋₁	-116 ⁺¹¹ ₋₃	-97 ⁺⁷ ₋₈	-86 ⁺¹¹ ₋₁₄	-86 ⁺¹⁸ ₋₁₅	-85 ⁺¹ ₋₄
$\text{EW}_{\text{blue,fit}}^{\text{H}\beta}$ [Å]	0.40 ^{+0.01} _{-0.05}	0.82 ^{+0.12} _{-0.13}	0.29 ^{+0.01} _{-0.01}	0.24 ^{+0.04} _{-0.01}	0.94 ^{+0.13} _{-0.13}	0.39 ^{+0.08} _{-0.09}	0.28 ^{+0.08} _{-0.07}	0.17 ^{+0.01} _{-0.02}
$L_{\text{blue}}^{\text{H}\alpha}$ [erg s ⁻¹]	2.5 ^{+0.4} _{-0.3} × 10 ²⁶	4.9 ^{+0.9} _{-0.9} × 10 ²⁶	3.5 ^{+0.1} _{-0.1} × 10 ²⁶	2.9 ^{+0.1} _{-0.2} × 10 ²⁶	5.0 ^{+0.2} _{-0.3} × 10 ²⁶	6.8 ^{+1.2} _{-1.4} × 10 ²⁶	3.5 ^{+1.3} _{-0.7} × 10 ²⁶	6.1 ^{+0.0} _{-0.4} × 10 ²⁶
$L_{\text{blue}}^{\text{H}\beta}$ [erg s ⁻¹]	1.4 ^{+0.1} _{-0.2} × 10 ²⁶	2.9 ^{+0.4} _{-0.5} × 10 ²⁶	1.0 ^{+0.1} _{-0.1} × 10 ²⁶	8.6 ^{+0.1} _{-0.1} × 10 ²⁵	3.5 ^{+0.5} _{-0.5} × 10 ²⁶	2.4 ^{+0.5} _{-0.6} × 10 ²⁶	1.8 ^{+0.5} _{-0.5} × 10 ²⁶	2.4 ^{+0.1} _{-0.3} × 10 ²⁶
α ($=\epsilon_{\text{blue}}^{\text{H}\alpha}/\epsilon_{\text{blue}}^{\text{H}\beta}$)	1.75 ± 0.31	1.67 ± 0.39	3.35 ± 0.16	3.42 ± 0.46	1.45 ± 0.22	2.81 ± 0.82	1.91 ± 0.77	2.51 ± 0.26
$\log \epsilon_{\text{blue}}^{\text{H}\alpha}$ [erg s ⁻¹ cm ⁻² sr ⁻¹]	6.4 ^{+0.2} _{-0.2}	6.4 ^{+0.2} _{-0.2}	5.9 ^{+0.1} _{-0.1}	5.9 ^{+0.1} _{-0.1}	6.5 ^{+0.1} _{-0.1}	6.0 ^{+0.3} _{-0.2}	6.3 ^{+0.4} _{-0.3}	6.1 ^{+0.1} _{-0.1}
$A_{\text{blue}}^{\text{H}\alpha}$ [10 ¹⁹ cm ²]	1.6 ^{+1.1} _{-0.7}	2.8 ^{+2.3} _{-1.5}	6.9 ^{+2.1} _{-1.6}	6.1 ^{+2.6} _{-2.1}	2.3 ^{+1.1} _{-0.8}	9.9 ^{+9.6} _{-5.8}	2.5 ^{+4.1} _{-1.8}	7.3 ^{+2.4} _{-2.2}
(1) Upper limit $\epsilon_{\text{blue}}^{\text{H}\alpha}$ case (e.g., $\log \epsilon_{\text{blue}}^{\text{H}\alpha}$ [erg s ⁻¹ cm ⁻² sr ⁻¹] = 6.0 for Flare Y6)								
$\log \text{EM}_{\text{blue}}^{(1)}$ [cm ⁻⁵]	32.6–33.0	32.7–33.1	30.9–31.2	30.9–31.2	32.8–33.2	31.5–32.1	32.3–32.7	31.5–32.1
$\log n_e^{(1)}$ [cm ⁻³]	11.1–11.5	11.2–11.5	10.3–11.5	10.3–11.5	11.2–11.5	10.5–11.5	11.0–11.5	10.6–11.5
$D_{\text{blue,upp}}^{(1)}$ [cm] ^c	R_{star}	R_{star}	R_{star}	R_{star}	R_{star}	R_{star}	R_{star}	R_{star}
$D_{\text{blue,low}}^{(1)}$ [cm]	4.0 × 10 ⁹	5.0 × 10 ⁹	7.9 × 10 ⁷	7.9 × 10 ⁷	6.3 × 10 ⁹	3.2 × 10 ⁸	2.0 × 10 ⁹	3.2 × 10 ⁸
$M_{\text{blue,upp}}^{(1)}$ [g] ($n_e/n_H = 0.17$)	1.9 × 10 ¹⁸	4.2 × 10 ¹⁸	7.3 × 10 ¹⁷	7.0 × 10 ¹⁷	3.0 × 10 ¹⁸	7.5 × 10 ¹⁸	3.7 × 10 ¹⁸	3.5 × 10 ¹⁸
$M_{\text{blue,low}}^{(1)}$ [g] ($n_e/n_H = 0.47$)	4.1 × 10 ¹⁶	7.8 × 10 ¹⁶	4.9 × 10 ¹⁵	3.6 × 10 ¹⁵	1.1 × 10 ¹⁷	1.5 × 10 ¹⁶	1.8 × 10 ¹⁶	1.8 × 10 ¹⁶
(2) Lower limit $\epsilon_{\text{blue}}^{\text{H}\alpha}$ case (e.g., $\log \epsilon_{\text{blue}}^{\text{H}\alpha}$ [erg s ⁻¹ cm ⁻² sr ⁻¹] = 5.8 for Flare Y6)								
$\log \text{EM}_{\text{blue}}^{(2)}$ [cm ⁻⁵]	31.7–32.1	31.8–32.2	30.5–30.7	30.5–30.7	32.2–32.6	30.6–31.0	30.9–31.2	30.8–31.2
$\log n_e^{(2)}$ [cm ⁻³]	10.7–11.5	10.7–11.5	10.1–11.5	10.1–11.5	10.9–11.5	10.1–11.5	10.3–11.5	10.2–11.5
$D_{\text{blue,upp}}^{(2)}$ [cm] ^c	R_{star}	R_{star}	R_{star}	R_{star}	R_{star}	R_{star}	R_{star}	R_{star}
$D_{\text{blue,low}}^{(2)}$ [cm]	5.0 × 10 ⁸	6.3 × 10 ⁸	3.2 × 10 ⁷	3.2 × 10 ⁷	1.6 × 10 ⁹	4.0 × 10 ⁷	7.9 × 10 ⁷	6.3 × 10 ⁷
$M_{\text{blue,upp}}^{(2)}$ [g] ($n_e/n_H = 0.17$)	6.8 × 10 ¹⁷	1.5 × 10 ¹⁸	3.7 × 10 ¹⁷	3.5 × 10 ¹⁷	1.5 × 10 ¹⁸	1.7 × 10 ¹⁸	5.9 × 10 ¹⁷	9.7 × 10 ¹⁷
$M_{\text{blue,low}}^{(2)}$ [g] ($n_e/n_H = 0.47$)	5.1 × 10 ¹⁵	9.9 × 10 ¹⁵	1.9 × 10 ¹⁵	1.4 × 10 ¹⁵	2.7 × 10 ¹⁶	1.9 × 10 ¹⁵	7.1 × 10 ¹⁴	3.5 × 10 ¹⁵
$M_{\text{blue,upp}}$ [g]	6.1 × 10 ¹⁸		7.3 × 10 ¹⁷	7.0 × 10 ¹⁷	3.0 × 10 ¹⁸	7.5 × 10 ¹⁸	3.7 × 10 ¹⁸	3.5 × 10 ¹⁸
$M_{\text{blue,low}}$ [g]	1.5 × 10 ¹⁶		1.9 × 10 ¹⁵	1.4 × 10 ¹⁵	2.7 × 10 ¹⁶	1.9 × 10 ¹⁵	7.1 × 10 ¹⁴	3.5 × 10 ¹⁵
$E_{\text{kin,upp}}$ [erg]	2.2 × 10 ³²		5.4 × 10 ³¹	4.5 × 10 ³¹	1.7 × 10 ³²	2.4 × 10 ³²	7.2 × 10 ³¹	1.9 × 10 ³²

Table 6
(Continued)

	Y3		Y6	Y18	Y23	E1	E2	A3
	[3] ^a	[5] ^a						
$E_{\text{kin,low}}$ [erg]	7.9×10^{29}		1.5×10^{29}	1.0×10^{29}	1.6×10^{30}	8.7×10^{28}	2.9×10^{28}	2.1×10^{29}
$E_{u,\text{flare}}$ [erg] ^d	$<5.6 \times 10^{31}$		$<7.2 \times 10^{31}$...	1.6×10^{32}	...	1.1×10^{31}	$>2.7 \times 10^{31}$
$E_{U,\text{flare}}$ [erg] ^d	4.6×10^{31}
$E_{g,\text{flare}}$ [erg] ^d	$<1.2 \times 10^{32}$		$<1.6 \times 10^{32}$...	2.2×10^{32}	...	7×10^{30}	$>1.4 \times 10^{31}$
$E_{V,\text{flare}}$ [erg] ^d	2.4×10^{31}
$E_{\text{TESS,flare}}$ [erg] ^d	$<2.6 \times 10^{32}$	
$E_{\text{bol,flare}}^{(1)}$ [erg] ^c	$<6.2 \times 10^{32}$		$<8.0 \times 10^{32}$	4.2×10^{32}	1.8×10^{33}	...	1.2×10^{32}	$>3.0 \times 10^{32}$
$E_{\text{H}\alpha,\text{flare}}$ [erg] ^d	1.7×10^{31}		$>3.9 \times 10^{31}$	$(1.5-1.6) \times 10^{31}$	$>1.1 \times 10^{31}$	2.9×10^{31}	5.8×10^{30}	$>5.3 \times 10^{31}$
$E_{\text{Xray,flare}}(0.5-2.0 \text{ keV})$ [erg] ^d	2.6×10^{32}	
$E_{\text{Xray,flare}}(\text{GOES band})$ [erg] ^d	4.7×10^{31}		$>3.6 \times 10^{31}$	$(1.4-1.5) \times 10^{31}$	$>1.0 \times 10^{31}$	2.7×10^{31}	5.4×10^{30}	$>4.9 \times 10^{31}$
$E_{\text{bol,flare}}^{(2)}$ [erg] ^c	7.8×10^{32}		$>6.0 \times 10^{32}$	$(2.3-2.5) \times 10^{32}$	$>1.7 \times 10^{32}$	4.5×10^{32}	9.0×10^{31}	$>8.2 \times 10^{32}$
$E_{\text{bol,flare}}$ [erg] ^c	7.8×10^{32}		6.0×10^{32} -8.0×10^{32}	2.3×10^{32} -4.2×10^{32}	1.7×10^{32} -1.8×10^{33}	4.5×10^{32}	9.0×10^{31} -1.2×10^{32}	3.0×10^{32} -1.0×10^{34}

Notes.

^a Blue wing asymmetries were seen twice (20 minutes \times 2) during Flare Y3. The values for these two asymmetries, which occurred at around time [3] and [5] in Figure 8, are listed separately here. As for the mass and kinetic energy values, the sum of the two asymmetries are listed.

^b $v_{\text{H}\alpha,\text{blue,max}}, v_{\text{H}\beta,\text{blue,max}}, v_{\text{H}\gamma,\text{blue,max}}, v_{\text{H}\delta,\text{blue,max}}, v_{\text{H}\epsilon,\text{blue,max}}, v_{\text{CaK},\text{blue,max}}, v_{\text{CaH},\text{blue,max}}, v_{\text{Ca8542},\text{blue,max}}, v_{\text{NaD1\&D2},\text{blue,max}}, v_{\text{HeD3},\text{blue,max}}$: the maximum velocity values of blue wing enhancements measured by eye, for H α , H β , H γ , H δ , H ϵ , Ca II K, Ca II H, Ca II 8542, Na I D1 and D2, and He I D3 lines. [NB] means this line does not show blue wing asymmetry (see Table 5). There are no observation data of H γ , H δ , H ϵ , Ca II H&K lines for Flare Y18, which was observed with SMARTS 1.5 m/CHIRON.

^c Stellar radius (R_{star}) of YZ CMi, EV Lac, and AD Leo are 2.1×10^{10} , 2.5×10^{10} , and 3.0×10^{10} cm, respectively (see Table 1).

^d $E_{\text{H}\alpha,\text{flare}}, E_{u,\text{flare}}, E_{U,\text{flare}}, E_{g,\text{flare}}, E_{V,\text{flare}}$, and $E_{\text{TESS,flare}}$ are flare energies in H α line, u band, U band, g band, V band, and TESS band, respectively, which are taken from Table 4. As for Flare Y3, $E_{\text{Xray,flare}}(0.5-2.0 \text{ keV})$ and $E_{\text{Xray,flare}}(\text{GOES band})$ are the soft X-ray energies in 0.5–2.0 keV and the GOES band (1.5–12.4 keV) from the NICER X-ray spectra. As for other flares, $E_{\text{Xray,flare}}(\text{GOES band})$ are estimated from the flare energies in H α line using the scaling law from Haisch (1989; see Section 4.3).

^e $E_{\text{bol,flare}}^{(1)}$ and $E_{\text{bol,flare}}^{(2)}$ are the flare bolometric energy with the two different methods described in Section 4.3, respectively. $E_{\text{bol,flare}}$ is the resultant bolometric flare energy used for Figure 47.

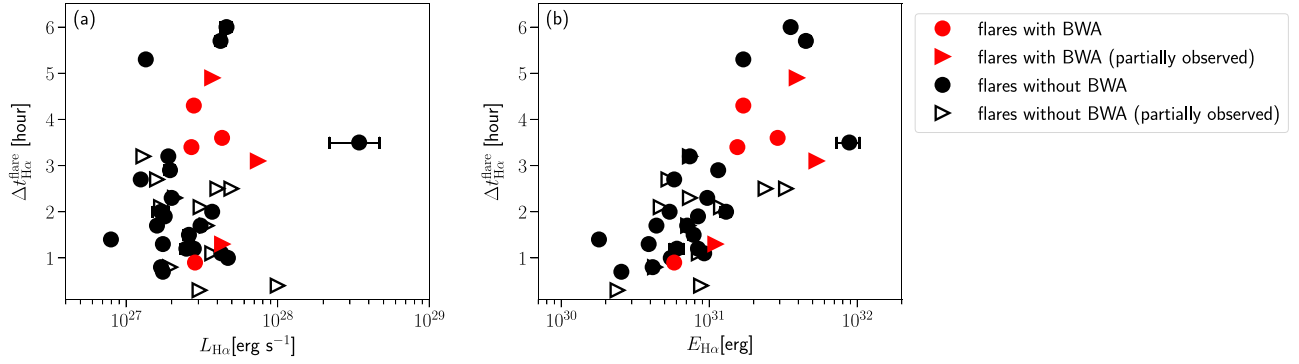


Figure 37. (a) Scatter plot of the H α flare peak luminosity ($L_{H\alpha}$) and H α flare duration ($\Delta t_{H\alpha}^{\text{flare}}$). Red filled circles and red rightward filled triangles represent the flares with blue wing asymmetries (BWA), while the latter ones correspond to the flares whose H α flare phase was only partially observed (only the lower limit values for $\Delta t_{H\alpha}^{\text{flare}}$ are listed in Tables 4 and 5). As for these stars, the plotted $L_{H\alpha}$ values can be the lower limit values. Black filled circles and black rightward open triangles are the same as the above red points but for the flares without BWAs. (b) Same as (a), but for the H α flare energy ($E_{H\alpha}$) and H α flare duration ($\Delta t_{H\alpha}^{\text{flare}}$).

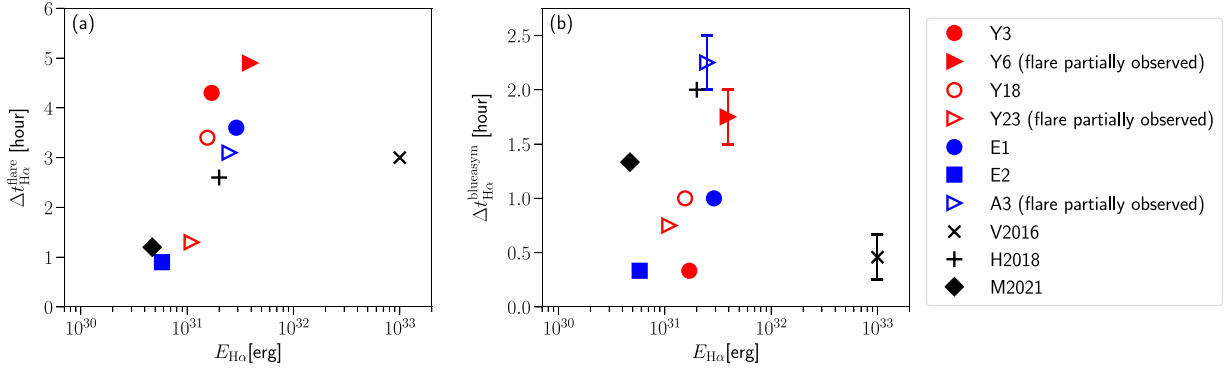


Figure 38. Scatter plots of the H α flare energy ($E_{H\alpha}$), H α flare duration ($\Delta t_{H\alpha}^{\text{flare}}$), and duration of H α blue asymmetries ($\Delta t_{H\alpha}^{\text{blueasym}}$) for the flares with blue wing asymmetries (see Table 5). In addition to the 7 flares reported in this study, three events from the previous papers (V2016, H2018, and M2021 in Table 5) are also plotted. As for Flares Y6, Y23, and A3, the H α flare phase was only partially observed, and the plotted $E_{H\alpha}$ and $\Delta t_{H\alpha}^{\text{blueasym}}$ values can be the lower limit values. As for Flare Y3, $\Delta t_{H\alpha}^{\text{blueasym}} = 20 \text{ minutes} \times 2$ is listed in Table 5, but the single data point of $\Delta t_{H\alpha}^{\text{blueasym}} = 20 \text{ minutes} = 0.33 \text{ hr}$ is only plotted here.

Figure 37 shows the scatter plots of the H α flare peak luminosity, energy, and duration values of the 7 flares with blue wing asymmetries and the remaining 34 flares observed in this study. Blue wing asymmetries could be seen both in relatively large and long, and small and short flares, although it would be difficult to statistically conclude this point only from the limited number of observed samples in this study.

The duration of H α blue wing asymmetries ($\Delta t_{H\alpha}^{\text{blueasym}}$ in Table 5) ranges from 20 minutes to 2.5 hr (Figure 38). Comparing Figures 38(a) and (b), there is some variation among the relations of $\Delta t_{H\alpha}^{\text{flare}}$ and $\Delta t_{H\alpha}^{\text{blueasym}}$.

As a notable example, Flare Y3 showed clear short-lived H α blue wing asymmetries twice (20 minutes \times 2 at the times [3] and [5]) during the entire Flare Y3 in H α line lasting over 4 hr (Figures 8 and 10). Similarly, Vida et al. (2016) also reported three distinct blue wing enhancements spanning more than 3 hr (“V2016” in Table 5). In contrast, Flares Y23, E1, and A3 showed H α blue wing asymmetries over almost all the observed phases of the flares (Figures 26, 30, and 34), although initial phases of the flares were not observed during Flares Y23 and A3. Similarly, Honda et al. (2018) also reported a continuous blue asymmetry of H α line over all the phase of the flare (H2018 in Table 5). As another notable point, the blue wing asymmetry velocities showed gradual decays during Flares Y6 and Y23 (Figures 16 and 26). In particular, Flare Y6 showed clear H α blue wing enhancement (blue wing asymmetry) up to $\sim -200 \text{ km s}^{-1}$ in early phase of the flare, while the line profile gradually shifted to the red-wing enhancement

(red wing asymmetry) up to $\sim +200 \text{ km s}^{-1}$, during the H α flare over 4.9 hr (Figure 16). In the middle time between blue wing asymmetry and red wing asymmetry, the H α line profile showed almost symmetric broadening with $\pm 150 \text{ km s}^{-1}$. These red wing asymmetries could be caused by the chromospheric condensation, flare-driven coronal rain or post-flare loop, as summarized in Section 4.5. This example (Flare Y6) may show that both blue and red wing asymmetries of H α line can evidently occur during the same flare of a mid-M-dwarf, which suggests dynamic plasma motions upward and downward during the same flare.

It is noted that the possible change from blue wing enhancement to the red-wing enhancement during a flare was also reported in Muheki et al. (2020a).

However, it can be also possible that Flare Y6 consists of different consecutive flares showing blue wing asymmetries and red wing asymmetries, respectively, considering that the flare light curve showed multiple peaks (see Figure 14).

There is also a notable difference among the intensities of red wing of the H α line when the blue wing shows an excess enhancement (blue wing asymmetry). As for Flares Y3, Y6, and A3, the red wing of the H α line is broadened up to $\sim +150 \text{ km s}^{-1}$ when the blue wing is more enhanced up to $\sim -200 \text{ km s}^{-1}$ (Figures 10, 16, and 34). In contrast, during Flares Y18 and E2, the red wing of the H α line is broadened only up to $\sim +50\text{--}100 \text{ km s}^{-1}$ when the blue wing is enhanced up to $\sim -200 \text{ km s}^{-1}$ (Figures 22 and 30). These differences might suggest that H α line symmetric broadening or red-wing

enhancements, which have been often observed during stellar flares (e.g., Namekata et al. 2020; Wollmann et al. 2023), could occur to some extent simultaneously with larger $H\alpha$ blue wing enhancements (see also Section 4.5). In a relevant context, Honda et al. (2018) reported the possible existence of absorption components in the red wing of the $H\alpha$ line when the $H\alpha$ line showed blue wing asymmetry.

The intensities of WL continuum fluxes also showed various properties even among these 7 flares (the “WLF” column in Table 5). Flare Y3 did not show clear WL continuum flux enhancements, while flare emissions were observed for $\gtrsim 4$ hr in various chromospheric lines and NICER soft X-ray data (Figure 8; see also Section 4.4 for detailed discussions of NICER soft X-ray data). There were very small *suggestive* increases in u and g bands and TESS data around time 6–8 hr in Figures 8(b) and (c), although they are still a bit smaller than the WL flare detection thresholds (see Section 3.2). We can speculate that these small *suggestive* increases could be caused by the emission lines (e.g., Balmer lines) included in u , g , and TESS bands (see Figure 1). This flare could be possibly categorized to so-called NWL flares, which are often seen in the case of solar flares (e.g., Watanabe et al. 2017). Maehara et al. (2021) also reported the $H\alpha$ blue wing asymmetry during an NWL flare (“M2021” in Table 5). As for Flare Y6, there are short WL continuum flux enhancements in the middle/late phase of the flare (around time 10.0–10.5 and 12.0–12.5 hr in Figure 14), but there are no other clear WL enhancements that are considered to be physically associated with the early increasing phase of the whole $H\alpha$ flare, so this flare could be categorized into NWL flare as the whole flare event.

As described in Section 4.1, the 31 flares are classified as WL flares among the 35 flares with enough data sets to judge whether the flares are WL flares. The remaining 4 flares (Flares Y3, Y5, Y6, and Y26) are classified as NWL flares in this study, while three of them (Flares Y3, Y5, and Y26) showed slight possible WL increases almost comparable to the photometric errors, and Flare Y6 showed WL emissions in the middle/late phase of the $H\alpha$ and $H\beta$ flare emission. As a result, as for the 7 flares with clear blue wing asymmetries discussed here (Flares Y3, Y6, Y18, Y23, E1, E2, and A3), 5 flares (Flares Y3, Y6, Y18, Y23, and E2) have enough data sets for judging whether they are WL flares. Among these 5 flares, three flares (Flares Y18, Y23, and E2) are classified as WL flares, and two flares (Flares Y3 and Y6) are candidate NWL flares as described in the above. These results can suggest that blue wing asymmetries of chromospheric lines can be seen both during *clear* WL and *candidate* NWL flares. However, it should be noted the NWL flares in this study could actually be weak WL flares, since the ground-based photometry used for most of the flares in this study have relatively large photometric errors, and high-precision TESS photometry is only available for six flares, and it only observes the red wavelength range (6000–10000 Å). This is not the best wavelength range for stellar flare observations compared with blue optical wavelength range (e.g., U and u bands), since the M-dwarf flares generally have larger amplitudes in the blue optical wavelength range than in the red range (Hawley & Pettersen 1991; Kowalski et al. 2010; Brasseur et al. 2023).

In Table 5, we list which chromospheric lines showed blue wing asymmetries ([B] and [NB], as explained in a footnote of the table) in addition to $H\alpha$ line. Large variety is seen also for this point. Among the seven flares with $H\alpha$ blue wing asymmetries, all seven flares in this study showed blue wing

asymmetries also in $H\beta$ lines; though, the $H\beta$ data of Flare Y18 was not so clear (Figure 20). Flares Y6 and E2 showed blue wing asymmetries in higher-order Balmer lines up to $H\beta$ and $H\gamma$ lines, respectively, but they did not show blue wing asymmetries in chromospheric lines other than Balmer lines (e.g., Ca II lines, Na I D1 and D2 lines, and He I D3 lines). Flares Y3 and E1 showed blue wing asymmetries not only in Balmer lines up to $H\epsilon$ and $H\delta$ lines, respectively, but also in Ca II H&K lines. Moreover, Flares Y23 and A3 showed blue wing asymmetries in almost all chromospheric lines we investigated, except for Ca II 8542 and Na I D1 and D2, respectively. Blue wing asymmetries in multiple chromospheric lines have been investigated in several previous studies. Flare V2016 on M4 dwarf V374Peg from Vida et al. (2016; in Table 5) showed blue asymmetries in $H\alpha$, $H\beta$, and $H\gamma$ lines (see also the reanalysis results in Leitzinger et al. 2022), while it is not clearly mentioned whether He I line showed blue asymmetries or not in the discussions of Vida et al. (2016), Leitzinger et al. (2022). A flare on EV Lac in Figure 7 of Muheki et al. (2020b) also showed blue wing asymmetry only in $H\alpha$ line but not in $H\beta$ and He I lines. In contrast, a flare on AD Leo in Figure 6 of Muheki et al. (2020a) showed blue asymmetries both in $H\alpha$ and $H\beta$ lines.

The velocities of blue wing enhancements in these various chromospheric lines are listed in Table 6 ($v_{\text{blue,max}}$ in the table). The velocities are different among different lines, and the lower-order Balmer lines especially $H\alpha$ line tend to show larger velocities of blue wing asymmetries or wider blue wing tails, while higher-order Balmer lines, Ca II lines, Na I D1 and D2, and He I D3 lines show smaller velocities.²⁶

We speculate that these differences can be caused by the differences of optical depth and line wing broadening physics among other chromospheric lines as described in the following. The differences of optical depth and line wing broadening physics (e.g., Stark effect) can affect these differences in the flaring atmosphere (e.g., Kowalski et al. 2022), while those of optical depth can also affect the emission from prominences (e.g., Okada et al. 2020).

These differences can be clues to investigate how blue wing asymmetries occur associated with flares on mid-M-dwarfs. For example, there is a difference of optical depth among different Balmer lines, and $H\alpha$ line is more optically thick than other Balmer lines (e.g., Drake & Ulrich 1980; Heinzel et al. 1994a). Then, the visibility difference of Balmer lines could be a clue to constrain density and total emitting area values of the upward-moving plasma that caused the blue wing enhancements during flares. However, in order to interpret these differences more quantitatively in detail, it is necessary to conduct observation-based modeling studies incorporating radiative transfer physics of stellar (erupting) prominences and flaring atmospheres (e.g., Kowalski et al. 2022; Leitzinger et al. 2022). Comparisons with the multiwavelength Sun-as-a-star observation data of solar (erupting) prominences and solar flares are also very important for further quantitative discussions (e.g., Namekata et al. 2022a; Otsu et al. 2022; Lynch et al. 2023).

²⁶ Some of the data could be affected from the lower S/Ns at bluer wavelengths (e.g., Figure 20), but most of the data have enough S/N values to determine $v_{\text{blue,max}}$ (e.g., Figure 15). Furthermore, the velocity differences can be still seen if we integrate the data over longer time so that the data have higher S/Ns (e.g., integrating from time 9.3–10.5 hr in Figure 16). Then, it is not possible to explain all the difference trends (i.e., $H\alpha$ having largest $v_{\text{blue,max}}$ values) only from the lower S/N at bluer wavelengths. Some noisy data (e.g., Figure 20) could be affected, but the overall trends discussed in the following of this paragraph would not be affected.

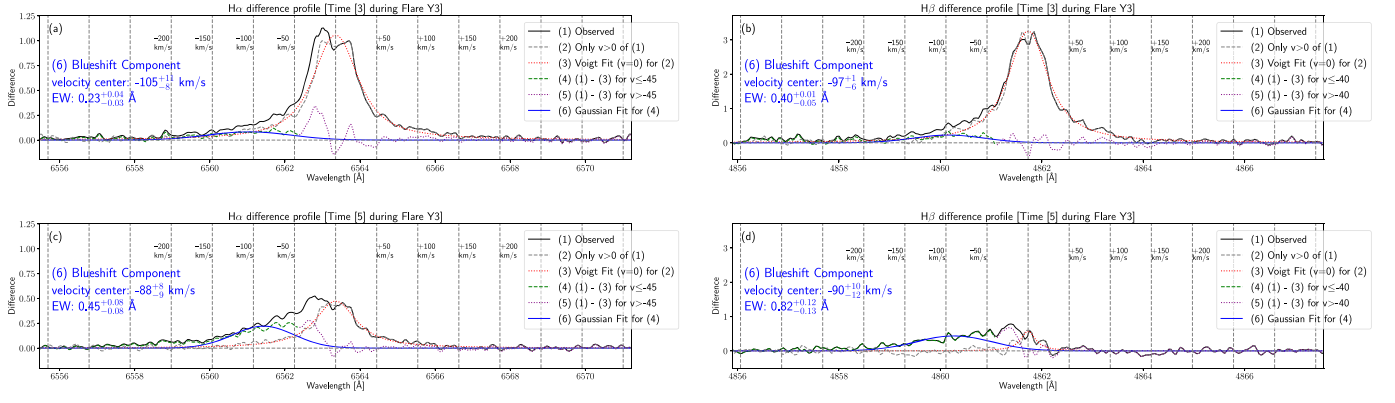


Figure 39. (a) Line profile change of the $H\alpha$ emission line from the quiescent phase at time [3] during Flare Y3, which is the same as the $H\alpha$ difference profile shown in Figure 9(f). The horizontal and vertical axes represent the wavelength and flux normalized by the continuum. The gray vertical dashed lines with velocity values represent the Doppler velocities from the $H\alpha$ line center. The black solid line (1) indicates the observed line profile change. The gray dashed line (2) shows the symmetric line profile created by folding the red part (>0 km s $^{-1}$) of the original spectrum (1) to the blue part (<0 km s $^{-1}$). The red dotted line (3) represents a Voigt function fit to the profile (2), assuming the line-of-sight velocity of 0 km s $^{-1}$. The blue solid line (6) shows a Gaussian fit to the residuals in the range shorter than the threshold velocity (≤ -45 km s $^{-1}$), which is shown with the green dashed line (4). This threshold velocity of -45 km s $^{-1}$ was determined by trial and error and by eye so that only the line wing component is used for the fitting. The range longer than the threshold velocity (> -45 km s $^{-1}$) is plotted with the purple dotted line (5). The result of the Gaussian fitting (6) (line-of-sight velocity and equivalent width of blueshifted excess components) is shown in blue characters in the left side of the panel. The error values of the fitting results are obtained by changing the threshold velocities by ± 15 km s $^{-1}$ (i.e., 45 ± 15 km s $^{-1}$ in this case). (b) Same as (a) but for $H\beta$ line. The threshold velocity for the Gaussian fitting (6) is set to be $-40 (\pm 15)$ km s $^{-1}$. (c) Same as (a) but at time [5] during Flare Y3, which is the same as another $H\alpha$ difference profile shown in Figure 9(f). (d) Same as (c) but for $H\beta$ line.

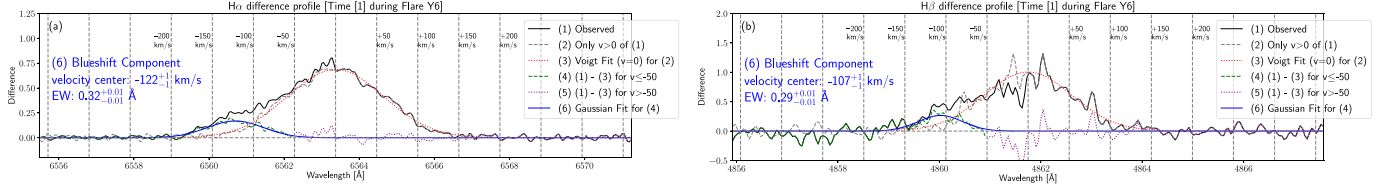


Figure 40. (a) Same as Figure 39(a) but for the $H\alpha$ profile at time [1] during Flare Y6, which is the same as the $H\alpha$ difference profile shown in Figure 15(b). The red dotted line (3) represents the result of Gaussian fit instead of Voigt fit. The threshold velocity for the Gaussian fitting (6) is set to be $-50 (\pm 15)$ km s $^{-1}$. (b) Same as (a) but for $H\beta$ line.

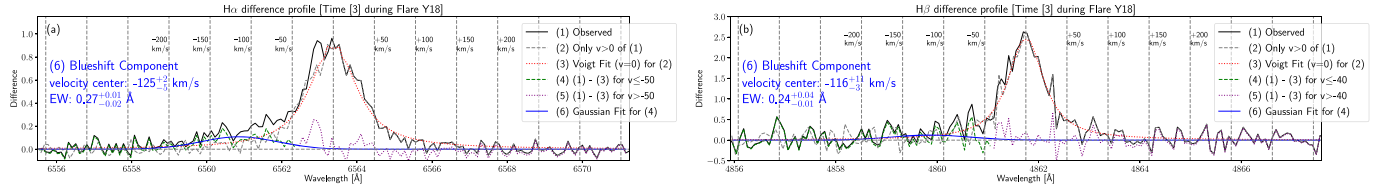


Figure 41. (a) Same as Figure 39(a) but for the $H\alpha$ profile at time [3] during Flare Y18, which is the same as the $H\alpha$ difference profile shown in Figure 20(f). The threshold velocity for the Gaussian fitting (6) is set to be $-50 (\pm 15)$ km s $^{-1}$. (b) Same as (a) but for $H\beta$ line. The threshold velocity for the Gaussian fitting (6) is set to be $-40 (\pm 15)$ km s $^{-1}$.

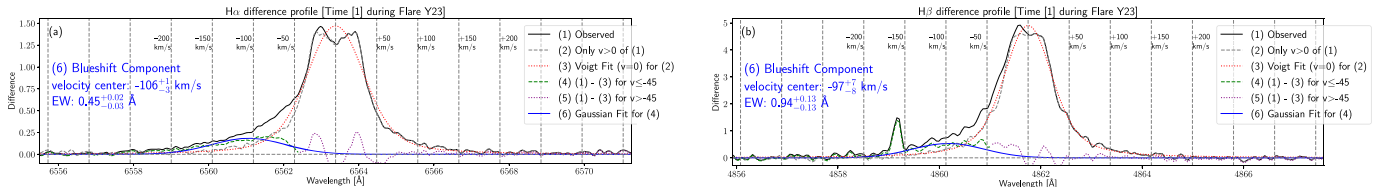


Figure 42. (a) Same as Figure 39(a) but for the $H\alpha$ profile at time [1] during Flare Y23, which is the same as the $H\alpha$ difference profile shown in Figure 25(b). The threshold velocity for the Gaussian fitting (6) is set to be $-45 (\pm 15)$ km s $^{-1}$. (b) Same as (a) but for $H\beta$ line.

4.3. Blue Wing Asymmetries and Possible Stellar Mass Ejections

Using the line fitting method similar to Maehara et al. (2021), we estimated the velocities of blue wing excess components of $H\alpha$ and $H\beta$ lines (Figures 39–45).

We note that, in this line fitting method (see Maehara et al. 2021; Inoue et al. 2023), there is an assumption that the flare emission other than the component causing the blue wing

asymmetry shows completely symmetric emission, and the red wing is not affected by any flare-related processes. If the red wing is affected by the flare-related processes simultaneously, then the measured blue wing asymmetry properties could be somewhat overestimated or underestimated.

As shown with the line (3) in Figures 39(a) and (b), we first fitted the $H\alpha$ and $H\beta$ difference profiles (the quiescent component subtracted profiles) with the Voigt functions,

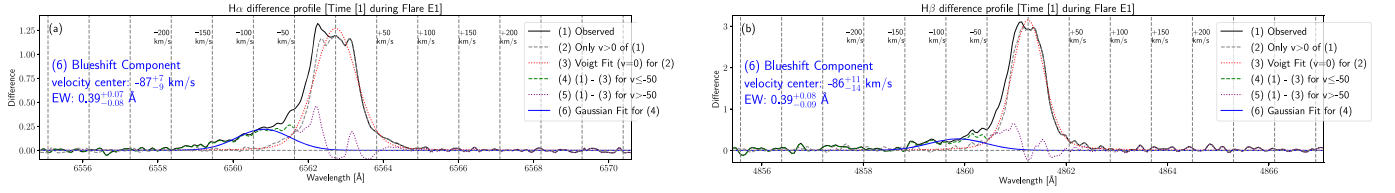


Figure 43. (a) Same as Figure 39(a) but for the $H\alpha$ profile at time [1] during Flare E1, which is the same as the $H\alpha$ difference profile shown in Figure 29(b). The threshold velocity for the Gaussian fitting (6) is set to be $-50 (\pm 15) \text{ km s}^{-1}$. (b) Same as (a) but for $H\beta$ line.

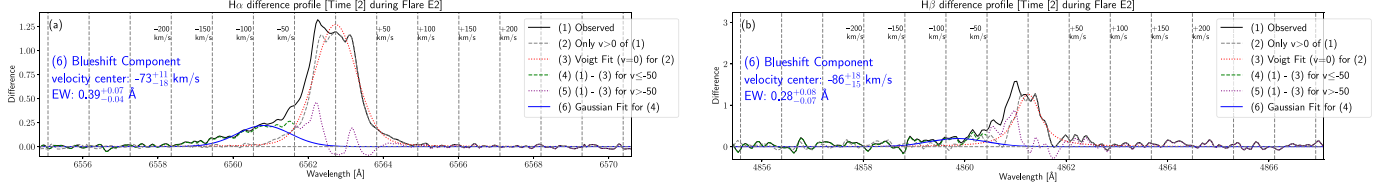


Figure 44. (a) Same as Figure 39(a) but for the $H\alpha$ profile at time [2] during Flare E2, which is the same as the $H\alpha$ difference profile shown in Figure 29(b). The threshold velocity for the Gaussian fitting (6) is set to be $-50 (\pm 15) \text{ km s}^{-1}$. (b) Same as (a) but for $H\beta$ line.

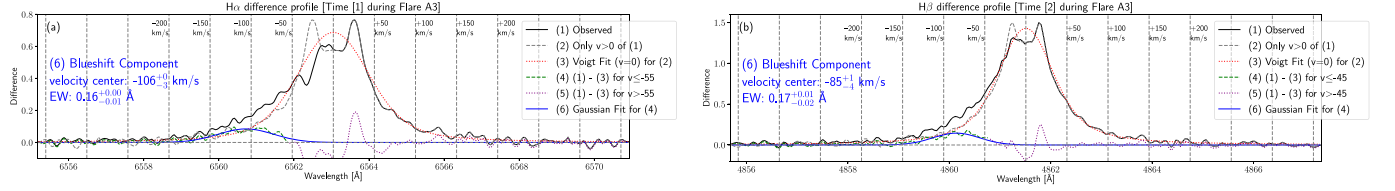


Figure 45. (a) Same as Figure 39(a) but for the $H\alpha$ profile at time [1] during Flare A3, which is the same as the $H\alpha$ difference profile shown in Figure 33(b). The threshold velocity for the Gaussian fitting (6) is set to be $-55 (\pm 15) \text{ km s}^{-1}$. (b) Same as (a) but for $H\beta$ line at time [2] during Flare A3, which is the same as the $H\beta$ difference profile shown in Figure 33(d). The threshold velocity for the Gaussian fitting (6) is set to be $-45 (\pm 15) \text{ km s}^{-1}$. We note the $H\alpha$ data at time [1] in (a) while $H\beta$ data at time [2] in (b), since the $H\beta$ observation started later than $H\alpha$ (there are no $H\beta$ data at time [1]) in Figure 32.

assuming the line-of-sight velocity of 0 km s^{-1} and only using the red part ($>0 \text{ km s}^{-1}$) of the original spectra (line (2)). Next, we calculated the residuals between the fitted Voigt functions and the observed spectra, which are shown with lines (4) and (5) in Figures 39(a) and (b). Finally, the residual was fitted with the Gaussian function to estimate the blue wing excess component (line (6) in Figures 39(a) and (b)). In this Gaussian fitting process, the wavelength ranges shorter than the threshold velocities (-45 and -40 km s^{-1} for $H\alpha$ and $H\beta$ profiles in Figures 39(a) and (b), respectively) were only used (line (4)). These threshold velocities were determined by trial-and-error and by eye, so that asymmetries at the line center components (line (5)) do not affect the fitting, and only the blue wing excess components are used for the Gaussian fitting (line (6)). Figures 39(a) and (b), which are described here, show the results of the first blue asymmetry component of Flare Y3. The fitting results of the second blue asymmetry component of Flare Y3 are shown in Figures 39(c) and (d). The fitting results of blue asymmetry components of other six flares (Flares Y6, Y18, Y23, E1, E2, and A3) are shown in Figures 40–45. As for Flare Y6 shown in Figure 40, the Gaussian fitting was conducted instead of the initial Voigt fitting (line (3)), considering the line profile of the original spectra (line (1)). The threshold velocities of the Gaussian fitting (6) (e.g., -45 and -40 km s^{-1} for $H\alpha$ and $H\beta$ profiles in Figures 39(a) and (b)) are different among the events and lines, and the values are shown in the figures. The results of Gaussian fitting (6) (line-of-sight velocity and EW of blue wing enhancement components of $H\alpha$ and $H\beta$ lines) are shown with blue characters in Figures 39–45, and these values are listed in Table 6 ($v_{\text{blue,fit}}^{\text{H}\alpha}$, $\text{EW}_{\text{blue,fit}}^{\text{H}\alpha}$, $v_{\text{blue,fit}}^{\text{H}\beta}$, $\text{EW}_{\text{blue,fit}}^{\text{H}\beta}$). The error values of these fitting

results are roughly obtained by changing the threshold velocities by $\pm 15 \text{ km s}^{-1}$. This range, $\pm 15 \text{ km s}^{-1}$, is roughly assumed by considering the accuracy of the *by-eye* determination of the threshold velocity. For example, in the case of the first asymmetry component (time [3]) of Flare Y3, $v_{\text{blue,fit}}^{\text{H}\alpha} = -105_{-8}^{+11} \text{ km s}^{-1}$, and $\text{EW}_{\text{blue,fit}}^{\text{H}\alpha} = 0.23_{-0.03}^{+0.04} \text{ \AA}$, $v_{\text{blue,fit}}^{\text{H}\beta} = -97_{-6}^{+1} \text{ km s}^{-1}$, and $\text{EW}_{\text{blue,fit}}^{\text{H}\beta} = 0.40_{-0.05}^{+0.01} \text{ \AA}$, by considering the threshold velocities of -45 ± 15 and $-40 \pm 15 \text{ km s}^{-1}$ for $H\alpha$ and $H\beta$ profiles in Figures 39(a) and (b). In addition, it is noted that the $H\beta$ profile of Flare Y18 in Figure 41(b) is particularly noisy, the error values for this event can be larger than those estimated here, and we have to keep this in mind in the following analyses.

The estimated Doppler velocities of the 7 blueshift (blue wing asymmetry) events ($v_{\text{blue,fit}}^{\text{H}\alpha}$) range from -73 to -122 km s^{-1} (Table 6).

Since the asymmetries do not recur periodically both in the blue and red wings independently of flares, these 7 blue wing asymmetries should be more likely to be related to flares, and cannot be explained by the rotationally modulated emission from the corotating prominence (e.g., Jardine et al. 2020). These velocities (73 – 122 km s^{-1}) are also a bit larger than the upward velocities of blue asymmetries observed in $H\alpha$ line mainly in the early phase of solar flares (e.g., Canfield et al. 1990; Heinzel et al. 1994b). For reference, such blue asymmetries of solar flares have been also observed in other chromospheric lines (e.g., Mg II lines) mainly in the early phase (e.g., Tei et al. 2018; Huang et al. 2019; Li et al. 2019). The durations of these solar blue asymmetries (a few minutes) are 1 or 2 orders of magnitude shorter than those of the blue wing asymmetries in this study ($\Delta t_{\text{H}\alpha}^{\text{blue,asym}} = 20 \text{ minutes} \text{--} 2.5 \text{ hr}$ in Table 5). In contrast, the

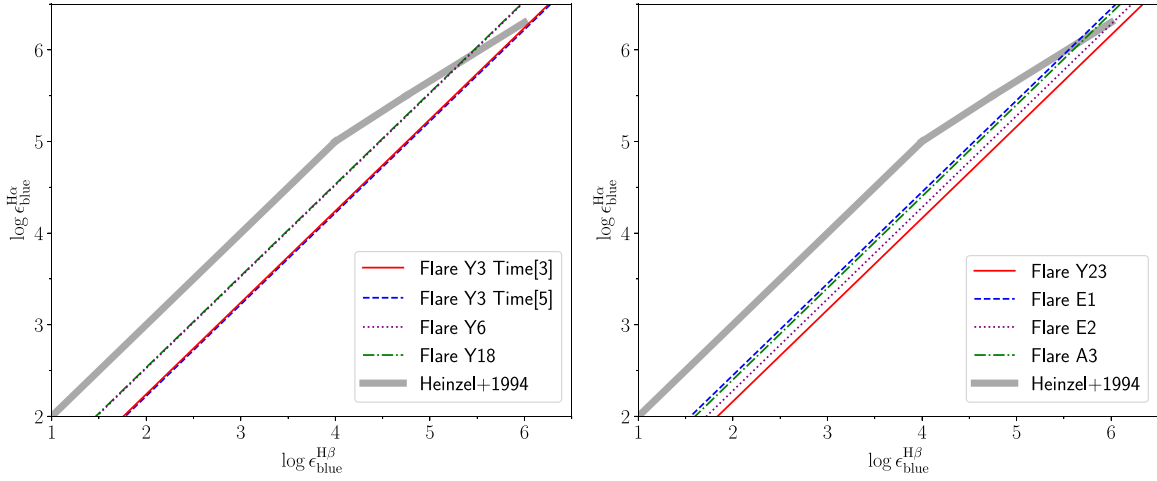


Figure 46. Relations between $H\alpha$ and $H\beta$ line integrated intensities emitted from the prominence. Observed relations between $\epsilon_{\text{blue}}^{H\alpha}$ and $\epsilon_{\text{blue}}^{H\beta}$ (Equation (13)) of the blue wing asymmetry events are plotted with red solid lines, blue dashed lines, purple dotted lines, and green dashed-dotted lines. The gray shaded area represents the result of the theoretical calculation of the NLTE slab model of solar prominence (taken from Figure 1 of Heinzel et al. 1994a).

velocities of the blue wing asymmetries in this study ($73\text{--}122\text{ km s}^{-1}$) are in the same range of solar prominence/filament eruptions (e.g., $10\text{--}400\text{ km s}^{-1}$ according to Gopalswamy et al. 2003). The timescale of solar prominence/filament eruptions observed in $H\alpha$ line is roughly 20 minutes–1 hr (Namekata et al. 2022c; Otsu et al. 2022), and this could be comparable or a bit shorter than the durations of the blue wing asymmetries in this study ($\Delta t_{\text{H}\alpha}^{\text{blueasym}} = 20\text{ minutes--}2.5\text{ hr}$). In the case of stellar flares, since we cannot obtain spatial information of the stellar surface, such prominence/filament eruption may be a possible cause of the blue wing asymmetries in chromospheric lines associated with flares. We note that Leitzinger et al. (2022) suggested that, unlike the Sun, the “filament” can be visible in emission even on the stellar disk in the case of M-dwarfs, since the stellar background emission components are quite weak. In the following of this subsection, we discuss the blue wing asymmetries detected in this study, from the viewpoint of stellar prominence eruptions.

The estimated EW values of the $H\alpha$ and $H\beta$ emissions from blueshifted excess components ($\text{EW}_{\text{blue,fit}}^{H\alpha}$ and $\text{EW}_{\text{blue,fit}}^{H\beta}$ in Table 6) can be converted to the luminosities of $H\alpha$ and $H\beta$ emissions ($L_{\text{blue}}^{H\alpha}$ and $L_{\text{blue}}^{H\beta}$ in Table 6), by applying $\text{EW}_{\text{blue,fit}}^{H\alpha}$ and $\text{EW}_{\text{blue,fit}}^{H\beta}$ values into Equation (7). As done in Maehara et al. (2021), Inoue et al. (2023), if we assume the simple slab NLTE emission model of solar prominences (e.g., Heinzel et al. 1994a) can be applied to the upward-moving plasma (possible prominence eruptions) showing the blueshifted excess components (blue wing asymmetries) on the M-dwarfs, the luminosities of $H\alpha$ and $H\beta$ emissions ($L_{\text{blue}}^{H\alpha}$ and $L_{\text{blue}}^{H\beta}$) can be calculated as

$$L_{\text{blue}}^{H\alpha} = \iint \epsilon_{\text{blue}}^{H\alpha} dA d\Omega = 2\pi A_{\text{blue}}^{H\alpha} \epsilon_{\text{blue}}^{H\alpha}, \quad (10)$$

and

$$L_{\text{blue}}^{H\beta} = \iint \epsilon_{\text{blue}}^{H\beta} dA d\Omega = 2\pi A_{\text{blue}}^{H\beta} \epsilon_{\text{blue}}^{H\beta}, \quad (11)$$

where $\epsilon_{\text{blue}}^{H\alpha}$ and $\epsilon_{\text{blue}}^{H\beta}$ are the $H\alpha$ and $H\beta$ line integrated intensities (see Table 1 of Heinzel et al. 1994a),²⁷ and $A_{\text{blue}}^{H\alpha}$ and $A_{\text{blue}}^{H\beta}$ are the area of the region emitting $H\alpha$ and $H\beta$ lines. If we

assume $H\alpha$ and $H\beta$ emissions originate from the same area ($A_{\text{blue}}^{H\alpha} = A_{\text{blue}}^{H\beta}$), these two, Equations (10) and (11), are combined into one equation:

$$\frac{\epsilon_{\text{blue}}^{H\alpha}}{\epsilon_{\text{blue}}^{H\beta}} = \frac{L_{\text{blue}}^{H\alpha}}{L_{\text{blue}}^{H\beta}} \equiv \alpha. \quad (12)$$

The α values calculated from $L_{\text{blue}}^{H\alpha}$ and $L_{\text{blue}}^{H\beta}$ values are listed in Table 6 (note the error values of $L_{\text{blue}}^{H\alpha}$, $L_{\text{blue}}^{H\beta}$, and α values in Table 6 are from those of $\text{EW}_{\text{blue,fit}}^{H\alpha}$ and $\text{EW}_{\text{blue,fit}}^{H\beta}$ values). Then, we get linear relations between logarithms of $H\alpha$ and $H\beta$ line integrated intensities:

$$\log \epsilon_{\text{blue}}^{H\alpha} = \log \alpha + \log \epsilon_{\text{blue}}^{H\beta}, \quad (13)$$

and these relations are plotted in Figure 46.

Heinzel et al. (1994a) conducted the theoretical calculation of the NLTE slab model of solar prominence, and estimated the relation between $H\alpha$ and $H\beta$ line integrated intensities (Figure 1 therein). If we assume this relation can be applied to the upward-moving plasma showing the present blueshifted excess components, we can roughly determine the values of $\epsilon_{\text{blue}}^{H\alpha}$, by comparing Equation (13) with the theoretical relation as in Figure 46. The resultant values of $\epsilon_{\text{blue}}^{H\alpha}$ are listed in Table 6. The error values of $\epsilon_{\text{blue}}^{H\alpha}$ listed in Table 6 are from the errors of α values and the scatter of the data points in Figure 1 of Heinzel et al. (1994a; \approx the width of the gray shaded area in Figure 46).

By adapting Figure 5 of Heinzel et al. (1994a), these values of $\log \epsilon_{\text{blue}}^{H\alpha}$ [$\text{erg s}^{-1} \text{cm}^{-2} \text{sr}^{-1}$] = 5.9–6.4 correspond to the optical thicknesses of the $H\alpha$ line ($\tau_{\text{H}\alpha}$) roughly ranging from 10 to 300 ($\log \tau_{\text{H}\alpha} \sim 1.0\text{--}2.5$). Using the resultant $\epsilon_{\text{blue}}^{H\alpha}$ values and Equation (10), the $A_{\text{blue}}^{H\alpha}$ values are obtained as listed in Table 6. The resultant values of $A_{\text{blue}}^{H\alpha} \sim 10^{19}\text{--}10^{20} \text{ cm}^2$ roughly correspond to 0.5%–4% of the visible stellar surface of the target stars (YZ CMi, EV Lac, and AD Leo). This value can be a bit smaller than or comparable to the area of starspots estimated from the amplitude of rotational modulations (e.g., the total spot coverage $\sim 6\%\text{--}17\%$ for YZ CMi in Maehara et al. 2021).

In Figure 15 of Heinzel et al. (1994a), the correlation between $H\alpha$ line integrated intensity ($\epsilon_{\text{blue}}^{H\alpha}$) and EM

²⁷ Heinzel et al. (1994a) used the symbol “ E ” for the line integrated intensities, but “ ϵ ” is used in this study so that this cannot be confused with flare energies.

$EM_{\text{blue}} = n_e^2 D$ is provided, where n_e and D are the electron density and geometrical thickness of the prominence, respectively.²⁸ By adapting this correlation, the EM_{blue} values are obtained as listed in Table 6. In this table, the EM_{blue} values are separately listed for two cases (e.g., $EM_{\text{blue}}^{(1)}$ and $EM_{\text{blue}}^{(2)}$). These two cases correspond to upper and lower limit values of $\epsilon_{\text{blue}}^{\text{H}\alpha}$ values (e.g., $\log \epsilon_{\text{blue}}^{\text{H}\alpha} = 6.0$, and 5.8 [$\text{erg s}^{-1} \text{cm}^{-2} \text{sr}^{-1}$] for Flare Y6), respectively, which come from the error range of $\epsilon_{\text{blue}}^{\text{H}\alpha}$ in Table 6 (e.g., $\log \epsilon_{\text{blue}}^{\text{H}\alpha} [\text{erg s}^{-1} \text{cm}^{-2} \text{sr}^{-1}] = 5.9^{+0.1}_{-0.1}$ for Flare Y6). Assuming the observed electron density range of solar prominences ($\log n_e [\text{cm}^{-3}] = 10\text{--}11.5$ from Hirayama 1986), the geometrical thickness $D_{\text{blue}} (=EM_{\text{blue}}/n_e^2)$ can be estimated from the EM_{blue} . Since this assumed range of n_e could be wide, here, we have another rough constraint that the prominence geometrical thickness is no larger than the stellar radius ($D_{\text{blue}} \leq R_{\text{star}}$). From this constraint, the lower limit of n_e can be determined as $n_e \geq \sqrt{EM_{\text{blue}}/R_{\text{star}}}$. The resultant estimated range of n_e and D_{blue} are listed in Table 6. For example, $\log n_e^{(1)} [\text{cm}^{-3}] = 10.3\text{--}11.5$, and $D_{\text{blue}}^{(1)} = 7.9 \times 10^7 \text{cm} - R_{\text{star}} (=2.0 \times 10^{10} \text{cm})$ for the upper limit $\epsilon_{\text{blue}}^{\text{H}\alpha}$ case of Flare Y6.

With the estimated surface area ($A_{\text{blue}}^{\text{H}\alpha}$) and geometrical thickness (D_{blue}) values, we can estimate the mass of the upward-moving plasma showing the blueshifted excess components (M_{blue}):

$$M_{\text{blue}} \sim A_{\text{blue}}^{\text{H}\alpha} D_{\text{blue}} n_{\text{H}} m_{\text{H}} \quad (14)$$

$$= A_{\text{blue}}^{\text{H}\alpha} \left(\frac{EM_{\text{blue}}}{n_e^2} \right) n_{\text{H}} m_{\text{H}} \quad (15)$$

$$= A_{\text{blue}}^{\text{H}\alpha} \left(\frac{EM_{\text{blue}}}{n_e} \right) \left(\frac{n_e}{n_{\text{H}}} \right)^{-1} m_{\text{H}}, \quad (16)$$

where n_{H} is the total hydrogen density, and m_{H} is the mass of hydrogen atom. Here, we roughly assume the prominence ionization fraction from Table 1 of Labrosse et al. (2010), and $i = n_e/n(\text{H}^0) \approx n(\text{H}^+)/n(\text{H}^0) = 0.2 - 0.9$, where $n(\text{H}^+)$ and $n(\text{H}^0)$ are the proton density and neutral hydrogen density, respectively. From this,

$$\frac{n_e}{n_{\text{H}}} = \left(\frac{n_e}{n(\text{H}^0)} \right) \left(\frac{n(\text{H}^0)}{n_{\text{H}}} \right) \quad (17)$$

$$= \left(\frac{n_e}{n(\text{H}^0)} \right) \left(\frac{n(\text{H}^0)}{n(\text{H}^0) + n(\text{H}^+)} \right) \quad (18)$$

$$\approx \left(\frac{n_e}{n(\text{H}^0)} \right) \left(\frac{n(\text{H}^0)}{n(\text{H}^0) + n_e} \right) \quad (19)$$

$$= i/(i + 1) \quad (20)$$

$$= 0.17 - 0.47. \quad (21)$$

Then, for example, the upper and lower limit of the prominence mass in the case of Flare Y6 are estimated as follows:

$$M_{\text{blue,upp}} \sim A_{\text{blue,upp}}^{\text{H}\alpha} \left(\frac{EM_{\text{blue,upp}}^{(1)}}{n_{e,\text{low}}^{(1)}} \right) \left(\left(\frac{n_e}{n_{\text{H}}} \right)_{\text{low}} \right)^{-1} m_{\text{H}} \quad (22)$$

²⁸ It is noted that the definition of emission measure for the H α emission here ($EM_{\text{blue}} = n_e^2 D$, from Heinzel et al. 1994a) is different from that for the X-ray emission in Section 4.4 ($EM = n^2 V$, where n is the electron density, and V is the volume, from Shibata & Yokoyama 2002).

$$\sim \left((6.9, +, 1.6), \times, 10^{19}, \right), \left(\frac{10^{31.2}}{10^{10.3}} \right), (0.17)^{-1} (1.7 \times 10^{-24}) \quad (23)$$

$$\sim 7.3 \times 10^{17} \text{ g}, \quad (24)$$

and

$$M_{\text{blue,low}} \sim A_{\text{blue,low}}^{\text{H}\alpha} \left(\frac{EM_{\text{blue,low}}^{(2)}}{n_{e,\text{upp}}^{(2)}} \right) \left(\left(\frac{n_e}{n_{\text{H}}} \right)_{\text{upp}} \right)^{-1} m_{\text{H}} \quad (25)$$

$$\sim \left((6.9, -, 1.6), \times, 10^{19}, \right), \left(\frac{10^{30.5}}{10^{11.5}} \right), (0.47)^{-1} (1.7 \times 10^{-24}) \quad (26)$$

$$\sim 1.9 \times 10^{15} \text{ g}. \quad (27)$$

It must be noted that there is an important assumption that we simply applied the solar prominence model of Heinzel et al. (1994a) for estimating the parameters (e.g., mass) of the upward-moving plasma (prominence eruptions) of M-dwarfs. It is assumed that the parameter space of the prominence plasma (e.g., density, temperature) is the same for the Sun and M-dwarfs. The models of Heinzel et al. (1994a) are computed for solar incident radiation (solar intensity and spectral energy distribution, and line profile shapes) and for a fixed height of 10,000 km above the solar surface. These model setups can be different between the Sun and M-dwarfs. The resulting prominence parameters can also depend crucially on the scattering of the incident radiation since the emission of solar prominence is dominated by this scattering process (see Section 2 of Heinzel et al. 1994a). Moreover, Heinzel et al. (1994a) do not calculate the models of erupting prominences but those of static prominences. This can also affect the calculation results because of the Doppler dimming and brightening effects (e.g., Heinzel & Rompolt 1987; Gontikakis et al. 1997). These effects affect different lines in different ways, and for example, the parameter α in Equation (12) can be affected.

It is then important to assess the reliability of the obtained values by conducting the calculation of erupting prominences of M-dwarfs. However, the discussions on prominence parameters (e.g., mass) in this study already include errors with 2 or 3 orders of magnitude with various other assumptions (e.g., prominence shapes), and we only conduct broad discussions over many orders of magnitude in the following (see Figure 47). So in this study, we only use the simple assumption of solar prominence model from Heinzel et al. (1994a), and the calculation of erupting prominences of M-dwarfs is beyond the scope of this study, considering the main focus of this paper is reporting the blue wing asymmetries from the huge campaign observations. We demonstrate that, as a next study, it is important to conduct the NLTE model calculations of eruption prominences in the M-dwarf stellar atmosphere (see Leitzinger et al. 2022) and reevaluate the prominence parameters (e.g., mass) more accurately.

We also estimated the kinetic energy of the upward-moving plasma showing the blueshifted excess components ($E_{\text{kin,upp}}$ and $E_{\text{kin,low}}$ in Table 6) from the velocity values of H α blue asymmetry components ($v_{\text{blue,fit}}^{\text{H}\alpha}$) and these mass values ($M_{\text{blue,upp}}$ and $M_{\text{blue,low}}$) listed in Table 6. When we estimate $E_{\text{kin,upp}}$ and $E_{\text{kin,low}}$ values here, we simply used the line-of-sight velocity value $v_{\text{blue,fit}}^{\text{H}\alpha}$ as we use the same method with our previous studies estimating kinetic energies using Doppler shift

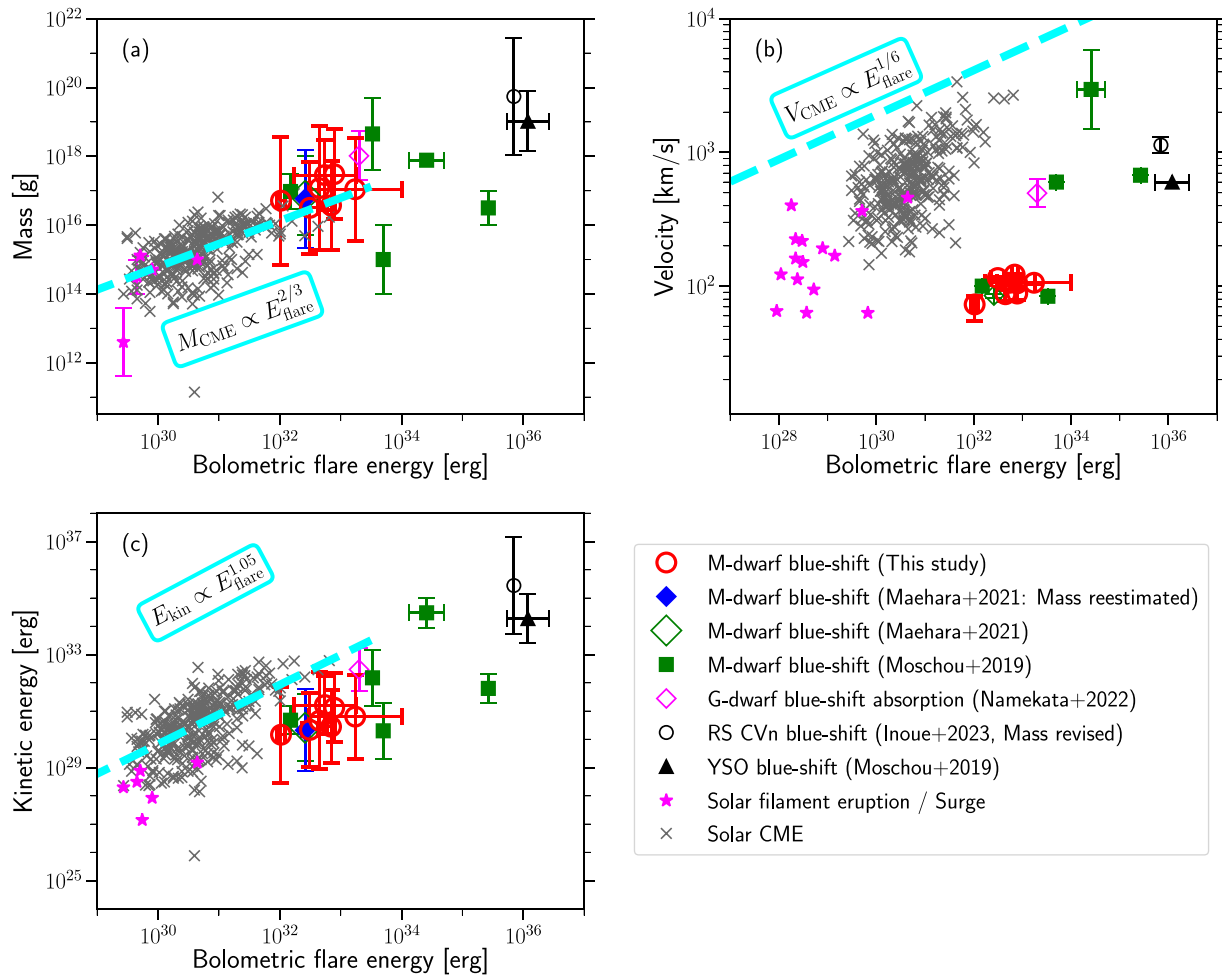


Figure 47. Mass, velocity, and kinetic energy as a function of flare bolometric energy, for solar and stellar flares and prominence eruptions and CMEs. (a) Mass of prominence eruptions and CMEs as a function of flare bolometric energy. Red open circles represent the seven blueshift (blue wing asymmetry) events on M-dwarfs (YZ CMi, EV Lac, ADLeo) reported in this study (Table 6). The blue filled diamond and the green open diamond are the blueshift event on M-dwarf YZ CMi reported in Maehara et al. (2021). The latter is the original data point, while the former is the data point with the mass value reestimated in this study. Green filled squares and the black filled upward triangle are blueshift events on M-dwarfs and a young stellar object (YSO), respectively, which are reported in Moschou et al. (2019). The pink open diamond represents the blueshift absorption event on the young Sun-like star EK Dra reported in Namekata et al. (2022c), while the black open filled circle denotes the blueshift event on the RS CVn type binary star reported in Inoue et al. (2023). It is noted that the mass value of Inoue et al. (2023) is slightly revised in this study as described in Section 4.3. Pink filled star marks correspond to filament eruptions and surges on the Sun taken from Namekata et al. (2022c), while gray crosses are CME events on the Sun taken from Yashiro & Gopalswamy (2009; see also Drake et al. 2013). We acknowledge that the data of Yashiro & Gopalswamy (2009) were provided through private communication with Dr. Seiji Yashiro. The cyan dashed line represents the relation $M_{\text{CME}} \propto E_{\text{flare}}^{2/3}$ shown by Takahashi et al. (2016), which is fitted to the solar CME data points in this figure. (b) Velocity of prominence eruptions and CMEs as a function of flare bolometric energy. Pink filled star marks represent the filament eruptions on the Sun from Seki et al. (2019), and the other symbols are the same as in (a). The scaling law denoted by the cyan dashed line ($V_{\text{CME}} \propto E_{\text{flare}}^{1/6}$) taken from Takahashi et al. (2016) was plotted to show the upper limit of CME speeds as a function of flare magnitude (see Equation (9) of Takahashi et al. 2016). (c) Kinetic energy of prominence eruptions and CMEs as a function of flare bolometric energy. Symbols are plotted in the same way as in (a). The scaling relation denoted by the cyan dashed line ($E_{\text{kin}} \propto E_{\text{flare}}^{1.05}$) is obtained from Namekata et al. (2022c), which is also fitted to the solar CME data points in this figure.

velocities (e.g., Maehara et al. 2021; Namekata et al. 2022c; Inoue et al. 2023). We must keep in mind the effects that the line-of-sight velocity is always smaller than or equal to the true velocity, and the $E_{\text{kin,upp}}$ values here cannot be true *upper limit* values, when we discuss the kinetic energy values in the following.

As also done in the previous studies (e.g., Moschou et al. 2019; Maehara et al. 2021; Namekata et al. 2022c; Inoue et al. 2023), these estimated mass ($M_{\text{blue}}^{\text{H}\alpha}$), velocity ($v_{\text{blue,fit}}^{\text{H}\alpha}$), and kinetic energy (E_{kin}) of the upward-moving plasma (or prominence eruptions) showing blue wing enhancements (blue wing asymmetries) can be discussed as a function of flare energy (Figure 47). In Figure 47, we use flare bolometric energy ($E_{\text{bol,flare}}$, see Osten & Wolk 2015) for more general

discussions, instead of GOES-band X-ray energy used in some previous studies (e.g., Moschou et al. 2019; Maehara et al. 2021).

We estimated the flare bolometric energies with the following two methods. We simply used both values to estimate the value ranges of bolometric energies. We note that both methods include several assumptions and/or ambiguities. For example, the earlier method relies on the ground-based (ARCSAT and LCO) photometric data including some data gaps in this study. The latter relies on the scaling law between $\text{H}\alpha$ and GOES X-ray band flare energies from Haisch (1989), which only used a small number of stellar flares. Moreover, the $\text{H}\alpha$ and GOES X-ray emission components consist of roughly up to a few percent of the total flare energy, and they are

emitted in the upper part of the stellar atmosphere (chromosphere and corona) while the dominant part of bolometric energy is emitted as WL emission from the lower atmosphere (e.g., Emslie et al. 2012; Osten & Wolk 2015). For more precise and accurate estimations of flare bolometric energies, more comprehensive multiwavelength observation data to estimate flare energies from X-rays to optical are important. This point should be kept in mind when discussing flare bolometric energies in the following, while we only conduct the order-of-magnitude discussions for flare energy values in Figure 47.

In the first method, we convert the flare energies in the u and U bands into bolometric energies assuming the energy partitions of Osten & Wolk (2015), since most of the flares in this study were observed in either u or U bands, and the flare amplitude S/N s in u or U bands are generally better than those in g or V bands in this study (see light-curve figures in Section 3). The fraction of U -band flare energy to the bolometric energy is $E_{U, \text{flare}}/E_{\text{bol,flare}} \sim 0.11$ (Table 2 of Osten & Wolk 2015). Then, assuming the luminosity ratio of U and u bands in Table 3, the fraction of u band to the bolometric energy is $E_{u, \text{flare}}/E_{\text{bol,flare}} \sim 0.09$.

The resultant energy values from this first method are listed as $E_{\text{bol,flare}}^{(1)}$ in Table 6. $E_{\text{bol,flare}}^{(1)}$ values of Flares Y23 and E2 were estimated to be $E_{\text{bol,flare}}^{(1)} = 1.8 \times 10^{33}$ and 1.2×10^{32} erg, respectively, from the observed $E_{u, \text{flare}}$ values, and that of Flare Y18 was to be $E_{\text{bol,flare}}^{(1)} = 4.2 \times 10^{32}$ erg from the observed $E_{U, \text{flare}}$ value. As for Flares Y3 and Y6, the upper limit of bolometric energies could be estimated to be $E_{\text{bol,flare}}^{(1)} < 6.2 \times 10^{32}$ and $< 8.0 \times 10^{32}$ erg from the observed upper limit of $E_{u, \text{flare}}$ value. As for Flare A3, only the lower limit of bolometric energy was estimated to be $E_{\text{bol,flare}}^{(1)} > 3.0 \times 10^{32}$ erg from the observed lower limit of $E_{u, \text{flare}}$, since the flare already started when the observation started. Flare E1 did not have simultaneous photometric data.

In the second method, we convert the GOES-band X-ray (1.5–12.4 keV = 1–8 Å range, $E_{\text{Xray,flare}}$ (GOES band)) into bolometric energies ($E_{\text{bol,flare}}$) assuming the energy partitions of Osten & Wolk (2015) ($E_{\text{Xray,flare}}$ (GOES band) = $0.06E_{\text{bol,flare}}$ in Table 2 therein). As for Flare Y3, the GOES-band X-ray energy estimated from NICER X-ray spectra in Section 3.2 is used here ($E_{\text{Xray,flare}}$ (GOES band) = 4.7×10^{31} erg). As for the other flares without NICER X-ray data in this study, the GOES-band X-ray energy was converted from the $H\alpha$ flare energy ($E_{H\alpha, \text{flare}}$), using the empirical relationship between $H\alpha$ and GOES-band soft X-ray flare energies in Figure 2 and Equation (1) of Haisch (1989). The resultant energy values from this first method are listed as $E_{\text{bol,flare}}^{(2)}$ in Table 6.

Using the bolometric energies estimated with these two methods ($E_{\text{bol,flare}}^{(1)}$ and $E_{\text{bol,flare}}^{(2)}$), the resultant $E_{\text{bol,flare}}$ values are estimated and shown in Table 6 and in Figure 47. As for Flares Y6, Y18, Y23, and E2, the ranges of $E_{\text{bol,flare}}$ values are estimated by simply taking the value differences of $E_{\text{bol,flare}}^{(1)}$ and $E_{\text{bol,flare}}^{(2)}$. As for Flare Y3, we only used $E_{\text{bol,flare}}^{(2)}$ for $E_{\text{bol,flare}}$ value, since the estimated upper limit value of $E_{\text{bol,flare}}^{(1)}$ is smaller than $E_{\text{bol,flare}}^{(2)}$. As for Flare E1, only $E_{\text{bol,flare}}^{(2)}$ is used for $E_{\text{bol,flare}}$ value since there were no photometric data. As for Flare A3, $E_{\text{bol,flare}}^{(1)}$ is used for the lower limit of $E_{\text{bol,flare}}$ value. The upper limit of $E_{\text{bol,flare}}$ is set to be 10^{34} erg, very roughly assuming that the total flare energy is not larger than 1 order of

magnitude larger than the limit $E_{\text{bol,flare}}^{(2)} > 8.2 \times 10^{32}$ erg in the second method from the available $H\alpha$ observation data.

In Figure 47, the bolometric energies of solar events (the pink filled star marks and gray crosses) are plotted, assuming the energy conversion from GOES X-ray band to bolometric energy for solar flares: $E_{\text{GOES}} = 0.01E_{\text{bol,flare}}$ (Emslie et al. 2012; Osten & Wolk 2015). As for the data from Namekata et al. (2022c), Inoue et al. (2023), the bolometric energy values estimated in these papers are used in Figure 47.

As for the event from Maehara et al. (2021; listed as “M2021” in Table 5), we estimated to be $E_{\text{bol,flare}} = 2.6 \times 10^{32}$ erg from their reported $H\alpha$ flare energy ($E_{H\alpha} = 4.7 \times 10^{30}$ erg) on the basis of the above second method using the scaling relation of Haisch (1989).²⁹ It is noted Maehara et al. (2021) included the TESS data, but this event did not show clear WL emission and can be categorized as an NWL flare.

The bolometric energies of the stellar blueshift events from Moschou et al. (2019; including the event “V2016” in Table 5) are plotted in Figure 47, assuming the energy conversion relation from GOES X-ray band energy to bolometric energy $E_{\text{GOES}} = 0.06E_{\text{bol,flare}}$, which is the scaling relation for active stars in Osten & Wolk (2015).

Moschou et al. (2019) originally included the events observed from X-ray absorptions, but only the events detected by blueshifts of chromospheric lines are plotted in Figure 47 for simple comparison with blueshift events reported in this study.

In addition, the mass value of the M-dwarf blueshift event of Maehara et al. (2021) is reestimated to be 2.2×10^{15} – 1.5×10^{18} g (blue filled diamonds in Figures 47(a) and (c)), by assuming the $F_{\text{blue}}^{H\alpha}$ range from the 7 M-dwarf events in this study ($\log F_{\text{blue}}^{H\alpha} [\text{erg s}^{-1} \text{cm}^{-2} \text{sr}^{-1}] = 5.9$ – 6.4) and using the almost the same estimation method as in this study. Only the difference of the method with this study is that we assume the $F_{\text{blue}}^{H\alpha}$ range, since Maehara et al. (2021) only had $H\alpha$ data, and we cannot determine $F_{\text{blue}}^{H\alpha}$ value from the relation of $F_{\text{blue}}^{H\alpha}$ and $F_{\text{blue}}^{H\beta}$ (see Figure 46). The mass value of the blueshift event of the RS Canum Venaticorum (CVn)-type star from our previous paper, Inoue et al. (2023), is also slightly revised from 9.5×10^{17} – 1.4×10^{21} to 1.1×10^{18} – 2.7×10^{21} g. This is because, in Inoue et al. (2023), although we used the same basic equations with this study (see Equation 16), we mistakenly assumed $n_e/n_H = n_e/n(H^0) = 0.2$ – 0.9 , which is incorrect. The correct value is $n_e/n_H = 0.17$ – 0.47 (see Equation (21)), and the resultant mass value range is slightly affected (the lower limit value becomes double). The overall discussions do not change since there were already a larger range of values.

As we can see in Figure 47(b), the maximum observed line-of-sight velocities of the 7 blueshift (blue wing asymmetry) events reported in this study ($v_{\text{blue,fit}}^{H\alpha}$) range from 73 to 122 km s^{−1}. These values are in the same range of solar filament and prominence eruptions associated with CMEs (10–400 km s^{−1} in Gopalswamy et al. 2003; see also the pink star marks in Figure 47(b)). These values are also roughly comparable to the M-dwarf blueshift event from Maehara et al.

²⁹ Maehara et al. (2021) reported $E_{\text{GOES}} = 8 \times 10^{31}$ erg (see also Figure 10 therein). However, the X-ray band luminosity in the 0.04–2.0 keV band is not a proper GOES bandpass energy (see Equation (5) of Maehara et al. 2021 and Equation (1) of Moschou et al. 2019). The correct value is $E_{\text{GOES}} = 4.4 \times 10^{30}$ erg using the $E_{\text{GOES}}-E_{H\alpha}$ scaling relation of Haisch (1989). It is then noted that the relative location in the x -axis between the data of Maehara et al. (2021) and those of other events (e.g., the events from Moschou et al. 2019) is a bit changed in Figure 47 from Figure 10 of Maehara et al. (2021), although overall order-of-magnitude discussions are not affected.

(2021; the green open diamond mark) and some of the events from Moschou et al. (2019; the green filled square marks). In addition, the velocities of M-dwarf blue wing asymmetries from the other papers (Vida et al. 2019; Muheki et al. 2020a; Muheki et al. 2020b) are also in the similar ranges (e.g., the observed maximum velocities of M-dwarf blue wing asymmetries are $100\text{--}300\text{ km s}^{-1}$ in Vida et al. 2019).

It has been discussed whether blue wing asymmetries on M-dwarfs cause stellar CMEs (Vida et al. 2016; Moschou et al. 2019; Vida et al. 2019; Muheki et al. 2020b; Maehara et al. 2021).

The blue wing velocities have been compared with escape velocities, as one potential interpretation that the observed velocities are relatively slow (e.g., Moschou et al. 2019; Vida et al. 2019; Muheki et al. 2020b). For example, the velocities of blueshift events ($73\text{--}122\text{ km s}^{-1}$) in this study are smaller than the escape velocities at the stellar surface ($\sim 600\text{ km s}^{-1}$ for YZ CMi, EV Lac, and AD Leo). However, this cannot simply lead to the conclusion that the plasma is not ejected from the star, as the blueshift events only provide the lower limit of the velocities and as summarized in the following, based on the relevant discussions and similar interpretations in previous papers (e.g., Moschou et al. 2019; Vida et al. 2019; Maehara et al. 2021; Namekata et al. 2022c). Gopalswamy et al. (2003) showed that the average CME core velocity ($\sim 350\text{ km s}^{-1}$) and average CME velocity ($\sim 610\text{ km s}^{-1}$) are ~ 4 and ~ 8 times larger than that of the associated prominence eruptions ($\sim 80\text{ km s}^{-1}$). This indicates that prominences with initial slow speeds are accelerated as they are lifted up, and they evolve into CMEs. However, this indicates that, if we assume similar acceleration mechanism would work,³⁰ these prominence eruptions would be accelerated into $\sim 300\text{--}1000\text{ km s}^{-1}$. This value is generally larger than the escape velocities at $\sim 2\text{--}3 R_{\text{star}}$ ($\sim 300\text{--}450\text{ km s}^{-1}$), and the prominence eruptions with the velocity of $\sim 100\text{ km s}^{-1}$ could evolve into CMEs. Moreover, the observed blueshift velocities are line-of-sight velocities, and the radial velocities of prominence eruptions can be larger considering the projection angle effect, which suggests that these prominence eruptions could evolve into CMEs with faster velocities. In addition, it is noted that red-wing enhancements were observed during some flares with blue wing asymmetries (especially late-phase red wing asymmetry during Flare Y6) as summarized in Section 4.2, which indicates that some of the materials fell back to the stellar surface. This phenomenon is often observed in the case of solar filament and/or prominence eruptions even in the case that they evolve into CMEs (Wood et al. 2016; Namekata et al. 2022c; Otsu et al. 2022).

The erupted masses of the 7 blueshift events are estimated to be $M_{\text{blue}}^{\text{H}\alpha} \sim 10^{15}\text{--}10^{19}\text{ g}$ (Table 6). We note that some blueshift events have long durations (e.g., $\Delta t_{\text{H}\alpha}^{\text{blueasym}} \sim 2\text{ hr}$ in the case of Flares Y6 and A3), and it could be speculated that these events were observed as superpositions of multiple consecutive flare events (see models of sympathetic eruptions as in Török et al. 2011; Lynch & Edmondson 2013; Lynch et al. 2016). This

might cause the underestimate of mass since we only used the data at the peak of the continuous blue wing asymmetry events, and more detailed studies are necessary in the future. In another point, we assumed the theoretical calculation results of Heinzel et al. (1994a) for the mass estimation process (e.g., Figure 46), but this is only the calculation for solar prominences.

As described in the earlier part of this subsection, this could significantly affect the reliability of the results presented here, and it is important to conduct the NLTE model calculations of prominences in the M-dwarf stellar atmosphere for more accurate mass estimations in the future (see Leitzinger et al. 2022). Although there is a very large range of uncertainty of the mass estimation method, Figure 47(a) shows that these estimated mass of the 7 blueshift events are roughly on the relation expected from solar CMEs (the cyan line in Figure 47(a)), and are roughly on the same relation with other stellar events in the previous studies (Moschou et al. 2019; Maehara et al. 2021; Namekata et al. 2022c). In addition, Vida et al. (2019) reported the masses from M-dwarf blue wing asymmetries are $10^{15}\text{--}10^{18}\text{ g}$, and this range is roughly the same as that of the 7 events in this study. These results might suggest that these possible prominence eruptions on M-dwarfs could share a common underlying mechanism with solar filament and/or prominence eruptions and CMEs (i.e., magnetic energy release; Aarnio et al. 2012; Drake et al. 2013; Takahashi et al. 2016; Kotani et al. 2023), although the large uncertainty of the mass estimation method should be considered.

In contrast, Figure 47(c) shows that kinetic energies of the 7 blueshift events ($E_{\text{kin}} \sim 10^{29}\text{--}10^{32}\text{ erg}$ in Table 6) are roughly 2 orders of magnitude smaller than the relation expected from solar CMEs (the cyan line in Figure 47(c)), as also indicated in the previous studies (Maehara et al. 2021; Namekata et al. 2022c).

First, it is noted that these small kinetic energies can be at least partly affected by the fact that the Doppler velocities measured from spectra are always the lower limits of real velocities because of projection effects. Moreover, these small kinetic energies can be also understood through a solar analogy. As described above, the velocities of filament and/or prominence eruptions are 4–8 times lower than the corresponding CMEs (e.g., Gopalswamy et al. 2003), and the kinetic energies of filament and/or prominence eruptions are typically smaller (the pink filled star marks in Figure 47(c)). Therefore, the kinetic energy for stellar events estimated from the velocity of M-dwarf blueshift events would be 1–2 orders of magnitude smaller than the solar CME trend (Maehara et al. 2021; Namekata et al. 2022c).

However, it is still not clear whether the prominence eruptions on M-dwarfs can really cause CMEs. Recent numerical studies (e.g., Drake et al. 2016; Alvarado-Gómez et al. 2018; Sun et al. 2022) have discussed that CMEs would be suppressed by the strong overlying magnetic fields. Zeeman Doppler Imaging (ZDI) observations in Morin et al. (2008) suggested that the mid-M-dwarf flare stars investigated in this study (YZ CMi, EV Lac, and AD Leo) have mainly axisymmetric large-scale poloidal fields. In the case of these three stars, the magnetic energy in dipole mode accounts for 56%–75% of the whole magnetic energy, and such large-scale and strong dipole magnetic fields may cause the suppression or deceleration of CMEs. In one possibility, the small kinetic energies that the 7 blueshift events shown in Figure 47(c) could be explained by the deceleration by the overlying magnetic

³⁰ We note that, although this assumption on the acceleration can be certainly possible on the basis of the solar observations and/or models of prominence eruptions and CMEs (e.g., Otsu et al. 2022), this can be also only speculation, considering that the acceleration is not (or cannot be) observed within the available observational data set of Balmer lines in this paper. Future observations of blueshifts simultaneously with other CME detection methods may help create more understanding (see the brief remark in the later part of this subsection).

fields (e.g., Alvarado-Gómez et al. 2018; Moschou et al. 2019). The recent paper Bellotti et al. (2023) reported that AD Leo still showed mainly axisymmetric large-scale poloidal fields in 2019 April–June, when Flare A3 was observed, while the numerical CME modeling incorporating the ZDI results (see Alvarado-Gómez et al. 2018) is beyond the scope of this paper (a future research topic). There were no reported ZDI magnetic field observations during our campaign for the other 6 blueshift events (on YZ CMi and EV Lac), and we do not know how the real magnetic topologies were when we observed these 6 blueshift events, since magnetic field topologies can change with time (Morin et al. 2008; Bellotti et al. 2023). Then, in the future, it is important to conduct more simultaneous flare campaign and magnetic field observations. In addition, future observations of blueshifts simultaneously with other CME detection methods (e.g., UV/X-ray dimmings as in Veronig et al. 2021; Loyd et al. 2022; radio bursts as in Zic et al. 2020) may help whether and how prominence eruptions detected as blueshifts of chromospheric lines could be evolved into CMEs, since different methods could be sensitive to different phases of the CME evolution (e.g., Figure 1 of Namekata et al. 2022b).

Mass, velocity, and kinetic energy of the possible prominence eruptions of M-dwarfs shown in Figure 47 could eventually lead to understanding the statistical properties of M-dwarf CMEs with more observational samples in the future, although it is still not clear whether they can really cause CMEs. This would help us to evaluate the effects of CMEs on exoplanets orbiting around M-dwarfs (e.g., loss of atmosphere, atmospheric chemistry, radiation dose; see Lammer et al. 2007; Segura et al. 2010; Scheucher et al. 2018; Tilley et al. 2019; Yamashiki et al. 2019; Airapetian et al. 2020; Chen et al. 2021; Grayver et al. 2022). Furthermore, it has been discussed that stellar mass loss from filament and/or prominence eruptions and CMEs could significantly affect the evolution of stellar mass and angular momentum loss (Osten & Wolk 2015; Cranmer 2017; Odert et al. 2017; Vidotto 2021; Wood et al. 2021), and more observational samples of prominence eruptions would provide more insights in the case of M-dwarfs.

4.4. Coronal Parameters from NICER Soft X-Ray Data and Implications for Flare Emission Process

Soft X-ray emission during a stellar flare is caused by the chromospheric evaporation process, which is coronal plasma filling of coronal magnetic loops (e.g., Güdel et al. 2004; Shibata & Magara 2011). Soft X-ray spectroscopic and photometric data can help us to investigate the physical parameters of coronal plasma and magnetic loops such as temperature, loop length, electron density, magnetic field strength (e.g., Shibata & Yokoyama 2002; Osten et al. 2006; Raassen et al. 2007; Pillitteri et al. 2022).

Flare Y3, which showed blue wing asymmetry of Balmer lines, was observed also in NICER soft X-ray data as described in Section 3.2. The temperature (T) and EM ($EM = n^2V$) values of the quiescent (nonflaring) and flare components are estimated from the model fitting of X-ray spectra (Figures 12(e) and 13), and the resultant values are listed in Table 7. Here, n is the electron density, and V is the volume. Shibata & Yokoyama (1999, 2002) discussed the scaling laws of T and EM for solar and stellar flares on the basis of the magnetic reconnection model, which considers the energy balance between conduction cooling and reconnection heating (see Shibata & Magara 2011 for review). The scaling laws derived by Shibata & Yokoyama

Table 7

Coronal Parameters of Flare Y3 (on YZ CMi) from NICER Soft X-Ray Data

Coronal Temperature (T) and Emission Measure ($EM = n^2V$)		
Quiescent (preflare) phase	$T_1 = 3.1 \times 10^6$ K	$EM_1 = 1.8 \times 10^{51}$ cm $^{-3}$
	$T_2 = 1.1 \times 10^7$ K	$EM_2 = 9.4 \times 10^{50}$ cm $^{-3}$
Flare peak	$T = 1.1 \times 10^7$ K	$EM = 2.2 \times 10^{51}$ cm $^{-3}$
Coronal magnetic field (B) and loop length (L)		
$n_0 = 10^{11}$ cm $^{-3}$	$B \sim 50$ G	$L \sim 1.4 \times 10^{10}$ cm $= 0.66R_{\text{star}}$
$n_0 = 10^{12}$ cm $^{-3}$	$B \sim 100$ G	$L \sim 5.5 \times 10^9$ cm $= 0.26R_{\text{star}}$
$n_0 = 10^{13}$ cm $^{-3}$	$B \sim 200$ G	$L \sim 2.2 \times 10^9$ cm $= 0.10R_{\text{star}}$

Note. n_0 is the preflare coronal density. $R_{\text{star}} = 0.30R_{\odot}$ (Table 1).

(2002) show that the flare magnetic field strength (B) and characteristic length of the flare loop (L) can be expressed in terms of the flare EM ($EM = n^2V$), the preflare coronal electron density (n_0), and flare temperature (T):

$$B = 50 \left(\frac{EM}{10^{48} \text{ cm}^{-3}} \right)^{-1/5} \left(\frac{n_0}{10^9 \text{ cm}^{-3}} \right)^{3/10} \left(\frac{T}{10^7 \text{ K}} \right)^{17/10} \text{ G}, \quad (28)$$

$$L = 10^9 \left(\frac{EM}{10^{48} \text{ cm}^{-3}} \right)^{3/5} \left(\frac{n_0}{10^9 \text{ cm}^{-3}} \right)^{-2/5} \left(\frac{T}{10^7 \text{ K}} \right)^{-8/5} \text{ cm}. \quad (29)$$

Here, simple order-of-magnitude estimates are used, and the emitting volume is given by $V = L^3$. This simple method derived by Shibata & Yokoyama (2002) was validated with Sun-as-a-star observations and can estimate the loop length and magnetic field strength with an accuracy of a factor of 3 (Namekata et al. 2017a). As we have shown in Figure 12, the temperature and EM of the flare component at the peak of Flare Y3 are $T = 1.1 \times 10^7$ K, and $EM = 2.2 \times 10^{51}$ cm $^{-3}$ (Table 7). The X-ray spectrum of quiescent (preflare) phase was well fitted with the two temperature components: $T_1 = 3.1 \times 10^6$ K, and $T_2 = 1.1 \times 10^7$ K. The hot quiescent plasma temperature (T_2) is close to the Y3 flare peak temperature. It is also higher than the hot quiescent plasma temperature reported in the earlier XMM-Newton observation of YZ CMi (~ 0.64 keV $= 7.4 \times 10^6$ K), while the EM is similar to the quiescent emission during the XMM-Newton observation (Raassen et al. 2007). This result may suggest that the preflare phase contains emission from the decay of a previous flare.

Since there were no simultaneous grating X-ray line observations that can be used for estimating preflare densities in our NICER data, we use the previous measurements of quiescent electron densities n_0 of a dMe flare star similar to the target star YZCMi (dM4e flare star). Osten et al. (2006) measured electron densities of the quiescent atmosphere of the d3.5 me flare star EV Lac using transition region and coronal lines. Their measurements indicate nearly constant electron densities ($n \sim 10^{11}$ cm $^{-3}$) between $T = 10^{5.2}$ and $10^{6.4}$ K, while, at higher coronal temperatures, there is a sharp increase of 2 orders of magnitude in density ($n \sim 10^{13}$ cm $^{-3}$ at $T = 10^{6.9} - 10^{7.0}$ K) (see Figure 9 therein). Taking into account the measured preflare temperature values ($T_1 = 3.1 \times 10^6$ K, and $T_2 = 1.1 \times 10^7$ K in the above) and the results of

Osten et al. (2006), we consider three cases of preflare densities of $n_0 = 10^{11}$, 10^{12} , and 10^{13} cm^{-3} when we estimate magnetic field B and loop length L values from Equations (28) and (29). With the flare peak temperature and EM $T = 1.1 \times 10^7 \text{ K}$, and $\text{EM} = 2.2 \times 10^{51} \text{ cm}^{-3}$ in the above, B and L values are estimated to be $B \sim 50 \text{ G}$ and $L \sim 1.4 \times 10^{10} \text{ cm} = 0.66 R_{\text{star}}$, if $n_0 = 10^{11} \text{ cm}^{-3}$. R_{star} is the radius of the target star YZ CMi (Table 1). $B \sim 100 \text{ G}$ and $L \sim 5.5 \times 10^9 \text{ cm} = 0.26 R_{\text{star}}$, if $n_0 = 10^{12} \text{ cm}^{-3}$, and $B \sim 200 \text{ G}$ and $L \sim 2.2 \times 10^9 \text{ cm} = 0.10 R_{\text{star}}$, if $n_0 = 10^{13} \text{ cm}^{-3}$. They are listed in Table 7.

These estimated values ($B = 50\text{--}200 \text{ G}$, and $L = 2.2 \times 10^9\text{--}1.4 \times 10^{10} \text{ cm} = 0.10\text{--}0.66 R_{\text{star}}$; Table 7) can be compared with the estimation results of previous studies. First, our result suggests that flare loop length is at least larger than $L \sim 0.10 R_{\text{star}}$, and this is roughly consistent with the result of Maehara et al. (2021). They estimated that at least 10%–20% of stellar surface of YZ CMi would be covered by starspots on the basis of the rotational modulations of TESS and ground-based photometric data. Moreover, Maehara et al. (2021) also discussed the statistical relation of flare energy and duration from optical flares observed by TESS, and estimated the B and L values of YZ CMi (Figure 14 therein), by using the method based on the magnetic reconnection model proposed by Namekata et al. (2017b). As a result, the B and L values estimated from NICER X-ray data ($B = 50\text{--}200 \text{ G}$, and $L = 2.2 \times 10^9\text{--}1.4 \times 10^{10} \text{ cm}$) in this study are roughly in the range of those from flare duration statistics of TESS data in Maehara et al. (2021).³¹ The consistency among different methods can support the validity of the method used in this study. In addition, the derived loop length is similar to the estimated length of a flare observed from YZ CMi with the EUVE satellite in 1994 ($0.14\text{--}0.50 R_{\text{star}}$, Mullan et al. 2006). This paper also reported a gigantic flare with a loop length of $1.1\text{--}1.5 R_{\text{star}}$ from the star.

The B and L values estimated in this study would be helpful for future modeling studies discussing the blue wing asymmetries of M-dwarf flares. These values can be helpful for modeling how the prominences erupt associated with flares (see Shibata & Magara 2011; Fan 2018) and cause blue wing asymmetries of Balmer lines. For example, the loop lengths can be closely related with the timescale of flares (Maehara et al. 2015; Reep & Airapetian 2023), and coronal magnetic field strength can be a factor that determines the CME evolution (e.g., Alvarado-Gómez et al. 2018; Sun et al. 2022). Moreover, this kind of X-ray observation has been still very limited for blue wing asymmetry events: for example, a flare on M5.5 dwarf CN Leo in Fuhrmeister et al. (2008), Liefke et al. (2010), that on M5.5 dwarf Proxima Centauri reported in Fuhrmeister et al. (2011), and that on K-dwarf AB Dor in Lalitha et al. (2013). It is necessary to increase the number of X-ray observations of blue asymmetry flares for further statistical discussions.

In this subsection, we assumed preflare coronal electron density of YZ CMi $n_0 = 10^{11}\text{--}10^{13} \text{ cm}^{-3}$. This is orders of

magnitude larger than that of the Sun $n_{0,\odot} \sim 10^9\text{--}10^{10} \text{ cm}^{-3}$ (e.g., Shibata & Yokoyama 2002; Allred et al. 2005).

Such higher preflare coronal density is also expected for M-dwarfs from the theoretical point of view because photospheric density of M-dwarfs is higher than that of the Sun (Sakaue & Shibata 2021). In order to predict the preflare coronal density more consistently, we need to develop a multicoronal loop model extending the method considered by Takasao et al. (2020). Higher preflare coronal density can be discussed with the propagation of nonthermal electron beam along the coronal loop, which are important to understand strong WL emission of M-dwarf flares (e.g., Allred et al. 2006; Namekata et al. 2020).

Then, we conducted simple calculations to determine the stopping lengths for high-energy electrons in M-dwarf preflare corona of various electron densities. In these calculations, we integrated the analytic formula from Holman et al. (2011), Holman (2012):

$$\frac{dE}{dl} = -0.150 \left(\frac{\Lambda_{ee}}{23} \right) n_{10} \left(\frac{20}{E} \right) [\text{keV Mm}^{-1}] \quad (30)$$

for initial energy E_0 (see Figure 48), where l is the path length, E is the kinetic energy of the electron in keV, n_{10} is the ambient electron density in units of 10^{10} cm^{-3} , and Λ_{ee} is the Coulomb logarithm (e.g., Allred et al. 2015).

Figure 48 shows the contour of stopping lengths for monoenergetic electron beams in constant density fully ionized slabs. This simple calculation result shown in Figure 48 suggests that a significant (or at least some) fraction of the electron beams can be stopped in high density (e.g., $n_0 \gtrsim 10^{11} \text{ cm}^{-3}$) preflare coronal loop, especially for soft power-law distributions of the electron beams with $\delta \gtrsim 7$. We note that these simple monoenergetic calculations very roughly appropriate very “soft” power-law distributions of the electron beams with the spectral index $\delta \gtrsim 7$, which are often determined in solar flare hard X-ray observations (e.g., Milligan et al. 2014; Thalmann et al. 2015; Warmuth & Mann 2016; Kowalski et al. 2019). For the hard power-law case of $\delta \sim 3\text{--}5$ and low-energy cutoff $\gg 10 \text{ keV}$, there would be enough high-energy electrons to penetrate the dense coronae and produce continuum radiation in the chromosphere and/or photosphere. This calculation result in Figure 48 can be consistent with the fact that Flare Y3 does not show clear WL emission (see Table 5), and may suggest absence of strong electron beams (e.g., F13 beam in Kowalski 2016) for this NWL flare. This might also suggest that thermal conduction heating can largely contribute to causing chromospheric line emissions and soft X-ray emission during Flare Y3 (e.g., Hori et al. 1997). However, there could be other explanations of the cause of NWL flares (see Watanabe et al. 2017), and more detailed calculations (e.g., density stratification along the loop, power-law distributions of electron energies) as done in recent radiative hydrodynamic calculations (e.g., RADYN calculations; Allred et al. 2006; Namekata et al. 2020; Kowalski et al. 2022) are necessary for detailed quantitative discussions. The brief discussion in this section also suggests detailed investigations of coronal densities using X-ray high resolution spectra (e.g., Güdel 2004; Osten et al. 2006; Pillitteri et al. 2022) are important as a next-step study for understanding WL emission of M-dwarf flares with and without chromospheric line wing asymmetries.

³¹ Bicz et al. (2022) derived relatively larger loop length values ($L = 10^{10}\text{--}10^{11} \text{ cm}$) and smaller magnetic field values ($B = 15\text{--}45 \text{ G}$) from the duration statistics of TESS data, although they also used the same scaling relation proposed by Namekata et al. (2017b) as done in Maehara et al. (2021). This difference can be caused by the definition of flare duration: they defined total duration as flare duration and applied it into the same scaling relation of Namekata et al. (2017b), but the coefficient of the original scaling relation of Namekata et al. (2017b) is determined with the e-folding decay time (not flare “total” duration) of solar flares. We note that, because of this, the larger loop length and smaller magnetic field values were estimated in Bicz et al. (2022).

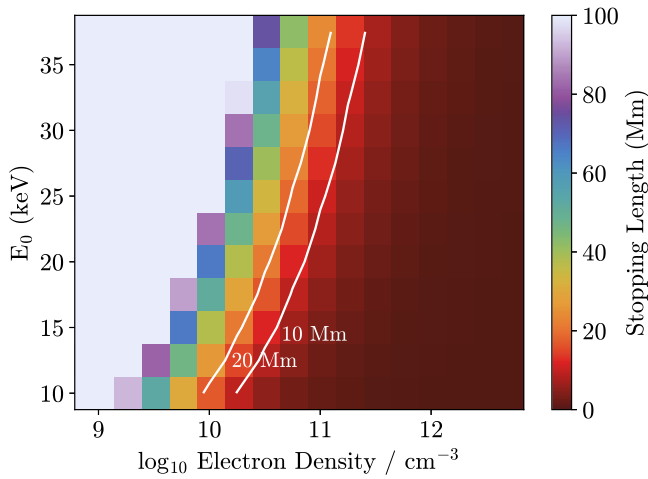


Figure 48. Contour of stopping lengths for monoenergetic electron beams with initial kinetic energy E_0 in constant density slabs (fully ionized). Two white lines show the stopping lengths of 10 and 20 Mm.

In addition, we also note that stellar flare energy partitions among different wavelengths (e.g., WL, X-ray, $H\alpha$) have been discussed in several recent observational studies (Osten & Wolk 2015; Guarcello et al. 2019; Paudel et al. 2021; Stelzer et al. 2022). In particular, it is interesting to compare optical WL energy partitions in the case of stellar flares to big solar flares (Emslie et al. 2012; Cliver et al. 2022). From this point of view, NWL flares like this Flare Y3 can be interesting, since they were not incorporated well in the discussions of the above previous studies. For example, in the case of Flare Y3, X-ray energy is larger than TESS-band WL and $H\alpha$ energies ($E_{X(0.5-2.0\text{ keV})} = 2.6 \times 10^{32}$ erg, $E_{\text{TESS}} < 2.6 \times 10^{32}$ erg, and $E_{H\alpha} = 1.7 \times 10^{31}$ erg).

It could also be interesting to note that the location of the flares (e.g., limb darkening effect) could also affect the observed energy partitions (Woods et al. 2006). In future studies, it is important to discuss this point statistically with a much larger number of multiwavelength data of WL flares and NWL flares.

4.5. Additional Notable Properties Other Than Blue Asymmetries

In addition to blue wing asymmetries, the 41 flares detected in this study also showed various notable properties. Clear red wing asymmetries (enhancements of red wing of $H\alpha$ line) were also observed in at least 11 flares among the total 41 flares (these flares are marked with “R” in Table 4). Flares Y6, Y17, and E5 in Section 3.3, Appendices A.7, and A.13 are remarkable examples of flares with red wing asymmetries among these 11 flares. One possible cause of the red wing asymmetries is the process called chromospheric condensations, which is the downward flow of cool plasma in the chromosphere (e.g., Ichimoto & Kurokawa 1984; Longcope 2014; Graham & Cauzzi 2015; Kowalski et al. 2017). Another possible cause is the flare-driven coronal rain or the post-flare loop (e.g., Antolin 2020; Wu et al. 2022; Wollmann et al. 2023). Flares Y8, E5, and A2 showed $H\alpha$ and $H\beta$ symmetric line broadenings with $\gtrsim 300\text{--}400\text{ km s}^{-1}$, accompanied by large WL flares (see Appendices A.3, A.13, and A.18). These broadenings can be caused by high-energy nonthermal electron beams penetrating into the lower atmosphere (e.g., Oks & Gershberg 2016; Namekata et al. 2020;

Kowalski et al. 2022). In particular, Flare E5 (in Appendix A.13) can be the most interesting since this flare showed both red wing asymmetries and broad symmetric broadenings accompanied by large WL flares. These additional notable properties are important topics of stellar flares, and these flares will be discussed in detail in our future papers.

As described in the above, our flare data also include a large number of light curves of various chromospheric lines (e.g., $H\alpha$, $H\beta$, $H\gamma$, $H\delta$, Ca K, Ca II 8542, Na I D1 and D2, He I D3) whose line formation heights are different (e.g., Vernazza et al. 1981; Heinzel 2019). In some (or many) cases, different chromospheric lines evolve differently. For example, during Flare Y3, which also showed blue wing asymmetries, $H\alpha$ and Ca II K evolved similarly while other Balmer lines, Ca II 8542, Na I D1 and D2, and He I D3 lines decayed faster (Figure 8). These differences can provide us clues to investigate temperature and density evolution of the chromosphere during flares (e.g., time decrement of Balmer lines; e.g., Hawley & Pettersen 1991; Kowalski et al. 2013), and it is important to compare with radiative hydrodynamic modeling results as well as solar flare observation results. These points will also be investigated more in our future papers.

In addition to flares, Figures 2–7 show that the $H\alpha$ and $H\beta$ EW values of the quiescent phase (nonflare phase) exhibit some variabilities among the observation dates. In particular, Figures 3(a) and (b) show some quasi-periodic modulations of $H\alpha$ and $H\beta$ EW values, and this could be related with the rotational modulations (Toriumi et al. 2020; Maehara et al. 2021; Namekata et al. 2022d; Schöfer et al. 2022), considering the YZ CMi’s rotation period of 2.77 days (Table 1). This topic is being highlighted in recent studies, including possible relations with flare activities. Maehara et al. (2021) suggested that the amplitude of rotational modulations of YZ CMi in the $H\alpha$ line can change depending on the difference in flare activity (flare frequency) during each observation run. In contrast, Schöfer et al. (2022) showed there were no clear periodic rotational modulations in $H\alpha$ line of YZ CMi and EV Lac, while the photometric indexes (e.g., TiO 7050 Å index, TESS photometry) of them showed clear periodic modulations. These modulations of chromospheric lines in the quiescent phase (nonflare phase) will also be discussed more in detail in our future papers possibly with more data set.

5. Summary and Conclusions

We conducted the time-resolved simultaneous optical spectroscopic and photometric observations of mid-M-dwarf flare stars YZ CMi, EV Lac, and AD Leo. High-dispersion spectroscopic observations were obtained using APO 3.5 m and CTIO/SMARTS 1.5 m telescopes, and various chromospheric lines ($H\alpha$, $H\beta$, $H\gamma$, $H\delta$, $H\epsilon$, Ca II H&K, Ca II 8542, He I D3, and Na I D1 and D2 lines) were investigated. As a result, 41 flares (Flares Y1–Y29 on YZ CMi, Flares E1–E9 on EV Lac, and Flares A1–A3 on AD Leo) were detected (Table 4) during the 31 nights over 2 yr (2019 January–2021 February). The energy ranges of the observed 41 flares are $10^{30}\text{--}10^{32}$ erg in the $H\alpha$ line, and $10^{30}\text{--}10^{33}$ erg in u - and g -band continuum bands (Figure 36). Among the 41 flares, seven flares (Flares Y3, Y6, Y18, Y23, E1, E2, and A3) showed clear blue wing asymmetries in $H\alpha$ line. There are various correspondences in flare properties (e.g., durations of blue wing asymmetries, intensities of WL emissions, blue wing asymmetries in various chromospheric

lines) as listed in Tables 5 and 6, and the key findings of this study are as follows.

- (i) The duration of the $H\alpha$ blue wing asymmetries range from 20 minutes to 2.5 hr (Table 5). As a notable example, Flare Y3 showed short-lived $H\alpha$ blue wing asymmetries twice (20 minutes \times 2) during the $H\alpha$ flare over 4 hr (Figure 10). In contrast, Flares Y23, E1, and A3 showed continuous $H\alpha$ blue wing asymmetries over almost all the observed phases of the flares (Figures 26, 30, and 34). As another notable point, the velocities of blue wing asymmetries showed gradual decays during Flares Y6 and Y23 (Figures 16 and 26). In particular, Flare Y6 showed the gradual shift from blue wing asymmetry to red wing asymmetry, during the $H\alpha$ flare over 4.9 hr (Figure 16).
- (ii) Among the seven flares with blue wing asymmetries, two flares (Flares Y3 and Y6) are categorized as candidate NWL flares, and three flares (Flares Y18, Y23, and E2) are clearly WL flares (Table 5), while the remaining two flares (Flares E1 and A3) do not have enough data coverage of simultaneous spectroscopic and photometric data to judge whether they are WL or NWL flares. For reference, among all the 41 flares, 4 flares are categorized as candidate NWL flares, and 31 flares are clear WL flares (Table 5), while the remaining 6 flares do not have enough data coverage of simultaneous spectroscopic and photometric data. These results can suggest that blue wing asymmetries of chromospheric lines can be commonly seen both during WL and candidate NWL flares.
- (iii) All of the seven flares showed blue wing asymmetries also in the $H\beta$ line, but there is a large variety in which other chromospheric lines showed blue wing asymmetries ([B] and [NB] in Table 5). For example, two flares (Flares Y6 and E2) showed blue wing asymmetries only in lower-order Balmer lines (up to $H\beta$ and $H\gamma$ lines, respectively). In contrast, the other two flares (Flares Y23 and A3) showed blue wing asymmetries in almost all the chromospheric lines (except for Ca II 8542 and Na I D1 and D2, respectively). The velocities of blue wing enhancements are different among different lines, and the lower-order Balmer lines especially the $H\alpha$ line tend to show larger velocities of blue wing asymmetries, while higher-order Balmer lines, Ca II lines, Na I D1 and D2, and He I D3 lines show smaller velocities ($v_{\text{blue,max}}$ in Table 6). It is speculated that these differences can be caused by the differences of optical depth and line wing broadening physics, but observation-based modeling studies incorporating radiative transfer physics (e.g., Leitzinger et al. 2022) and a comparison with solar flare data are necessary for further quantitative discussions.
- (iv) The line-of-sight velocities of the blue wing excess components (blue wing asymmetries) are estimated to range from -73 to -122 km s^{-1} ($v_{\text{blue,fit}}^{H\alpha}$ in Table 6), and these are in the same range of solar prominence/filament eruptions (Figure 47(b)). These velocity values ($73\text{--}122 \text{ km s}^{-1}$) represent possible prominence eruptions of M-dwarfs, and they are smaller than the escape velocities at the stellar surface ($\sim 600 \text{ km s}^{-1}$ for YZ CMi, EV Lac, and AD Leo). The prominence eruptions could evolve into CMEs, assuming that the similar acceleration mechanism from prominence eruptions to

- CMEs on the Sun would work also in these M-dwarf cases (see also (vii) for the necessity of further investigations).
- (v) Assuming the relation from the NLTE slab model calculation of solar prominences (Heinzel et al. 1994a), the surface flux densities of the upward-moving plasma causing blueshifts are estimated from the luminosity ratio of blue wing asymmetry components in $H\alpha$ and $H\beta$ lines (see Figure 46). Using these values, the erupted mass of the seven blueshift (blue wing asymmetry) events are estimated to be $M_{\text{blue}}^{H\alpha} \sim 10^{15}\text{--}10^{19} \text{ g}$ (Table 6). These estimated mass of the seven blueshift events are roughly on the relation expected from solar CMEs, and are roughly on the same relation with other stellar events in the previous studies (Figure 47(a)). This might suggest that these possible prominence eruptions on M-dwarfs could share a common underlying mechanism with solar filament and/or prominence eruptions and CMEs (i.e., magnetic energy release), although the large uncertainty of the mass estimation method should be considered.
- (vi) In contrast, the kinetic energies of the seven blueshift events ($E_{\text{kin}} \sim 10^{29}\text{--}10^{32} \text{ erg}$ in Table 6) are roughly 2 orders of magnitude smaller than the relation expected from solar CMEs (Figure 47(c)), as also shown in previous studies. These small kinetic energies can be understood if we assume the velocity difference/evolution of prominence eruptions and CMEs.
- (vii) The mass, velocity, and kinetic energy of the possible prominence eruptions of M-dwarfs in this study (Figure 47) could eventually lead to understanding the statistical properties of M-dwarf CMEs with more observational samples in the future. However, it is still not clear whether the prominence eruptions on M-dwarfs can really cause CMEs (e.g., possible suppression by overlying magnetic field), as discussed in Section 4.3. Further investigations are also necessary for understanding the observed various properties of blue wing asymmetries. Future observations of blueshifts simultaneously with other CME detection methods (e.g., UV/X-ray dimmings as in Veronig et al. 2021; Loyd et al. 2022; radio bursts as in Zic et al. 2020) are important to investigate whether and how prominence eruptions detected as blueshifts of chromospheric lines could be evolved into CMEs.
- (viii) One flare (Flare Y3) was also observed with NICER soft X-ray data, which enabled us to estimate the flare magnetic field and length of the flare loop of a flare with blue wing asymmetry in chromospheric lines. The coronal temperature (T) and EM values are estimated from the model fitting of soft X-ray spectra (Table 7). Using the simple scaling law of T and EM (Shibata & Yokoyama 2002), the flare magnetic field strength (B) and characteristic length of the flare loop (L) are estimated to be $B = 50\text{--}200 \text{ G}$, and $L = 2.2 \times 10^9\text{--}1.4 \times 10^{10} \text{ cm} = 0.10\text{--}0.66 R_{\text{star}}$ (Table 7). The B and L values estimated in this study would be helpful for future modeling studies discussing blue wing asymmetries of M-dwarf flares.
- (ix) The preflare coronal density value of $n_0 = 10^{11}\text{--}10^{13} \text{ cm}^{-3}$ is assumed to interpret the soft X-ray data of this Flare Y3. A significant (or at least some) fraction of the electron beams can be stopped in such a high density (e.g., $n_0 > 10^{11} \text{ cm}^{-3}$) preflare coronal loop (Figure 48), especially for soft power-law distributions of the electron beams with $\delta \gtrsim 7$. This could be consistent with the fact

that this Flare Y3 did not show clear WL emission. It should be also noted that, in the case of this Flare Y3, soft X-ray energy dominates WL and $H\alpha$ energies ($E_X(0.5\text{--}2.0\text{ keV}) = 2.6 \times 10^{32}\text{ erg}$, $E_{\text{TESS}} < 1.8 \times 10^{31}\text{ erg}$, and $E_{H\alpha} = 1.7 \times 10^{31}\text{ erg}$).

- (x) In addition to blue wing asymmetries, our flare data of this study also showed various notable properties, as summarized in Section 4.5. For example, clear red wing asymmetries (enhancements of red wing of $H\alpha$ line) were also observed in at least 11 flares among the total 41 flares, while three flares showed symmetric line broadenings with $>300\text{--}400\text{ km s}^{-1}$ accompanied by large WL flares. These topics will be discussed in detail in our future papers.

Acknowledgments

The authors thank the anonymous referee for the detailed and constructive comments, which improved the whole paper very much. We acknowledge Dr. Seiji Yashiro for providing the solar CME data. This work was supported by JSPS (Japan Society for the Promotion of Science) KAKENHI grant Nos. 21J00106 (Y.N.), 20K04032, 20H05643 (H.M.), 21J00316 (K.N.), and 21H01131 (H.M., S.H., K.I., D.N., K.S.), and Japan Science and Technology Agency (JST) CREST grant No. JPMJCR1761 (K.I.). A.F.K. and Y.N. acknowledge support from NASA ADAP award program No. 80NSSC21K0632. Y.N. was supported by JSPS Overseas Research Fellowship Program, and JSPS Postdoctoral Research Fellowship Program. K.N. was supported by JSPS Postdoctoral Research Fellowship Program. K.H. was supported by NASA under award No. 80GSFC21M0002. We also acknowledge the International Space Science Institute and the supported International Team 464, “The Role Of Solar And Stellar Energetic Particles On (Exo)Planetary Habitability (ETERNAL, <http://issibern.ch/teams/exoeternal/>)”; and Team 510, “Solar Extreme Events: Setting Up a Paradigm (SEESUP, <https://issibern.ch/teams/solextremeevent/>).”

In this study, we used the observation data obtained with the Apache Point Observatory (APO) 3.5 and 0.5 m telescopes, which are owned and operated by the Astrophysical Research Consortium. We are grateful to APO 3.5 m observing specialists (Candace Gray, Jack Dembicky, Russet McMillan, Theodore Rudyk, and David DeColibus) and other staff members of Apache Point Observatory for their contributions in carrying out our observations. We used APO observation time allocated to the University of Colorado (CU) and the University of Washington (UW). We appreciate CU and UW members for their help to plan our observations. This research also used data from the SMARTS 1.5 m telescope at Cerro Tololo Inter-American Observatory (CTIO), and this telescope is operated as part of the SMARTS Consortium. We appreciate the SMARTS Principal Scientist Todd Henry and the other staff members for their large contributions in carrying out our observations. This research makes use of observations from the Las Cumbres Observatory (LCO) global telescope network. We used the LCO observation time allocated to the University of Colorado. This paper includes data collected with the TESS mission, obtained from the Mikulski Archive for Space Telescopes (MAST) at the Space Telescope Science Institute (STScI). The specific observations analyzed can be accessed via doi:[10.17909/rv7c-zn98](https://doi.org/10.17909/rv7c-zn98). Funding for the TESS mission is provided by the NASA Explorer Program. STScI is operated by the Association of Universities for

Research in Astronomy, Inc., under NASA contract NAS 5-26555. NICER analysis software and data calibration were provided by the NASA NICER mission and the Astrophysics Explorers Program. This research also has made use of the Spanish Virtual Observatory (SVO) Filter Profile Service (<http://svo2.cab.inta-csic.es/theory/fps/>) supported from the Spanish MINECO through grant AYA2017-84089.

Facilities: ARC, CTIO:1.5m, LCOGT, TESS, NICER.

Appendix

Flare Light Curves and $H\alpha$ and $H\beta$ Spectra of the Observation Dates When Blue Wing Asymmetries Were Not Detected

In this appendix, we describe the detailed flare light curve and flare $H\alpha$ and $H\beta$ spectra from the observation dates when blue wing asymmetries were not detected (see Section 3.1 and Table 4). Additional notable properties seen in these flares other than blue wing asymmetries are briefly summarized in Section 4.5 and will be discussed in detail in future papers.

A.1. Flare Y1 Observed on 2019 January 26

On 2019 January 26, a flare (Flare Y1) was detected in $H\alpha$ and $H\beta$ lines as shown in Figure 49(a). During this Flare Y1, the $H\alpha$ and $H\beta$ EWs increased up to 10.1 Å and 15.5 Å, respectively, and the flare duration in $H\alpha$ ($\Delta t_{H\alpha}^{\text{flare}}$) is 1.5 hr (Table 4). In addition to the enhancements in Balmer emission lines, the continuum brightness observed by ARCSAT g band and TESS increased by $\sim 100\%$ and $\sim 3\%$, respectively (Figures 49(b) and (c)). We note that there were no ARCSAT u -band data during Flare Y1 since we only took g -band data for most of the time because of unstable weather on that date. Flare Y1 was not identified in NICER X-ray data since the flare occurred during the observation gap caused by the orbital period of ISS (Figure 49(d)). We estimated L_g , L_{TESS} , E_g , E_{TESS} , $L_{H\alpha}$, $L_{H\beta}$, $E_{H\alpha}$, and $E_{H\beta}$ values, and they are listed in Table 4 (see Section 2.5 for the estimation method).

Figures 50 and 51 show the $H\alpha$ and $H\beta$ line profiles during Flare Y1. We could not see any significant line wing asymmetries during this flare. We can see clear line-wing broadening of the $H\alpha$ and $H\beta$ line profiles ($H\alpha$, $\pm 150\text{ km s}^{-1}$; $H\beta$, $\pm 200\text{--}250\text{ km s}^{-1}$), which is especially seen around the flare peak time (see the time [1] in Figures 49–51). We note that, as for the $H\alpha$ and $H\beta$ lines, the larger enhancements in the line wings contributed to a bigger total EWs at [1] than [2], while the peak intensities at the line centers are smaller at [1] than at [2] (Figures 49 and 50).

A.2. Flares Y4 and Y5 Observed on 2019 January 28

On 2019 January 28, two flares (Flares Y4 and Y5) were detected in $H\alpha$ and $H\beta$ lines as shown in Figure 52(a). During Flare Y4, the $H\alpha$ and $H\beta$ EWs increased up to 12.1 Å and 19.1 Å, respectively, and $\Delta t_{H\alpha}^{\text{flare}}$ is 1.0 hr (Table 4). In addition to the enhancements in Balmer emission lines, the continuum brightness observed by ARCSAT u and g bands and TESS increased by $\sim 70\%$, $\sim 4\text{--}5\%$, and $\sim 0.5\%$, respectively, during Flare Y4 (Figures 52(b) and (c)). During Flare Y5, the $H\alpha$ and $H\beta$ EWs increased up to 9.9 Å and 14.9 Å, respectively, and $\Delta t_{H\alpha}^{\text{flare}}$ is 1.3 hr (Table 4). The continuum brightness increase observed by ARCSAT u and g bands and TESS during Flare Y5 is not clear compared with Flare Y4 ($3\sigma_u = 15\%$, $3\sigma_g = 2.3\%$, and $3\sigma_{\text{TESS}} = 0.29\%$), although

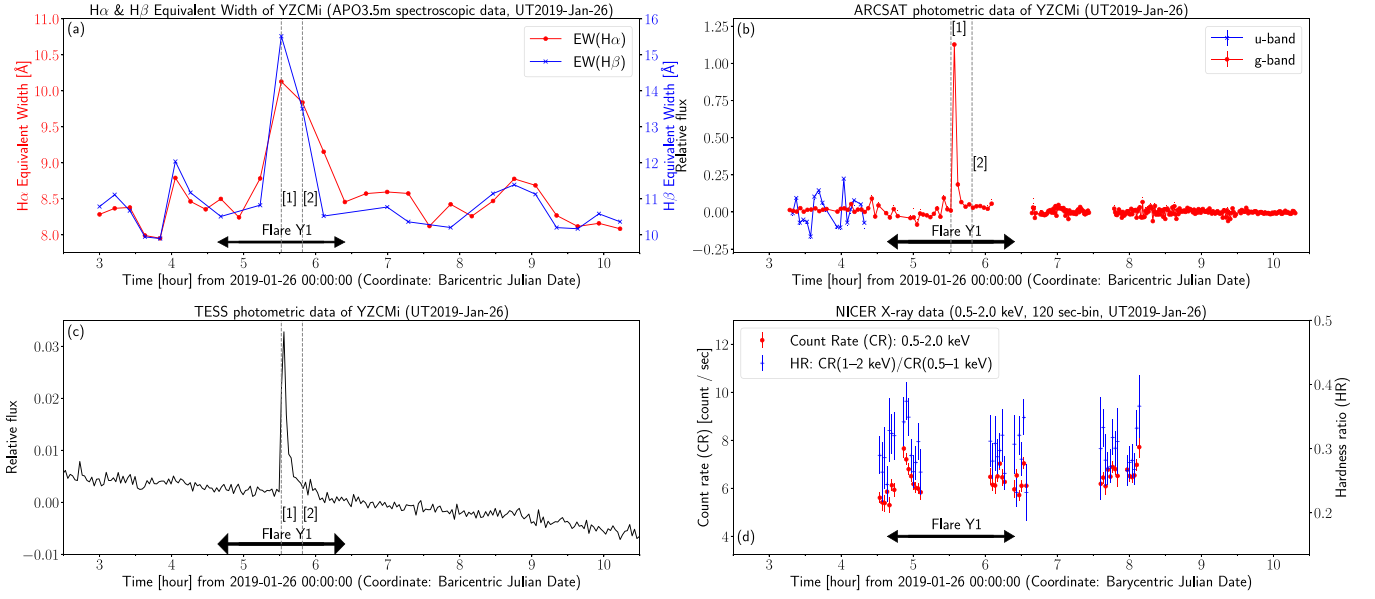


Figure 49. Light curves of YZ CMi on 2019 January 26 showing Flare Y1, which are plotted similarly with Figures 8(a)–(d). The gray dashed lines with numbers ([1], [2]) correspond to the time shown with the same numbers in Figures 50 and 51.

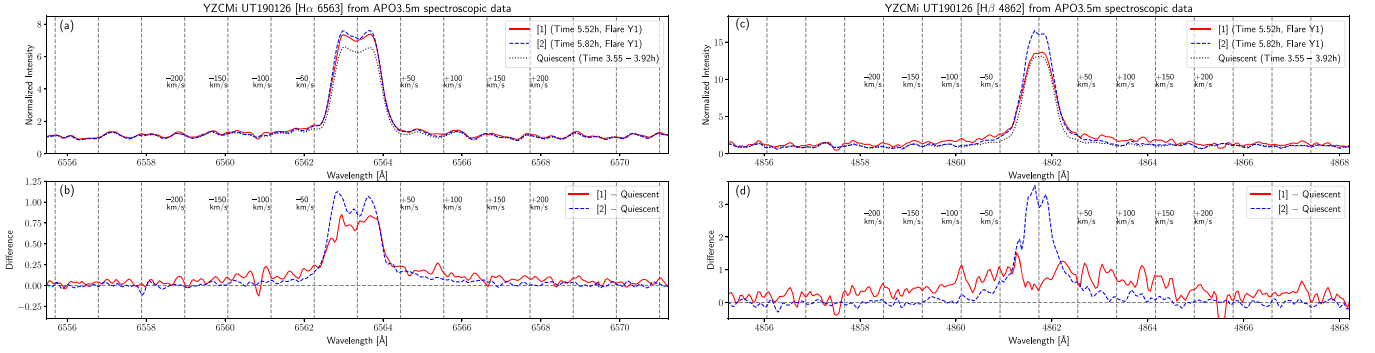


Figure 50. Line profiles of the $H\alpha$ and $H\beta$ emission lines during Flare Y1 (at the time [1] and [2]) on 2019 January 26 from APO 3.5 m spectroscopic data, which are plotted similarly with Figure 9.

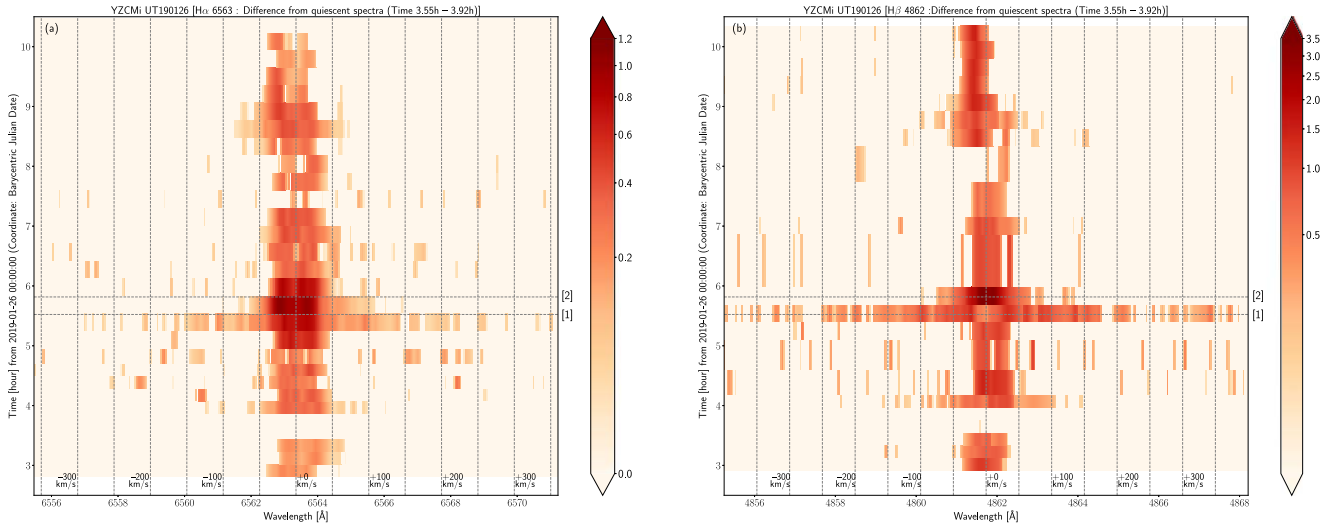


Figure 51. Time evolution of the $H\alpha$ and $H\beta$ line profiles covering Flare Y1 on 2019 January 26, which are shown similarly with Figure 10. The gray horizontal dashed lines indicate the time [1] and [2], which are shown in Figures 49 (light curves) and 50 (line profiles).

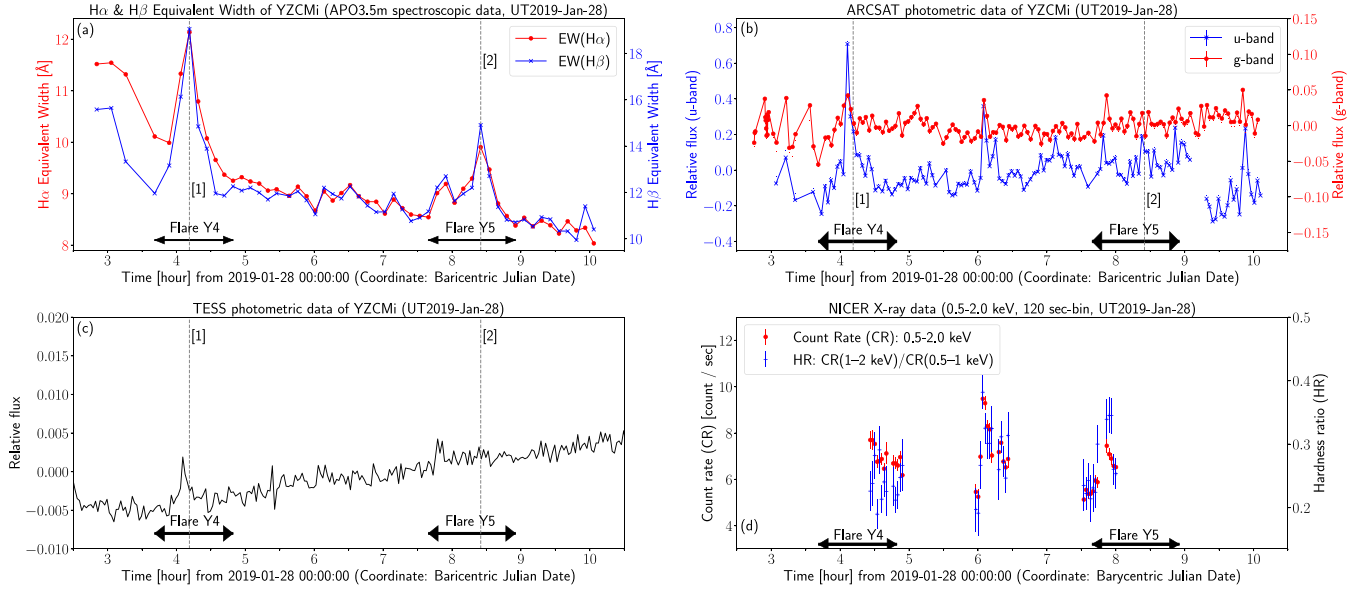


Figure 52. Light curves of YZ CMi on 2019 January 28 showing Flares Y4 and Y5, which are plotted similarly with Figures 8(a)–(d). The gray dashed lines with numbers ([1], [2]) correspond to the time shown with the same numbers in Figures 53 and 54.

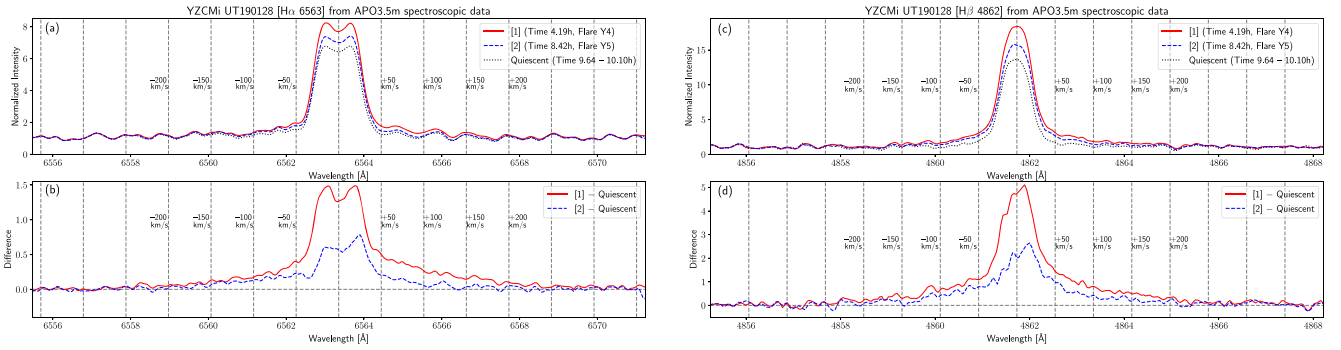


Figure 53. Line profiles of the $H\alpha$ and $H\beta$ emission lines during Flares Y4 and Y5 (at the time [1] and [2]) on 2019 January 28 from APO 3.5 m spectroscopic data, which are plotted similarly with Figure 9.

there might exist a small increase around the time 7.8–8.0 hr (Figures 52(b) and (c)).

Both the peaks of Flares Y4 and Y5 in $H\alpha$ and $H\beta$ lines were in the gaps of the NICER X-ray observation, and we cannot identify the X-ray emission from these flares in NICER X-ray data (Figure 52(d)). L_g , L_{TESS} , E_g , E_{TESS} , $L_{H\alpha}$, $L_{H\beta}$, $E_{H\alpha}$, and $E_{H\beta}$ values are estimated and listed in Table 4.

The $H\alpha$ and $H\beta$ line profiles during Flares Y4 and Y5 are shown in Figures 53 and 54. At around the peak time of Flare Y4, we can see line-wing broadening (from -150 – 200 to $+200$ – 250 km s^{-1}), and the red wing was slightly enhanced compared with the blue wing (red wing asymmetry; the time [1] in Figures 52–54). This slight red wing asymmetry is seen in both $H\alpha$ and $H\beta$ lines.

A.3. Flares Y7 and Y8 Observed on 2020 January 14

On 2020 January 14, two flares (Flares Y7 and Y8) were detected in $H\alpha$ and $H\beta$ lines as shown in Figures 55(a) and (c). During Flare Y7, the $H\alpha$ and $H\beta$ EWs increased up to 10.0 Å and 14.7 Å, respectively, and the flare duration in $H\alpha$ $\Delta t_{H\alpha}^{\text{flare}}$ is 2.9 hr (Table 4). In addition to the enhancements in Balmer emission lines, the continuum brightness observed with ARCSAT u and g bands increased by $\sim 40\%$ and $\sim 4\%$,

respectively, associated with the $H\alpha$ and $H\beta$ emissions of Flare Y7 (Figures 55(b) and (d)). As for Flare Y8, the $H\alpha$ and $H\beta$ EWs increased up to 18.0 Å and 37.8 Å, respectively, but only the initial 0.4 hr of the flare was observed (Figures 55(a) and (c)). In addition to these enhancements in Balmer emission lines, the continuum brightness observed with ARCSAT u and g bands increased by $\sim 4000\%$ and $\sim 400\%$, respectively (Figures 55(b) and (d)) during the observed initial phase of the flare.

L_u , L_g , E_u , E_g , $L_{H\alpha}$, $L_{H\beta}$, $E_{H\alpha}$, and $E_{H\beta}$ values are estimated and listed in Table 4. We note that the flare energy values of Flare Y8 listed here are only the lower limit and are expected to be much smaller than the real total energy values, since only the initial 0.4 hr data of the flare were observed.

The $H\alpha$ and $H\beta$ line profiles during Flares Y7 and Y8 are shown in Figures 56 and 57. During Flare Y7, the blue wing of $H\alpha$ line could be slightly enhanced (up to -200 km s^{-1}) only at around the time [1], while the red wing could be slightly enhanced (up to $+250$ – 300 km s^{-1}) at around the time [2] (Figures 56(b), and 57(a)). Since the blue wing enhancement was so small, we cannot judge that this flare shows clear blue wing asymmetry. In the later phase of Flare Y7 (around time [3] and [4]), the wing enhancements of the $H\alpha$ line profile were

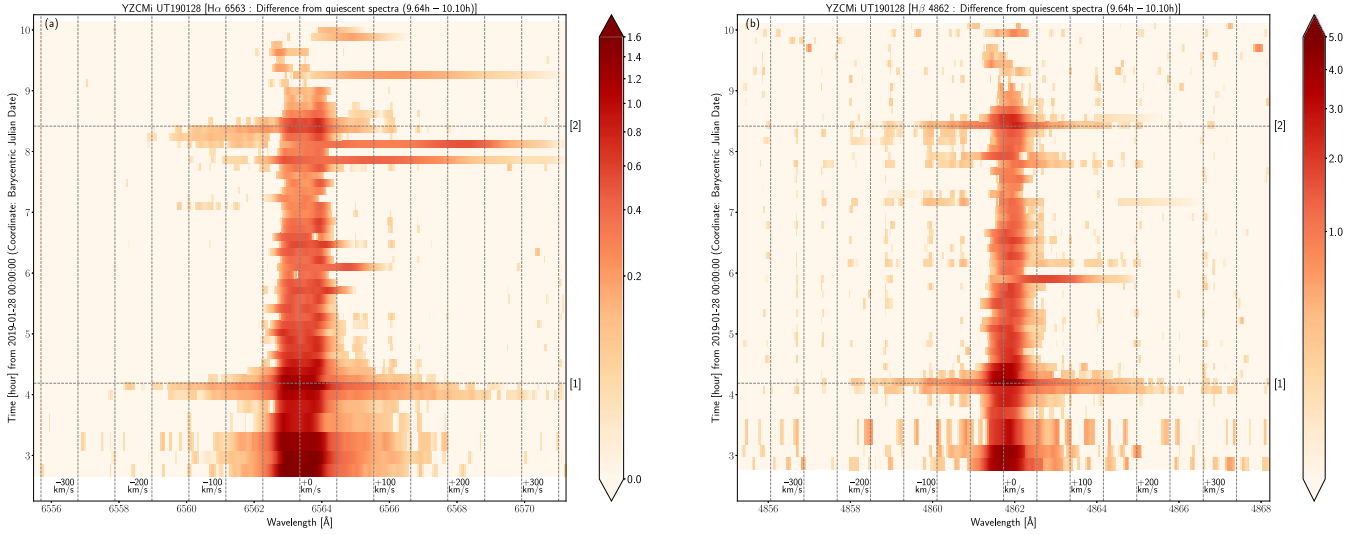


Figure 54. Time evolution of the $H\alpha$ and $H\beta$ line profiles covering Flares Y4 and Y5 on 2019 January 28, which are shown similarly with Figure 10. The gray horizontal dashed lines indicate the time [1] and [2], which are shown in Figures 52 (light curves) and 53 (line profiles).

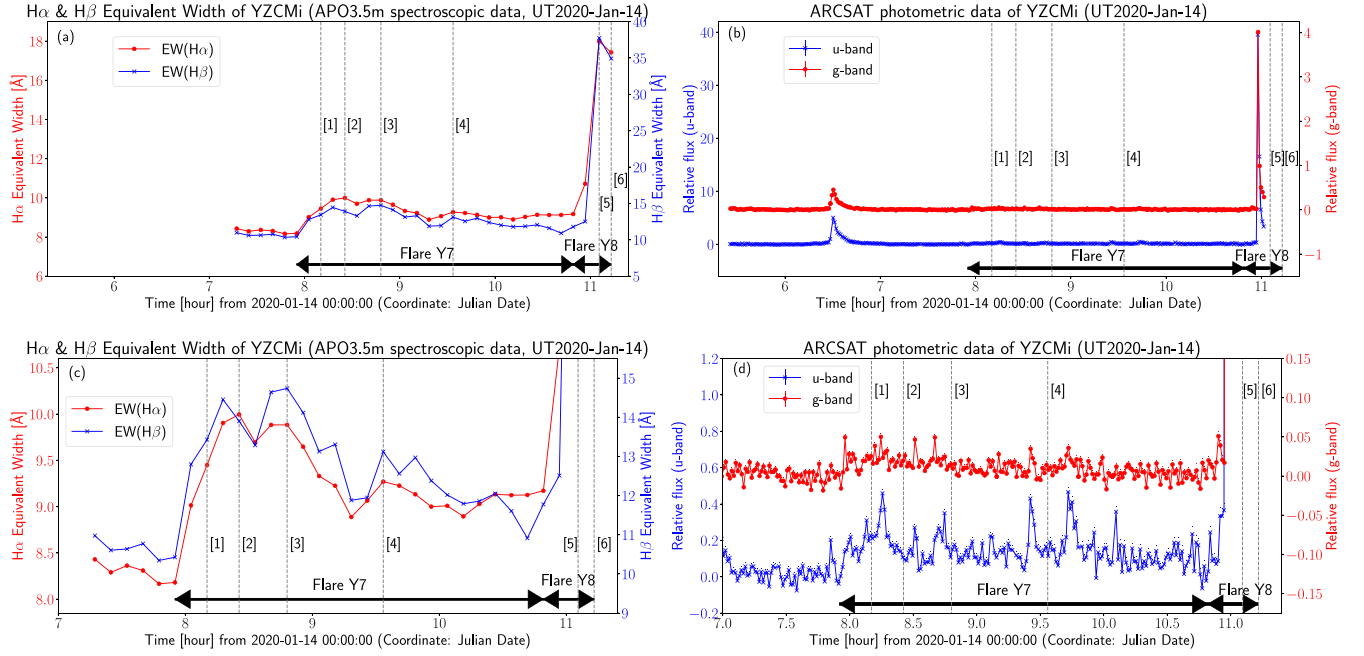


Figure 55. (a) and (b) Light curves of YZ CMi on 2020 January 14 showing Flares Y7 and Y8, which are plotted similarly with Figures 14(a) and (b). The gray dashed lines with numbers ([1]–[6]) correspond to the time shown with the same numbers in Figures 56 and 57. (c) and (d) Enlarged panels of (a) and (b).

weaker while the line center enhancement continued over 2 hr (Figures 56(f), and 57(a)). A similar time evolution was seen also in the $H\beta$ line, but the line wing asymmetries at around the time [1] and [2] were unclear compared with those of $H\alpha$ line (Figures 56(d), and 57(b)). As for Flare Y8, only the initial phase of the flare was observed, but probably the flare peak in $H\alpha$ and $H\beta$ lines was observed. Both $H\alpha$ and $H\beta$ line profiles show remarkable and symmetric line wing enhancements (± 250 – 300 km s^{-1} for $H\alpha$ line and ± 300 – 350 km s^{-1} for $H\beta$ line) (Figures 56(j), (l) and 57). There was the continuum intensity enhancement during the flare, but the peak of the continuum intensity could be a few minutes earlier than the peak of $H\alpha$ and $H\beta$ line EWs (Figures 55(a) and (b)).

We also note that, as for the $H\alpha$ and $H\beta$ lines, the larger enhancements in the line wings contributed to a bigger total

EWs at [5] than [6], while the peak intensities at the line centers are smaller at [5] than at [6] (Figures 55 and 56).

A.4. Flares Y9, Y10, and Y11 Observed on 2020 January 16

On 2020 January 16, three flares (Flares Y9, Y10, and Y11) were detected in $H\alpha$ and $H\beta$ lines as shown in Figure 58(a). Flare Y9 already started when the observation started. The $H\alpha$ and $H\beta$ EWs decreased from 11.9 \AA and 21.3 \AA , respectively, and the flare duration in $H\alpha$ $\Delta t_{H\alpha}^{\text{flare}}$ is $>1.7 \text{ hr}$ (Table 4). In addition to the enhancements in Balmer emission lines, the continuum brightness observed with LCO U and V bands increased at least by $\sim 250\%$ and $\sim 45\%$, respectively, associated with Flare Y9 before the $H\alpha$ and $H\beta$ observation started (Figure 58(b)). We note the continuum brightness

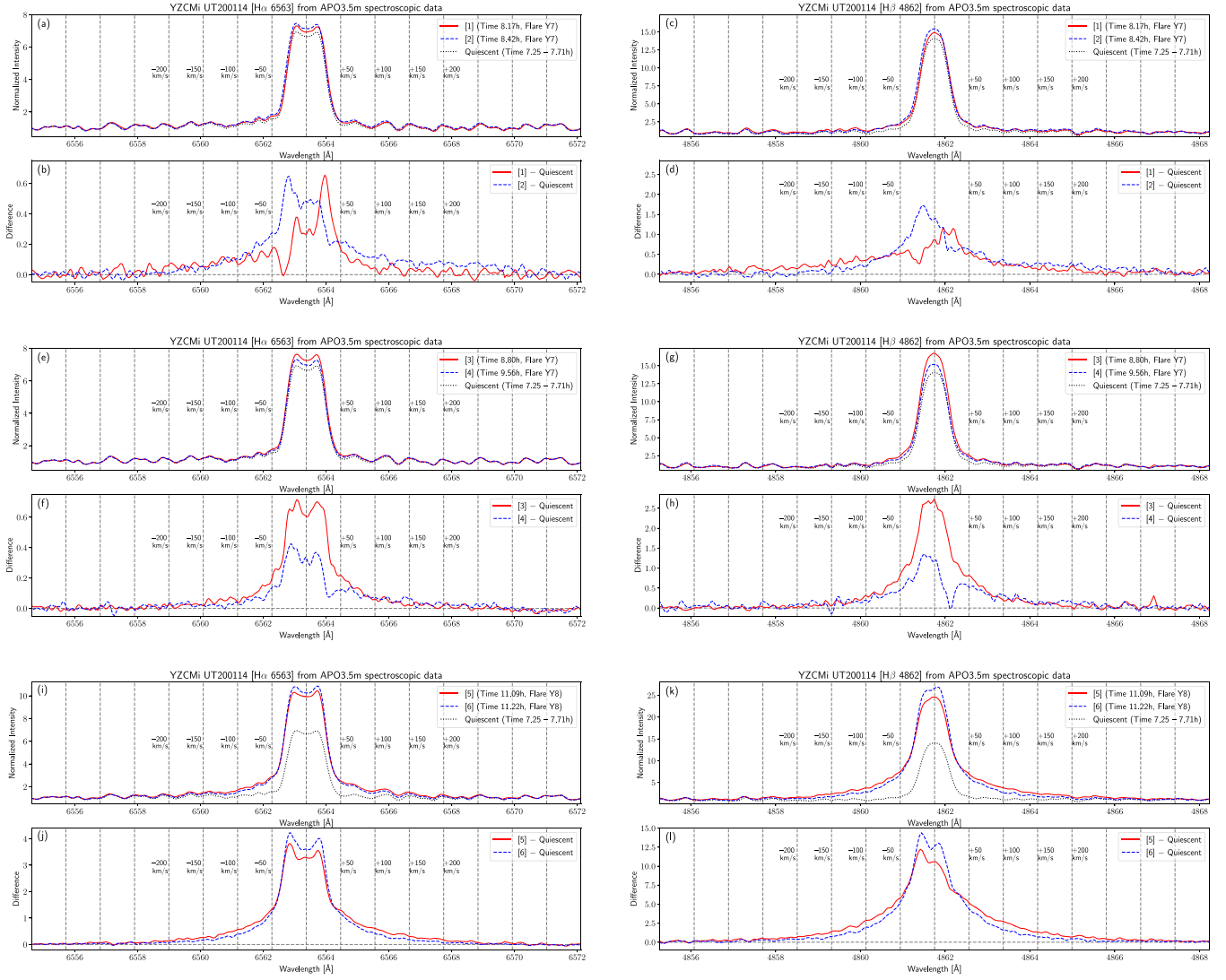


Figure 56. Line profiles of the $H\alpha$ and $H\beta$ emission lines during Flares Y7 and Y8 on 2020 January 14 (at the time [1]–[6]) from APO 3.5 m spectroscopic data, which are plotted similarly with Figure 9.

increase already started even before the LCO observation started, and the amplitude values described here ($\sim 250\%$ and $\sim 45\%$) can be only lower limit values. Flare Y10 occurred soon after Flare Y9. The $H\alpha$ and $H\beta$ EWs increased up to 11.3 \AA and 20.5 \AA , respectively, and $\Delta t_{H\alpha}^{\text{flare}}$ is 1.2 hr (Table 4). In addition to these enhancements in Balmer emission lines, the continuum brightness observed with LCO U band increased at least by $\sim 100\%$ during Flare Y10 (Figure 58(b)). Since LCO photometric data have some gaps during the flare, it is difficult to measure the brightness increase amplitude in V -band data, and the amplitude value in U band described here can be also only the lower limit value. As for Flare Y11, the $H\alpha$ and $H\beta$ EWs increased up to 11.9 \AA and 20.8 \AA , respectively, and the flare duration in $H\alpha$ $\Delta t_{H\alpha}^{\text{flare}}$ is 2.0 hr (Table 4). In addition to these enhancements in Balmer emission lines, the continuum brightness observed with LCO U and V bands increased at least by $\sim 200\%$ – 250% and $\sim 30\%$ – 35% , respectively, during Flare Y11 (Figure 58).

L_U , L_V , E_U , E_V , $L_{H\alpha}$, $L_{H\beta}$, $E_{H\alpha}$, and $E_{H\beta}$ values are estimated and listed in Table 4. We note that the L_U , L_V , E_U , and E_V values of the three flares (Flares Y9, Y10, and Y11) described

here can be only the lower limit values, since Flare Y9 already started before the observation started, and LCO photometric observations have some gaps during all the three flares. (We do not calculate L_V and E_V values because of the large gaps during Flare Y10 in V band.) It is noted that the main peaks of WL emissions corresponding to the $H\alpha$ and $H\beta$ emissions are covered in U -band observations without any effects from the gaps. In addition, $L_{H\alpha}$, $L_{H\beta}$, $E_{H\alpha}$, and $E_{H\beta}$ values of Flare Y9 are only the lower limit values, since the flare already started when the observation started, and it can be possible the flare peak time in $H\alpha$ and $H\beta$ lines was before the observation started.

The $H\alpha$ and $H\beta$ line profiles during Flares Y9, Y10, and Y11 are shown in Figures 59 and 60. During Flare Y9, there are no clear line wing asymmetries in $H\alpha$ and $H\beta$ lines, while there are slight blue part enhancements at -20 to -25 km s^{-1} from the line center of $H\alpha$ and $H\beta$ lines (the time [1] and [2] in Figures 59 and 60). Around the peak time of Flare Y10 and Flare Y11 (the time [3]–[6] in Figures 59 and 60), we can see the red-wing enhancements up to $\sim +200 \text{ km s}^{-1}$ in $H\alpha$ line and those up to $+150$ – $+200 \text{ km s}^{-1}$ in $H\beta$ line. The red wing asymmetry in $H\alpha$ line can be seen during most of the decay

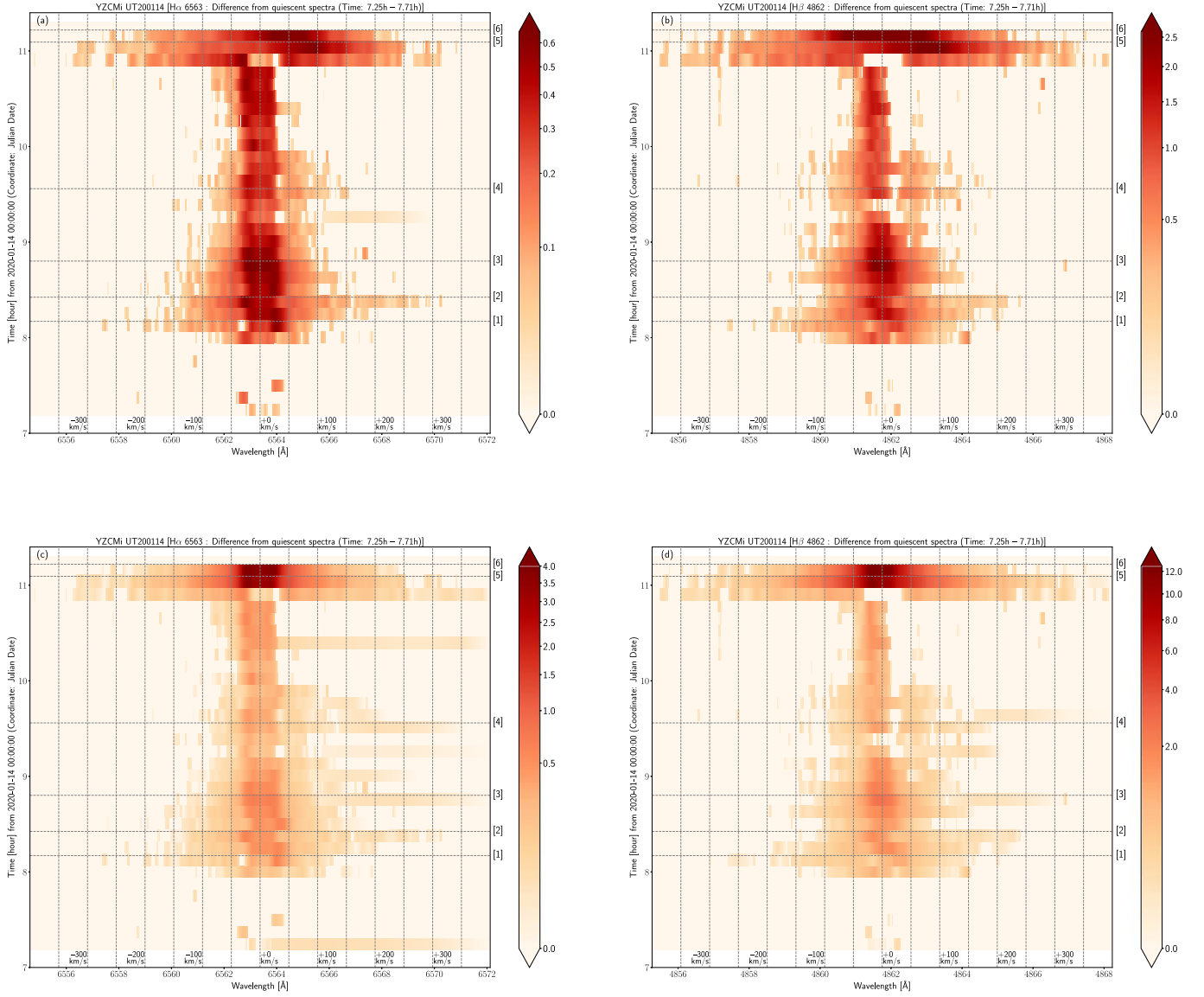


Figure 57. (a) and (b) Time evolution of the H α and H β line profiles covering Flares Y7 and Y8 on 2020 January 14, which are plotted similarly with Figure 16. The gray horizontal dashed lines indicate the time [1]–[6], which are shown in Figures 55(a) and (c) (light curves) and Figure 56 (line profiles). (c) and (d) Same as panels (a) and (b), but the ranges of the color map contours are different.

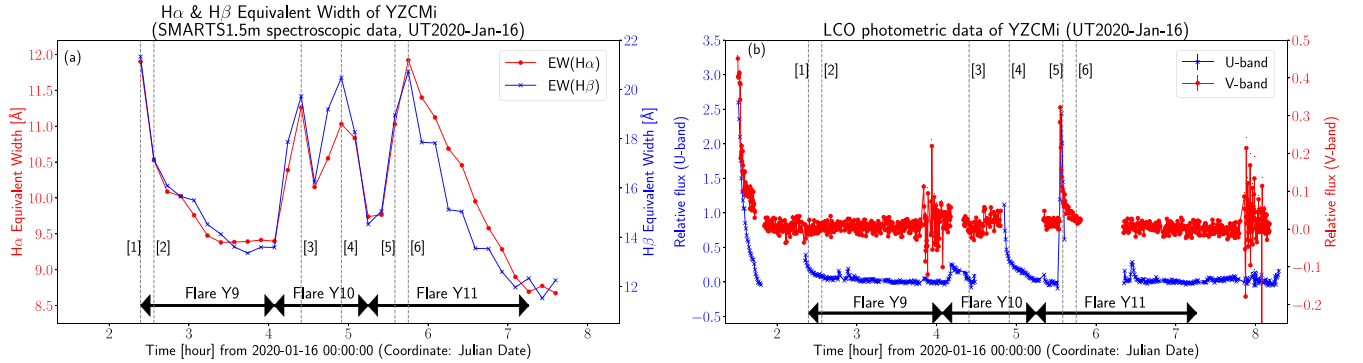


Figure 58. Light curves of YZCMi on 2020 January 16 showing Flares Y9, Y10, and Y11, which are plotted similarly with Figures 19(a) and (b). The gray dashed lines with numbers ([1]–[6]) correspond to the time shown with the same numbers in Figures 59 and 60.

phase in the case of Flare Y11. The peak time of red wing asymmetries roughly corresponds to the flare peak time in continuum brightness, comparing Figures 58 and 60.

A.5. Flares Y12 and Y13 Observed on 2020 January 18

On 2020 January 18, two flares (Flares Y12 and Y13) were detected in H α and H β lines as shown in Figures 61(a) and (c).

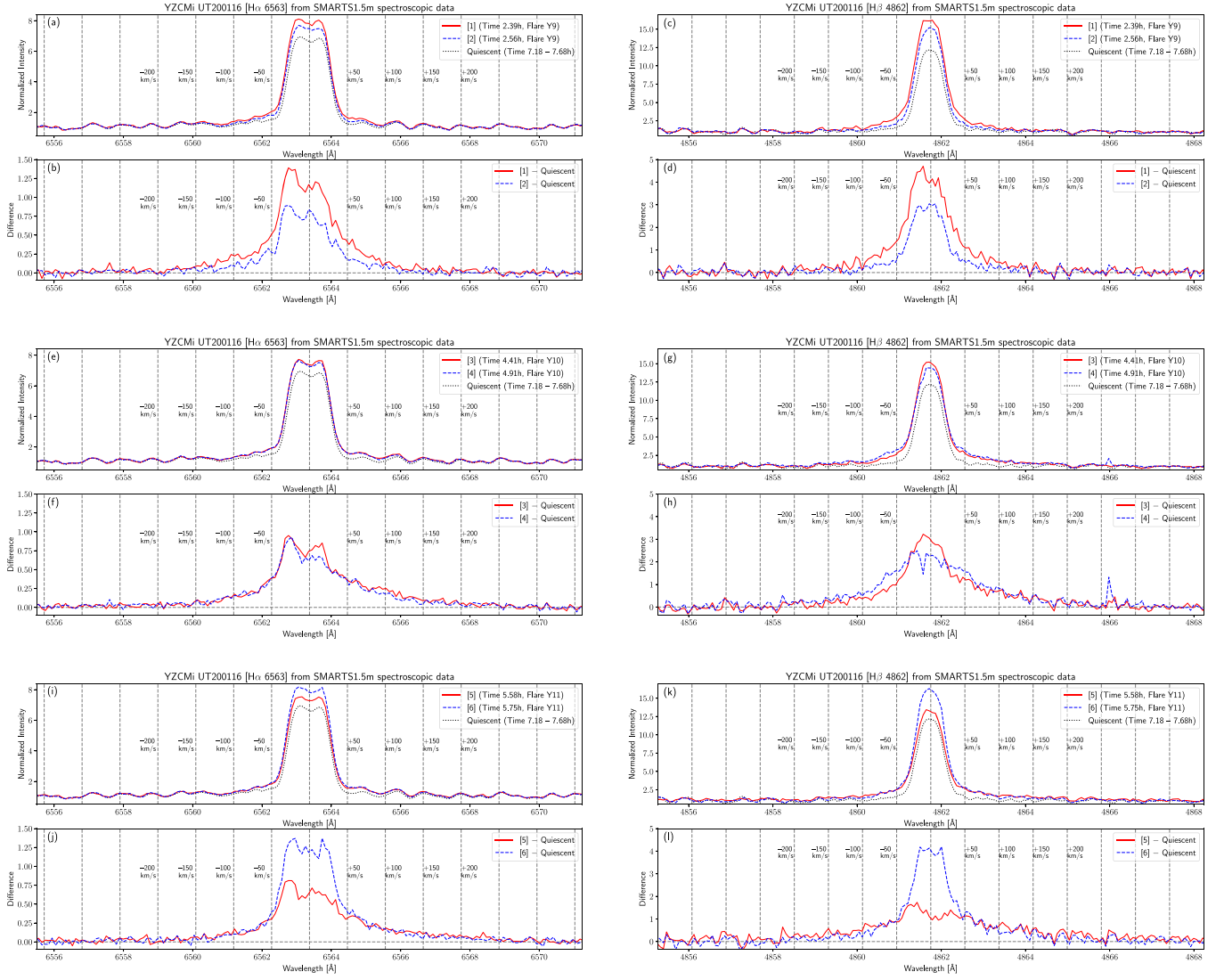


Figure 59. Line profiles of the $H\alpha$ and $H\beta$ emission lines during Flares Y9, Y10, and Y11 on 2020 January 16 (at the time [1]–[6]) from SMARTS 1.5 m spectroscopic data, which are plotted similarly with Figure 9.

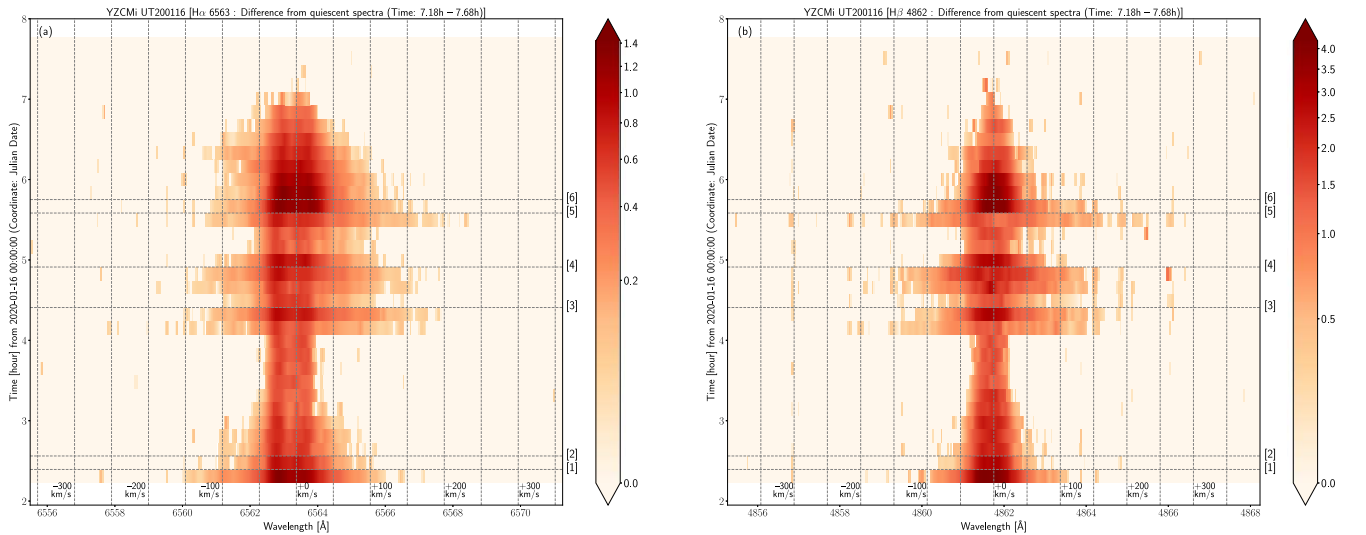


Figure 60. Time evolution of the $H\alpha$ and $H\beta$ line profiles covering Flares Y9, Y10, and Y11 on 2020 January 16, which are plotted similarly with Figure 16. The gray horizontal dashed lines indicate the time [1]–[6], which are shown in Figures 58 (light curves) and 59 (line profiles).

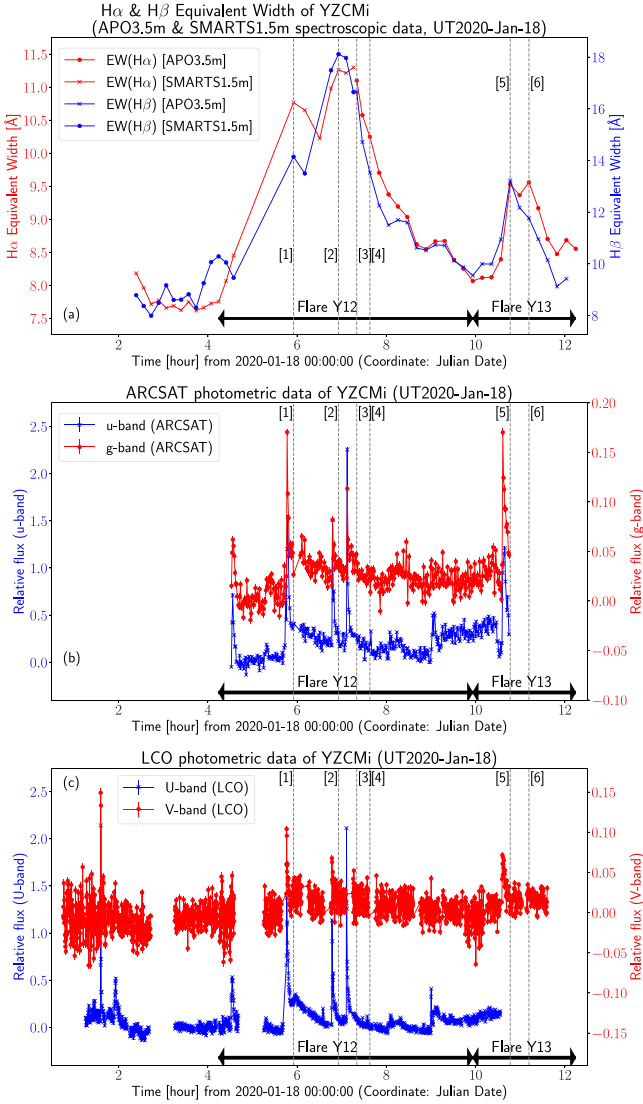


Figure 61. Light curves of YZ CMi on 2020 January 18 showing Flares Y12 and Y13, which are plotted similarly with Figures 14(a) and (b). In panel (a), red circles and blue asterisks correspond to $H\alpha$ and $H\beta$ EWs from APO 3.5 m data, respectively, while red asterisks and blue circles correspond to $H\alpha$ and $H\beta$ EWs from SMARTS 1.5 m data, respectively. The ARCSAT u - and g -band photometric data are plotted in (b), while LCO U - and V -band photometric data are plotted in (c). The gray dashed lines with numbers ([1]–[6]) correspond to the time shown with the same numbers in Figures 62 and 63.

As for Flare Y12, the $H\alpha$ and $H\beta$ EWs increased up to 11.3 Å and 18.1 Å, respectively, and $\Delta t_{H\alpha}^{\text{flare}}$ is 5.7 hr (Table 4). In addition to these enhancements in Balmer emission lines, the continuum brightness observed with ARCSAT u and g band and LCO U and V band increased at least by $\sim 220\%$ – 230% , $\sim 17\%$, $\sim 210\%$ – 220% , and $\sim 10\%$ – 11% , respectively, during Flare Y12 (Figures 61(b) and (d)). Since LCO photometric data have some observation gaps during the flare, the amplitude value in U and V band described here can be only the lower limit values. As for Flare Y13, the $H\alpha$ and $H\beta$ EWs increased up to 9.6 Å and 13.2 Å, respectively, and $\Delta t_{H\alpha}^{\text{flare}}$ is 2.3 hr (Table 4). In addition to these enhancements in Balmer emission lines, the continuum brightness observed with ARCSAT u and g band and LCO V band increased at least by $\sim 120\%$, $\sim 17\%$, and $\sim 7\%$ – 8% , respectively, during Flare Y13 (Figures 61(b) and (d)). There are no LCO U -band

observations over the most phases of Flare Y13. We also note that, since ARCSAT photometric observation ended before Flare Y13 in $H\alpha$ and $H\beta$ lines ended, some additional brightness changes in u and g band might exist.

L_U , L_u , L_g , L_V , E_U , E_u , E_g , E_V , $L_{H\alpha}$, $L_{H\beta}$, $E_{H\alpha}$, and $E_{H\beta}$ values are estimated and listed in Table 4. We note that the L_U , L_V , E_U , and E_V values can be only the lower limit values since the LCO observation has gaps during Flare Y12. We note that, since ARCSAT photometric observation ended before Flare Y13 (in Balmer lines) ended, the L_u , L_g , E_u , and E_g values can be only the lower limit values.

The $H\alpha$ and $H\beta$ line profiles during Flares Y12 and Y13 are shown in Figures 62 and 63. During Flare Y12, the red wing of $H\alpha$ and $H\beta$ lines could be slightly enhanced (up to $\sim +100 \text{ km s}^{-1}$) for ~ 2 hr (time [1]–[4] in Figures 62 and 63). During Flare Y13, the line profiles of $H\alpha$ and $H\beta$ lines did not show clear wing asymmetries.

A.6. Flares Y14 and Y15 Observed on 2020 January 19

On 2020 January 19, two flares (Flares Y14 and Y15) were detected in $H\alpha$ and $H\beta$ lines as shown in Figure 64(a). There could be another flare at around the time 5.0–6.5 hr (Figure 64(a)) considering the brightness increases in continuum bands (Figures 64(b) and (c)), but the spectroscopic data have an observation gap at around the time 5.0–6.5 hr because of the relatively bad S/N of the data. As for Flare Y14, the $H\alpha$ and $H\beta$ EWs increased up to 10.8 Å and 17.0 Å, respectively, and $\Delta t_{H\alpha}^{\text{flare}}$ is 1.2 hr (Table 4). In addition to these enhancements in Balmer emission lines, the continuum brightness observed with ARCSAT u and g band and LCO U and V band increased at least by $\sim 40\%$, $\sim 4\%$, $\sim 40\%$, and $\sim 2\%$ – 3% , respectively, during Flare Y14 (Figures 64(b) and (c)). As for Flare Y15, the $H\alpha$ and $H\beta$ EWs increased up to 10.9 Å and 19.4 Å, respectively. Only the initial phase (~ 0.3 hr) of Flare Y15 was observed. In addition to these enhancements in Balmer emission lines, the continuum brightness observed with ARCSAT u and g band increased by $\sim 925\%$, and $\sim 147\%$, respectively, during Flare Y15 (Figures 64(b) and (d)). The LCO observation ended before Flare Y15.

L_U , L_u , L_g , L_V , E_U , E_u , E_g , E_V , $L_{H\alpha}$, $L_{H\beta}$, $E_{H\alpha}$, and $E_{H\beta}$ values are estimated and listed in Table 4. We note that, since Flare Y15 was partially observed (only the initial ~ 0.3 hr) in Balmer lines (Figure 64(a)), the peak luminosity and energy values of Flare Y15 listed here could be only the lower limit values.

The $H\alpha$ and $H\beta$ line profiles during Flares Y14 and Y15 are shown in Figures 65 and 66. During both flares, there were no clear line wing asymmetries. The $H\alpha$ line wings at around the peak time of Flares Y14 and Y15 showed almost symmetric line broadenings with ± 100 – 150 and ± 150 – 200 km s^{-1} , respectively.

A.7. Flares Y16 and Y17 Observed on 2020 January 20

On 2020 January 20, two flares (Flares Y16 and Y17) were detected in $H\alpha$ and $H\beta$ lines as shown in Figures 67(a) and (c). Flare Y16 already started when the observation started. As for Flare Y16, the $H\alpha$ and $H\beta$ EWs increased up to 13.3 Å and 23.0 Å, respectively, and $\Delta t_{H\alpha}^{\text{flare}}$ is > 2.5 hr (Table 4). In addition to these enhancements in Balmer emission lines, the continuum brightness observed with ARCSAT u and g band increased at least by $\sim 75\%$, and $\sim 6\%$ in the later phase (at around time 4 hr), respectively, during Flare Y16 (Figure 67(b)). We note that the start time of ARCSAT photometric observation is later than that

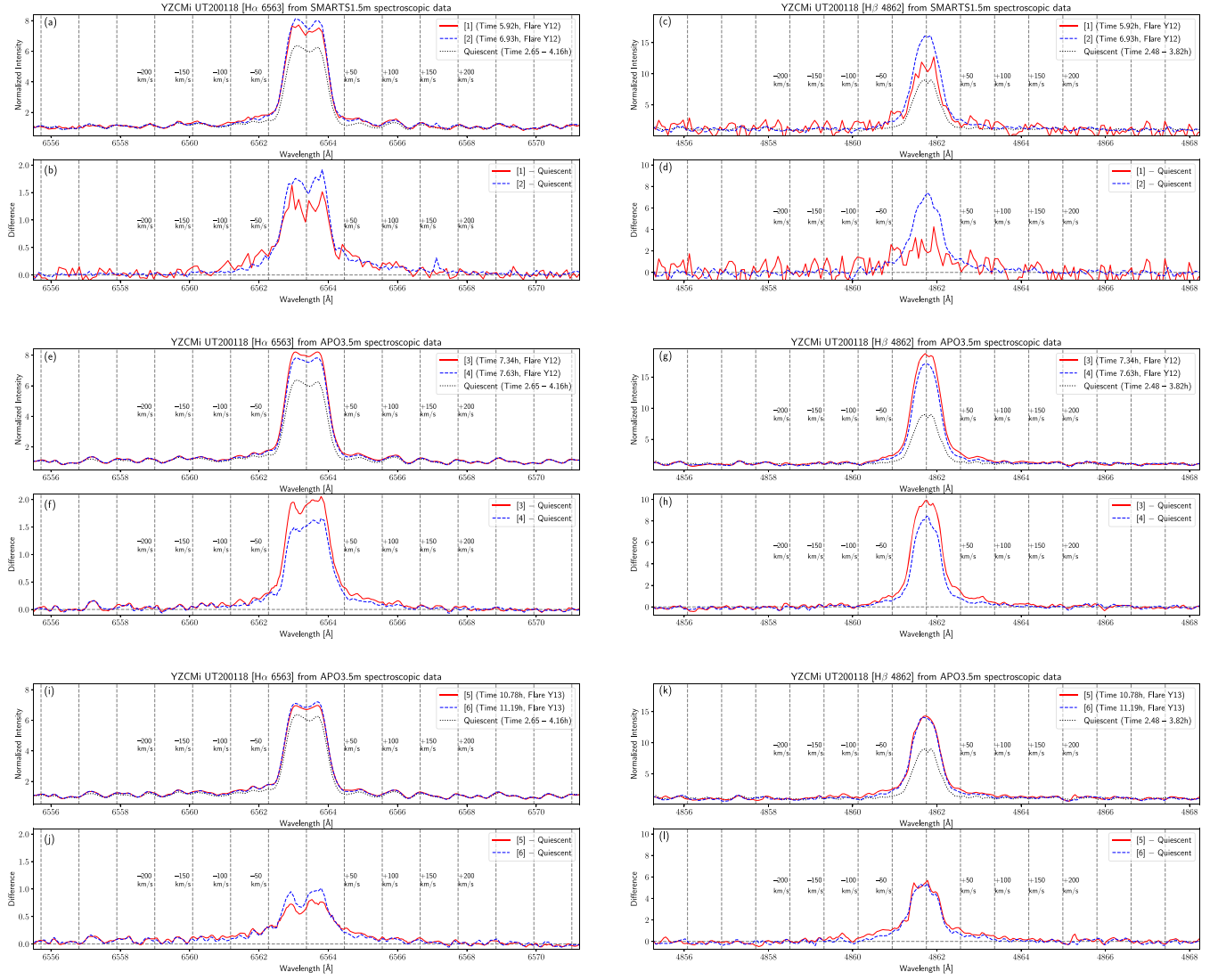


Figure 62. (a)–(d) Line profiles of the $H\alpha$ and $H\beta$ emission lines at the time [1] and [2] during Flare Y12 on 2020 January 18 from SMARTS 1.5 m spectroscopic data, which are plotted similarly with Figure 9. (e)–(h) Same as (a)–(d), but those at the time [3] and [4] during Flare Y12 from APO 3.5 m spectroscopic data. (i)–(l) Same as (a)–(d), but those at the time [5] and [6] during Flare Y13.

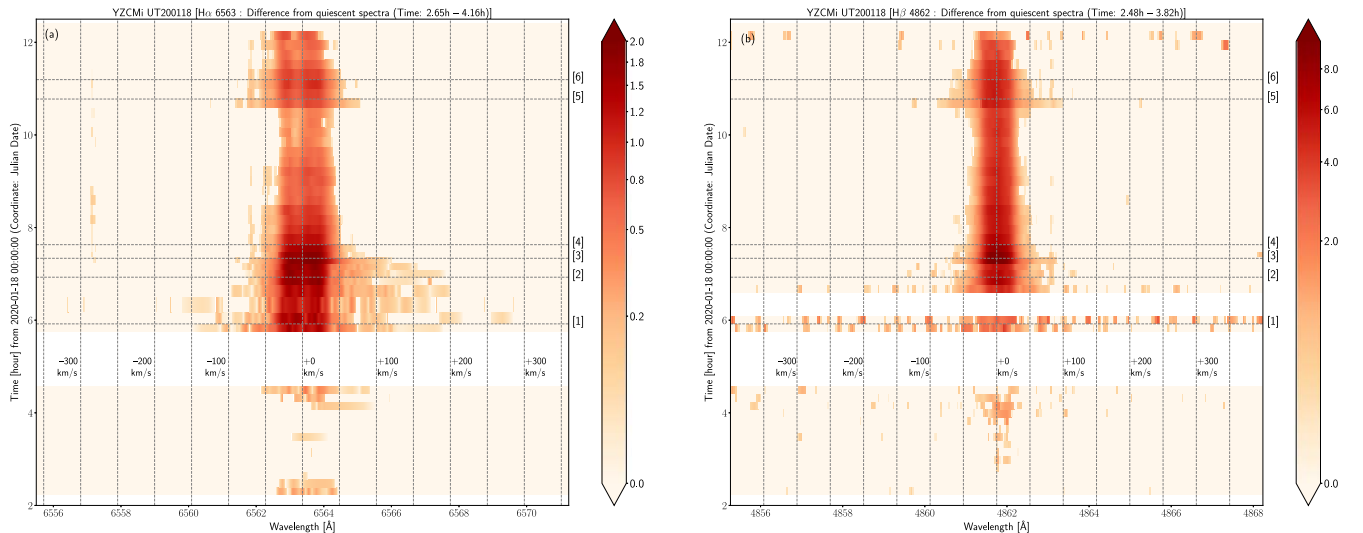


Figure 63. Time evolution of the $H\alpha$ and $H\beta$ line profiles covering Flares Y12 and Y13 on 2020 January 18, which are plotted similarly with Figure 16. The gray horizontal dashed lines indicate the time [1]–[6], which are shown in Figures 61 (light curves) and 62 (line profiles).

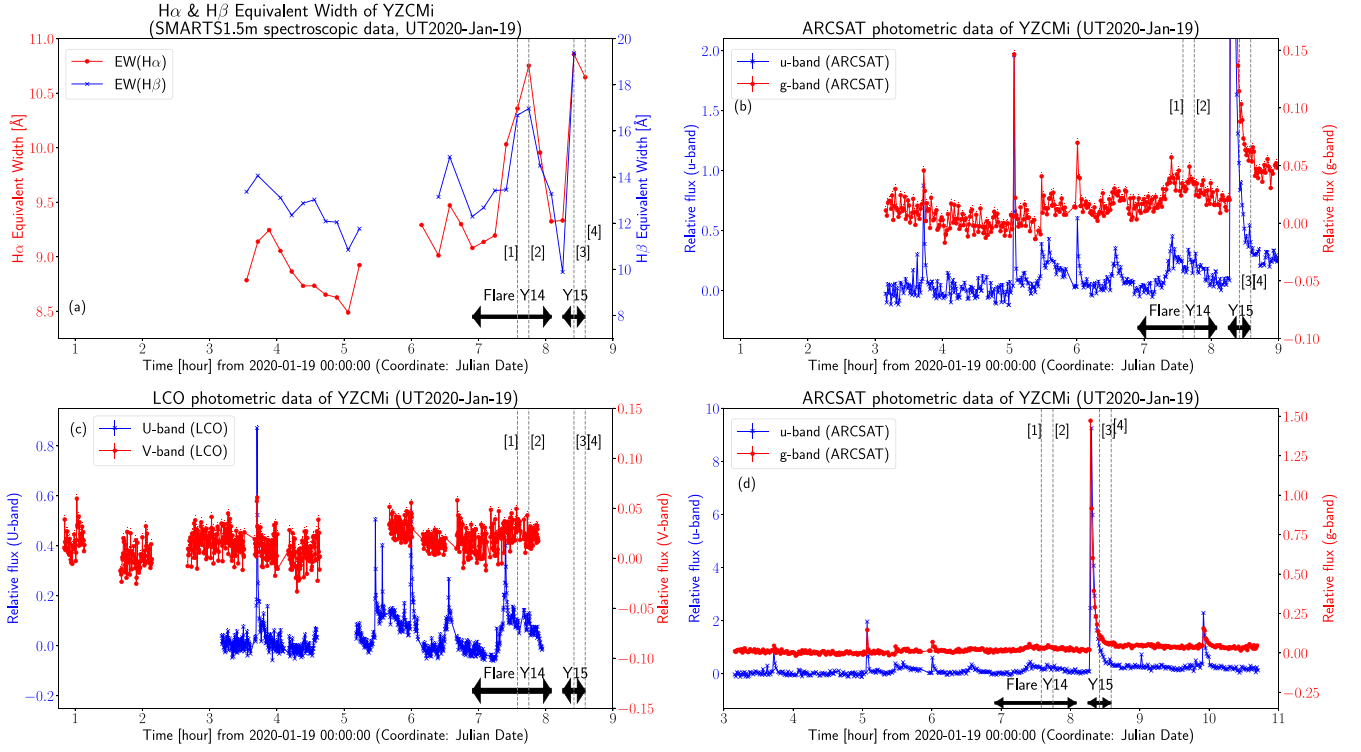


Figure 64. Light curves of YZ CMi on 2020 January 19 showing Flares Y14 and Y15, which are plotted similarly with Figure 61. In panel (a), red circles and blue asterisks correspond to H α and H β EWs from SMARTS 1.5 m data. The ARCSAT u - and g -band photometric data are plotted in (b) and (d), while the LCO U - and V -band photometric data are plotted in (c). The ranges of horizontal and vertical axes are different between (b) and (d), while the range of horizontal axis in (b) is the same as those of (a) and (c). The gray dashed lines with numbers ([1]–[4]) correspond to the time shown with the same numbers in Figures 65 and 66.

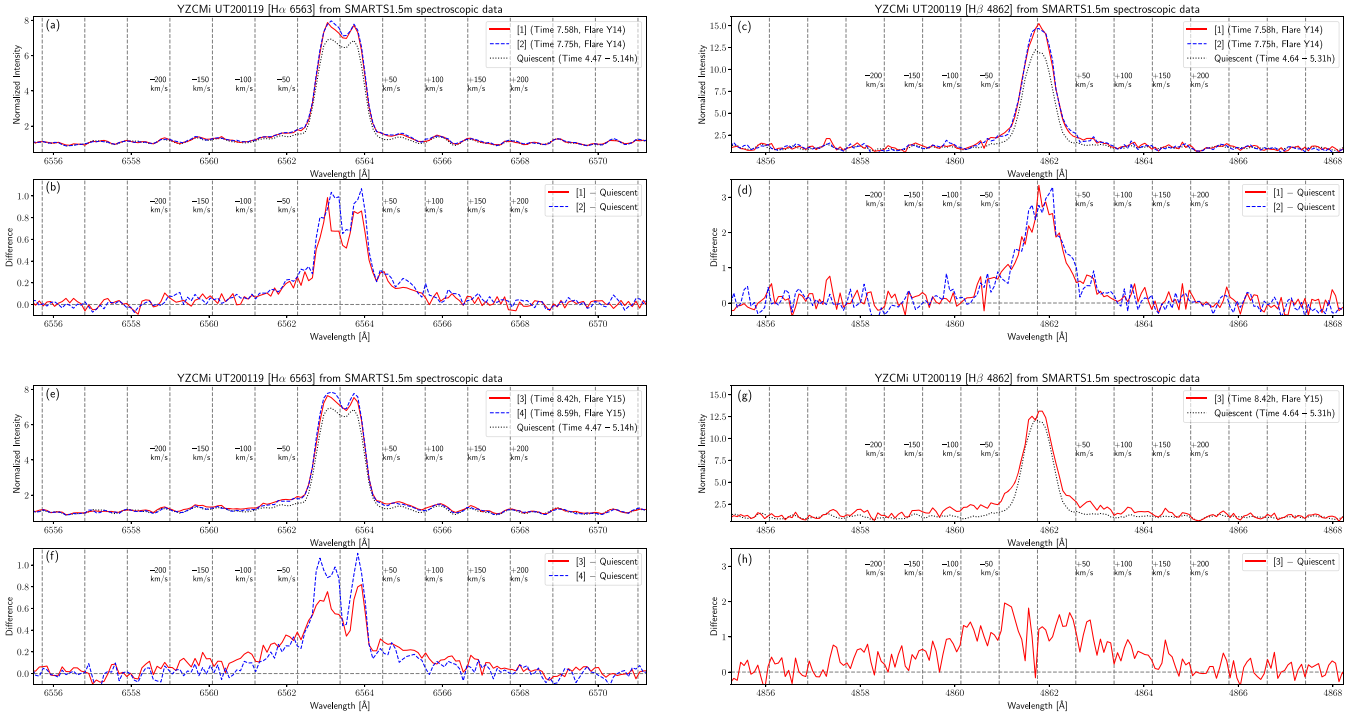


Figure 65. Line profiles of the H α and H β emission lines during Flares Y14 and Y15 on 2020 January 19 (at the time [1]–[4]) from SMARTS 1.5 m spectroscopic data, which are plotted similarly with Figure 9. The H β data at the time [4] were not plotted in (g) and (h), because of the bad S/N of the spectroscopic data.

of spectroscopic observations, and the continuum brightness increases with larger amplitude can be missed. We also note that there is a continuum brightness increase with $\sim 10\%$ – 15% in LCO V band just before the spectroscopic observation started

(Figure 67(d)). As for Flare Y17, the H α and H β EWs increased up to 13.5 Å and 25.5 Å , respectively, and $\Delta t_{\text{H}\alpha}^{\text{flare}}$ is 6.0 hr (Table 4). In addition to these enhancements in Balmer emission lines, the continuum brightness observed with ARCSAT u and g

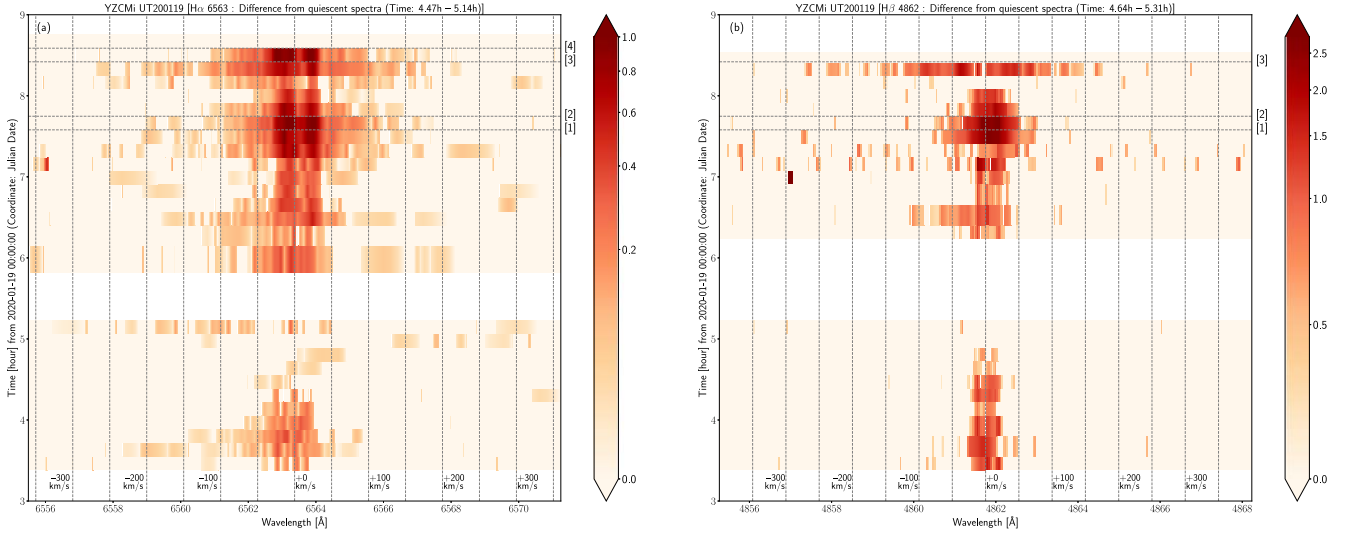


Figure 66. Time evolution of the $H\alpha$ and $H\beta$ line profiles covering Flares Y14 and Y15 on 2020 January 19, which are plotted similarly with Figure 16. The gray horizontal dashed lines indicate the time [1]–[4], which are shown in Figures 64 (light curves) and 65 (line profiles).

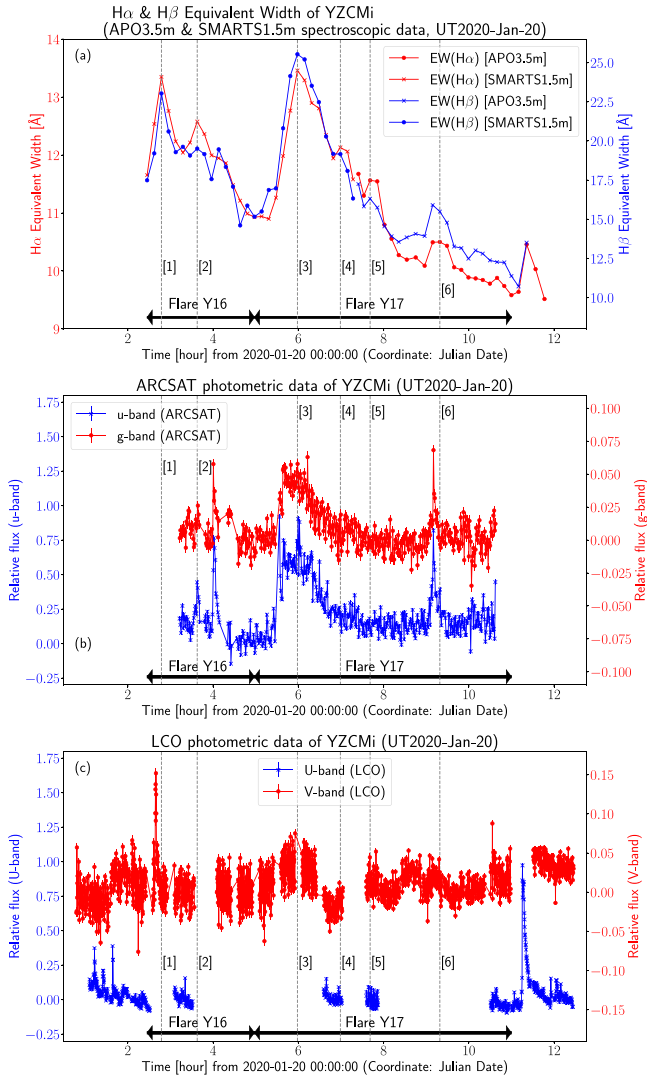


Figure 67. Light curves of YZ CMi on 2020 January 20 showing Flares Y16 and Y17, which are plotted similarly with Figure 61. The gray dashed lines with numbers ([1]–[6]) correspond to the time shown with the same numbers in Figures 68 and 69.

band and LCO V band increased by $\sim 75\%$, $\sim 7\%$, and $\sim 5\%$, respectively, during Flare Y17 (Figures 67(b) and (d)). We note that there are gaps of the LCO photometric observations also during Y17, and the continuum brightness increases with larger amplitude might be missed.

L_u , L_g , L_V , E_u , E_g , E_V , $L_{H\alpha}$, $L_{H\beta}$, $E_{H\alpha}$, and $E_{H\beta}$ values are estimated and listed in Table 4. The L_u , L_g , L_V , E_u , E_g , E_V values of Flare Y16 are only the lower limit values, since only the later phase in u and g bands and only the earlier phase in V band was observed, respectively (Figure 67). The $L_{H\alpha}$, $L_{H\beta}$, $E_{H\alpha}$, and $E_{H\beta}$ values of Flare Y16 described here are also only the lower limit values, since the initial phase of Flare Y16 was not observed.

The $H\alpha$ and $H\beta$ line profiles during Flares Y16 and Y17 are shown in Figures 68 and 69. During Flare Y16, the red wing of $H\alpha$ line (up to $\sim +150 \text{ km s}^{-1}$) was slightly enhanced (time [1], [2] in Figures 68(b)), while, around the $H\alpha$ line center, the blue part (~ -20 to -30 km s^{-1}) was slightly enhanced (time [1] in Figures 68(b)). This slight enhancement of red wing of $H\alpha$ line continued almost until the end of Flare Y16 (Figure 69(a)). The $H\beta$ line profile change during Flare Y16 was a bit different from that of $H\alpha$ line. There were no red-wing enhancements in the $H\beta$ line profile, and it could be possible there was a slight blue wing enhancement ($\sim -100 \text{ km s}^{-1}$). The $H\alpha$ line profile during Flare Y17 showed the properties similar to Flare Y16. The red wing of $H\alpha$ line (up to $\sim +200 \text{ km s}^{-1}$) was slightly enhanced over the early phase of the flare (time [3]–[5] in Figures 68(f), (j), and 69(a)). However, this red-wing enhancement was not clear in $H\beta$ line, and it could be possible that there was a slight blue wing enhancement ($\sim -100 \text{ km s}^{-1}$) in the early phase of the flare (time [3] in Figures 68(h) and 69(b)).

A.8. Flare Y20 Observed on 2020 January 22

On 2020 January 22, one flare (Flare Y20) was detected in $H\alpha$ and $H\beta$ lines as shown in Figure 70(a). As for Flare Y20, the $H\alpha$ and $H\beta$ EWs increased up to 9.5 \AA and 11.2 \AA , respectively, and $\Delta t_{H\alpha}^{\text{flare}}$ is 2.0 hr (Table 4). In addition to these enhancements in Balmer emission lines, the continuum brightness observed with LCO U and V band increased at least by

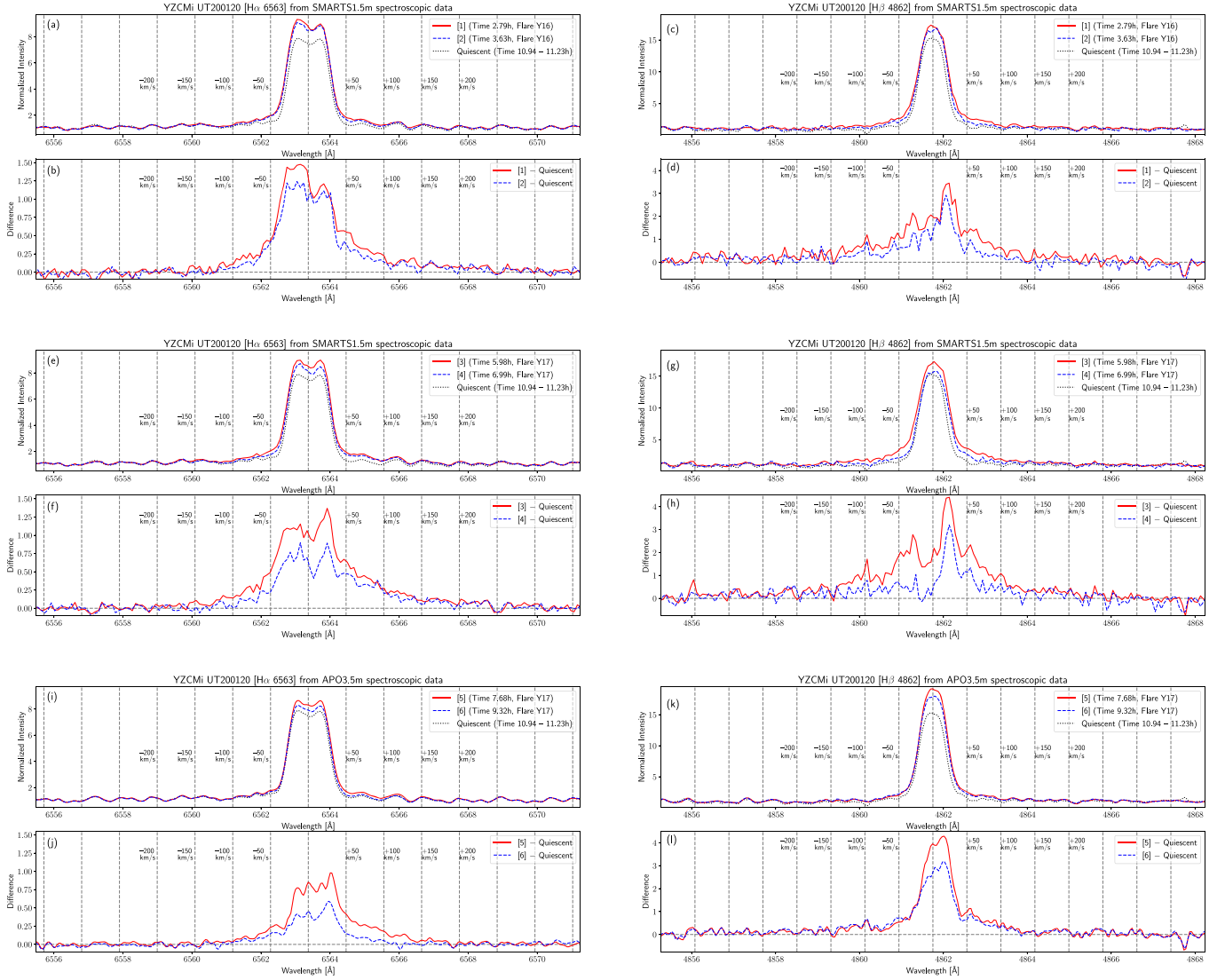


Figure 68. (a)–(d) Line profiles of the $H\alpha$ and $H\beta$ emission lines at the time [1] and [2] during Flares Y16 and Y17 on 2020 January 20 from SMARTS 1.5 m spectroscopic data, which are plotted similarly with Figure 9. (e)–(h) Same as (a)–(d), but those at the time [3] and [4] during Flare Y17 from SMARTS 1.5 m spectroscopic data. (i)–(l) Same as (a)–(d), but those at the time [5] and [6] during Flare Y17 from APO 3.5 m spectroscopic data.

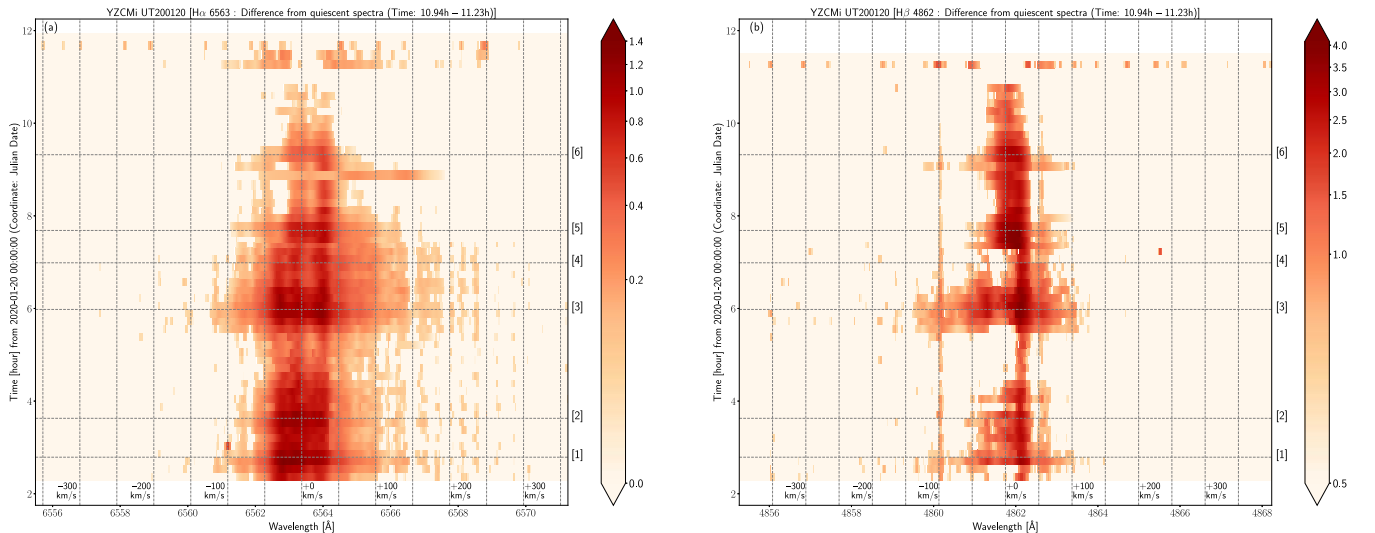


Figure 69. Time evolution of the $H\alpha$ and $H\beta$ line profiles covering Flares Y16 and Y17 on 2020 January 20, which are plotted similarly with Figure 16. The gray horizontal dashed lines indicate the time [1]–[6], which are shown in Figures 67 (light curves) and 68 (line profiles).

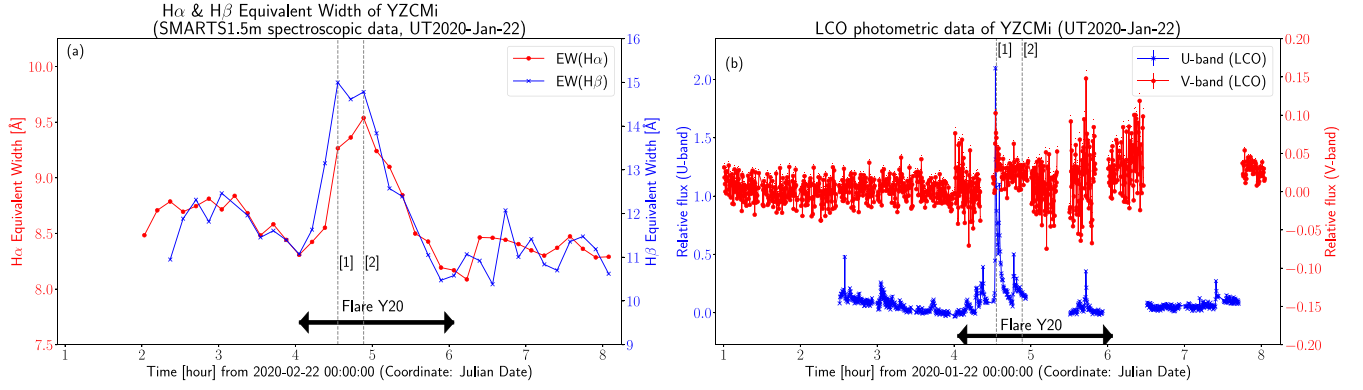


Figure 70. Light curves of YZ CMi on 2020 January 22 showing Flare Y20, which are plotted similarly with Figures 19(a) and (b). The gray dashed lines with numbers ([1], [2]) correspond to the time shown with the same numbers in Figures 71 and 72.

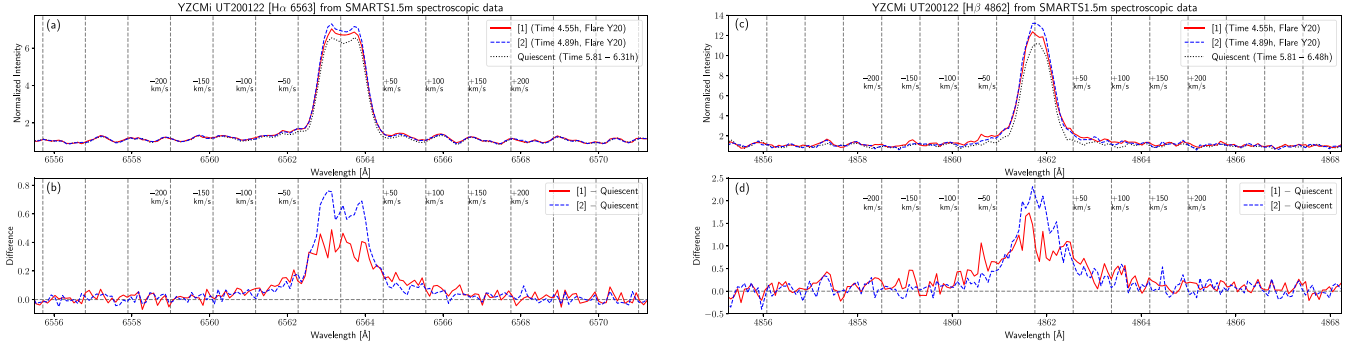


Figure 71. Line profiles of the $H\alpha$ and $H\beta$ emission lines during Flare Y20 on 2020 January 22 (at the time [1] and [2]) from SMARTS 1.5 m spectroscopic data, which are plotted similarly with Figure 9.

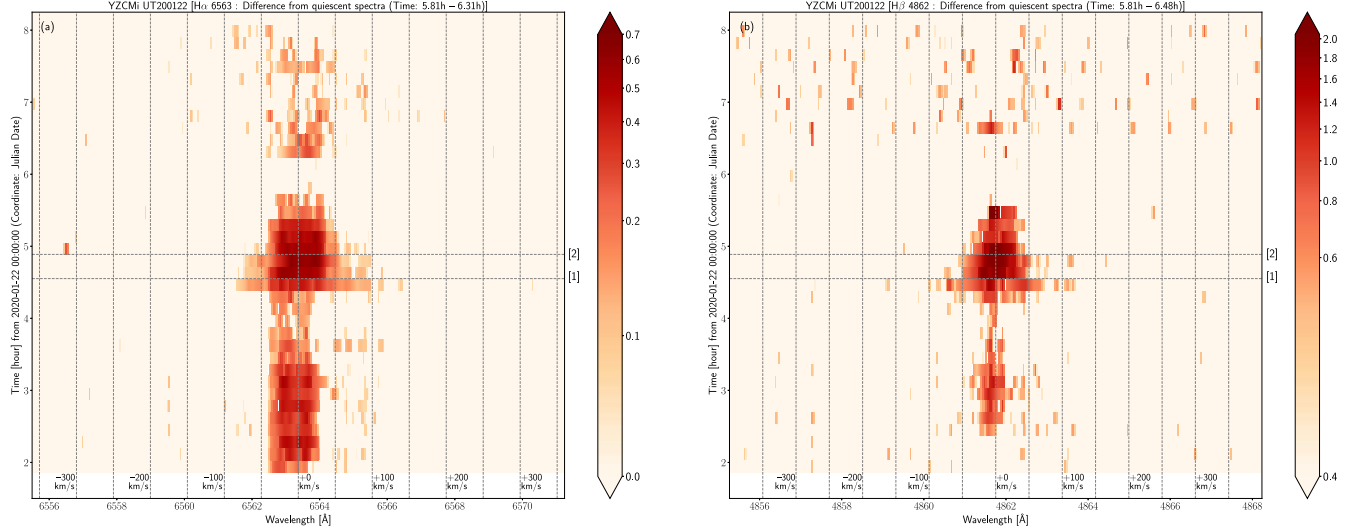


Figure 72. Time evolution of the $H\alpha$ and $H\beta$ line profiles covering Flare Y20 on 2020 January 22, which are plotted similarly with Figure 16. The gray horizontal dashed lines indicate the time [1] and [2], which are shown in Figures 70 (light curves) and 71 (line profiles).

$\sim 200\%$ – 210% , and $\sim 5\%$, respectively, during Flare Y20 (Figure 70(b)). We note that the LCO photometric observation has gaps during Flare Y20, and it could be possible that we missed the continuum brightness increases during the gap time.

L_U , L_V , E_U , E_V , $L_{H\alpha}$, $L_{H\beta}$, $E_{H\alpha}$, and $E_{H\beta}$ values are estimated and listed in Table 4. Since the LCO observation has gaps during Flare Y20 (Figure 70(b)), the energy values in U and V bands could be only the lower limit values.

The $H\alpha$ and $H\beta$ line profiles during Flare Y20 are shown in Figures 71 and 72. During Flare Y20, there were no clear blue

or red wing asymmetries in $H\alpha$ and $H\beta$ lines (time [1], [2] in Figures 71(b) and (d)), and the line profiles showed roughly symmetrical broadenings with $\sim \pm 150 \text{ km s}^{-1}$.

A.9. Flares Y21 and Y22 Observed on 2020 January 23

On 2020 January 23, two flares (Flares Y21 and Y22) were detected in $H\alpha$ and $H\beta$ lines as shown in Figure 73(a). As for Flare Y21, the $H\alpha$ and $H\beta$ EWs increased up to 9.8 \AA and 15.9 \AA , respectively, and $\Delta t_{H\alpha}^{\text{flare}}$ is 1.7 hr (Table 4). The

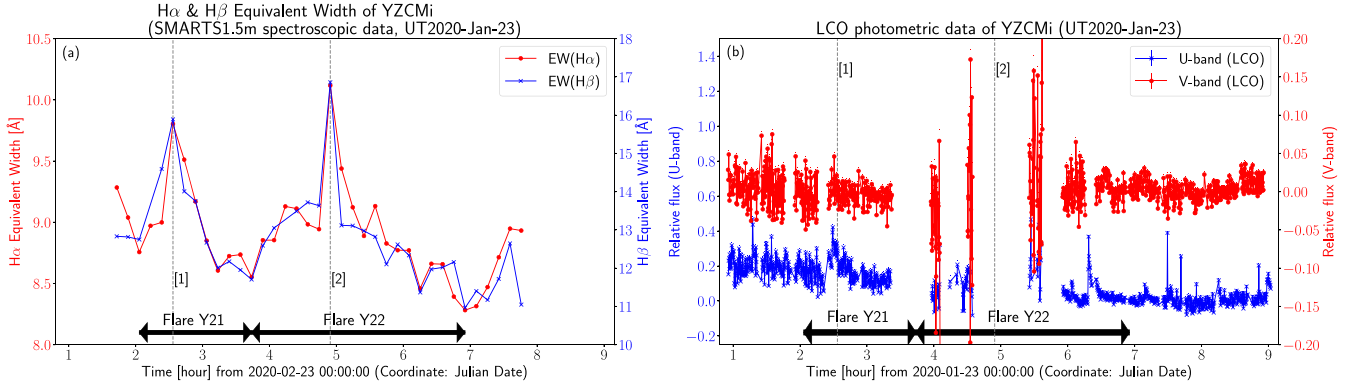


Figure 73. Light curves of YZ CMi on 2020 January 23 showing Flares Y21 and Y22, which are plotted similarly with Figures 19(a) and (b). The gray dashed lines with numbers ([1], [2]) correspond to the time shown with the same numbers in Figures 74 and 75.

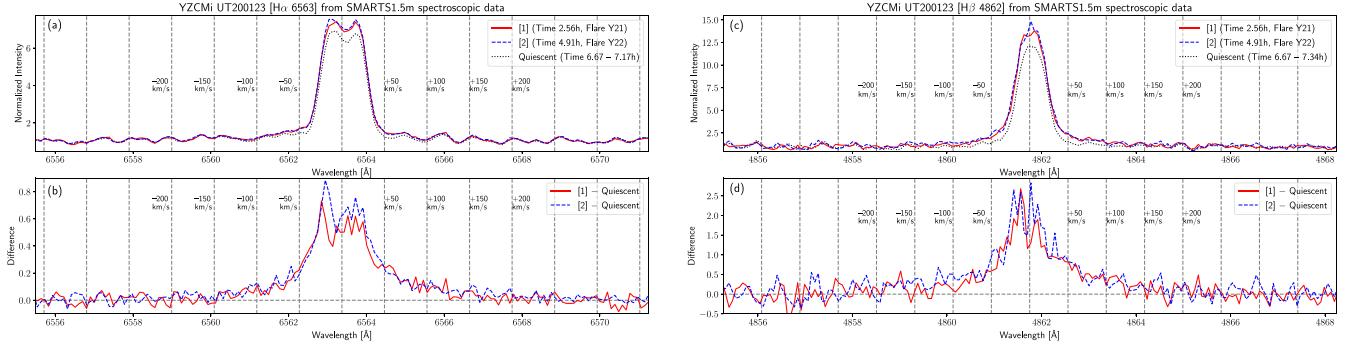


Figure 74. Line profiles of the $H\alpha$ and $H\beta$ emission lines during Flares Y21 and Y22 on 2020 January 23 (at the time [1] and [2]) from SMARTS 1.5 m spectroscopic data, which are plotted similarly with Figure 9.

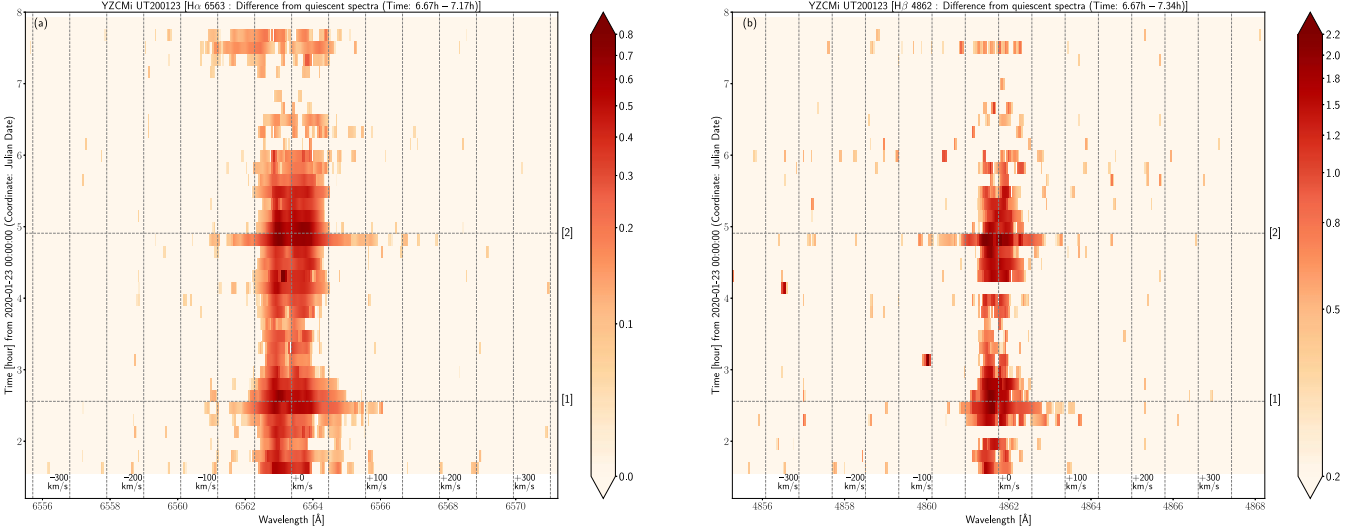


Figure 75. Time evolution of the $H\alpha$ and $H\beta$ line profiles over Flares Y21 and Y22 on 2020 January 23, which are plotted similarly with Figure 16. The gray horizontal dashed lines indicate the time [1] and [2], which are shown in Figures 73 (light curves) and 74 (line profiles).

continuum brightness is observed with LCO U band by $\sim 10\%$ – 20% during Flare Y21 (Figure 73(b)). The brightness increase in V band is not larger than the photometric error in V band ($3\sigma_V = 3.7\%$). As for Flare Y22, the $H\alpha$ and $H\beta$ EWs increased up to 10.1 \AA and 16.9 \AA , respectively, and $\Delta t_{H\alpha}^{\text{flare}}$ is 3.2 hr (Table 4). For most of the time during Flare Y22, there were no LCO photometric observation data (Figure 73(b)), and so, we cannot know whether there was the increase of the continuum brightness.

L_U , L_V , E_U , E_V , $L_{H\alpha}$, $L_{H\beta}$, $E_{H\alpha}$, and $E_{H\beta}$ values are estimated and listed in Table 4. As for Flare Y22, no L_U , L_V , E_U , and E_V values are estimated because of no LCO photometric observation data.

The $H\alpha$ and $H\beta$ line profiles during Flares Y21 and Y22 are shown in Figures 74 and 75. During Flares Y21 and Y22, there were no clear blue or red wing asymmetries in $H\alpha$ and $H\beta$ lines (time [1], [2] in Figures 74(b) and (d)), and the line profiles showed roughly symmetrical broadenings with $\sim \pm 150$ – 200 km s^{-1} at around the peak time of the flares.

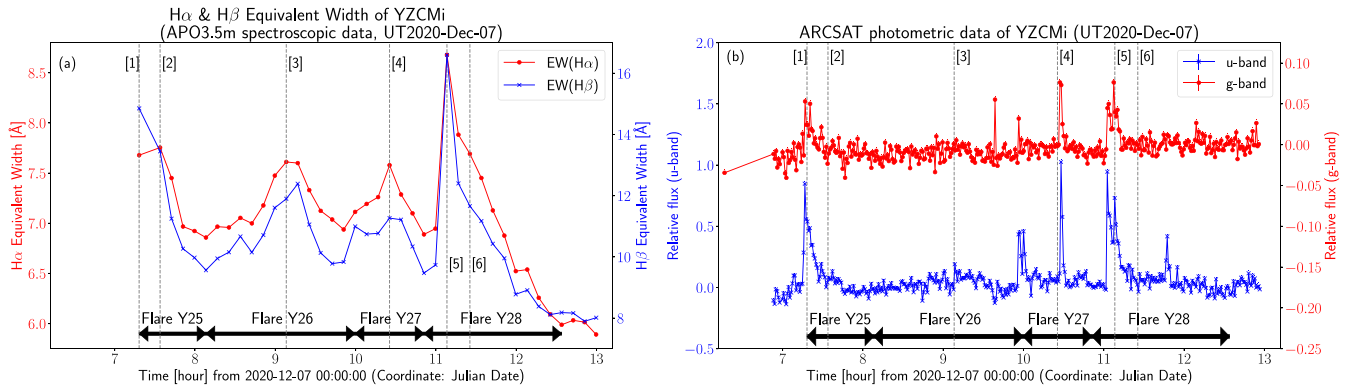


Figure 76. Light curves of YZ CMi on 2020 December 7 showing Flares Y25, Y26, Y27, and Y28, which are plotted similarly with Figures 14(a) and (b). The gray dashed lines with numbers ([1]–[6]) correspond to the time shown with the same numbers in Figures 77 and 78.

A.10. Flares Y25, Y26, Y27, and Y28 Observed on 2020 December 7

On 2020 December 7, four flares (Flares Y25, Y26, Y27, and Y28) were detected in $H\alpha$ and $H\beta$ lines as shown in Figure 76(a). Flare Y25 already started when the spectroscopic observation started. The $H\alpha$ and $H\beta$ EWs decreased from 7.8 Å and 14.9 Å, respectively, and $\Delta t_{H\alpha}^{\text{flare}}$ is >0.8 hr (Table 4). The photometric observation captured a bit earlier phase of the flare since it started ~ 0.5 hr before the spectroscopic observation started. During Flare Y25, the continuum brightness observed with ARCSAT u and g bands increased by $\sim 80\%$ and $\sim 5\%$ – 6% , respectively (Figure 76(b)). As for Flare Y26, the $H\alpha$ and $H\beta$ EWs increased up to 7.6 Å and 12.4 Å, respectively, and $\Delta t_{H\alpha}^{\text{flare}}$ is 1.9 hr (Table 4).

The continuum brightness increases with ARCSAT u and g bands are not enough larger than the photometric error ($3\sigma_u = 9.2\%$ and $3\sigma_g = 2.3\%$), and it is judged that there are no clear WL emissions, although there are some slight possible increase in u band at around 9.1–9.2 hr (Figure 76(b)).

As for Flare Y27, the $H\alpha$ and $H\beta$ EWs increased up to 7.6 Å and 11.3 Å, respectively, and $\Delta t_{H\alpha}^{\text{flare}}$ is 0.8 hr (Table 4). In addition to these enhancements in Balmer emission lines, the continuum brightness observed with ARCSAT u and g bands increased by $\sim 100\%$ and $\sim 7\%$ – 8% , respectively, during Flare Y27 (Figure 76(b)). As for Flare Y28, the $H\alpha$ and $H\beta$ EWs increased up to 8.7 Å and 16.6 Å, respectively, and $\Delta t_{H\alpha}^{\text{flare}}$ is 1.7 hr (Table 4). In addition to these enhancements in Balmer emission lines, the continuum brightness observed with ARCSAT u and g bands increased by $\sim 90\%$ – 100% and $\sim 7\%$ – 8% , respectively, during Flare Y28 (Figure 76(b)).

L_u , L_g , E_u , E_g , $L_{H\alpha}$, $L_{H\beta}$, $E_{H\alpha}$, and $E_{H\beta}$ values (including upper limit values) are estimated and listed in Table 4. Since the initial phase of Flare Y25 was not observed in the spectroscopic observation, the $L_{H\alpha}$, $L_{H\beta}$, $E_{H\alpha}$, and $E_{H\beta}$ values of Flare Y25 estimated here are only lower limit values.

The $H\alpha$ and $H\beta$ line profiles during Flares Y25, Y26, Y27, and Y28 are shown in Figures 77 and 78. During Flare Y25, there were no clear blue or red wing asymmetries in $H\alpha$ and $H\beta$ lines (time [1] and [2] in Figures 77 and 78), and the line profiles showed roughly symmetrical broadenings with $\sim \pm 150$ – 200 km s $^{-1}$ ($H\alpha$) and $\sim \pm 250$ – 300 km s $^{-1}$ ($H\beta$) at around the peak time of the flares (time [1] in Figures 77 and 78). During Flares Y26 and Y27, there were no clear blue or red wing asymmetries in $H\alpha$ and $H\beta$ lines (time [3] and [4] in Figures 77 and 78), and the line profiles showed roughly symmetrical broadenings with $\sim \pm 100$ – 150 km s $^{-1}$ at around the

peak time of the flares. During Flare Y28, there were no clear blue wing asymmetries in $H\alpha$ and $H\beta$ lines (time [5] and [6] in Figures 77 and 78), and the line profiles showed broadenings with $\sim \pm 150$ – 200 km s $^{-1}$ ($H\alpha$) and $\sim \pm 200$ – 250 km s $^{-1}$ ($H\beta$) at around the peak time of the flares (time [5] in Figures 77 and 78).

A.11. Flare Y29 Observed on 2021 January 31

On 2021 January 31, one flare (Flare Y29) was detected in $H\alpha$ and $H\beta$ lines as shown in Figure 79(a). During Flare Y29, the $H\alpha$ and $H\beta$ EWs increased up to 8.6 Å and 11.3 Å, respectively, and $\Delta t_{H\alpha}^{\text{flare}}$ is 5.3 hr (Table 4). In addition to the enhancements in Balmer emission lines, the continuum brightness observed by ARCSAT u and g bands and TESS increased by $\sim 140\%$, $\sim 17\%$ – 18% , and $\sim 0.5\%$, respectively, during Flare Y29 (Figures 79(b) and (c)). L_u , L_g , L_{TESS} , E_u , E_g , E_{TESS} , $L_{H\alpha}$, $L_{H\beta}$, $E_{H\alpha}$, and $E_{H\beta}$ values are estimated and listed in Table 4.

The $H\alpha$ and $H\beta$ line profiles during Flare Y29 are shown in Figures 80 and 81. During Flare Y29, there were no clear blue or red wing asymmetries in $H\alpha$ and $H\beta$ lines (time [1]–[4] in Figures 80 and 81), and the line profiles showed roughly symmetrical broadenings with $\sim \pm 100$ – 150 km s $^{-1}$ at around the peak time of the emission changes.

A.12. Flares E3 and E4 Observed on 2020 August 26

On 2020 August 26, two flares (Flares E3 and E4) were detected on EV Lac in $H\alpha$ and $H\beta$ lines as shown in Figure 82(a). Flare E3 already started before the spectroscopic observation started. As for Flare E3, the $H\alpha$ and $H\beta$ EWs decreased from 6.1 Å and 10.4 Å, respectively, and $\Delta t_{H\alpha}^{\text{flare}}$ is >2.3 hr (Table 4). In addition to these enhancements in Balmer emission lines, the continuum brightness observed with ARCSAT u band increased by $\sim 20\%$ – 25% during Flare E3 (Figure 82(b)), while the increase in g band is not so clear and comparable to the photometric error ($3\sigma_g = 2.1\%$). It is noted that the clear brightness increase in u and g bands at around time 5 hr (Figure 82(b)) could be related with Flare E3, since the flare already started when the observation started (Figure 82(a)).

As for Flare E4, the $H\alpha$ and $H\beta$ EWs increased up to 5.9 Å and 10.8 Å, respectively, and $\Delta t_{H\alpha}^{\text{flare}}$ is >2.1 hr (Table 4). Flare E4 did not end before the spectroscopic observation finished. In addition to these enhancements in Balmer emission lines, the continuum brightness observed with ARCSAT u and g bands increased by $\sim 25\%$ – 30% and $\sim 3\%$ – 4% , respectively, during Flare E4 (Figure 82(b)).

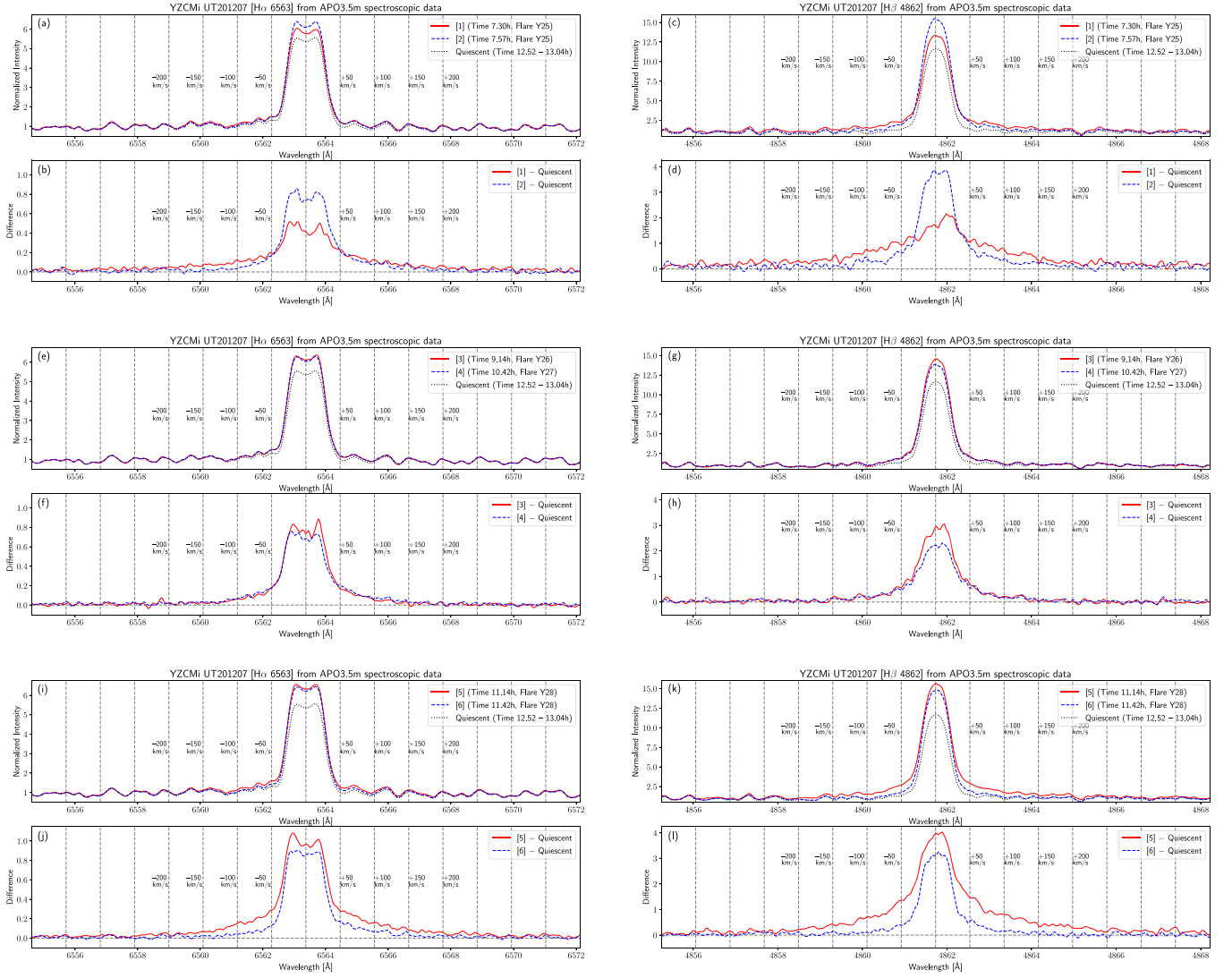


Figure 77. Line profiles of the $H\alpha$ and $H\beta$ emission lines during Flares Y25, Y26, Y27, and Y28 on 2020 December 7 (at the time [1]–[6]) from APO 3.5 m spectroscopic data, which are plotted similarly with Figure 9.

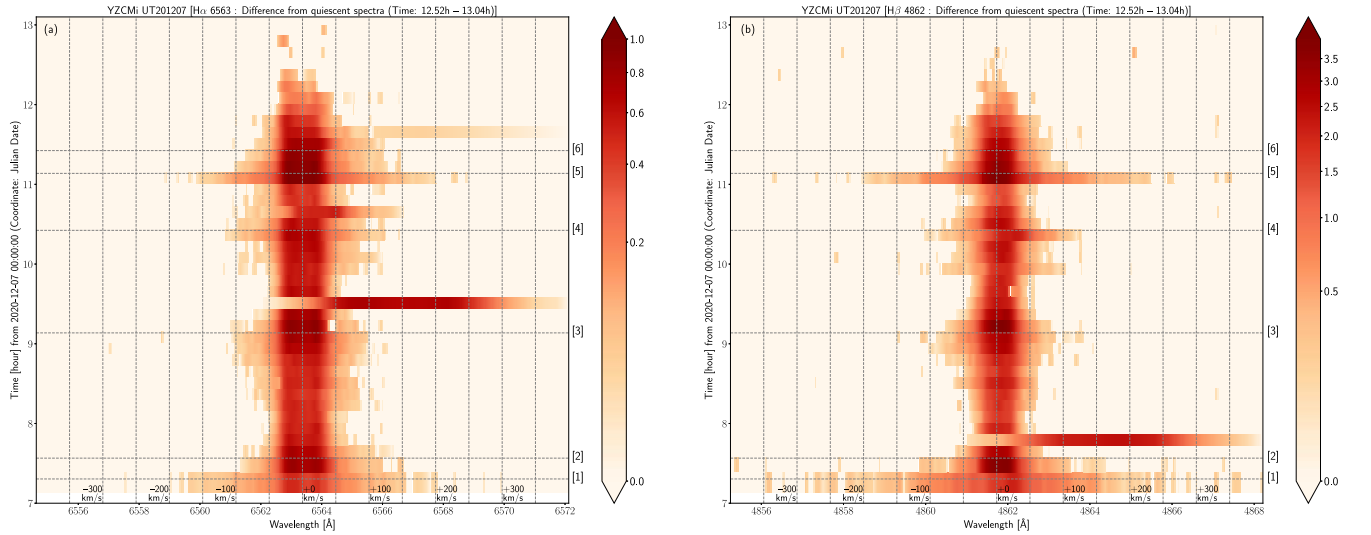


Figure 78. Time evolution of the $H\alpha$ and $H\beta$ line profiles covering Flares Y25, Y26, Y27, and Y28 on 2020 December 7, which are plotted similarly with Figure 16. The gray horizontal dashed lines indicate the time [1]–[6], which are shown in Figures 76 (light curves) and 77 (line profiles).

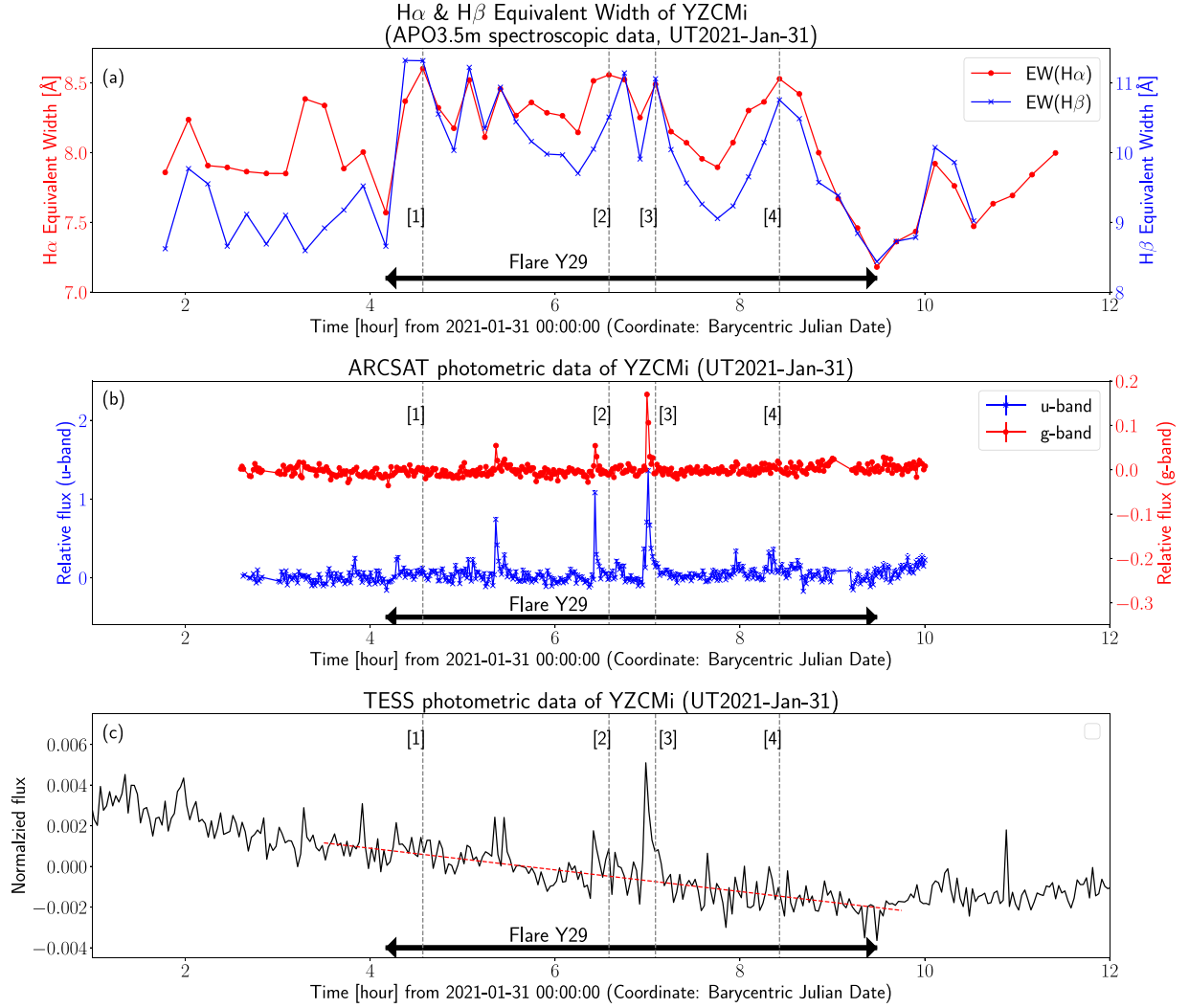


Figure 79. Light curves of YZ CMi on 2021 January 31 showing Flare Y29, which are plotted similarly with Figures 8(a)–(c). The gray dashed lines with numbers ([1]–[4]) correspond to the time shown with the same numbers in Figures 80 and 81. In (c), the red solid line is plotted to identify quiescent level of the TESS data.

L_u , L_g , E_u , E_g , $L_{H\alpha}$, $L_{H\beta}$, $E_{H\alpha}$, and $E_{H\beta}$ values are estimated and listed in Table 4. Since the flare already started before the spectroscopic observation began, the $L_{H\alpha}$, $L_{H\beta}$, $E_{H\alpha}$, and $E_{H\beta}$ values of Flare E3 listed here can be only lower limit values. Since the flare did not end before the spectroscopic observation finished, the $L_{H\alpha}$, $L_{H\beta}$, $E_{H\alpha}$, and $E_{H\beta}$ values of Flare E4 can be also only lower limit values.

The $H\alpha$ and $H\beta$ line profiles during Flares E3 and E4 are shown in Figures 83 and 84. During Flares E3, there were no clear blue or red wing asymmetries in $H\alpha$ and $H\beta$ lines (time [1] in Figures 83 and 84), and the line profiles showed roughly symmetrical broadenings with $\sim\pm 150$ – 200 km s $^{-1}$ at around the peak time of the flares (time [1] in Figures 83 and 84). During Flares E4, there were also no clear blue or red wing asymmetries in $H\alpha$ and $H\beta$ lines (time [2] in Figures 83 and 84), and the line profiles showed roughly symmetrical broadenings with $\sim\pm 150$ – 200 km s $^{-1}$ ($H\alpha$) and $\sim\pm 200$ – 250 km s $^{-1}$ ($H\beta$) at around the peak time of the flares (time [2] in Figures 83 and 84).

A.13. Flare E5 Observed on 2020 August 27

On 2020 August 27, one flare (Flare E5) was detected on EV Lac in $H\alpha$ and $H\beta$ lines as shown in Figures 85(a) and (c). As

for Flare E5, the $H\alpha$ and $H\beta$ EWs increased up to 17.4 Å and 40.6 Å, respectively, and $\Delta t_{H\alpha}^{\text{flare}}$ is 3.5 hr (Table 4). In addition to these enhancements in Balmer emission lines, the continuum brightness observed with ARCSAT u and g bands increased by $\sim 3230\%$ and $\sim 430\%$, respectively, during Flare E5 (Figures 82(b)). L_u , L_g , E_u , E_g , $L_{H\alpha}$, $L_{H\beta}$, $E_{H\alpha}$, and $E_{H\beta}$ values are estimated and listed in Table 4.

The $H\alpha$ and $H\beta$ line profiles during Flare E5 are shown in Figures 86 and 87. At around the peak time of Flares E5 (e.g., time [1] and [2] in Figures 86 and 87), the line profiles of $H\alpha$ and $H\beta$ lines show roughly symmetrical broadenings or possibly slight red wing asymmetries with $\sim\pm 600$ – 800 km s $^{-1}$ ($H\alpha$) and $\sim\pm 600$ – 700 km s $^{-1}$ ($H\beta$). During the decay phase of Flare E5 (e.g., time [3] and [4] in Figures 86 and 87), the line profiles of $H\alpha$ and $H\beta$ lines show clear red wing asymmetries for 2 hr (Figure 87).

A.14. Flare E6 Observed on 2020 August 29

On 2020 August 29, one flare (Flare E6) was detected on EV Lac in $H\alpha$ and $H\beta$ lines as shown in Figure 88(a). Flare E6 already started before the spectroscopic observation started. As for Flare E6, the $H\alpha$ and $H\beta$ EWs increased up to 5.2 Å and 7.2 Å, respectively, and $\Delta t_{H\alpha}^{\text{flare}}$ is >2.7 hr (Table 4). In addition

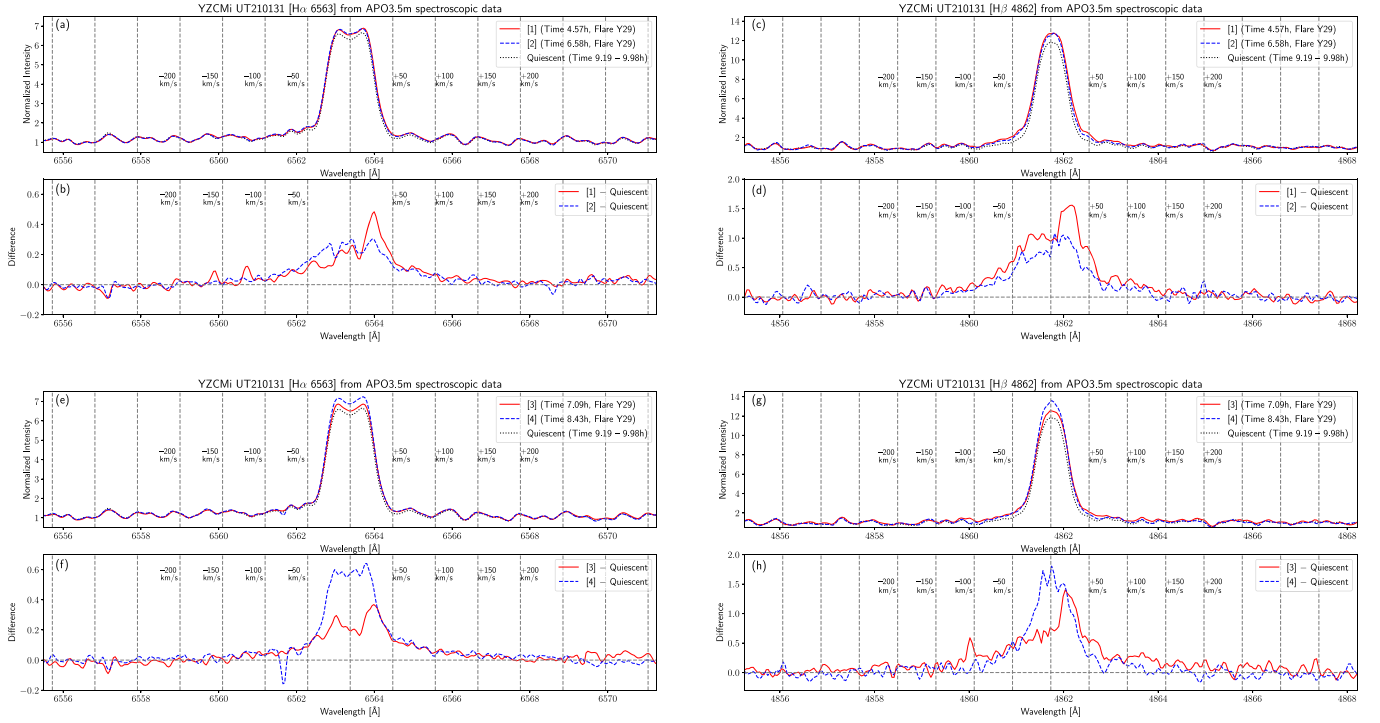


Figure 80. Line profiles of the $H\alpha$ and $H\beta$ emission lines during Flare Y29 on 2021 January 31 (at the time [1]–[4]) from APO 3.5 m spectroscopic data, which are plotted similarly with Figure 9.

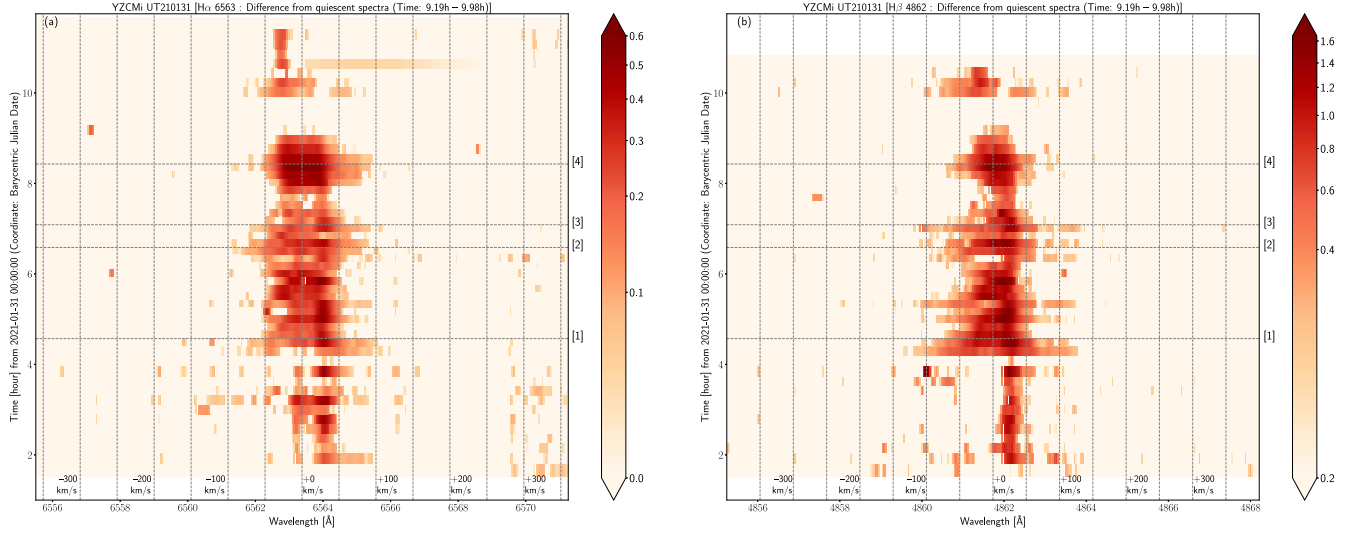


Figure 81. Time evolution of the $H\alpha$ and $H\beta$ line profiles covering Flare Y29 on 2021 January 31, which are plotted similarly with Figure 10. The gray horizontal dashed lines indicate the time [1]–[4], which are shown in Figures 79 (light curves) and 80 (line profiles).

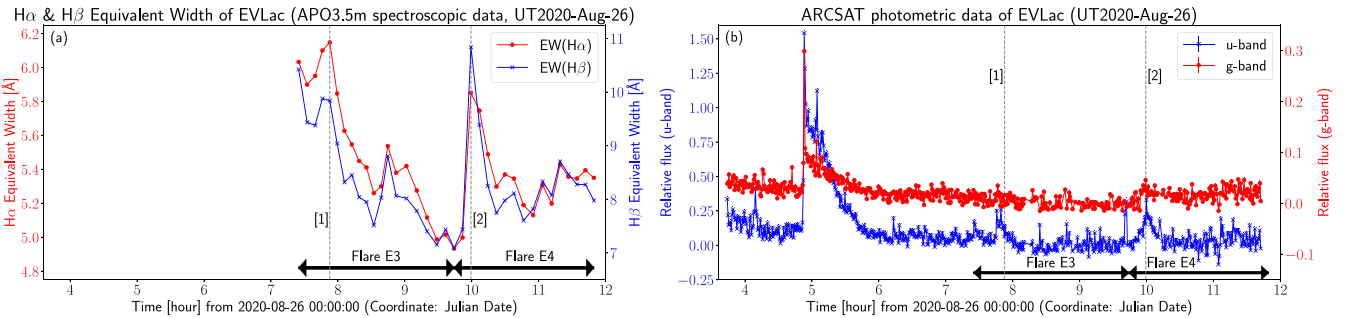


Figure 82. Light curves of EV Lac on 2020 August 26 showing Flares E3 and E4, which are plotted similarly with Figures 14(a) and (b). The gray dashed lines with numbers ([1] and [2]) correspond to the time shown with the same numbers in Figures 83 and 84.

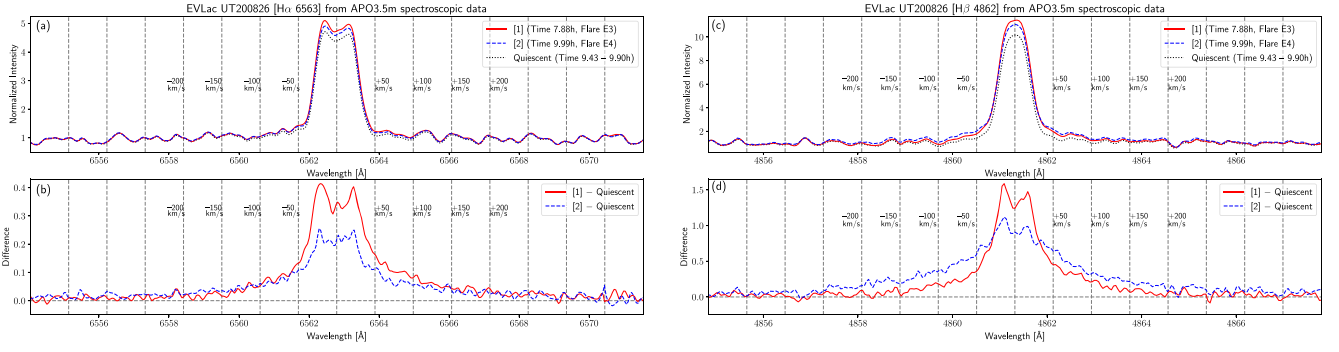


Figure 83. Line profiles of the $H\alpha$ and $H\beta$ emission lines during Flares E3 and E4 on 2020 August 26 (at the time [1] and [2]) from APO 3.5 m spectroscopic data, which are plotted similarly with Figure 9.

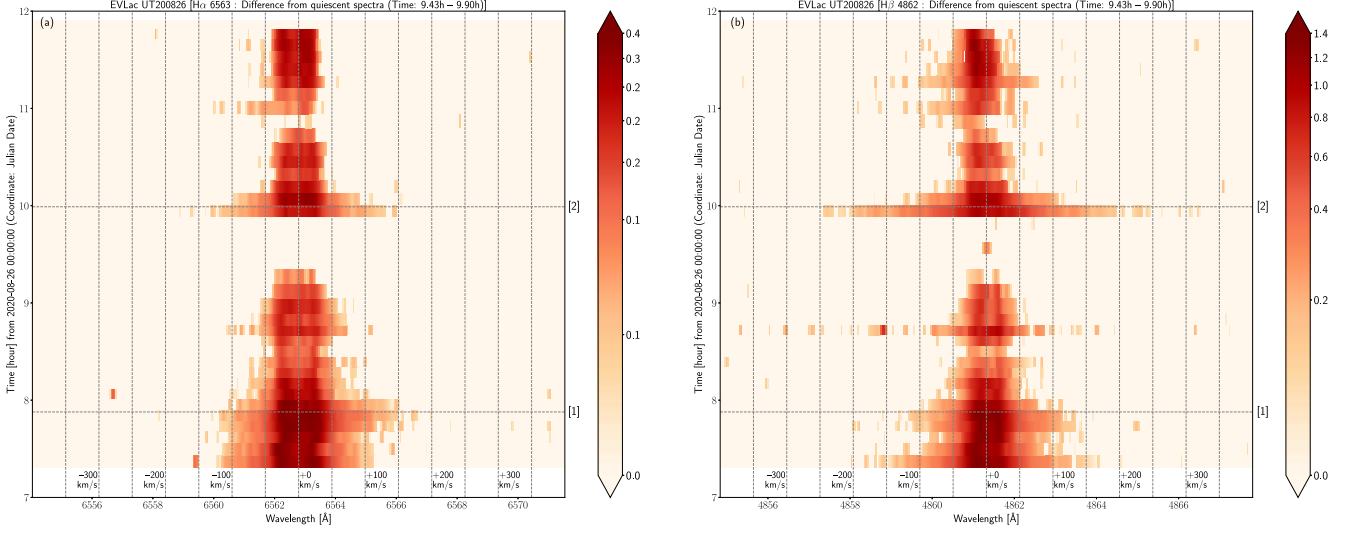


Figure 84. Time evolution of the $H\alpha$ and $H\beta$ line profiles covering Flares E3 and E4 on 2020 August 26, which are plotted similarly with Figure 16. The gray horizontal dashed lines indicate the time [1] and [2], which are shown in Figures 82 (light curves) and 83 (line profiles).

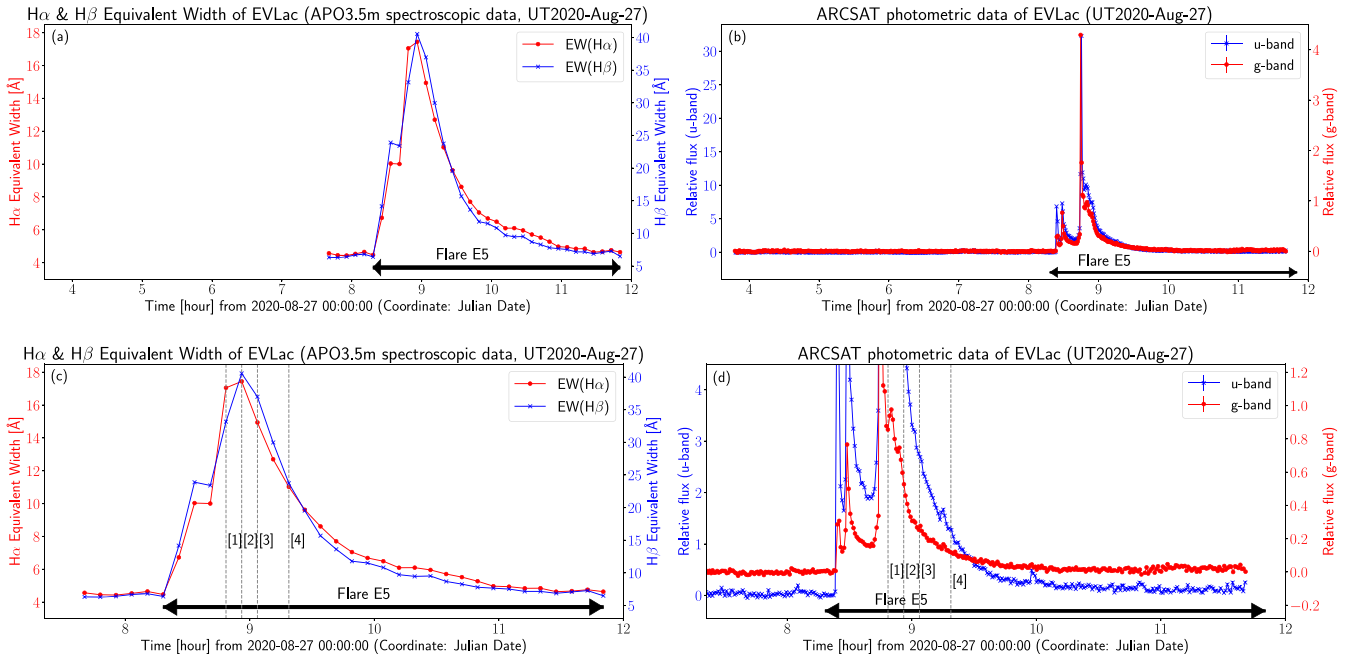


Figure 85. Light curves of EV Lac on 2020 August 27 showing Flare E5, which are plotted similarly with Figures 14(a) and (b). (c) and (d) are enlarged panels of (a) and (b). The gray dashed lines with numbers ([1]–[4]) in (c) and (d) correspond to the time shown with the same numbers in Figures 86 and 87.

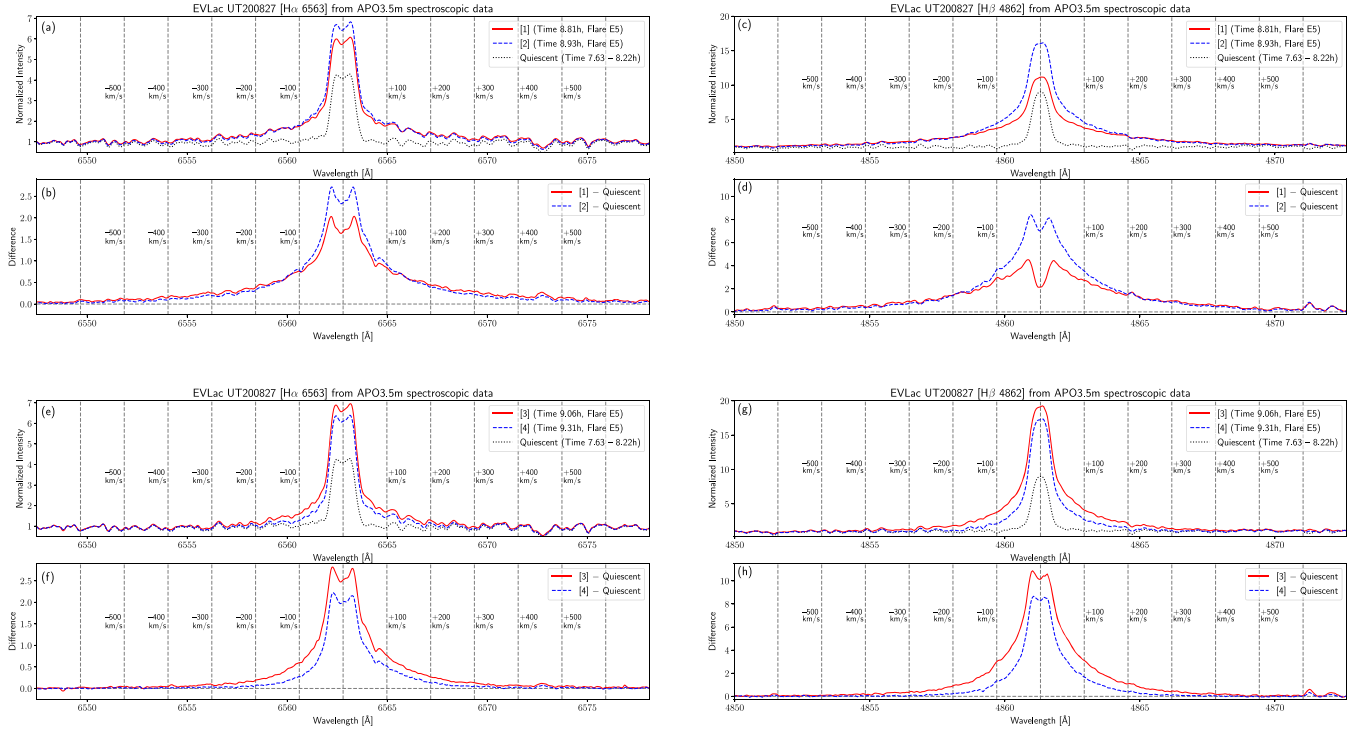


Figure 86. Line profiles of the $H\alpha$ and $H\beta$ emission lines during Flare E5 on 2020 August 27 (at the time [1]–[4]) from APO 3.5 m spectroscopic data, which are plotted similarly with Figure 9.

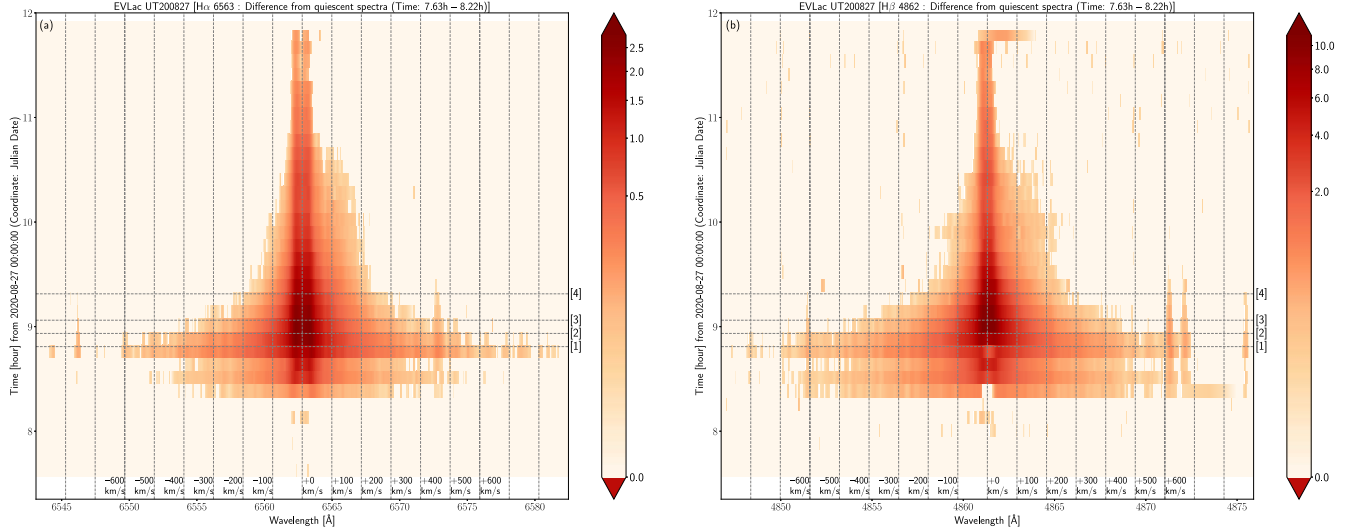


Figure 87. Time evolution of the $H\alpha$ and $H\beta$ line profiles covering Flare E5 on 2020 August 27, which are plotted similarly with Figure 16. The gray horizontal dashed lines indicate the time [1]–[4], which are shown in Figures 85 (light curves) and 86 (line profiles).

to these enhancements in Balmer emission lines, the continuum brightness observed with ARCSAT u and g bands increased by $\sim 20\%$ and $\sim 2\%$, respectively, during Flare E6 (Figure 88(b)).

L_u , L_g , E_u , E_g , $L_{H\alpha}$, $L_{H\beta}$, $E_{H\alpha}$, and $E_{H\beta}$ values are estimated and listed in Table 4. Since the flare already started before the spectroscopic observation began, the luminosity and energy values of Flare E6 estimated here can be only lower limit values.

The $H\alpha$ and $H\beta$ line profiles during Flare E6 are shown in Figures 89 and 90. There were no clear blue or red wing asymmetries during Flare E6.

A.15. Flare E7 Observed on 2020 September 1

On 2020 September 1, one flare (Flare E7) was detected on EV Lac in $H\alpha$ and $H\beta$ lines as shown in Figure 91(a). Flare E7 already started before the spectroscopic observation started. The $H\alpha$ and $H\beta$ EWs increased up to 8.5 \AA and 11.7 \AA , respectively, and $\Delta t_{H\alpha}^{\text{flare}}$ is $> 2.1 \text{ hr}$ (Table 4). There are some gaps of ARCSAT photometric observation data during Flare E7, and the flare itself had already started when the observation started (Figure 73(b)). Because of these, we cannot know whether this flare is a WL flare or not, and we also do not

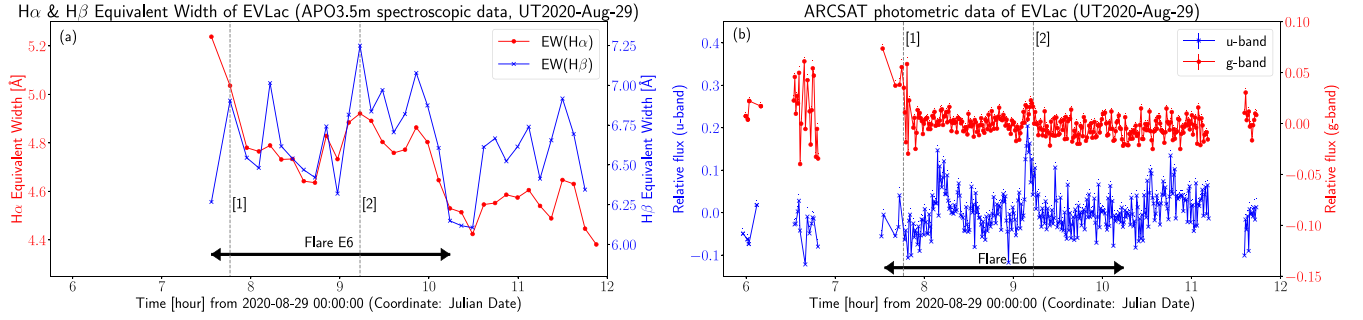


Figure 88. Light curves of EV Lac on 2020 August 29 showing Flare E6, which are plotted similarly with Figures 14(a) and (b). The gray dashed lines with numbers ([1] and [2]) correspond to the time shown with the same numbers in Figures 89 and 90.

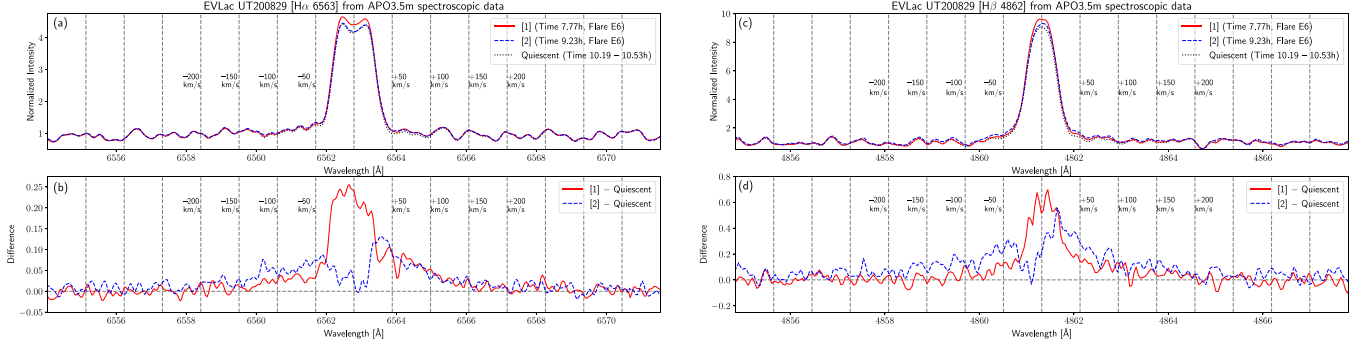


Figure 89. Line profiles of the H α and H β emission lines during Flare E6 on 2020 August 29 (at the time [1] and [2]) from APO 3.5 m spectroscopic data, which are plotted similarly with Figure 9.

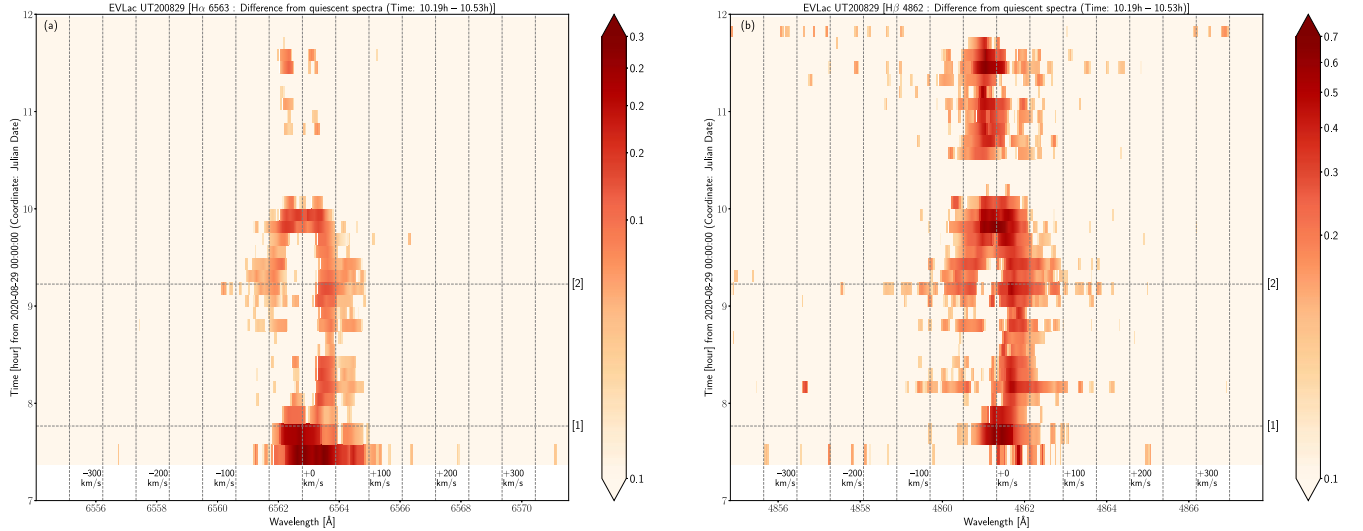


Figure 90. Time evolution of the H α and H β line profiles covering Flare E6 on 2020 August 29, which are plotted similarly with Figure 16. The gray horizontal dashed lines indicate the time [1] and [2], which are shown in Figures 88 (light curves) and 89 (line profiles).

estimate luminosities and energies in photometric bands for this flare. $L_{H\alpha}$, $L_{H\beta}$, $E_{H\alpha}$, and $E_{H\beta}$ values are estimated and listed in Table 4. Since the flare already started before the spectroscopic observation began, the luminosity and energy values of Flare E7 estimated here can be only lower limit values.

The H α and H β line profiles during Flare E7 are shown in Figures 92 and 93. There were no clear red or blue wing asymmetries in the H α and H β lines during Flare E7.

A.16. Flares E8 and E9 Observed on 2020 September 2

On 2020 September 2, two flares (Flares E8 and E9) were detected on EV Lac in H α and H β lines as shown in

Figure 94(c). As for Flare E8, the H α and H β EWs increased up to 4.6 Å and 6.8 Å, respectively, and $\Delta t_{H\alpha}^{\text{flare}}$ is 1.4 hr (Table 4). In addition to these enhancements in Balmer emission lines, the continuum brightness observed with ARCSAT u band increased by $\sim 45\%$ – 50% while that with g band did not show clear increases compared with photometric error ($3\sigma_g = 2.5\%$), during Flare E8 (Figure 94(d)). As for Flare E9, the H α and H β EWs increased up to 4.9 Å and 7.9 Å, respectively, and $\Delta t_{H\alpha}^{\text{flare}}$ is 2.7 hr (Table 4). In addition to these enhancements in Balmer emission lines, the continuum brightness observed with ARCSAT u band increased by $\sim 25\%$ while that with g band did not show clear increases compared

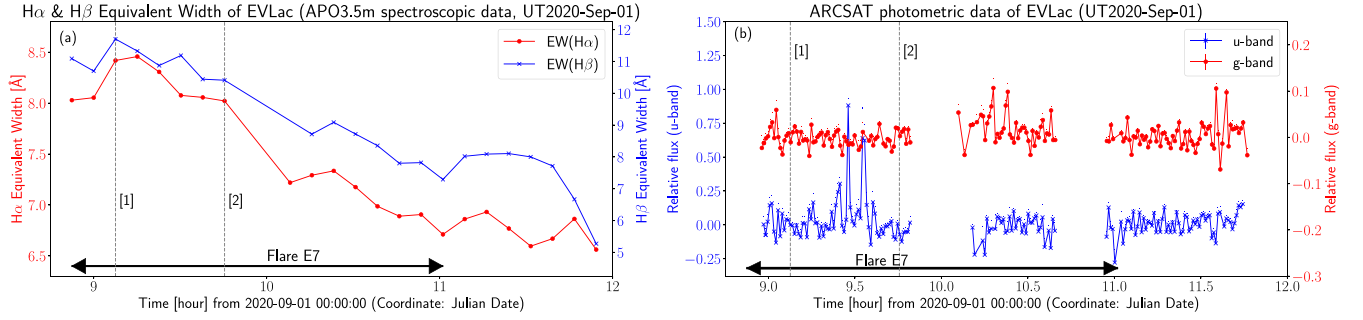


Figure 91. Light curves of EV Lac on 2020 September 1 showing Flare E7, which are plotted similarly with Figures 14(a) and (b). The gray dashed lines with numbers ([1] and [2]) correspond to the time shown with the same numbers in Figures 92 and 93.

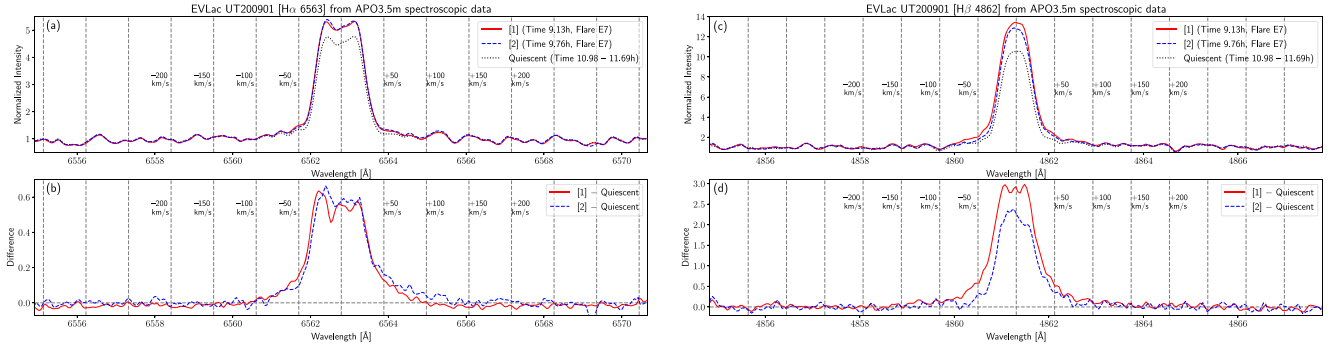


Figure 92. Line profiles of the $H\alpha$ and $H\beta$ emission lines during Flare E7 on 2020 September 1 (at the time [1] and [2]) from APO 3.5 m spectroscopic data, which are plotted similarly with Figure 9.

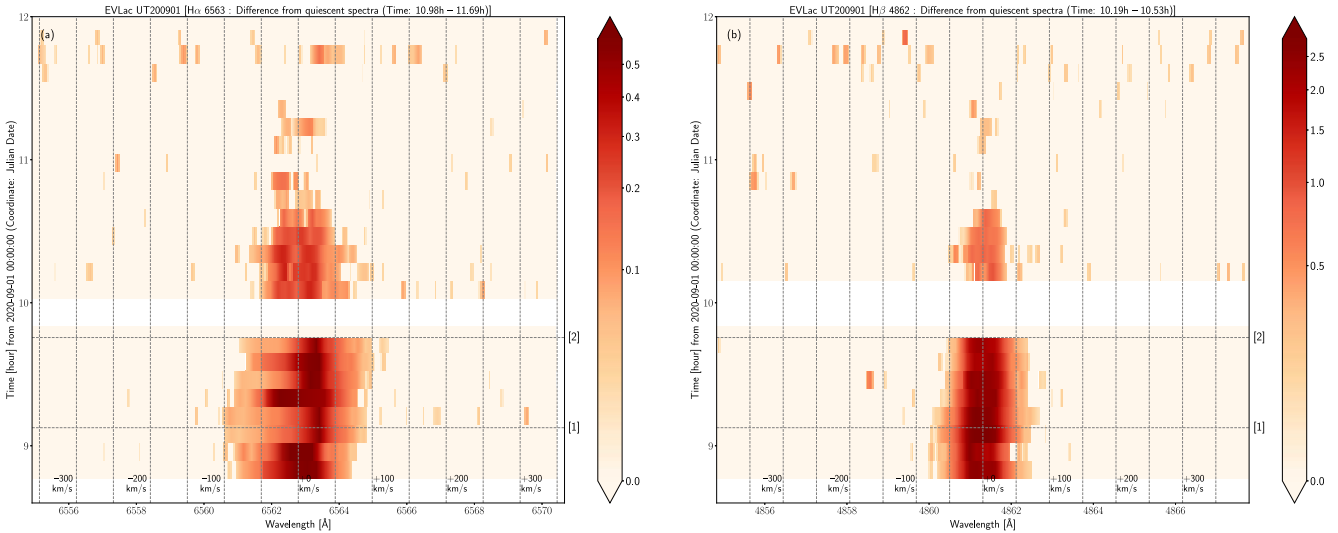


Figure 93. Time evolution of the $H\alpha$ and $H\beta$ line profiles covering Flare E7 on 2020 September 1, which are plotted similarly with Figure 16. The gray horizontal dashed lines indicate the time [1] and [2], which are shown in Figures 91 (light curves) and 92 (line profiles).

with photometric error ($3\sigma_g = 2.5\%$), during Flare E9 (Figure 94(d)). L_u , L_g , E_u , E_g , $L_{H\alpha}$, $L_{H\beta}$, $E_{H\alpha}$, and $E_{H\beta}$ values are estimated and listed in Table 4.

The $H\alpha$ and $H\beta$ line profiles during Flares E8 and E9 are shown in Figures 95 and 96. There were no clear red or blue wing asymmetries in the $H\alpha$ and $H\beta$ lines during Flares E8 and E9. During Flare E9, the $H\alpha$ and $H\beta$ lines show the relatively symmetric line broadenings with ± 150 and ± 200 km s^{-1} , respectively (time [2]–[4] in Figures 95 and 96).

A.17. Flare A1 Observed on 2019 May 17

On 2019 May 17, one flare (Flare A1) was detected on AD Leo in $H\alpha$ and $H\beta$ lines as shown in Figure 97(a). Flare A1 already started when the observation started. The $H\alpha$ and $H\beta$ EWs increased up to 4.9 Å and 5.5 Å, respectively, and $\Delta t_{H\alpha}^{\text{flare}}$ is > 1.4 hr (Table 4). For most of the time of Flare A1, there was no photometric observation of ARCSAT, so we do not know whether there were the continuum brightness changes during Flare A1 (Figure 97(b)). $L_{H\alpha}$, $L_{H\beta}$, $E_{H\alpha}$, and $E_{H\beta}$ values

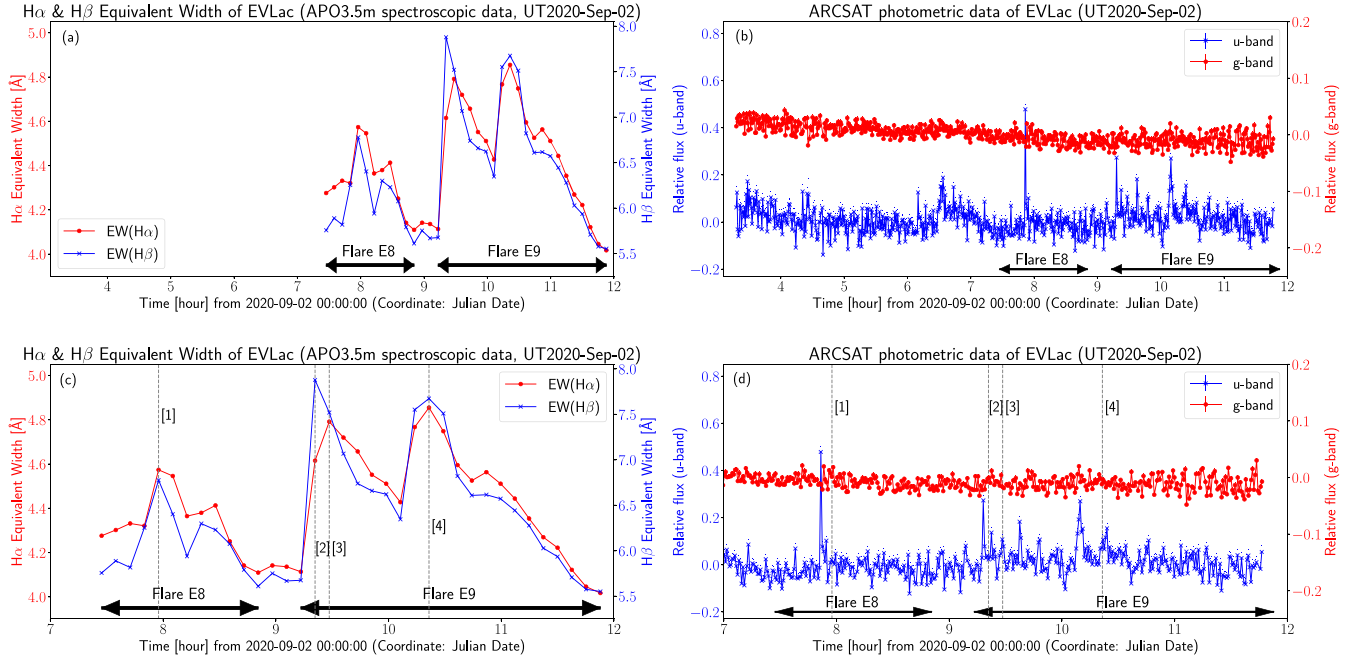


Figure 94. Light curves of EV Lac on 2020 September 2 showing Flares E8 and E9, which are plotted similarly with Figures 14(a) and (b). (c) and (d) are enlarged panels of (a) and (b). The gray dashed lines with numbers ([1]–[4]) in (a) and (b) correspond to the time shown with the same numbers in Figures 95 and 96.

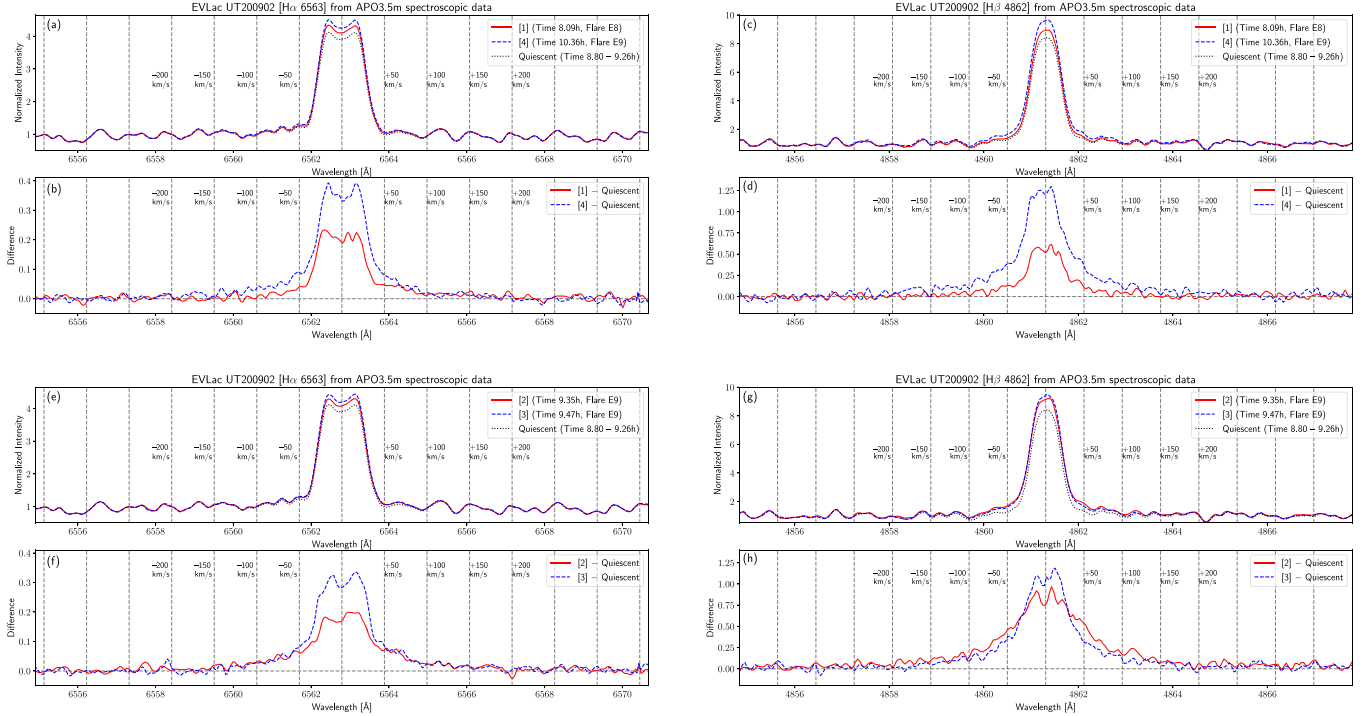


Figure 95. Line profiles of the Hα and Hβ emission lines during Flares E8 and E9 on 2020 September 2 (at the time [1]–[4]) from APO 3.5 m spectroscopic data, which are plotted similarly with Figure 9. The profiles at the time [1] and [4] are in (a)–(d), while those at the time [2] and [3] are in (e)–(h).

are estimated and listed in Table 4. The flare peak luminosities and flare energies described here can be lower limit values since Flare A1 already started when the spectroscopic observation started.

The Hα and Hβ line profiles during Flare A1 are shown in Figures 98 and 99. During Flare A1, the Hα and Hβ lines showed the line broadenings with ± 200 and ± 150 km s⁻¹,

respectively. At around time [1], the blue wing of Hα line could be very slightly enhanced, but it is not so clear, and we do not judge this flare showed blue wing asymmetry (Figure 98(b)).

A.18. Flare A2 Observed on 2019 May 18

On 2019 May 18, one flare (Flare A2) was detected on AD Leo in Hα and Hβ lines as shown in Figure 100(a). The Hα

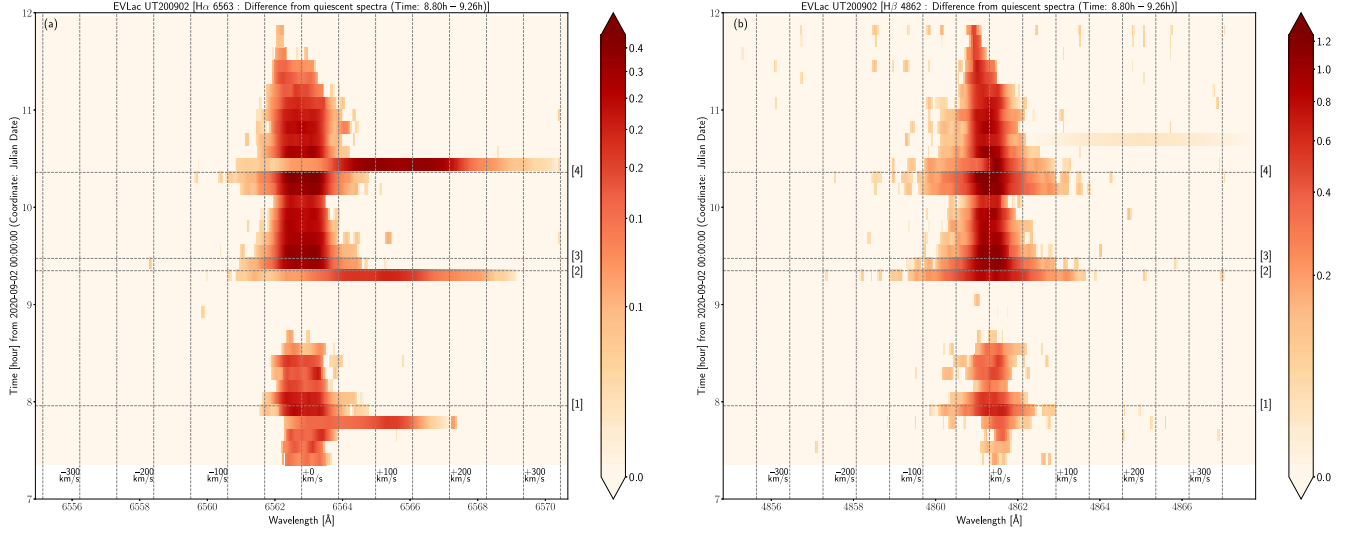


Figure 96. Time evolution of the H α and H β line profiles covering Flares E8 and E9 on 2020 September 2, which are plotted similarly with Figure 16. The gray horizontal dashed lines indicate the time [1]–[4], which are shown in Figures 94 (light curves) and 95 (line profiles).

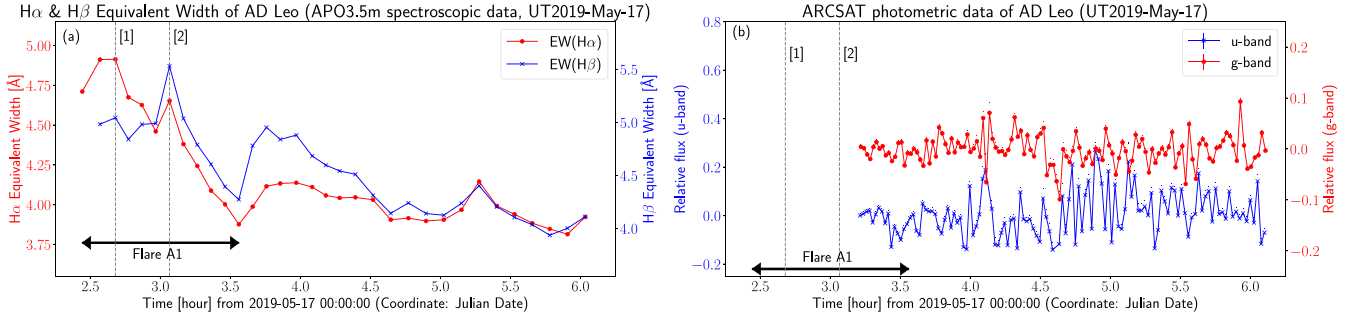


Figure 97. Light curves of AD Leo on 2019 May 17 showing Flare A1, which are plotted similarly with Figures 14(a) and (b). The gray dashed lines with numbers ([1] and [2]) correspond to the time shown with the same numbers in Figures 98 and 99.

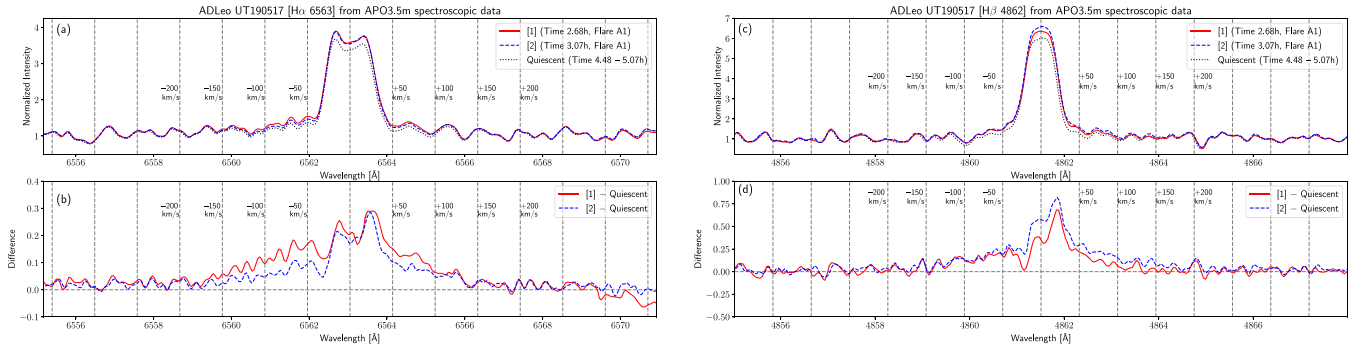


Figure 98. Line profiles of the H α and H β emission lines during Flare A1 on 2019 May 17 (at the time [1] and [2]) from APO 3.5 m spectroscopic data, which are plotted similarly with Figure 9.

and H β EWs increased up to 5.1 Å and 7.6 Å, respectively, and $\Delta t_{\text{H}\alpha}^{\text{flare}}$ is 1.0 hr (Table 4). In addition to these enhancements in Balmer emission lines, the continuum brightness observed with ARCSAT u and g bands increased by $\sim 50\%$ and $\sim 4\text{--}5\%$, respectively, during Flare A2 (Figure 100(b)). L_u , L_g , E_u , E_g , $L_{\text{H}\alpha}$, $L_{\text{H}\beta}$, $E_{\text{H}\alpha}$, and $E_{\text{H}\beta}$ values are estimated and listed in Table 4.

The H α and H β line profiles during Flare A2 are shown in Figures 101 and 102. During Flare A2, the H α and H β lines show the line broadenings with $-250\text{--}+300$ and $-250\text{--}+400\text{ km s}^{-1}$, respectively. In particular, at around time [1], the red wings of H α and H β lines were lightly enhanced. (Figures 101(b)). This red wing asymmetry was more clearly seen in H β line than in H α line (Figures 101(d)).

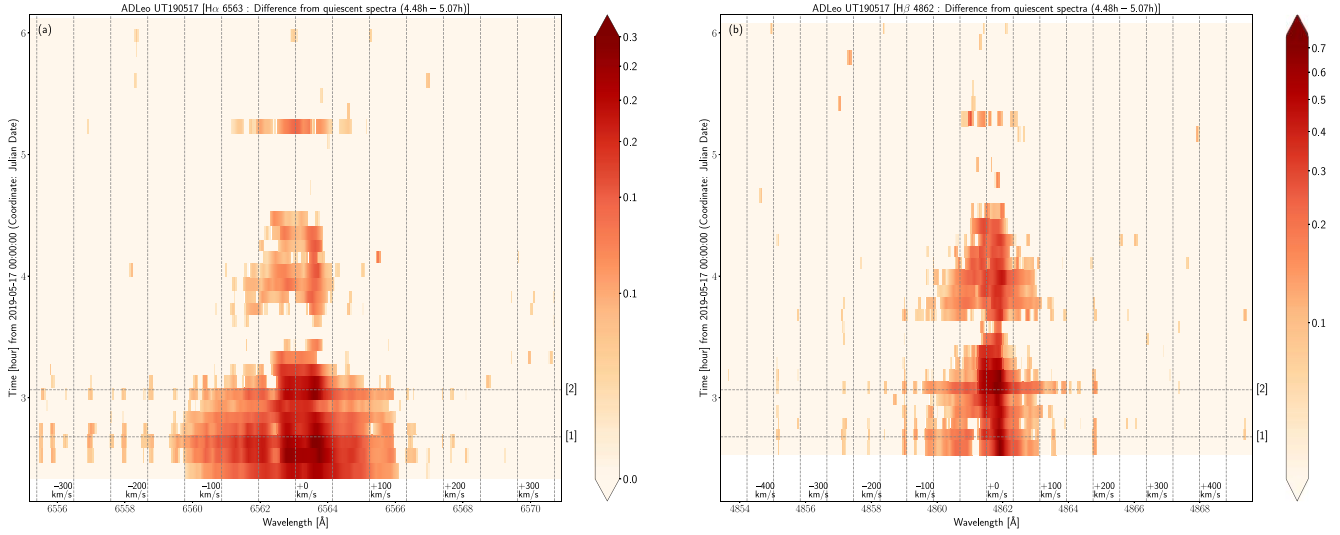


Figure 99. Time evolution of the $H\alpha$ and $H\beta$ line profiles covering Flare A1 on 2019 May 17, which are plotted similarly with Figure 16. The gray horizontal dashed lines indicate the time [1] and [2], which are shown in Figures 97 (light curves) and 98 (line profiles).

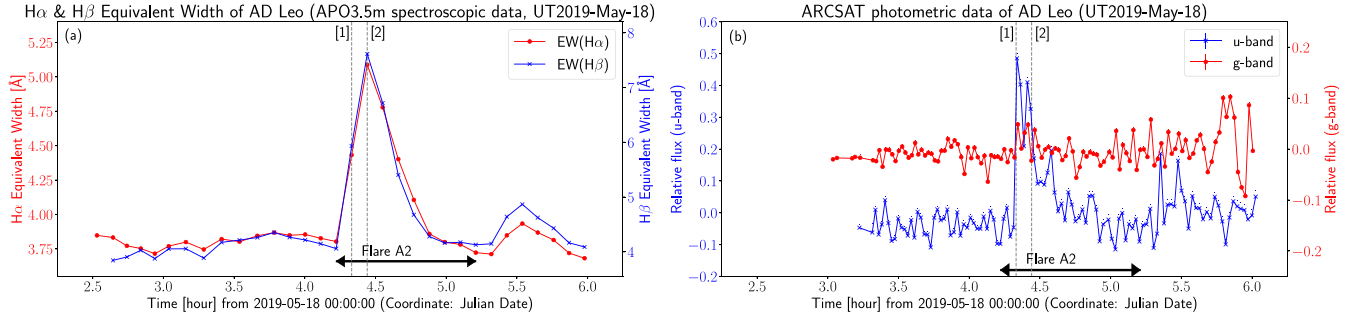


Figure 100. Light curves of AD Leo on 2019 May 18 showing Flare A2, which are plotted similarly with Figures 14(a) and (b). The gray dashed lines with numbers ([1] and [2]) correspond to the time shown with the same numbers in Figures 101 and 102.

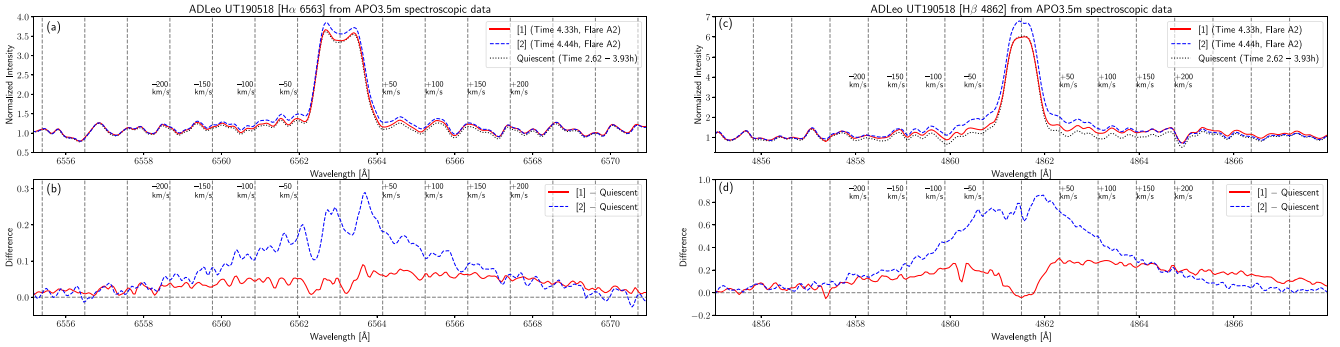


Figure 101. Line profiles of the $H\alpha$ and $H\beta$ emission lines during Flare A2 on 2019 May 18 (at the time [1] and [2]) from APO 3.5 m spectroscopic data, which are plotted similarly with Figure 9.

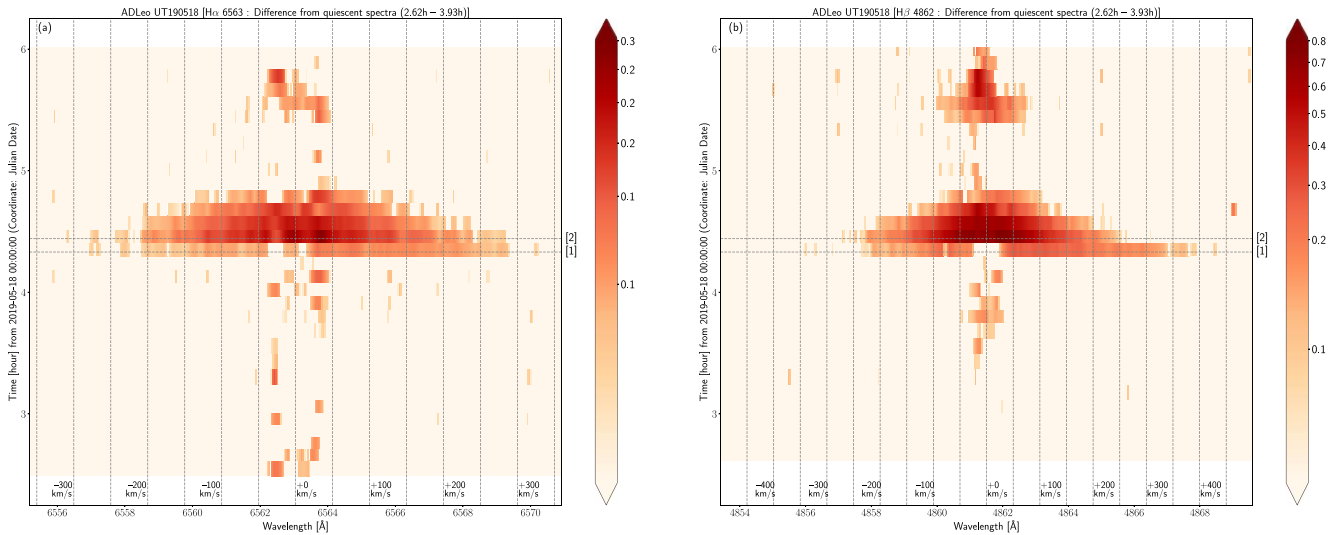


Figure 102. Time evolution of the H α and H β line profiles covering Flare A2 on 2019 May 18, which are plotted similarly with Figure 16. The gray horizontal dashed lines indicate the time [1] and [2], which are shown in Figures 100 (light curves) and 101 (line profiles).

ORCID iDs

Yuta Notsu <https://orcid.org/0000-0002-0412-0849>
 Adam F. Kowalski <https://orcid.org/0000-0001-7458-1176>
 Hiroyuki Maehara <https://orcid.org/0000-0003-0332-0811>
 Kosuke Namekata <https://orcid.org/0000-0002-1297-9485>
 Kenji Hamaguchi <https://orcid.org/0000-0001-7515-2779>
 Teruaki Enoto <https://orcid.org/0000-0003-1244-3100>
 Isaiah I. Tristan <https://orcid.org/0000-0001-5974-4758>
 Suzanne L. Hawley <https://orcid.org/0000-0002-6629-4182>
 James R. A. Davenport <https://orcid.org/0000-0002-0637-835X>
 Satoshi Honda <https://orcid.org/0000-0001-6653-8741>
 Kai Ikuta <https://orcid.org/0000-0002-5978-057X>
 Shun Inoue <https://orcid.org/0000-0003-3085-304X>
 Daisaku Nogami <https://orcid.org/0000-0001-9588-1872>
 Kazunari Shibata <https://orcid.org/0000-0003-1206-7889>

References

- Aarnio, A. N., Matt, S. P., & Stassun, K. G. 2012, *ApJ*, **760**, 9
 Airapetian, V. S., Barnes, R., Cohen, O., et al. 2020, *IAASB*, **19**, 136
 Airapetian, V. S., Glocer, A., Gronoff, G., Hébrard, E., & Danchi, W. 2016, *NatGe*, **9**, 452
 Allred, J. C., Hawley, S. L., Abbott, W. P., & Carlsson, M. 2005, *ApJ*, **630**, 573
 Allred, J. C., Hawley, S. L., Abbott, W. P., & Carlsson, M. 2006, *ApJ*, **644**, 484
 Allred, J. C., Kowalski, A. F., & Carlsson, M. 2015, *ApJ*, **809**, 104
 Alvarado-Gómez, J. D., Drake, J. J., Cohen, O., Moschou, S. P., & Garraffo, C. 2018, *ApJ*, **862**, 93
 Antolin, P. 2020, *PAPF*, **62**, 014016
 Aulanier, G., Démoulin, P., Schrijver, C. J., et al. 2013, *A&A*, **549**, A66
 Battersby, S. 2019, *PNAS*, **116**, 23368
 Bellotti, S., Morin, J., Lehmann, L. T., et al. 2023, *A&A*, **676**, A56
 Benz, A. O., & Güdel, M. 2010, *ARA&A*, **48**, 241
 Berlicki, A. 2007, in ASP Conf. Ser. 368, *The Physics of Chromospheric Plasmas*, ed. P. Heinzel, I. Dorotović, & R. J. Rutten (San Francisco, CA: ASP), 387
 Bicz, K., Falewicz, R., Pietras, M., Siarkowski, M., & Preś, P. 2022, *ApJ*, **935**, 102
 Brasseur, C. E., Osten, R. A., Tristan, I. I., & Kowalski, A. F. 2023, *ApJ*, **944**, 5
 Brown, T. M., Baliber, N., Bianco, F. B., et al. 2013, *PASP*, **125**, 1031
 Buzulukova, N., & Tsurutani, B. 2022, *FrASS*, **9**, 1017103
 Canfield, R. C., Penn, M. J., Wulser, J.-P., & Kiplinger, A. L. 1990, *ApJ*, **363**, 318
 Chen, H., Zhan, Z., Youngblood, A., et al. 2021, *NatAs*, **5**, 298
 Cliver, E. W., Schrijver, C. J., Shibata, K., & Usoskin, I. G. 2022, *LRSP*, **19**, 2
 Collins, K. A., Kielkopf, J. F., Stassun, K. G., & Hessman, F. V. 2017, *AJ*, **153**, 77
 Cranmer, S. R. 2017, *ApJ*, **840**, 114
 Crespo-Chacón, I., Montes, D., García-Alvarez, D., et al. 2006, *A&A*, **452**, 987
 Crosley, M. K., & Osten, R. A. 2018, *ApJ*, **856**, 39
 Davenport, J. R. A. 2016, *ApJ*, **829**, 23
 Davenport, J. R. A., Becker, A. C., Kowalski, A. F., et al. 2012, *ApJ*, **748**, 58
 Davenport, J. R. A., Hawley, S. L., Hebb, L., et al. 2014, *ApJ*, **797**, 122
 Davenport, J. R. A., Mendoza, G. T., & Hawley, S. L. 2020, *AJ*, **160**, 36
 Drake, J. J., Cohen, O., Garraffo, C., & Kashyap, V. 2016, in IAU Symp. 320, *Solar and Stellar Flares and their Effects on Planets*, ed. A. G. Kosovichev, S. L. Hawley, & P. Heinzel (Cambridge: Cambridge Univ. Press), 196
 Drake, J. J., Cohen, O., Yashiro, S., & Gopalswamy, N. 2013, *ApJ*, **764**, 170
 Drake, S. A., & Ulrich, R. K. 1980, *ApJS*, **42**, 351
 Eason, E. L. E., Giampapa, M. S., Radick, R. R., Worden, S. P., & Hege, E. K. 1992, *AJ*, **104**, 1161
 Emslie, A. G., Dennis, B. R., Shih, A. Y., et al. 2012, *ApJ*, **759**, 71
 Fan, Y. 2018, *ApJ*, **862**, 54
 Fausnaugh, M. M., Burke, C. J., Caldwell, D. A., et al. 2019, TESS Data Release Notes: Sector 7, DR9 NASA/TM-2019-220170, NASA, <https://ntrs.nasa.gov/citations/20190002170>
 Fausnaugh, M. M., Burke, C. J., Caldwell, D. A., et al. 2021, TESS Data Release Notes: Sector 34, DR50 NASA/TM-20210012992, NASA, <https://ntrs.nasa.gov/citations/20210012992>
 Feinstein, A. D., Montet, B. T., Ansdell, M., et al. 2020, *AJ*, **160**, 219
 Fisher, G. H., Canfield, R. C., & McClymont, A. N. 1985, *ApJ*, **289**, 414
 Flores Soriano, M., & Strassmeier, K. G. 2017, *A&A*, **597**, A101
 Fuhrmeister, B., Czesla, S., Schmitt, J. H. M. M., et al. 2018, *A&A*, **615**, A14
 Fuhrmeister, B., Lalitha, S., Poppenhäuser, K., et al. 2011, *A&A*, **534**, A133
 Fuhrmeister, B., Liefke, C., Schmitt, J. H. M. M., & Reiners, A. 2008, *A&A*, **487**, 293
 Gaia Collaboration, Brown, A. G. A., Vallenari, A., et al. 2018, *A&A*, **616**, A1
 Gendreau, K. C., Arzoumanian, Z., Adkins, P. W., et al. 2016, *Proc. SPIE*, **9905**, 99051H
 Gershberg, R. E. 2005, *Solar-type Activity in Main-sequence Stars* (Berlin: Springer)
 Gontikakis, C., Vial, J. C., & Gouttebroze, P. 1997, *A&A*, **325**, 803
 Gopalswamy, N., Shimojo, M., Lu, W., et al. 2003, *ApJ*, **586**, 562
 Graham, D. R., & Cauzzi, G. 2015, *ApJL*, **807**, L22
 Graham, D. R., Cauzzi, G., Zangrilli, L., et al. 2020, *ApJ*, **895**, 6
 Grayver, A., Bower, D. J., Saur, J., Dorn, C., & Morris, B. M. 2022, *ApJL*, **941**, L7
 Guarcello, M. G., Micela, G., Sciortino, S., et al. 2019, *A&A*, **622**, A210
 Güdel, M. 2004, *A&ARv*, **12**, 71
 Güdel, M., Audard, M., Reale, F., Skinner, S. L., & Linsky, J. L. 2004, *A&A*, **416**, 713
 Güdel, M., Benz, A. O., Schmitt, J. H. M. M., & Skinner, S. L. 1996, *ApJ*, **471**, 1002
 Gunn, A. G., Doyle, J. G., Mathioudakis, M., Houdebine, E. R., & Avgoloupis, S. 1994, *A&A*, **285**, 489

- Haisch, B. M. 1989, *A&A*, **219**, 317
- Hamaguchi, K., Reep, J. W., Airapetian, V., et al. 2023, *ApJ*, **944**, 163
- Hawley, S. L., Davenport, J. R. A., Kowalski, A. F., et al. 2014, *ApJ*, **797**, 121
- Hawley, S. L., & Fisher, G. H. 1992, *ApJS*, **78**, 565
- Hawley, S. L., Fisher, G. H., Simon, T., et al. 1995, *ApJ*, **453**, 464
- Hawley, S. L., & Pettersen, B. R. 1991, *ApJ*, **378**, 725
- Hawley, S. L., Walkowicz, L. M., Allred, J. C., & Valenti, J. A. 2007, *PASP*, **119**, 67
- Heinzel, P. 2019, in *The Sun as a Guide to Stellar Physics*, ed. O. Engvold, J.-C. Vial, & A. Skumanich (Amsterdam: Elsevier), 157
- Heinzel, P., Gouttebroze, P., & Vial, J. C. 1994a, *A&A*, **292**, 656
- Heinzel, P., Karlicky, M., Kotrc, P., & Svestka, Z. 1994b, *SoPh*, **152**, 393
- Heinzel, P., & Rempolt, B. 1987, *SoPh*, **110**, 171
- Hilton, E. J. 2011, PhD thesis, Univ. of Washington
- Hirayama, T. 1986, *NASCP*, **2442**, 149
- Holman, G. D. 2012, *ApJ*, **745**, 52
- Holman, G. D., Aschwanden, M. J., Aurass, H., et al. 2011, *SSRv*, **159**, 107
- Honda, S., Notsu, Y., Namekata, K., et al. 2018, *PASJ*, **70**, 62
- Hong, J., Li, Y., Ding, M. D., & Zhou, Y.-H. 2020, *ApJ*, **890**, 115
- Hori, K., Yokoyama, T., Kosugi, T., & Shibata, K. 1997, *ApJ*, **489**, 426
- Houdebine, E. R., Foing, B. H., Doyle, J. G., & Rodono, M. 1993, *A&A*, **274**, 245
- Houdebine, E. R., Foing, B. H., & Rodono, M. 1990, *A&A*, **238**, 249
- Howard, W. S., Corbett, H., Law, N. M., et al. 2019, *ApJ*, **881**, 9
- Howard, W. S., Corbett, H., Law, N. M., et al. 2020, *ApJ*, **902**, 115
- Huang, N., Xu, Y., Sadykov, V. M., Jing, J., & Wang, H. 2019, *ApJL*, **878**, L15
- Hunt-Walker, N. M., Hilton, E. J., Kowalski, A. F., Hawley, S. L., & Matthews, J. M. 2012, *PASP*, **124**, 545
- Ichimoto, K., & Kurokawa, H. 1984, *SoPh*, **93**, 105
- Ikuta, K., Namekata, K., Notsu, Y., et al. 2023, *ApJ*, **948**, 64
- Inoue, S., Maehara, H., Notsu, Y., et al. 2023, *ApJ*, **948**, 9
- Jackman, J. A. G., Wheatley, P. J., Acton, J. S., et al. 2021, *MNRAS*, **504**, 3246
- Jardine, M., Collier Cameron, A., Donati, J. F., & Hussain, G. A. J. 2020, *MNRAS*, **491**, 4076
- Johns-Krull, C. M., & Valenti, J. A. 2000, in *ASP Conf. Ser. 198, Stellar Clusters and Associations: Convection, Rotation, and Dynamos*, ed. R. Pallavicini, G. Micela, & S. Sciortino (San Francisco, CA: ASP), 371
- Johnson, E. N., Czesla, S., Fuhrmeister, B., et al. 2021, *A&A*, **651**, A105
- Kochukhov, O. 2021, *A&ARv*, **29**, 1
- Kotani, Y., Shibata, K., Ishii, T. T., et al. 2023, *ApJ*, **943**, 143
- Kowalski, A. F. 2016, in *IAU Symp. 320, Solar and Stellar Flares and their Effects on Planets*, ed. A. G. Kosovichev, S. L. Hawley, & P. Heinzel (Cambridge: Cambridge Univ. Press), 259
- Kowalski, A. F., Allred, J. C., Carlsson, M., et al. 2022, *ApJ*, **928**, 190
- Kowalski, A. F., Allred, J. C., Daw, A., Cauzzi, G., & Carlsson, M. 2017, *ApJ*, **836**, 12
- Kowalski, A. F., Butler, E., Daw, A. N., et al. 2019, *ApJ*, **878**, 135
- Kowalski, A. F., Hawley, S. L., Holtzman, J. A., Wisniewski, J. P., & Hilton, E. J. 2010, *ApJL*, **714**, L98
- Kowalski, A. F., Hawley, S. L., Wisniewski, J. P., et al. 2013, *ApJS*, **207**, 15
- Kuridze, D., Mathioudakis, M., Christian, D. J., et al. 2016, *ApJ*, **832**, 147
- Kuridze, D., Mathioudakis, M., Simões, P. J. A., et al. 2015, *ApJ*, **813**, 125
- Labrosse, N., Heinzel, P., Vial, J. C., et al. 2010, *SSRv*, **151**, 243
- Lacy, C. H., Moffett, T. J., & Evans, D. S. 1976, *ApJS*, **30**, 85
- Lalitha, S., Fuhrmeister, B., Wolter, U., et al. 2013, *A&A*, **560**, A69
- Lammer, H., Lichtenegger, H. I. M., Kulikov, Y. N., et al. 2007, *AsBio*, **7**, 185
- Leitzinger, M., & Odert, P. 2022, *SerAJ*, **205**, 1
- Leitzinger, M., Odert, P., & Heinzel, P. 2022, *MNRAS*, **513**, 6058
- Li, Y., Ding, M. D., Hong, J., Li, H., & Gan, W. Q. 2019, *ApJ*, **879**, 30
- Libbrecht, T., de la Cruz Rodríguez, J., Danilovic, S., Leenaerts, J., & Pazira, H. 2019, *A&A*, **621**, A35
- Liefke, C., Fuhrmeister, B., & Schmitt, J. H. M. M. 2010, *A&A*, **514**, A94
- Linsky, J. 2019, *Host Stars and their Effects on Exoplanet Atmospheres: An Introductory Overview*, Vol. 955 (Berlin: Springer)
- Longcope, D. W. 2014, *ApJ*, **795**, 10
- Loyd, R. O. P., Mason, J. P., Jin, M., et al. 2022, *ApJ*, **936**, 170
- Lynch, B. J., & Edmondson, J. K. 2013, *ApJ*, **764**, 87
- Lynch, B. J., Edmondson, J. K., Kazachenko, M. D., & Guidoni, S. E. 2016, *ApJ*, **826**, 43
- Lynch, B. J., Wood, B. E., Jin, M., et al. 2023, *BAAS*, **55**, 254
- Maehara, H., Notsu, Y., Namekata, K., et al. 2021, *PASJ*, **73**, 44
- Maehara, H., Shibayama, T., Notsu, S., et al. 2012, *Natur*, **485**, 478
- Maehara, H., Shibayama, T., Notsu, Y., et al. 2015, *EP&S*, **67**, 59
- Medina, A. A., Winters, J. G., Irwin, J. M., & Charbonneau, D. 2020, *ApJ*, **905**, 107
- Milligan, R. O., Kerr, G. S., Dennis, B. R., et al. 2014, *ApJ*, **793**, 70
- Mitra-Kraev, U., Harra, L. K., Güdel, M., et al. 2005, *A&A*, **431**, 679
- Miyake, F., Usoskin, I., & Poluianov, S. 2019, *Extreme Solar Particle Storms: The Hostile Sun* (Bristol: IOP Publishing)
- Morin, J., Donati, J. F., Petit, P., et al. 2008, *MNRAS*, **390**, 567
- Moschou, S.-P., Drake, J. J., Cohen, O., et al. 2019, *ApJ*, **877**, 105
- Muheki, P., Guenther, E. W., Mutabazi, T., & Jurua, E. 2020a, *A&A*, **637**, A13
- Muheki, P., Guenther, E. W., Mutabazi, T., & Jurua, E. 2020b, *MNRAS*, **499**, 5047
- Mullan, D. J., Mathioudakis, M., Bloomfield, D. S., & Christian, D. J. 2006, *ApJS*, **164**, 173
- Namekata, K., Ichimoto, K., Ishii, T. T., & Shibata, K. 2022a, *ApJ*, **933**, 209
- Namekata, K., Maehara, H., Honda, S., et al. 2022b, arXiv:2211.05506
- Namekata, K., Maehara, H., Honda, S., et al. 2022c, *NatAs*, **6**, 241
- Namekata, K., Maehara, H., Honda, S., et al. 2022d, *ApJL*, **926**, L5
- Namekata, K., Maehara, H., Sasaki, R., et al. 2020, *PASJ*, **72**, 68
- Namekata, K., Sakaue, T., Watanabe, K., Asai, A., & Shibata, K. 2017a, *PASJ*, **69**, 7
- Namekata, K., Sakaue, T., Watanabe, K., et al. 2017b, *ApJ*, **851**, 91
- Namizaki, K., Namekata, K., Maehara, H., et al. 2023, *ApJ*, **945**, 61
- Neupert, W. M. 1968, *ApJL*, **153**, L59
- Notsu, Y., Maehara, H., Honda, S., et al. 2019, *ApJ*, **876**, 58
- Notsu, Y., Shibayama, T., Maehara, H., et al. 2013b, *ApJ*, **771**, 127
- Odert, P., Leitzinger, M., Guenther, E. W., & Heinzel, P. 2020, *MNRAS*, **494**, 3766
- Odert, P., Leitzinger, M., Hanslmeier, A., & Lammer, H. 2017, *MNRAS*, **472**, 876
- Okada, S., Ichimoto, K., Machida, A., et al. 2020, *PASJ*, **72**, 71
- Okajima, T., Soong, Y., Balsamo, E. R., et al. 2016, *Proc. SPIE*, **9905**, 99054X
- Okamoto, S., Notsu, Y., Maehara, H., et al. 2021, *ApJ*, **906**, 72
- Oks, E., & Gershberg, R. E. 2016, *ApJ*, **819**, 16
- Osten, R. A., Hawley, S. L., Allred, J., et al. 2006, *ApJ*, **647**, 1349
- Osten, R. A., & Wolk, S. J. 2015, *ApJ*, **809**, 79
- Otsu, T., Asai, A., Ichimoto, K., Ishii, T. T., & Namekata, K. 2022, *ApJ*, **939**, 98
- Panos, B., Kleint, L., Huwiler, C., et al. 2018, *ApJ*, **861**, 62
- Parenti, S. 2014, *LRSP*, **11**, 1
- Paudel, R. R., Barclay, T., Schlieder, J. E., et al. 2021, *ApJ*, **922**, 31
- Paudel, R. R., Gizis, J. E., Mullan, D. J., et al. 2019, *MNRAS*, **486**, 1438
- Pillitteri, I., Argiroffi, C., Maggio, A., et al. 2022, *A&A*, **666**, A198
- Prigozhin, G., Gendreau, K., Doty, J. P., et al. 2016, *Proc. SPIE*, **9905**, 990511
- Raassen, A. J. J., Mitra-Kraev, U., & Güdel, M. 2007, *MNRAS*, **379**, 1075
- Reep, J. W., & Airapetian, V. S. 2023, *ApJ*, **958**, 9
- Reid, I. N., & Hawley, S. L. 2005, *New Light on Dark Stars: Red Dwarfs, Low-mass Stars, Brown Dwarfs* (Berlin: Springer)
- Reiners, A., & Basri, G. 2007, *ApJ*, **656**, 1121
- Remillard, R. A., Loewenstein, M., Steiner, J. F., et al. 2022, *AJ*, **163**, 130
- Ricker, G. R., Winn, J. N., Vanderspek, R., et al. 2015, *JATIS*, **1**, 014003
- Rodrigo, C., & Solano, E. 2020, in *Contributions to the XIV.0 Scientific Meeting (Virtual) of the Spanish Astronomical Society (La Laguna: SEA)*, 182
- Rodrigo, C., Solano, E., & Bayo, A. 2012, *SVO Filter Profile Service Version 1.0, IVOA*
- Saar, S. H., & Linsky, J. L. 1985, *ApJL*, **299**, L47
- Sakaue, T., & Shibata, K. 2021, *ApJ*, **919**, 29
- Scargle, J. D., Norris, J. P., Jackson, B., & Chiang, J. 2013, *ApJ*, **764**, 167
- Scheucher, M., Grenfell, J. L., Wunderlich, F., et al. 2018, *ApJ*, **863**, 6
- Schöfer, P., Jeffers, S. V., Reiners, A., et al. 2022, *A&A*, **663**, A68
- Segura, A., Walkowicz, L. M., Meadows, V., Kasting, J., & Hawley, S. 2010, *AsBio*, **10**, 751
- Seki, D., Otsuji, K., Ishii, T., et al. 2019, *SunGe*, **14**, 95
- Seki, D., Otsuji, K., Ishii, T. T., Asai, A., & Ichimoto, K. 2021, *EP&S*, **73**, 58
- Shibata, K., Isobe, H., Hillier, A., et al. 2013, *PASJ*, **65**, 49
- Shibata, K., & Magara, T. 2011, *LRSP*, **8**, 6
- Shibata, K., & Yokoyama, T. 1999, *ApJL*, **526**, L49
- Shibata, K., & Yokoyama, T. 2002, *ApJ*, **577**, 422
- Shibayama, T., Maehara, H., Notsu, S., et al. 2013, *ApJS*, **209**, 5
- Shoji, M., & Kurokawa, H. 1995, *PASJ*, **47**, 239
- Sinha, S., Srivastava, N., & Nandy, D. 2019, *ApJ*, **880**, 84
- Smith, R. K., Brickhouse, N. S., Liedahl, D. A., & Raymond, J. C. 2001, *ApJL*, **556**, L91
- Stelzer, B., Caramazza, M., Raetz, S., Argiroffi, C., & Coffaro, M. 2022, *A&A*, **667**, L9
- Sun, X., Török, T., & DeRosa, M. L. 2022, *MNRAS*, **509**, 5075

- Švestka, Z., Kopecký, M., & Blaha, M. 1962, *BAICz*, **13**, 37
- Takahashi, T., Mizuno, Y., & Shibata, K. 2016, *ApJL*, **833**, L8
- Takasao, S., Mitsuishi, I., Shimura, T., et al. 2020, *ApJ*, **901**, 70
- Tang, F. 1983, *SoPh*, **83**, 15
- Tei, A., Sakaue, T., Okamoto, T. J., et al. 2018, *PASJ*, **70**, 100
- Thalmann, J. K., Su, Y., Temmer, M., & Veronig, A. M. 2015, *ApJL*, **801**, L23
- Tilley, M. A., Segura, A., Meadows, V., Hawley, S., & Davenport, J. 2019, *AsBio*, **19**, 64
- Tokovinin, A., Fischer, D. A., Bonati, M., et al. 2013, *PASP*, **125**, 1336
- Toriumi, S., Airapetian, V. S., Hudson, H. S., et al. 2020, *ApJ*, **902**, 36
- Török, T., Panasenco, O., Titov, V. S., et al. 2011, *ApJL*, **739**, L63
- Tristan, I. I., Notsu, Y., Kowalski, A. F., et al. 2023, *ApJ*, **951**, 33
- Usoskin, I. G., & Kovaltsov, G. A. 2021, *GeoRL*, **48**, e94848
- Vanderspek, R., Doty, J. P., Fausnaugh, M., et al. 2018, TESS Instrument Handbook v0.1, TESS Science Office, https://archive.stsci.edu/files/live/sites/mast/files/home/missions-and-data/active-missions/tess/_documents/TESS_Instrument_Handbook_v0.1.pdf
- Vernazza, J. E., Avrett, E. H., & Loeser, R. 1981, *ApJS*, **45**, 635
- Veronig, A. M., Odert, P., Leitzinger, M., et al. 2021, *NatAs*, **5**, 697
- Vial, J.-C., & Engvold, O. 2015, *Solar Prominences* (Berlin: Springer)
- Vida, K., Kriskovics, L., Oláh, K., et al. 2016, *A&A*, **590**, A11
- Vida, K., Leitzinger, M., Kriskovics, L., et al. 2019, *A&A*, **623**, A49
- Vidotto, A. A. 2021, *LRSP*, **18**, 3
- Villadsen, J., & Hallinan, G. 2019, *ApJ*, **871**, 214
- Wang, S.-i., Hildebrand, R. H., Hobbs, L. M., et al. 2003, *Proc. SPIE*, **4841**, 1145
- Warmuth, A., & Mann, G. 2016, *A&A*, **588**, A115
- Watanabe, K., Kitagawa, J., & Masuda, S. 2017, *ApJ*, **850**, 204
- Wollmann, J., Heinzl, P., & Kabáth, P. 2023, *A&A*, **669**, A118
- Wood, B. E., Howard, R. A., & Linton, M. G. 2016, *ApJ*, **816**, 67
- Wood, B. E., Müller, H.-R., Redfield, S., et al. 2021, *ApJ*, **915**, 37
- Woods, T. N., Kopp, G., & Chamberlin, P. C. 2006, *JGRA*, **111**, A10S14
- Wu, Y., Chen, H., Tian, H., et al. 2022, *ApJ*, **928**, 180
- Yamashiki, Y. A., Machara, H., Airapetian, V., et al. 2019, *ApJ*, **881**, 114
- Yashiro, S., & Gopalswamy, N. 2009, in *IAU Symp. 257, Universal Heliophysical Processes*, ed. N. Gopalswamy & D. F. Webb (Cambridge: Cambridge Univ. Press), 233
- Zacharias, N., Finch, C. T., Girard, T. M., et al. 2013, *AJ*, **145**, 44
- Zhu, Y., Kowalski, A. F., Tian, H., et al. 2019, *ApJ*, **879**, 19
- Zic, A., Murphy, T., Lynch, C., et al. 2020, *ApJ*, **905**, 23